UNIVERSITY OF SOUTHAMPTON

in the
Faculty of Engineering, Science and Mathematics
School of Ocean and Earth Science

Palaeoclimatology, stratigraphy and biotic responses in the Middle Eocene

by

Kirsty M. Edgar

A thesis submitted for the degree
of Doctor of Philosophy

September 2008

UNIVERSITY OF SOUTHAMPTON

ABSTRACT

FACULTY OF ENGINEERING, SCIENCE AND MATHEMATICS
SCHOOL OF OCEAN AND EARTH SCIENCE

Doctor of Philosophy

PALAEOCLIMATOLOGY, STRATIGRAPHY AND BIOTIC RESPONSES IN THE MIDDLE EOCENE

by Kirsty M. Edgar

The Middle Eocene (37 to 49 million years ago, Ma) was characterised by warmer global temperatures and higher atmospheric carbon dioxide (pCO_2) levels than today with only small/non-existant icesheets. Because predicted pCO_2 levels for the coming century have not been seen on Earth since at least ∼40 Ma thus, the primary objective of this thesis is to improve our understanding of the nature, timing and consequences of carbon perturbations in the Middle Eocene between 39 and 43 Ma.

In Chapter 3, a new (instrument specific) methodology for measuring Mg/Ca in foramin–iferal calcite is developed to enable the simultaneous measurement of additional trace elements indicative of foraminiferal test contamination. This new methodology enables Mg/Ca data to be screened more efficiently for contamination and increases confidence in palaeoceanographic reconstructions based on the Mg/Ca palaeotemperature proxy.

In Chapter 4, new foraminiferal stable isotope records (∼5 kyr resolution) from Demerara Rise in the equatorial Atlantic are generated to test the hypothesis that the onset of continental ice sheets in the Northern Hemisphere occurred at ∼41.6 Ma in the Middle Eocene, 30 million years earlier than previously thought. The new data herein, indicate that if continental ice sheets were present, they were small and easily accommodated on Antarctica with no need to invoke storage of ice in the Northern Hemisphere.

The dearth of appropriate Middle Eocene sedimentary sections on which to work means that a well calibrated timescale for this interval remains to be produced. In Chapters 5 and 6, this problem is addressed using Middle Eocene sediments recovered from the Blake Nose plateau in the western North Atlantic. A new high resolution magnetic stratigraphy and new quantitative foraminiferal biostratigraphic counts were developed between 39.5 and 42.0 Ma, which allows re-assessment and refinement of previous magnetostratigraphic and biostratigraphic interpretations. This provides excellent age control for these sediments and new calibrations to the Geomagnetic Polarity Time Scale (GPTS).

In Chapter 7, the first high-resolution quantitative planktic foraminiferal assemblage counts were developed for the global warming event the Middle Eocene Climatic Optimum (MECO) between ∼39.5 and 41.5 Ma. New biotic records show that the MECO was accompanied by significant biotic shifts that suggest a shift from warm, oligotrophic surface waters to warmer, more productive surface waters during the MECO.

Contents

List of Figures

List of Tables

Declaration of Authorship

I, KIRSTY MARIE EDGAR declare that the thesis entitled "Palaeoclimatology, stratigraphy and biotic responses in the Middle Eocene" and the work presented in the thesis are both my own, and have been generated by me as the result of my own original research. I confirm that:

- this work was done wholly or mainly while in candidature for a research degree at this University;
- where any part of this thesis has previously been submitted for a degree or any other qualification at this University or any other institution, this has been clearly stated;
- where I have consulted the published work of others, this is always clearly attributed;
- where I have quoted from the work of others, the source is always given. With the exception of such quotations, this thesis is entirely my own work;
- I have acknowledged all main sources of help;
- where the thesis is based on work done by myself jointly with others, I have made clear exactly what was done by others and what I have contributed myself;
- parts of this work have been published as: **Edgar, K. M.**, Wilson, P. A., Sexton, P. F. and Suganuma, Y. No extreme bipolar glaciation during the main Eocene calcite compensation shift. *Nature*, 448:908-911, 2007.

Signed:

Date:

Acknowledgements

There are a number of people who have had a substantial impact on both me and my work during the course of my PhD whom I would like to thank.

First of all, to my supervisor Paul Wilson who has played a major role in making my time at Southampton so enjoyable. He has been an enthusiastic and supportive supervisor who has always encouraged me to take advantage of available opportunities. Despite the increasing demands on Paul's time in the last few years, he has always been happy to make time to look at new data sets and talk science. Armed with his trusty red pen, he has also provided excellent tutelage on scientific writing while trying to elucidate some of the intricacies of the English language to me (with limited success).

Phil Sexton spent many hours teaching me the 'ropes' in the lab and his enthusiasm for foraminifer taxonomy was contagious. He was also very patient putting up with my many, many questions during the early stages of my PhD before he migrated to sunny California.

Big thanks to Samantha Gibbs who has been a good friend and mentor during my time at Southampton. She went above and beyond the call of duty and read first drafts, some rather awful, of the majority of chapters in this thesis and provided valuable constructive criticisms that were much appreciated.

Dick Norris was an excellent and generous host during my three month visit to Scripps. He welcomed me into his lab and research group and included me in all activities including a fossil hunting fieldtrip to Nevada. He was an abundant source of knowledge and his boundless enthusiasm for a huge range of topics (including Harry Potter) was inspiring.

Thanks also to Heiko Pälike for inviting me to participate in the AMAT-03 cruise in 2006. This was an amazing experience that allowed me to to gain insight into the extensive behind-the-scenes work that is required to recover deep sea sediments, make new friends, visit some beautiful islands and also served to increase my enthusiasm to pursue a career in research.

Chris German helped to set up this PhD project before he migrated to WHOI.

I would like to extend a big thank you to all the people that have provided essential technical assistance, support and advice during my PhD. Mike Bolshaw provided training on the operation of the mass spectrometer. Dave Spanner helped to keep the mass spec lab running smoothly and efficiently. Richard Pearce for assistance on the scanning electron microscope. Matt Cooper provided general advice on geochemical problems, training in trace metal analysis and read an earlier draft of Chapter 3. Darryl Green provided essential technical guidance on the intricacies of the ICP-OES, interpreting

data sets and training on the various elements of ICP-OES method development. Andy Roberts for his expertise and advice on interpreting palaeomagnetic data sets and to Greig Patterson for his assistance on various instruments, keeping the palaeomagnetism lab running smoothly and formatting data sets.

Special thanks to Rebecca Bell, Jo Hopkins, Suzanne Maclachlan, Sarah Bennett, Tamzin Palmer, Chris Nicolle, Chris Jeffery, David Poulter and Mark Vardy for making my time in Southampton so memorable. Also to David Spofforth, Clara Bolton and Jennifer Stanford. It wouldn't have been the same without you guys.

I would also like to thank my parents who have been an endless source of support over the past few years.

This PhD benefited from conversations with Steve Bohaty, Ollie Friedrich, Kazuyoshi Moriya, Toby Tyrell, Heiko Pälike, Eelco Rohling, Helen Coxall, Carrie Lear, Dick Norris, Sam Gibbs, Phil Sexton and Suzanne Maclachlan.

Financial support for this work was provided by a NERC postgraduate studentship and a CASE studentship from Perkin Elmer. This work used samples provided by the Ocean Drilling Program.

Chapter 1

Introduction

1.1 Rationale for Eocene studies

Partial pressures of atmospheric carbon dioxide (pCO_2) predicted for the coming century (Meehl et al., 2007) have not been seen on Earth since the Eocene (Pagani et al., 2005), more than 40 million years ago (Ma) when the Earth was much warmer than today and was host to small or non existent continental ice sheets (Fig. 1.1). Close coupling of atmospheric pCO_2 and global temperature observed in records at the present day (Meehl et al., 2007) and in palaeoclimate records (Petit et al., 1999; Royer et al., 2001, 2004; Lüthi et al., 2008) indicates the need to increase our knowledge of climate and carbon cycle variability during past globally warm, high pCO_2 intervals and impacts on the Earth system in order to identify and quantify future feedbacks related to rising pCO_2.

1.2 Eocene Climate

The Eocene Epoch (34 - 55 Ma) represents an important interval in the evolution of Earth's climate from the extreme greenhouse warmth of the early Paleogene towards its modern regime of bipolar ice sheets (Fig. 1.1b) (Miller et al., 1991; Lear et al., 2000; Zachos et al., 2001). Yet, until relatively recently, we knew very little about the nature of this interval except on multi-million year timescales.

The Early Eocene was characterised by global climate substantially warmer than at the present day with either no or only very small continental ice sheets (Zachos et al., 1994, 2001). During the Early Eocene climatic optimum (EECO) between about 50 and 52 Ma, summer surface water temperatures in the Arctic Ocean are thought to have reached up to ∼20°C (Sluijs et al., 2006), an interpretation supported by the presence of fossil crocodilians and turtles in the Arctic circle and deciduous forests found up to 85°N

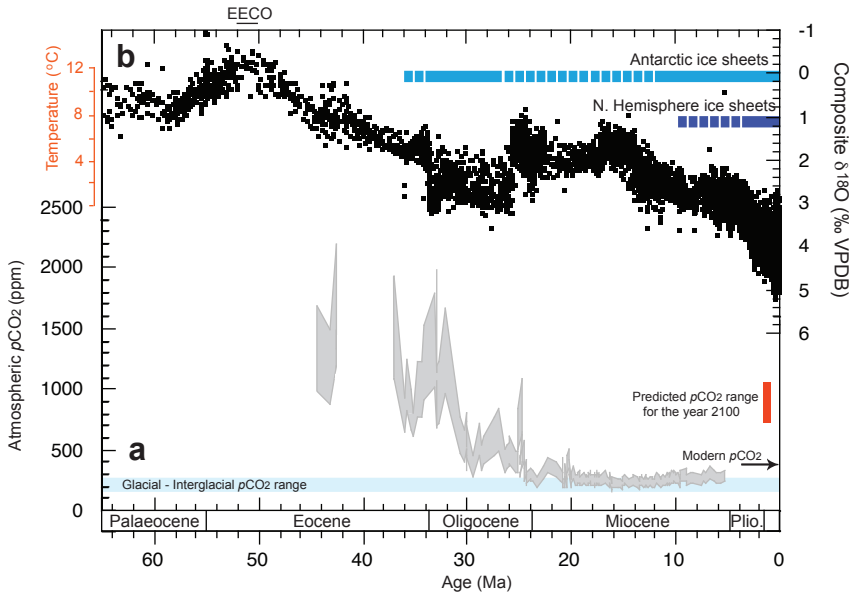

FIGURE 1.1: Cenozoic proxy records of atmospheric carbon dioxide and palaeotemperature. a) Alkenone based pCO_2 reconstruction (Pagani et al., 2005), calculated values are in broad agreement with those estimated using other pCO_2 proxies (Ekart et al., 1999; Pearson and Palmer, 2000; Berner and Kothavala, 2001; Demicco et al., 2003; Royer et al., 2004). Pale blue shaded region indicates the range of pCO_2 for the last 800 thousand years of Earth's history recorded in polar ice cores from Antarctica (Petit et al., 1999; Lüthi et al., 2008). Red bar highlights the range of pCO_2 values predicted for the year 2100 (Meehl et al., 2007). b) Global composite oxygen isotope record from benthic foraminiferal calcite, figure modified from Zachos et al. (2001). Horizontal blue bars show the standard view of the presence and extent of full scale/permanent ice sheets (solid bar) and those thought to have been partial/ephemeral (broken bar). EECO = Early Eocene Climatic Optimum.Temperature scale computed for ice-free ocean thus, only applicable for the time preceding the onset of large scale Antarctic glaciation at ∼34 Ma. Figure modified from Edgar et al. (2007).

(Wolfe, 1985; Greenwood and Wing, 1995; Markwick, 1998). Fossil and proxy evidence indicate severely reduced latitudinal thermal gradients in the Early Eocene compared to today most likely a response to high greenhouse gas concentrations in the atmosphere, mainly CO_2, which is estimated to have been 4 to 5 times higher than pre-anthropogenic pCO_2 levels (Pearson and Palmer, 1999; Ekart et al., 1999; Pearson and Palmer, 2000; Demicco et al., 2003; Pagani et al., 2005), plus continental configurations that increased atmospheric and ocean heat transport to high latitudes (Barron, 1985, 1987; Barron et al., 1993; Bice et al., 2000).

Following the EECO, Earth's baseline climate cooled substantially through the Middle and Late Eocene (Shackleton and Kennett, 1975; Miller et al., 1987; Barrera and Huber, 1991; Diester-Haass and Zahn, 1996; Lear et al., 2000; Zachos et al., 2001) eventually resulting in the onset of the first permanent continental ice sheets on Antarctica close to the Eocene-Oligocene boundary at ∼34 Ma (Fig. 1.1b) (Lear et al., 2000; Zachos et al., 2001; Coxall et al., 2005; Katz et al., 2008). Decreasing atmospheric pCO_2 is invoked as

the major cause of long-term climate deterioration (Raymo and Ruddiman, 1992; Berner et al., 1983; DeConto and Pollard, 2003; Huber et al., 2004), although Earth's orbital configuration (DeConto and Pollard, 2003; Coxall et al., 2005) and perhaps continental palaeogeography, i.e., the opening of ocean gateways (Kennett, 1977) also played a role.

Prior to the 1990's the relative paucity of continuous sedimentary successions from the Eocene and thus, availability of high-resolution palaeoceangraphic records led to the misleading impression that the Eocene was marked by only relatively gradual changes in global climate (Shackleton and Kennett, 1975; Miller et al., 1987; Barrera and Huber, 1991). In addition, the lack of available sections in which both magnetic and bio- stratigraphies are available has hindered the development of reliable age models at many deep sea sites. Thus, development of a reliable integrated biomagnetochronologic time scale (IBMS) for the Eocene remains elusive, yet is a fundamental prerequisite for palaeoceanographic studies to determine rates of change and the age order of events at widely separate sites.

Recent advances in our technological capabilities and new multi-hole drilling strategies to generate composite sections, have enabled the recovery of more continuous, expanded and shallowly buried Eocene sediments in which high-resolution records can be generated. These records have shed new light on the nature of the greenhouse-icehouse transition and indicate that the Eocene was characterised by significant climatic variability associated with changes in global carbon cycling on much shorter-time scales than previously appreciated. In particular, superimposed on the long-term Middle Eocene cooling trend are a number of transient warming events, e.g., between ∼44 and 42 Ma (Sexton et al., 2006a) and at 40 Ma (S. Bohaty, oral pers. comm., 2007) the Middle Eocene Climatic Optimum (MECO) (Bohaty and Zachos, 2003), and transient cooling events that may have been associated with the onset of the first small transient ice sheets on Antarctica as a pre-cursor to events at the Eocene-Oligocene boundary (Lyle et al., 2005). This finding is in conflict with the traditional view that past globally warm intervals were climatically relatively 'stable' and emphasises the need to better understand climate 'stability' in past warm, high pCO_2 worlds. The primary objective of this thesis is to improve our understanding of the nature, timing and consequences of carbon cycle perturbations of the Middle Eocene (39 - 43 Ma).

1.3 Thesis aims and outline

The specific aims of Chapters 3 through 7 are as follows.

1.3.1 Chapter 3: Optimization of an inductively coupled plasma-optical emission spectrometry method for the determination of trace metals in foraminiferal calcite.

1) Develop a methodology for measuring trace metals with low concentrations in foraminiferal calcite by inductively coupled plasma-optical emission spectrometry.

Trace metal ratios derived from foraminiferal calcite are increasingly utilised as proxies for palaeoenvironmental parameters with Mg/Ca, a palaeothermometer, one of the most important and widely applied (for deconvolving the dual temperature and oxygen isotopic composition of seawater signals recorded in the $\delta^{18}O$ of foraminiferal calcite). Increasingly, the importance of measuring additional trace metals alongside the desired Mg/Ca and Sr/Ca values has been recognised as an important way of screening values for contamination not removed during the cleaning process. **Chapter 3** aims to determine the optimum set-up on a dual view Perkin Elmer Inductively Coupled Plasma-Optical Emission Mass Spectrometer (ICP-OES) to facilitate the high-precision and accurate measurement of Mg, Ca and Sr in foraminiferal calcite simultaneously with the trace elements Al, Mn, Fe and Ti. These trace elements are introduced into the methodology in order to screen foraminiferal samples for contamination by either an oxide coating (Mn and Fe) or residual silicate material (Al, Fe and Ti).

1.3.2 Chapter 4: No extreme bipolar glaciation during the main Eocene calcite compensation shift

2) Evaluate the hypothesis that large transient continental ice sheets were present in both hemispheres close to the top of magnetochron C19r (∼41.6 Ma) in the Middle Eocene.

3) Document the link between transient carbon cycle perturbations and global climate change in magnetochrons C18 and C19.

The paradigm view is that the first large, permanent continental ice sheets of the Cenozoic developed on Antarctica at ∼34 Ma (Miller et al., 1991; Lear et al., 2000; Zachos et al., 2001) and that significant ice sheets did not develop in the Northern Hemisphere until much later between ∼11 and 5 Ma (Miller et al., 1991; Zachos et al., 2001; Holbourn et al., 2005). This view has recently been challenged by new records of ice rafting at high northern latitudes in the Eocene (Moran et al., 2006; Eldrett et al., 2007), the possibility of continental ice stored outside of Antarctica in the early Oligocene (Coxall et al., 2005), and geochemical records hypothesised to represent the onset of large continental ice sheets in both hemispheres around the top of magnetochron C19r (∼41.6 Ma) in the

Middle Eocene (Tripati et al., 2005). In **Chapter 4** the bipolar glaciation hypothesis is tested by generating new palaeoceanographic records in monospecific planktic and benthic foraminiferal calcite from the Atlantic Ocean. Deep-sea sediments recovered from ODP Site 1260 drilled in the tropical Atlantic are utilised because they provide an expanded sedimentary record across the critical interval that is host to well preserved benthic foraminifera. Revised ice volume budgets for the Middle Eocene are calculated using the new stable isotope records generated in this Chapter.

1.3.3 Chapter 5: Magnetic reversal stratigraphy of ODP Site 1051, Blake Nose

4) Refine and re-evaluate the existing magnetic stratigraphy at ODP Site 1051 between magnetochrons C19 and C17 (39.5 - 42.0 Ma).

The development of good age models at deep sea sites is fundamental in palaeoceanography to determining rates of change and the age order of events between widely spaced sites. However, the development of good age models at deep sea sites and thus, construction of a reliable geological time scale is hindered in the Middle Eocene (Pälike and Hilgen, 2008) by a lack of continuous sections on which to work and weak palaeomagnetic signals typically recorded by many carbonate-rich sediments in the Paleogene. In **Chapter 5** a new high-resolution magnetic reversal stratigraphy is generated for a ∼2.5 million year interval of the Middle Eocene at ODP Site 1051 in the western North Atlantic. This Chapter focuses on Site 1051 because existing low resolution magnetic stratigraphy, magnetochron boundaries resolved to $\geq \pm 2.5$ m, indicate that the sedimentary succession is relatively complete, at least to magnetochron level (Shipboard Scientific Party, 1998; Ogg and Bardot, 2001), and has a readily detectable magnetic signal but most importantly it hosts a complete planktic foraminiferal biozone E12 and the MECO. Thus, Site 1051 offers a unique opportunity to refine the existing magnetic stratigraphy and to improve the calibration of the biostratigraphic datums that occur in this interval to the Geomagnetic Polarity Time Scale (GPTS).

1.3.4 Chapter 6: Refining planktic foraminiferal biozone E12

5) Assess the reliability of datums defined by Orbulinoides beckmanni *and improve their calibration to the Geomagnetic Polarity Time Scale.*

The correlation of biostratigraphic datums to the GPTS in the Middle Eocene are particularly poorly constrained because of the lack of continuous sedimentary records and poor or no magnetic stratigraphy available at sites through this interval. In particular, the interval containing planktic foraminiferal biozone E12, defined by the first (FO) and last occurrence (LO) of the short-lived species *Orbulinoides beckmanni*, is rarely completely recovered because of a near global hiatus in many sedimentary sections close to the magnetochron C18r/18n boundary (∼40 Ma) and the absence of this marker species at higher latitudes. Biozone E12 is stratigraphically important because its divides what would otherwise be a 4 million interval of geological time and is a good stratigraphic marker for the MECO. In **Chapter 6**, the first high-resolution and quantitative abundance records of the planktic foraminiferal biomarker species *O. beckmanni* are presented. With these records, the reliability of *O. beckmanni's* FO and LO as biostratigraphic datums are assessed and used in conjunction with the new magnetic stratigraphy generated in Chapter 5 to improve the existing calibration to the GPTS. These records help to shed light on the palaeoecology, biogeography and evolutionary history of this species.

1.3.5 Chapter 7: Planktic foraminiferal response to the Middle Eocene Climatic Optimum

6) Document the ecological, environmental and evolutionary signals associated with the MECO using planktic foraminifera.

Our knowledge of how marine organisms respond to past global warming events is rather limited. Given current concerns over the fate of the marine biosphere in response to anthropogenically forced increases in pCO_2 this sort of information has never been more pertinent. The majority of high-resolution biotic studies in the fossil record thus far, have focussed on large scale carbon cycle perturbations such as the PETM, which is associated with prominent shifts in the composition of marine plankton assemblages (Kelly et al., 1996; Bujak and Brinkhuis, 1998; Bralower, 2002; Gibbs et al., 2006). But we know little about how marine organisms fared across transient events during other intervals of time characterised by different background conditions. Therefore, we don't yet know whether or not there are any common ecological signals that are associated with carbon-cycle led climate perturbations that may infer a common causal mechanism or even if there are major differences that may imply the existence of tolerance thresholds within the biotic response of organisms. **Chapter 7** aims to try and fill in some of the gaps in our knowledge by generating high-resolution abundance records of the major components of the planktic foraminiferal assemblage across the MECO. Two low latitude sites, ODP Sites 1051 and 1260 are utilised in this study to (1) document the response of the

planktic foraminifera to any environmental changes at the MECO and (2) determine any similarities and/or differences in the biotic response at low latitude. These records also permit comment on the likely global implications of the MECO.

Thesis chapters have been written with the view to being independently submitted for publication (subject to further work on some chapters), thus, there is some unavoidable repetition of text between chapters. Every effort has been made to keep this repetition to a minimum.

Chapter 2

Methods

2.1 Preparation of deep sea sediments

Sediment samples (20 cc in volume) were placed in a glass volumetric flask, with the exception of a small 'thumbnail' sized piece of bulk sediment retained from each sample in the original sample bag. The volumetric flask and sample were weighed and then dried in an oven at 50°C until no further weight loss was recorded, typically for 2 to 3 days, in order to obtain the sediment dry bulk weight. 100 ml of deionised water was added to each sample flask 30 minutes prior to sample washing, to aid disaggregation. Samples were then washed through a 63 μm sieve and the $\geq$63 μm size 'coarse' fraction was left to dry in the oven at 50°C overnight, weighed and then stored in glass vials. This method of sediment preparation allowed a coarse fraction record to be generated.

2.2 Methods for stable isotope analysis

2.2.1 Oxygen isotope systematics

There are three stable isotopes of oxygen (^{16}O, ^{17}O and ^{18}O) with abundances of 99.7630%, 0.0375% and 0.1995% respectively. The isotope ratio ^{18}O/^{16}O is normally determined in oxygen isotope studies because of the larger mass difference and higher natural abundances of ^{16}O and ^{18}O. Stable oxygen isotope ratios are reported using delta notation (δ^{18}O), as per mil (‰) relative to an international standard (equation 2.1), most commonly the Vienna PeeDee Belemnite (VPDB) standard (δ^{18}O and δ^{13}C = 0) for calcium carbonate samples (Epstein et al., 1953). A positive δ value indicates enrichment of the heavier isotope, relative to the standard and conversely, depletion of the heavier isotope is shown by a negative δ value.

$$\delta^{18}O = \frac{^{18}O/^{16}O_{sample} - \ ^{18}O/^{16}O_{standard}}{^{18}O/^{16}O_{standard}} \times 1000 \quad (2.1)$$

All carbon and oxygen stable isotope measurements presented in this thesis were determined on a PDZ Europa GEO 20-20 mass spectrometer equipped with a carbonate automated preparation system (CAPS). Samples are loaded into quartz vials and then placed into the sample carousel in the CAPS. The carousel in the CAPS holds 19 samples and five standards. Three standards are placed at the front of the carousel and two at the back to calibrate the sample isotopic values and correct for instrumental drift during the instrument run. Calcium carbonate samples are reacted with phosphoric acid (H_3PO_4) to produce carbon dioxide (CO_2) gas and water vapour (H_2O). The water vapour is removed by passing the CO_2 gas through a water trap maintained at -90°C. The dried CO_2, which has a much lower freezing point than H_2O, is cryogenically frozen into the inlet cold finger maintained at -180°C with liquid nitrogen. Small sample volumes ($\leq$ 180 μm) are analysed directly from the inlet cold finger whereas larger samples are transferred to an intermediary bellows system which controls the specific volume of sample gas subsequently analysed. Sample gas from either of these pathways is then carried into the mass spectrometer. The evolved CO_2 is ionized by electron bombardment derived from an electron source creating CO_2^+. The CO_2^+ are then focussed into an ion beam and accelerated past an electromagnet through a curved flight tube. The electromagnetic field causes the ions to diverge according to their mass and charge, with lighter ions most strongly deflected. After passing through the electromagnetic field, the separated ion beams are collected in three Faraday collector buckets, allowing the measurement of three different ion beams simultaneously, specifically $^{44}CO_2$, $^{45}CO_2$ and $^{46}CO_2$ molecules. The dual inlet system enables the isotopic composition to be measured by multiple comparisons of the ratio of the sample ion beam intensity to a reference gas of known isotopic composition (Mattey, 1997).

The 'raw' δ^{18}O values measured by the mass spectrometer require correction prior to conversion to the VPDB scale. The first correction, accounts for temperature dependent isotope fractionation between the δ^{18}O of the carbonate sample and the δ^{18}O of the evolved CO_2 (McCrea, 1950). The second, 'Craig' correction accounts for the presence of the rare ^{17}O isotope, which is included in the two mass ratios $^{45}CO_2/^{44}CO_2$ and $^{46}CO_2/^{44}CO_2$ measured by the mass spectrometer (Craig, 1965). δ^{18}O values can then be expressed relative to VPDB, based on replicate analysis of an in-house standard (SC-1) calibrated to NBS-19, with an external analytical precision of better than 0.1‰ for δ^{18}O and δ^{13}C.

All foraminiferal stable isotope (δ^{18}O and δ^{13}C) values presented in this thesis are on species separates of benthic and planktic foraminifera. Poorly preserved or broken individuals were not selected for analysis. All benthic foraminifera were picked from the size range 300 - 450 μm with as many whole individuals used as possible, up to a maximum

of 12 but typically 5 or less (∼150 to 600 μg). Planktic foraminifera were picked from the 250 - 300 μm size fraction and between 8 and 12 individuals were analysed (∼100 to 150 μg). All foraminifera were cleaned ultrasonically in deionised water prior to stable isotope analysis. Attempts were made to keep foraminiferal sample weights fairly constant to ensure that all samples ran in the same part of the instrument under similar conditions minimising any potential instrumental noise.

2.2.2 Oxygen isotope palaeothermometry

The precipitation of calcium carbonate (equation 2.2) from water, under equilibrium conditions, results in an isotopic offset between the two phases as a result of isotope exchange reactions. The isotopic fractionation factor (α) between calcium carbonate and water (equation 2.3) is temperature dependent (McCrea, 1950). The relationship between temperature and the oxygen isotope composition of carbonate ($\delta^{18}O_c$) was first empirically derived by McCrea (1950) but subsequently, there have been a number of revisions based on laboratory studies of both biologically and inorganically precipitated carbonate (Epstein et al., 1953; Craig, 1965; O'Neil et al., 1969; Erez and Luz, 1983; Kim and O'Neil, 1997; Bemis et al., 1998). However, the standard form of the equation describing the temperature-$\delta^{18}O_c$ relationship is shown in equation 2.4. Coefficients a, b and c are constants defined experimentally (Table 2.1). The oxygen isotopic composition of water ($\delta^{18}O_w$) is determined on CO_2 gas in equilibrium with the sample water at a constant temperature usually 25°C (Epstein and Mayeda, 1953) and is normally reported relative to Vienna Standard Mean Ocean Water (VSMOW) but can be related to the VPDB scale using equation 2.5 (Coplen et al., 1983). The overall effect of equilibrium isotope fractionation on the calcium carbonate-water system is equivalent to approximately 0.25‰ depletion in $\delta^{18}O_c$ for every 1°C temperature increase (Kim and O'Neil, 1997).

$$Ca^{2+} + 2HCO_3^- \Leftrightarrow CaCO_3 + CO_2 + H_2O \tag{2.2}$$

$$\alpha = \frac{^{18}O/^{16}O_{calcite}}{^{18}O/^{16}O_{water}} \tag{2.3}$$

$$T(^\circ C) = a + b(\delta^{18}O_c - \delta^{18}O_w) + c(\delta^{18}O_c - \delta^{18}O_w)^2 \tag{2.4}$$

$$\delta^{18}O_{PDB} = (0.97006 * \delta^{18}O_{VSMOW}) - 29.94 \tag{2.5}$$

TABLE 2.1: Comparison of commonly used calcite temperature: $\delta^{18}O$ relationships. Coefficient a is temperature when $\delta^{18}O_c$ - $\delta^{18}O_w = 0$, b is the slope, and c is the second order term for curvature (not always included) (Lea, 2004). PF and BF = planktic and benthic foraminifera, respectively. lab = laboratory culture based calibrations. The low light *Orbulina universa* calibration of Bemis et al. (1998) works well for warm water studies. For colder waters and certain benthic foraminiferal species the calibration of Shackleton (1974) is more appropriate.

Reference	Source	a	b	c
McCrea (1950)	Inorganic	16.0	-5.17	0.09
Epstein et al. (1953)	Mollusk	16.5	-4.30	0.14
O'Neil et al. (1969)	Inorganic	16.9	-4.38	0.10
Shackleton (1974)	BF	16.9	-4.00	-
Erez and Luz (1983)	PF (lab)	17.0	-4.52	0.03
Kim and O'Neil (1997)	Inorganic	16.1	-4.64	0.09
Bemis et al. (1998)	PF (lab)	16.5	-4.80	-

The oxygen isotope composition of calcium carbonate is, in part, controlled by the temperature of the water from which it precipitates. However, $\delta^{18}O_c$ is also a function of the $\delta^{18}O_w$ from which the carbonate precipitates. Seawater $\delta^{18}O_w$ can differ both temporally and spatially from from SMOW ($\delta^{18}O_w = 0‰$). Temporal variability in seawater $\delta^{18}O_w$ is largely determined by changes in continental ice volume, because the lighter isotope of oxygen (^{16}O) is preferentially stored in ice sheets leaving the remaining seawater preferentially enriched in the heavier (^{18}O) isotope. Additionally, spatial variations in seawater $\delta^{18}O_w$ arise from variations in the evaporation-precipitation ratio.

2.2.3 Carbon isotope systematics

Two stable isotopes of carbon occur in nature: ^{12}C and ^{13}C with abundances of 98.9% and 1.1%, respectively. The $^{13}C/^{12}C$ isotope ratio of a sample is measured and compared to the $^{13}C/^{12}C$ of a known standard. Carbon isotope ($\delta^{13}C$) values are reported as per mil (‰) difference relative to the VPDB standard (equation 2.6). Unlike for $\delta^{18}O$ no corrections are required to the raw $\delta^{13}C$ value prior to conversion to the VPDB scale. The $\delta^{13}C$ in marine calcite is controlled by the dissolved inorganic carbon (DIC) (Equation 2.7) of the seawater from which the carbonate precipitates. The biological carbon pump redistributes DIC and nutrients within the ocean via phytoplankton. Phytoplankton fix CO_2 into organic matter via photosynthesis, fractionating ^{12}C in preference of the heavier ^{13}C isotope (Park and Epstein, 1960), giving organic matter an average $\delta^{13}C$ of -20 to -23‰ VPDB (Hoefs, 1997) relative to surrounding waters which are enriched in ^{13}C. Thus, the top ∼100 m of the water column where photosynthesis is focussed becomes progressively enriched in ^{13}C and depleted in ^{12}C with increased productivity. In turn, carbonates precipitated from surface waters where dissolved carbon is strongly enriched in $\delta^{13}C$ will record the $\delta^{13}C$ enrichment. As organic matter sinks through the

water column and is remineralised, ^{12}C is released back into the water column and thus, carbonates precipitated at depth record lighter δ^{13}C values than those precipitated in surface waters. Thus, the biological pump effectively transfers ^{12}C from the surface to deep waters.

$$\delta^{13}C = \frac{^{13}C/^{12}C_{sample} - \ ^{13}C/^{12}C_{standard}}{^{13}C/^{12}C_{standard}} \times 1000 \tag{2.6}$$

$$DIC = CO_2(aq) + H_2CO_3 + HCO_3^- + CO_3^{2-} \tag{2.7}$$

2.3 Determining bulk sediment weight percent $CaCO_3$

Prior to analysis, bulk sediment samples (approximately 1 cm^3 in volume) were dried in an oven at 50°C for 48 hours, then ground into a powder using a mortar and pestle, and stored in glass vials ready for analysis. Bulk sediment weight percent $CaCO_3$ data was measured by high-precision coulometry on a UIC model 501 coulometer. Calibration of the instrument is performed using a pure, dried $CaCO_3$ standard, run at the beginning and end of each day, after each standard a blank is measured to check the instruments calibration. Additional measurements of the $CaCO_3$ standard were made between every 10 samples to assess instrument drift during the day. To determine the weight percent $CaCO_3$ ∼20 - 25 mg of sample is weighed out and placed in a glass reaction vial. The sample is reacted with 5 ml of 10% phosphoric acid liberating CO_2 from the sample. Evolved CO_2 is then passed into the coulometer cell, which is filled with a solution of ethanolamine and a colorimetric indicator (blue). CO_2 is absorbed by the solution and reacts with the ethanolamine to form a strong acid, causing the indicator colour to fade. The titration current is automatically activated and electrically generates a base to return the solution to its original colour. The electrical charge required to do this is displayed as a 'count' on the coulometer's digital screen. This 'count' is then normalised to the sample mass and cross-referenced with a standard to generate % inorganic carbon. Precision on sample measurements is ±0.5%.

2.4 Trace metal analysis

All trace metal data presented in this thesis were generated on a Perkin Elmer Optima 4300DV (Dual View) Inductively Coupled Plasma - Optical Emission Spectrometer (ICP-OES) equipped with a Perkin Elmer AS93plus autosampler (Fig. 2.1). Optimum emission wavelengths, detection limits, plasma viewing orientation, sample presentation system and detector measurement times for the determination of Mg/Ca and Sr/Ca in foraminiferal calcite simultaneously with the trace elements Al, Mn, Fe and Ti, to

monitor the efficiency of the oxidative cleaning procedure, are presented in Chapter 3. The sample is presented as a solution and is taken up by the autosampler and pumped by the peristaltic pump along a narrow tube to the nebuliser, where the sample is mixed with the carrier gas (Ar) to form an aerosol, making it easier for the sample to react in the plasma (Figure 2.1) (Perkin Elmer, 2002). The aerosol is then transferred into the spray chamber, where the sample droplets are sorted according to their size. Large droplets are removed from the sample mist and disposed of at this point to prevent them reaching the plasma where they may cause 'spiking' and adversely affect precision, smaller droplets are carried via the injector into the torch. The torch is comprised of three concentric quartz tubes; the central tube is the injector, which introduces the sample aerosol to the plasma, the second intermediate tube introduces the auxillary gas, which maintains the position of the plasma, and the final outer tube introduces a stream of argon gas, which is ignited to form the plasma. A solid-state radio frequency (RF) generator supplies RF energy at 40 MHz to a copper induction coil around the top end of the torch generating a high-frequency Tesla spark that ignites the argon gas from the torch generating the argon plasma which has a temperature of ∼6,000 to 10,000 K. The cooler end of the plasma tail is removed from the optical path by a shear gas, a 'thin wall' of of high-velocity air, to minimise interferences. The sample dissociates in the plasma and atoms are excited and ionised, once the atoms or ions are in their excited states, the subsequent decay of electrons to a lower, more stable energy state causes a particle of electromagnetic radiation or a photon (light) to be emitted. The wavelength of the photon released is unique to an element, each element is capable of a variety of energy states and thus emission wavelengths. However, the emission wavelength emitted by an element can overlap with those of other elements (Wang, 2004). Photons emitted from the plasma pass through an optical window, which can view the plasma 'radially' (side-on) or 'axially' (end-on), and into the spectrometer where the photons are focussed into a beam by a series of mirrors and through the entrance slit onto an Echelle polychromator, which separates the light into its component wavelengths. The separated emission wavelengths then travel to the Segmented-array Charge-coupled device (SCD) detector, which comprises hundreds of discrete sub-arrays each with between 20 and 80 photosensitive areas or 'pixels' strategically placed to capture specific individual emission wavelengths enabling the simultaneous measurement of thousands of different emission and background wavelengths between 165 - 782 nm. The signal intensity recorded by the targeted pixel for each emission wavelength is then converted to the concentration of that element in the sample by comparison with a calibration curve determined by a suite of calibration standards (Perkin Elmer, 2002).

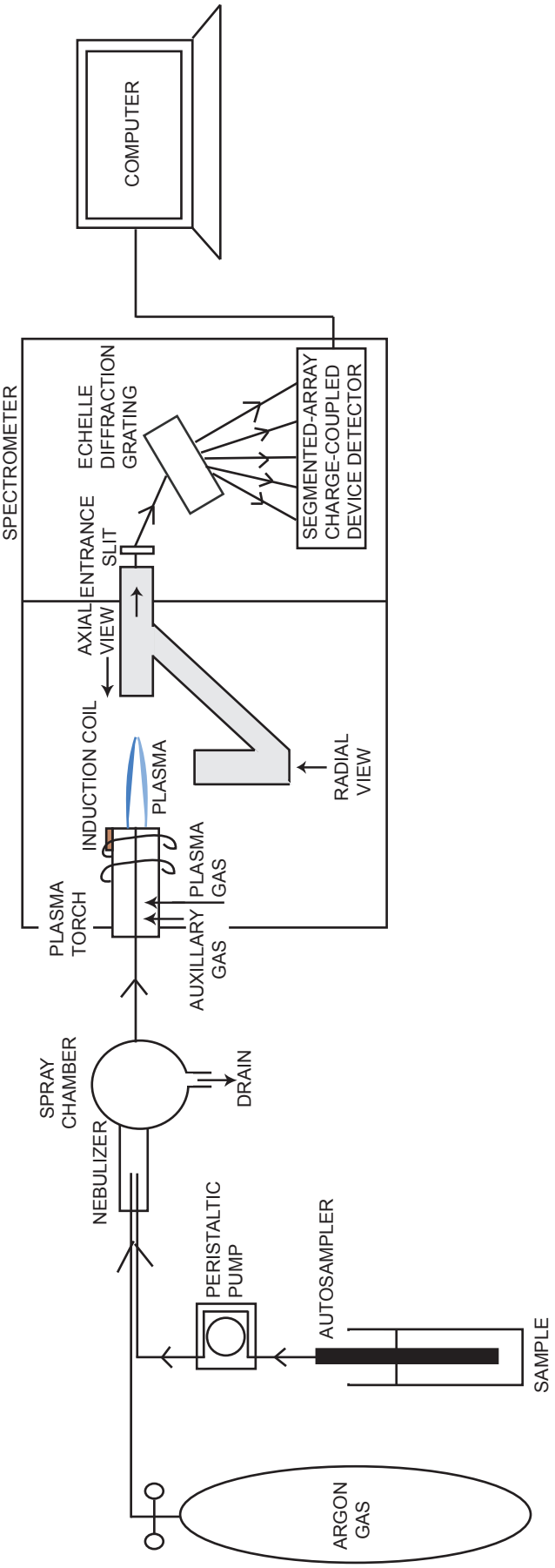

FIGURE 2.1: Simplified schematic illustration of the Perkin Elmer 4300DV Inductively Coupled Plasma-Optical Emission Spectrometer used in this study.

2.5 Planktic foraminiferal assemblage counts

Sediment samples were prepared as outlined in section 2.1. Inspection of segregated size fractions from the ≥63 μm 'coarse' fraction of a number of ODP Site 1051 samples, demonstrated that the the major components of the planktic foraminiferal assemblage and their response to the Middle Eocene Climatic Optimum could be identified in the ≥ 300 μm size fraction. The ≥300 μ size fraction of all samples was 'split' between 1 and 6 times until approximately 400 to 500 planktic foraminifera remained. Counts were made with a minimum of 350 individuals for samples from ODP Site 1051, Blake Nose and 400 individuals for ODP Site 1260, Demerara Rise. These values were considered the threshold above which % relative abundance data was representative of the planktic foraminiferal assemblage as a whole, based on rarefaction or 'collector's' curves developed for ODP sites 1051 and 1260 in this study (Figs 2.2 and 2.3 respectively).

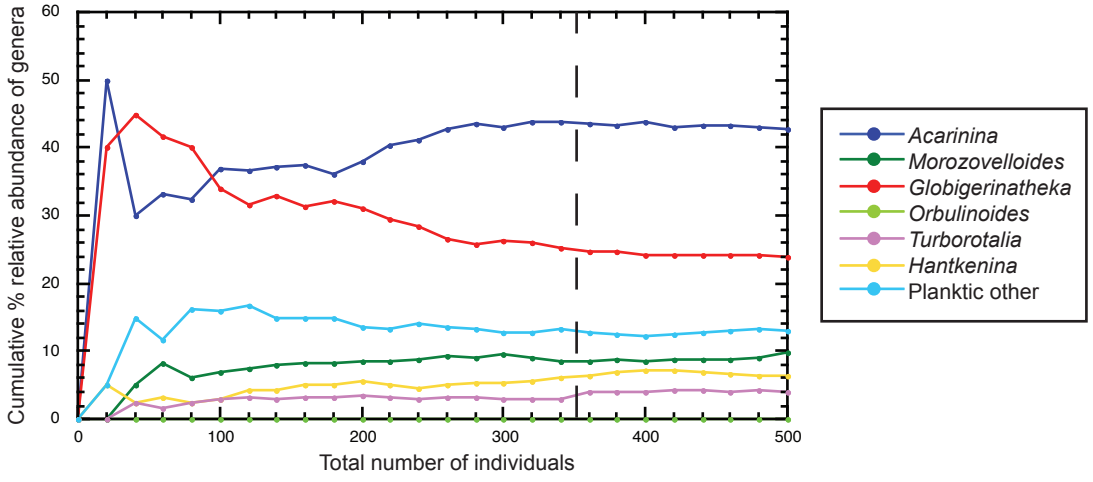

FIGURE 2.2: Rarefaction curve for ODP Site 1051. Plot of cumulative % relative abundance for planktic foraminiferal genera of interest against number of individuals counted in 1051A 11H-3 28.5-30.0 cm. Counts with less than 200 individuals show a large degree of variability in the % relative abundance calculated for each genera, indicating that counts with a small number of foraminifera are not representative of the assemblage. When more than 350 individuals are counted (vertical dashed line), the % relative abundance for each genera shows no further large changes and is consequently considered to be representative of the assemblage as a whole. Rarefaction curves assume random foraminifera distribution on the counting tray.

The Middle Eocene planktic foraminferal genera counted in the sample split of the ≥300 μm size fraction were *Morozovelloides, Acarinina, Hantkenina, Turborotalia, Subbotina* and *Globigerinatheka*. The planktic foraminfera species *Orbulinoides beckmanni* was also counted to refine the planktic biozone E12 (Pearson et al., 2006). All other genera were included in 'planktic other'. Taxonomic concepts were based on Pearson et al. (2006). Biotic data are presented as % relative abundance data.

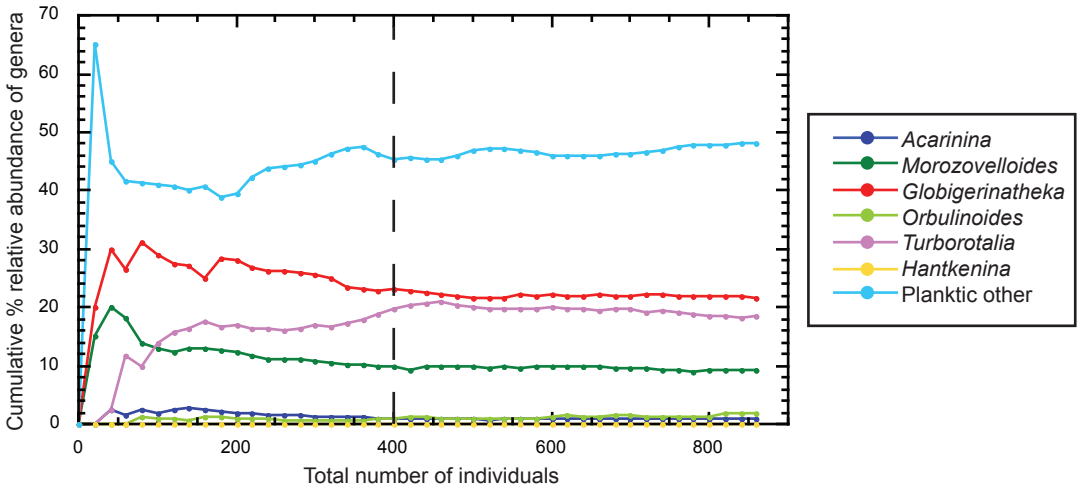

FIGURE 2.3: Rarefaction curve for ODP Site 1260. Plot of cumulative % relative abundance for planktic foraminiferal genera of interest in this study against number of individuals counted in 1260A 6R-2 147.0-148.5 cm. Counts with less than 200 individuals show a large degree of variability in the % relative abundance calculated for each genera, indicating that counts with a small number of foraminifera are not representative of the assemblage. When more than 400 individuals are counted (vertical dashed line), the % relative abundance for each genera levels shows no further large changes and is consequently considered to be representative of the assemblage as a whole. Rarefaction curves assume random foraminifera distribution on the counting tray.

2.5.1 Statistical analyses

Principle component analysis (PCA) is used to reduce the number of variables in the dataset to those that describe the largest amount of variation, i.e., identify the main variables that control the dominant patterns in the assemblage. The first principal component accounts for the largest amount of the variability in the signal, and each succeeding component accounts for as much of the remaining sample variability as possible. PCA was carried out using the programme *Primer*.

2.5.1.1 Diversity indices

The simplest measure of diversity is species richness, i.e., the number of species in any given sample. However, this not appropriate for the data set collected here in which a set number of planktic foraminiferal genera and biostratigraphically important species were counted. The *Shannon-Weiner index* (Equation 2.8) is another common diversity index frequently employed that incorporates both species richness and evenness providing a measure of the uncertainty in the sample, i.e., how difficult is it to predict correctly the species of the next individual picked, with low values relating to a low number of taxa with high abundances and higher values to samples with many taxa,

each with few individuals (Magguran, 1988). In this study Shannon-Weiner values are used to calculate the *Equitability* index (Equation 2.9) to better understand the pattern of diversity. Equitability provides a measure of the evenness with which individuals are distributed amongst the genera present in the sample. Equitability values range from 0 to 1. An equitability of 0 indicates that the assemblage is monospecific, i.e., the most extreme uneven population, and a value of 1 infers that the species are all present in equal proportions in the assemblage (Harper, 1999).

The Shannon-Weiner index is defined here as

$$H = -\Sigma(lnp_i) \tag{2.8}$$

Where H = Shannon-Weiner diversity index, p_i = proportion of the total sample represented by species i or in this case total sample represented by genera i.

The *Equitability* index is defined as

$$E = e^H/S \tag{2.9}$$

Where E = Equitabililty index, H = Shannon-Weiner index and S = the number of species (or in this study genera).

2.6 Determination of Natural Remanent Magnetism

Natural Remanent Magnetism (NRM) was measured on u-channels and discrete samples (8 cm^3 in volume) to reconstruct a palaeomagentic reversal stratigraphy for ODP Site 1051, Blake Nose. Samples were run on the 2-G cryogenic magnetometer using alternating field (AF) demagnetisation. This technique involves exposing the sample to an alternating magnetic field which linearly decreases in magnitude from a selected peak value to zero (Fig. 2.4). During each alternating cycle the magnetic moments or magnetisation of the grains with coercivities[1] less than the maximum magnetic field strength applied are cancelled out (demagnetising the sample at this field strength). Thus, only grains with a coercivity exceeding the peak magnetic field strength applied are preserved (Roberts, 2006).

The first of three axial (x, y and z) demagnetisation coils in the magnetometer is ramped up to the desired magnetic field strength and the sample is passed through the demagnetisation coil and an AF field that decays linearly in space (Fig. 2.4). Once the sample is demagnetised at the peak field strength, the magnetic field is reduced to zero and the

[1] coercivity is defined as the intensity of the magnetic field required to reduce the magnetization of a sample to zero (McElhinny and McFadden, 2000)

same process is repeated for the next two axial demagnetisation coils at the same field strength. The sample is then carried via a moving track into the superconducting quantum interference device (SQUID) sensors, which are immersed in liquid helium (∼4 K), and the NRM of the sample is measured. The weak paleomagnetisation of the sample induces a small dc current in the SQUID, which is measured and is proportional to the magnetisation of the sample. The sample is then demagnetised at progressively higher magnetic field strengths (in this study peak magnetic fields applied at 5, 10, 15, 20, 25, 30, 35, 40, 50 and 60 mT) and the remaining NRM is measured after each step. The magnetic signal carried by sediment u-channels is smoothed by a ∼10 cm moving window on the magnetometer, consequently, the first and last 5 cm of each u-channel were not included in the final data-set to avoid edge effects (Roberts, 2006). All u-channels were run through the magnetometer in the same orientation.

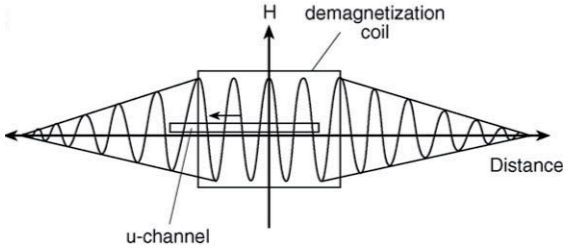

FIGURE 2.4: Alternating field (AF) demagnetisation through linear decay of magnetic field in space. Sample moved through demagnetisation coil that maintains peak field strength (H) for the duration of the sample's movement. Illustration not to scale from Fig. 3b in Roberts (2006).

2.6.1 Plotting demagnetisation datasets

NRM usually consists of two components: a primary component acquired during the rock/sediment formation (via thermoremanent, chemical or detrital magnetisation), this is the desired parameter in magnetic studies, and a secondary component acquired following rock formation that can modify or mask the primary NRM (e.g. drilling overprints or viscous remanent magnetism) (Gubbins and Herrero-Bervera, 2007). AF demagnetisation progressively removes the low-stability components typically secondary components by exposing the sample to increasingly large magnetic field strengths, leaving behind the more stable primary NRM. The easiest way of presenting stepwise demagnetisation data to identify primary and secondary NRM components is in a Zijderveld diagram (Fig. 2.5).

Zijderveld diagrams are a type of vector component plot that displays both magnetic intensity and directional data measured during stepwise demagnetisation of samples (Zijderveld, 1967). The base of each NRM vector measured is placed at the origin of the plot and projected onto two orthogonal planes with axes N, E, S, W and N, S, Up and Down respectively. The distance of the point from the origin is proportional to the

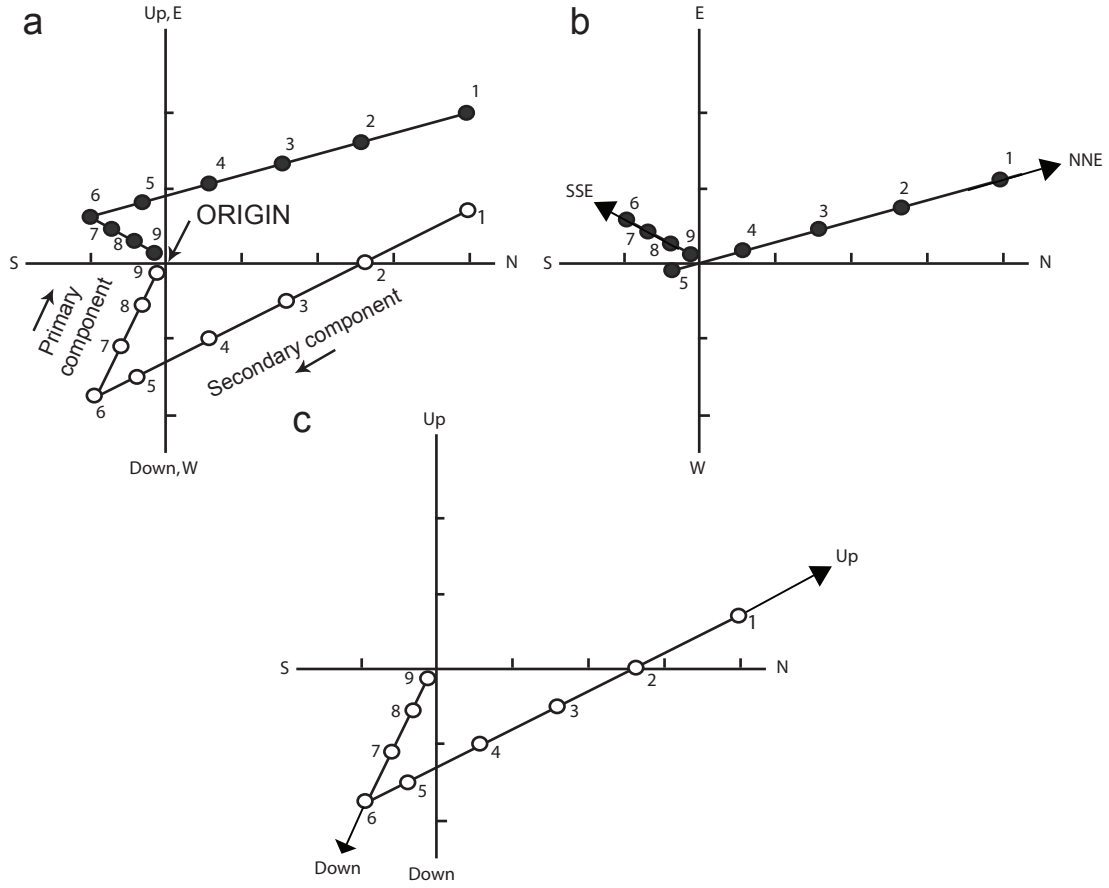

FIGURE 2.5: a) Zijderveld diagram showing demagnetisation behavior of sample with two NRM components. b) Declination is read in the horizontal plane (solid points). The first component (steps 1-6 in the demagnetisation procedure) represent a single secondary component in a NNE direction. The second primary component (steps 6-9 in the demagnetisation procedure) a SSE direction. c) Inclination is read in the vertical plane (open circles). Secondary NRM component (steps 1-6) has an upward inclination. The primary NRM component (steps 6-9) has a steep downward direction (McElhinny and McFadden, 2000).

intensity of that NRM vector (lowest intensities typically closest to the origin) (Butler, 1992). Zijderveld diagrams are created automatically for each sample in the computer programme *Z-plot*.

Declination is the angle between the magnetic field at a point on the Earth's surface and true north, values vary from 0-360° and inclination is the angle of the geomagnetic field relative to the surface of the Earth with a value between 0 and 90°. The solid data points numbered 1-9 on Figure 2.5b represent the endpoints of each demagentisation step projected onto the horizontal plane with the axes N, S and E, W. The declination of any NRM component, represented by a straight line in the Zijderveld diagram, can be determined by the direction of the line in the horizontal plane imagined to commence from the origin (Fig. 2.5b). For example, points 1-5 have an NNE orientation and do not decay towards the origin representing the removal of secondary NRM component. Steps 6-9 indicate a SSE NRM direction and the points decay towards the origin representing

the primary NRM component. Whereas the inclination is the angle of the geomagnetic field relative to the surface of the Earth with a value between 0 and 90°. The NRM vectors are projected onto the vertical plane containing the axes N, S and Up-Down. Inclination is represented by the open points in Figure 2.5c. Here points 1-6 have an upward secondary NRM orientation and steps 6-9 indicate a downward direction of the primary NRM component (McElhinny and McFadden, 2000).

Principal component analysis (PCA) was used to estimate the best least-squares regression line fit along the demagnetisation paths plotted on the Zijderveld diagram (Kirschvink, 1980), in other words the inclination and declination of the best fit line. A minimum of three successive data points thought to represent the primary NRM signal were selected for PCA, e.g., points 6-9 in Fig. 2.5. The precision of the best fit line was estimated by the maximum angular deviation (MAD). Generally lines with a MAD value of $\geq 15^{\circ}$ are thought to represent unstable magnetic behaviour and are generally excluded from palaeomagnetic studies, whereas those with a MAD value $\leq 10^{\circ}$ represent more reliable and stable magnetic behaviour, as shown in Figure 2.5 (Butler, 1992; McElhinny and McFadden, 2000).

2.6.2 Determination of Anhysteretic Remanent Magnetism

Anhysteretic remanent magnetisation (ARM) is a laboratory induced magnetism, imposed on a sample by applying a weak, constant dc magnetic field through the solenoid inside the z-axis demagnetisation coil in the 2-G magnetometer, during normal AF demagnetisation (Roberts, 2006). This is a destructive technique, that involves demagnetising the sediment with a very large magnetic field (90 mT) removing the NRM. The sample is then remagnetised at 0.05 mT, equivalent to the Earth's magnetic field strength, aligning all the magnetic carriers in the sediment in the same orientation, along the z-axis. The sample is then subjected to increasing magnetic AF strengths (in this study peak magnetic fields applied were 10, 20, 25, 30, 40 and 60 mT) remagnetising the magnetic carriers in the sample with a coercivity less than or equal to the applied field strength, along the z-axis. The difference in remanent magnetisation of the sample is measured after each step as described in section 2.7 (Gubbins and Herrero-Bervera, 2007).

Chapter 3

Optimization of an inductively coupled plasma-optical emission spectrometry method for the determination of trace metals in foraminiferal calcite

3.1 Introduction

The trace element chemistry of foraminiferal tests is frequently employed to reconstruct palaeoceanographic conditions. In particular, Mg/Ca ratios measured in foraminiferal calcite are a valuable tool for reconstructing palaeotemperatures in the ocean (Nürnberg et al., 1996; Rosenthal et al., 1997; Elderfield and Ganssen, 2000; Lear et al., 2000). The Mg/Ca proxy is based on the temperature dependent partitioning of Mg between calcite (biogenic and inorganic) and the water from which it precipitates, with increasing water temperature associated with increasing Mg content in calcite, an increase of ∼9% in Mg/Ca per °C for biogenic carbonate (Nürnberg et al., 1996; Lea et al., 1999; Elderfield and Ganssen, 2000) but only ∼3% per °C for inorganic carbonate (Katz, 1973). The correlation between increasing water temperature and Mg content in calcite arises because the substitution of Mg into calcite is endothermic, i.e., requires energy in the form of heat for the reaction to proceed, and thus is favored at higher temperatures (Chilingar, 1962; Katz, 1973). The Mg/Ca proxy is widely utilised because both stable oxygen isotopes (δ^{18}O) and Mg/Ca can be measured in foraminiferal calcite allowing the deconvolution of the dual temperature - δ^{18}O of seawater ($\delta^{18}O_{sw}$) contributions to the δ^{18}O signal recorded in calcite (Lear et al., 2000; Billups and Schrag, 2002; Lear et al., 2008). Extraction of the $\delta^{18}O_{sw}$ signal is crucial to understanding the evolution

of global climate, salinity variations and changes in global continental ice volume (Lear et al., 2000; Billups and Schrag, 2003; Lear et al., 2004, 2008). Sr/Ca measurements also derived from foraminiferal calcite, are routinely obtained as a bi-product of Mg/Ca analysis. Sr/Ca can be used to reconstruct long term changes in seawater Sr/Ca reflecting relative changes in contributions from continental and hydrothermal sources (Graham et al., 1982; Lear et al., 2003), although other factors such as seawater temperature, dissolution and as yet unspecified environmental factors may also be important (Stoll and Schrag, 1998; Stoll et al., 1999; Elderfield and Ganssen, 2000).

There are a number of factors that can bias the primary Mg/Ca in foraminiferal calcite leading to inaccurate palaeoclimate reconstructions, these include (1) the post-mortem addition of diagenetic calcite (Boyle, 1981, 1983), (2) selective dissolution of calcite (Rosenthal et al., 2000; Dekens et al., 2002), and (3) the presence of contaminant phases (Boyle, 1983; Barker and Elderfield, 2001; Barker et al., 2003; Pena et al., 2005). In particular, the presence of contaminant phases such as Mn-rich carbonate overgrowths, Mn-Fe oxide coatings, residual silicate material and clay particles are considered to be a problem for trace element analyses because they contain high abundances of additional trace elements, most importantly Mg. The effect of these contaminant phases on foraminiferal Mg/Ca are not well constrained but initial studies indicate a bias towards warmer palaeotemperature estimates by about 2 to 6°C (Boyle and Keigwin, 1985; Pena et al., 2005).

Currently, two main cleaning methodologies are in use for the removal of these contaminants: an 'oxidative' cleaning protocol and an 'oxidative/reductive' cleaning protocol. The oxidative cleaning protocol comprises a number of clay removal steps, an (oxidative) organic matter elimination step followed by a weak acid leaching (Elderfield and Ganssen, 2000; Barker et al., 2003). The more stringent cleaning method includes an additional reductive step aimed at removing Mn-Fe oxides from the foraminifera test (Boyle and Keigwin, 1985; Martin and Lea, 2002). The additional reductive step enables the measurement of Cd data, a palaeoproductivity proxy and watermass tracer (Boyle, 1988; Rosenthal et al., 1997), and appears to produce less noisy downcore records (C. H. Lear, oral pers. comm., 2007) but results in a loss of sample mass and reduces Mg/Ca values by up to 15% through partial dissolution of the sample, creating a potential bias towards cooler palaeotemperature estimates (Barker et al., 2003). It is unclear whether primary biogenic calcite or Mn-Fe oxide coatings are removed in this way. Since the contribution of Mg from Mn rich-carbonates and oxides is considered reasonably small (∼2-5%, Pederson and Price, 1982) the oxidative method is often adopted in Mg/Ca work because it is more conducive to samples with few foraminifera and is less time consuming. It is therefore essential that elements indicative of contamination are also measured to assess the efficiency of the cleaning methodology employed.

The effect of contamination on Mg/Ca ratios will vary significantly between samples and locations. For example, foraminifera from cold regions or deep waters will have low

Mg values and will be more prone to significant contamination than foraminifera from warmer locations and with higher Mg contents. Specific trace elements that can be measured in foraminiferal calcite to help screen for contamination are Mn, Fe, Al, Ti and Si. High concentrations of these elements or trace element/calcium ratios measured in foraminiferal calcite are frequently associated with elevated Mg/Ca values in downcore records and thus, provide important indicators of contamination. For example, high Mn/Ca values are indicative of the presence of an authigenic Mn-Fe oxide coating or Mn-rich carbonate on the foraminiferal test (Boyle, 1981, 1983), whereas high Fe/Ca ratios observed in foraminiferal samples may be from either a Mn-Fe oxide coating on the foraminiferal test or residual silicate material (Boyle and Keigwin, 1985; Barker et al., 2003). Examination of the Mn/Fe ratio enables the contamination source to be distinguished because silicate contamination will have significantly lower Mn/Fe ratios $\sim$0.05 mmol/mol than Mn-Fe oxide coatings $\geq$1 mmol/mol (Barker et al., 2003). Therefore, it is advantageous to also measure elements that are unique to clays and other silicate minerals, such as Al, Si or Ti, to indicate aluminosilicate contamination (Barker and Elderfield, 2001; Barker et al., 2003).

Palaeoceanographic problems increasingly involve large sample sets and it is important to develop reliable analytical techniques that enable both rapid sample throughput and high analytical precision. Inductively coupled plasma-optical emission spectrometry (ICP-OES) offers such a technique. It has a broad linear working range able to deal with the orders of magnitude concentration differences between calcium and minor or trace elements in foraminiferal calcite, while offering the advantages of high sample throughput and reasonable operating costs. However, the main advantage of ICP-OES over other techniques, e.g., inductively coupled plasma-mass spectrometry (ICP-MS) or flame absorption spectrometry, is the simultaneous determination of a large number of analytes, yielding improved accuracy and precision of values, and enabling much smaller sample sizes to be utilised. Reported precisions on Mg/Ca and Sr/Ca ratios in foraminiferal calcite by ICP-OES are typically less than 1% (Green et al., 2003; De Villiers et al., 2002; Wara et al., 2003; Andreasen et al., 2006). Recently, the importance of measuring trace elements alongside Mg/Ca and Sr/Ca data, to screen ratios for contamination, has been emphasized (Barker et al., 2003) and a number of laboratories are now adapting their methodologies to incorporate useful additional trace elements (Wara et al., 2003; Greaves et al., 2005; Andreasen et al., 2006).

At the National Oceanography Center, Southampton (NOCS) a novel high dilution technique has been developed with an instrument set-up specifically optimised for the determination of high-precision ($\leq$0.2%) Mg/Ca and Sr/Ca values in foraminiferal calcite (Green et al., 2003). Foraminiferal calcite samples are typically dissolved in HNO_3 and sample solutions made up with [Ca] between 1 and 5 ppm which enables the use of much smaller foraminiferal calcite samples than other techniques. It is relatively easy to ensure sample solutions fall within the required 1 to 5 ppm [Ca] range without the necessity

of performing two separate measurements on the ICP-OES, an initial rough assessment of the [Ca] content in the sample so that the sample can be prepared to fall within a set [Ca] range for the second main analytical measurement. Also, because only a small quantity of sample solution is required for each analysis, replicate measurements on the same sample can be made. Thus, the key objective of this chapter is to adapt/develop a methodology to facilitate the accurate high-precision measurements of Mg, Ca and Sr in foraminiferal calcite together with elements that might indicate contamination of the foraminiferal test by either an oxide coating (Mn and Fe) or residual silicate material (Al and Fe initially, Ti added later) by dual view ICP-OES. This involves determining the optimum instrument settings and sample presentation hardware for these measurements.

3.2 Methods

3.2.1 Instrumentation and operating conditions

All data presented in this chapter were generated using a Perkin Elmer Optima 4300 DV (Dual View) ICP-OES equipped with a Perkin Elmer AS93plus autosampler at NOCS (Fig. 2.1) (for instrument specifications see Table 3.1). Two different sample presentation systems, comprising a nebulizer coupled to a cyclonic spray chamber, were investigated in this study. A Glass Expansion "Conikal" nebulizer was selected for all instrument runs, because of its intermediate sample up-take rate suited to small foraminiferal samples (Green et al., 2003), and was coupled to either a Glass Expansion, "Twister" (baffled) or a "Tracey" (unbaffled) cyclonic spray chamber. A low volume cyclonic spray chamber was selected because this design has (1) a rapid washout time, facilitating rapid sample throughput and (2) yields higher precisions on element determinations and lower detection limits for trace elements than reported for other spray chamber designs (Maestre et al., 1999). A carrier gas flow rate of 0.7 L/min was adopted for the "Conikal" nebulizer based on work by Green et al. (2003) indicating that the peak signal-to-noise ratio for the most sensitive Mg and Ca wavelengths were obtained at this flow rate. The ICP-OES was configured to view the plasma radially for the more sensitive calcium, strontium and magnesium wavelengths (Table 3.2), to prevent saturation of any pixel on the detector array. Where possible, the emission lines were measured both radially and axially to determine the optimum viewing orientation for emission wavelengths. Aluminum, manganese, iron, titanium and the remaining magnesium and calcium wavelengths were viewed axially to take advantage of the greater sensitivity offered by this orientation, which is important when measuring samples with low concentrations and/or elements with low analytical sensitivities.

TABLE 3.1: Instrument settings for analytical runs on the Perkin Elmer Optima 4300 DV Inductively Coupled Plasma-Optical Emission Spectrometer.

Parameter	Setting
RF power	40 MHz
Argon plasma gas flow rate	0.70 L/min
Auxillary gas flow rate	1.40 L/min
Nebulizer gas flow rate	1.00 ml/min
Nebulizer	Glass Expansion, "Conikal"
Spray chamber	Glass Expansion, cyclonic spray chamber "Twister" or "Tracey"
Detector read time	10 s

TABLE 3.2: Emission lines and plasma viewing modes used in this study. Starred (*) Al emission lines were not measured in Runs 1 to 4 because of their low sensitivity for determination by ICP-OES and/or spectral interferences.

Element	λ (nm)	Plasma Viewing Mode(s)
Mg	280.2	Axial and Radial
Mg	279.5	Axial and Radial
Mg	285.2	Axial
Ca	315.9	Axial and Radial
Ca	317.9	Radial
Ca	422.7	Radial
Sr	407.7	Radial
Sr	421.5	Radial
Al	308.2*	Axial
Al	394.9*	Axial
Al	396.2	Axial
Mn	257.6	Axial
Mn	259.4	Axial
Fe	238.2	Axial
Fe	239.6	Axial
Fe	259.9	Axial
Ti	334.9	Axial
Ti	336.1	Axial
Ti	337.3	Axial

3.2.2 Solution preparation and typical analytical run

To minimise background contamination of test solutions and calibration standards by trace elements, low density polyethylene (LDPE) bottles and lids were (1) leached in 8 M HNO_3 for at least 72 hours, (2) rinsed three times in 18.2 MΩ Milli-Q water®, and (3) left to dry in a laminar permanent flow hood immediately prior to use. This study utilises synthetic multielement solutions to investigate the optimum instrument parameters and settings for the determination of trace element/calcium ratios in foraminifera. Element concentrations in calibration standards and test solutions are provided in the text. Calibration standards were made with different trace element/calcium ratios and with element concentrations bracketing sample concentrations. All multielement solutions and calibration standards were prepared gravimetrically using high purity Merck single-element Aristar® grade standard solutions, to minimise background intensities of trace elements, Romil SpA® nitric acid and 18.2 MΩ Milli-Q water®. Each instrument run consisted of a set of calibration standards followed by a number of test solutions, with a maximum number of 180 solutions capable of being handled by the autosampler in any single run, of which ∼150 could be samples. Typically only 50 to 80 solutions were used in any single instrument run (5 - 6 hr instrument run). Instrument drift within and between individual runs was monitored and measured values corrected using a synthetic multielement solution intially run after the calibration standards but thereafter between every ten samples. Either side of the drift monitor, measurements were made of a 'blank' solution (0.075 M HNO_3), the same acid used for sample dissolution and dilution, to check for any possible contamination. Ten replicate blank samples were also measured at the end of each run to calculate the limits of detection (LOD) and quantification (LOQ) for emission wavelengths. A minimum of 5 ml of solution was used to ensure correct uptake by the autosampler.

3.3 Results

3.3.1 Element sensitivity, limits of detection and quantification

High precision measurements of trace elements are analytically challenging because of (1) low trace element concentrations in foraminiferal tests, and (2) a large degree of variability in the instrument sensitivity to different element emission wavelengths. Therefore, this first experiment aims to determine the limits of detection (LOD) and quantification (LOQ) for the elements Al, Mn and Fe initially, to investigate the capabilities of the ICP-OES and determine the most sensitive element emission wavelengths for analysis. Ca, Mg and Sr are not included in this initial experiment because of the high sensitivity of these elements for determination by ICP-OES, their high relative abundance in foraminiferal calcite compared to Al, Mn, Fe and Ti, and low detection limits for these

elements by ICP-OES making them relatively easy to measure. Barker et al. (2003) defined trace element/calcium ratio values above which Mg/Ca data determined in the same foraminiferal sample should be discarded, 'rejection' values are 0.4 mmol/mol of Al/Ca, 0.02 mmol/mol of Mn/Ca and 0.1 mmol/mol of Fe/Ca. These rejection criteria provide a good starting point for investigating the ICP-OES limits because it is essential that the methodology employed should be sufficiently sensitive, to at least determine these values. While the rejection criteria of Barker et al. (2003) are a useful guide, absolute trace element/calcium values at which Mg/Ca data are considered suspect may vary significantly between samples and localities. An initial assessment of the LOD and LOQ, for each of the trace elements Al, Mn, and Fe on the ICP-OES, were determined using a set of three test solutions (Table 3.3). Each test solution was 'spiked' with Al, Mn and Fe with similar concentrations to those expected in real foraminiferal samples based on the rejection criteria of Barker et al. (2003) but without Ca. The instrument was calibrated using synthetic multielement solutions (Table 3.4).

TABLE 3.3: Trace element concentrations in test solutions used to determine the limits of detection and quantification for this study. Values in bold represent the test solutions in which the trace element/calcium rejection ratios defined by (Barker et al., 2003) can be measured quantitatively (see Table 3.5).

Test Solution	Al (ppb)	Fe (ppb)	Mn (ppb)
1	0.31	0.16	0.03
2	1.74	0.87	**0.16**
3	**3.04**	**1.51**	**0.29**

TABLE 3.4: Calibration standards used to derive calibration correlation coefficients of trace element emission wavelengths investigated in this study. Note that element concentrations are higher in the calibration standards than those in the test solutions (Table 3.3) to ensure a good calibration.

Standard	Al (ppb)	Fe (ppb)	Mn (ppb)
Std 1	31.560	2.972	15.678
Std 2	59.437	5.597	29.526
Std 3	124.967	11.742	61.945
Std 4	260.814	24.558	129.563
Std 5	616.936	58.091	306.471

The results of this initial investigation are shown in Table 3.5 which shows the LODs and LOQs for each of the investigated element emission wavelengths, calculated as three and ten times the standard deviation of the ten replicate blank determinations at the end of the instrument run, respectively. Mn has two sensitive emission lines (257.6 and 259.4 nm) that are readily determined by ICP-OES, as evidenced by their low LOD and LOQ values. The three emission lines for Fe investigated (238.2, 239.6 and 259.9 nm) all show similar LOD and LOQ values. Al has the highest LODs and LOQs calculated

TABLE 3.5: Limits of detection and quantification (LOD and LOQ) for emission wavelengths determined in test solutions 1 to 3 on the ICP-OES. Values in bold indicate the most sensitive emission wavelength for each element. r^2 = calibration correlation coefficients, used to assess instrument linearity.

Element & λ (nm)	View	LOD (ppb)	LOQ (ppb)	r^2
Al 396.147	Axial	0.67	2.23	0.999998
Al 308.21	Axial	4.41	14.71	0.999954
Al 394.97	Axial	0.62	2.08	0.999991
Mn 257.603	Axial	0.04	0.13	0.999996
Mn 259.366	Axial	0.04	0.13	0.999997
Fe 238.198	Axial	0.27	0.91	0.999997
Fe 239.564	Axial	0.25	0.82	0.999996
Fe 259.932	Axial	0.29	0.95	0.999997
Ti 334.93	Axial	0.04	0.12	0.999927
Ti 336.10	Axial	0.04	0.14	0.999897
Ti 337.261	Axial	0.07	0.22	0.999969

in this study, reflecting the low sensitivity for determination of this element by ICP-OES generally. For this reason, Al is frequently omitted from measurements of biogenic calcite by ICP-OES. In addition, Al can only be measured using the axial viewing mode on the ICP-OES, which maximises the number of atoms observed and increases the emission line count but this viewing option is not available on all ICP-OES instruments (Andreasen et al., 2006). Of the three Al emission lines investigated, the line at 308.2 nm is the least sensitive with LODs ∼7 times higher than the other two Al emission wavelengths (394.4 and 396.1 nm) and is hereafter omitted from this study, as is the 394.4 nm line because of potentially large spectral interferences with Ca. Subsequent instrument runs in later experiments enabled the determination of the LOD and LOQ for Ti, included in Table 3.5. Ti is a more sensitive element for determination by ICP-OES than Al, with a very low LOD value for two separate wavelengths (334.9 and 336.1 nm) and is therefore in principle at least more suited to screening Mg/Ca data for evidence of silicate contamination.

Comparison of Tables 3.3 and 3.5 demonstrate that, in test solution 1, trace element concentrations are below the LOD and the LOQ of the ICP-OES and can not be measured, whereas in test solution 2 trace element concentrations are sufficiently above the LOD but not the LOQ and therefore precisions are poor (≥10% RSD). It is only in test solution 3, that the concentrations of Al, Mn and Fe in the test solution can be quantified. Limits of quantification for the most sensitive emission wavelength for each element are given in Table 3.5 and correspond to element ratio quantification limits for a solution at [Ca] = 10 ppm of Al/Ca, 0.33 mmol/mol, Mn/Ca, 0.009 mmol/mol, Fe/Ca, 0.06 mmol/mol and Ti/Ca, 0.01 mmol/mol, all sufficiently below the rejection criteria of Barker et al. (2003). Element ratio concentrations are shown for [Ca] of 10 ppm because this is the concentration at which all four elements could be quantitatively measured.

As element concentrations approach the LOD and LOQ for an elements emission wavelength, calculated precisions become progressively poorer, e.g., ≥10% (RSD), for test solutions 1 and 2, compared to ≤3% (RSD) in test solution 3 in which element concentrations are above the LOQ, because the signal is increasingly dominated by background noise and spectral interferences.

This experiment indicates that, while the methodology currently adopted at NOCS for determining Mg/Ca and Sr/Ca data involving dilution of samples to a [Ca] range of 1 to 5 ppm, is excellent for generating high-precision Mg, Ca and Sr data (Green et al., 2003), it is unsuited to measurement of Al, Mn, Fe and Ti, which typically have low concentrations in these sorts of samples. To quantitatively measure the new trace elements requires working with samples at much higher [Ca] ≥10 ppm and thus, with higher trace element concentrations. This requires the development of a new technique for the ICP-OES at NOCS and the re-assessment of the ideal instrument set up and parameters to optimise the measurement the new trace elements Al, Mn , Fe and Ti while still maintaining a high level of precision on the desired Mg/Ca and Sr/Ca ratios.

3.3.2 Instrument Linearity

To assess the optimum sample presentation system and instrument settings for the determination of the trace elements Al, Mn, Fe and Ti on the ICP-OES, four instrument runs were carried out (Runs 1 - 4). Two different sample presentation systems were tested; "Conikal" nebulizer/"Tracey" spray chamber and "Conikal" nebulizer/"Twister" spray chamber combinations, and different instrument integration times were applied (Table 3.6). In each of the runs two sets of calibration standards were employed, both with a similar range of [Ca] (10 to 100 ppm) but different trace element concentrations to assess the range over which the most linear calibrations were obtained. One set of calibration standards have low trace element concentrations and are referred to as 'low' and the other set of calibration standards with higher trace element concentrations are labeled 'high' (Table 3.7). Each of the calibration standards were prepared with different Mg:Sr:Al:Mn:Fe:Ti:Ca ratios across a range of [Ca] to test the linearity of all of the analytes as fully as possible. It is important that calibration standards are made up with different element ratios to prevent a linear calibration arising solely from the doubling of element concentrations that may incorporate any contamination or interferences associated with the sample.

Instrument linearity is particularly important for accurately determining element ratios over the wide range of element concentrations found in foraminiferal samples. The Perkin Elmer ICP-OES typically shows very good linearity over a large range of element concentrations (Perkin Elmer, 2002), this is demonstrated by the high calibration correlation coefficients (r^2) ≥0.99999 obtained for the elements Al, Mn and Fe (in matrix free standards) (Table 3.5). The calibration correlation coefficient of Ti, determined in

TABLE 3.6: Instrument set-up and settings adopted for Runs 1 - 4. C/Tr ="Conikal" nebulizer and "Tracey" spray chamber, C/Tw = "Conikal" nebulizer and "Twister" spray chamber. All integration times were set manually following preliminary measurements of several of the calibration standards (see Section 3.3.3). Integration times in Runs 3 and 4 were doubled relative to Runs 1 and 2, to account for the loss of instrument sensitivity associated with use of the "Twister" spray chamber.

Setting	Run 1	Run 2	Run 3	Run 4
Sample presentation system	C/Tr	C/Tr	C/Tw	C/Tw
Read time	10 s	10 s	10 s	10 s
Integration time	10 ms	Ca, Mg & Sr = 10 ms Mn = 10 ms Al, Fe & Ti = 1 s	20 ms	Ca, Mg & Sr = 20 ms Mn = 20 ms Al, Fe & Ti = 2 s

TABLE 3.7: High and Low calibration standards employed in Runs 1 through 4 to determine calibration correlation coefficients. Starred (*) standards were both run ten times in Runs 1 - 4 to assess instrument precision. DM = Drift monitor, used in all instrument runs to correct measurements for drift. The first four standards denoted by the suffix 'L' are the 'low' set of calibration standards. Horizontal dashed lines denote element not included to assess matrix effects, interferences and any contamination.

Standard	Mg	Ca	Sr	Al	Mn	Fe	Ti
	ppb	ppm	ppb	ppb	ppb	ppb	ppb
Std 1L	12.89	11.26	12.60	9.91	0.24	0.79	0.10
Std 2L*	25.13	22.23	24.79	19.53	0.46	1.60	0.19
Std 3L	64.89	47.42	84.47	50.01	0.10	2.72	0.42
Std 4L	156.57	91.69	367.57	129.41	2.98	29.40	0.80
Std 1	11.08	12.61	12.26	50.02	11.28	8.75	1.06
Std 2**	24.38	21.34	23.64	94.95	21.62	12.46	2.04
Std 3	31.74	36.18	47.14	189.89	54.32	21.18	3.10
Std 4^{DM}	52.64	71.42	93.49	283.34	108.86	29.40	5.13
Std 5	62.11	94.032	139.59	-	-	-	-
Std 6	75.90	116.25	203.67	367.40	158.89	61.27	6.96
Std 7	95.46	164.28	384.50	431.15	197.27	115.14	9.33
Std 8	-	-	-	812.88	278.21	144.22	17.61

subsequent instrument runs is lower ≥0.9999, however this was determined in solutions containing Ca rather than just the trace elements (see Section 3.3.4). Comparison of the calibration correlation coefficients derived in the initial experiment in Section 3.3.1 for Al, Mn and Fe (Table 3.5), to the values determined in Run 1 - 4 (Table 3.8) also show a decrease in the r^2 values and linearity associated with the introduction of Ca to the standards.

Non-linear instrument responses typically arise as a function of detector saturation, matrix effects or interference between elements with overlapping spectra. In this study, calcium is considered the matrix element - it is the major component of foraminiferal tests comprising 40 wt% and is the most sensitive element for determination by ICP-OES, with the ability to moderate the sensitivity of other elements being measured. This can introduce serious errors to ratio determinations because [Ca] is not constant in sample solutions (see Section 3.3.4).

When the two ranges of calibration standards (high and low) are employed for a given sample presentation system, the better calibration correlation coefficients for the trace elements, shown in bold in Table 3.8, are consistently obtained over the 'high' calibration range because a larger number of counts of element emission wavelengths can be obtained. Of the two sample presentation systems tested the highest correlation calibration coefficients are typically obtained on element wavelengths using the "Conikal" nebuliser and "Twister" spray chamber configuration (Table 3.8).

TABLE 3.8: Linear calibration correlation coefficients for the two sample presentation systems investigated (Runs 2 and 4). C/Tr = "Conikal" nebulizer coupled to a "Tracey" spray chamber, C/Tw = "Conikal" nebulizer coupled to a "Twister" spray chamber. Columns entitled 'Low' and 'High' refer to the set of calibration standards used to determine the correlation coefficients (see Table 3.7).

		Correlation coefficient (r^2)			
		C/Tr	C/Tr	C/Tw	C/Tw
Element & λ (nm)	View	Low	High	Low	High
Al 396.1	Axial	0.992910	**0.999988**	0.999835	**0.999980**
Mn 257.6	Axial	0.994580	**0.999975**	0.989854	**0.999976**
Mn 258.4	Axial	0.976989	**0.999975**	0.977699	**0.999981**
Fe 238.2	Axial	0.999861	**0.999985**	0.999735	**0.999980**
Fe 239.6	Axial	0.999485	**0.999987**	0.999504	**0.999992**
Fe 259.9	Axial	0.999983	**0.999985**	0.999866	**0.999992**
Ti 334.9	Axial	0.999941	**0.999966**	0.999465	**0.999969**
Ti 336.1	Axial	0.998846	**0.999917**	0.998878	**0.999983**
Ti 337.3	Axial	0.999613	**0.999922**	0.999182	**0.999974**

3.3.3 Detector Synchronization

It is advantageous to measure all analytes for a single sample simultaneously to avoid time dependent effects within the instrument, particularly those relating to fluctuations in the plasma intensity. Fluctuations in the power delivered to the plasma can impact the sensitivity of element emission lines according to their individual excitation energies. This factor can become important when attempting high-precision measurements that require changes in element ratios to be minimised. The length of time during which the count of each element emission wavelength is made, the 'read' time, and the number of times within the read time that the individual pixels in the detector array need refreshing or 'emptying', the 'integration' time, are a function of the intensity of the emission wavelength and play a vital role in the accuracy and precision of the data generated. It is essential that the integration time is short enough to prevent saturation of any pixel on the detector array (recognised by a broadening of the spectral peak and a curved calibration profile), commonly by the matrix element Ca, but long enough to count a sufficient number of photons from less abundant or less sensitive elements and provide an accurate measurement. One of the advantages of the Perkin Elmer 4300 DV ICP-OES used in this study is that integration times can be set either automatically for the elements in any given solution, by taking a number of preliminary readings prior to the main analytical measurements, or can be user defined. However, automatically defined integration times are not always ideal and manual tuning of the integration time can significantly increase the precision of element measurements (Green et al., 2003). The main disadvantage of manually setting the integration and read times for each element is that not all measurements are made truly simultaneously because of disparate element intensities, introducing potential sources of errors to element ratios.

In this study, prior to the main set of analytical measurements, preliminary measurements were made on several of the calibration standards with intermediary element concentrations, to determine approximate integration times for each of the elements in the solutions. Optimum integration times were then investigated during four instrument runs, Runs 1 - 4 (see Table 3.6) using ten replicate determinations of two multielement solutions (standards 2 and 2L). In Runs 1 and 3, all seven elements (Ca, Mg, Sr, Al, Mn, Fe and Ti) were measured simultaneously with integration times of 10 and 20 ms, respectively. For Fe and Ti, the integration time in Runs 1 and 3 was much too short for sufficient counts of each emission wavelength to be made, thus very poor precisions were obtained $\geq$15% (RSD) (Table 3.9). In Runs 2 and 4, the integration time for Fe and Ti was increased to 1 and 2 s, respectively and much better precisions $\leq$10% (RSD) were obtained. Extending the integration time for Al appears to have little impact on data precision (except between Runs 3 and 4) but the low sensitivity of this element for determination by ICP-OES suggests that it is more appropriate to employ a longer integration time. Mn is a more sensitive element for determination by ICP-OES than Al, Fe and Ti and is therefore measured simultaneously with Ca, Mg and Sr. The highest

TABLE 3.9: Relative standard deviations (%) of 10 replicate determinations for two multielement solutions (calibration standards 2L and 2). (s) = simultaneous measurements. Horizontal line denotes precisions ≥50% (RSD). Element wavelength pairs in bold have the highest reported precisions.

	Run 1	Run 2		Run 3	Run 4	
Interelement ratio	Std 2L	Std 2L	Std 2	Std 2L	Std 2L	Std 2
Mg 280.3/Ca 315.9 radial (s)	0.88	0.95	**0.83**	0.75	0.66	**0.58**
Mg 279.5/Ca 315.9 radial (s)	0.25	0.59	**0.67**	0.21	0.31	**0.30**
Mg 280.2/Ca 317.9 radial (s)	0.90	0.97	**0.82**	0.72	0.64	**0.62**
Mg 279.5/Ca 317.9 radial (s)	0.29	0.58	**0.67**	0.25	0.29	**0.29**
Mg 279.5/Ca 422.6 radial (s)	0.81	0.57	**1.04**	0.70	0.37	**0.45**
Mg 280.2/Ca 422.6 radial(s)	0.31	0.95	**1.21**	0.40	0.69	**0.61**
Mg 285.2/Ca 315.9 axial (s)	0.98	0.65	**1.49**	0.24	0.51	**0.57**
Mg 280.2/Ca 315.9 axial (s)	0.17	0.46	**0.36**	0.22	0.12	**0.14**
Mg 279.5/Ca 315.9 axial (s)	0.09	0.95	**0.26**	0.12	0.12	**0.11**
Sr 407.7/Ca 315.9 radial (s)	0.15	0.21	**1.11**	0.36	0.19	**0.24**
Sr 421.5/Ca 315.9 radial (s)	0.32	0.17	**1.17**	0.37	0.31	**0.37**
Sr 407.7/Ca 317.9 radial (s)	0.17	0.20	**1.13**	0.40	0.19	**0.32**
Sr 421.5/Ca 317.9 radial (s)	0.33	0.22	**1.19**	0.40	0.29	**0.45**
Sr 407.7/Ca 422.6 radial (s)	0.22	0.30	**1.24**	0.29	0.13	**0.35**
Sr 421.5/Ca 422.6 radial (s)	0.35	0.18	**0.51**	0.30	0.21	**0.17**
Al 396.1/Ca 315.9 axial	1.58	1.56	**1.13**	4.65	1.70	**0.25**
Mn 257.6/Ca 315.9 axial (s)	13.27	-	**1.75**	26.07	16.23	**0.42**
Mn 259.4/Ca 315.9 axial (s)	21.52	22.26	**1.12**	14.82	12.74	**0.22**
Fe 238.2/Ca 315.9 axial	39.85	7.64	**0.47**	-	8.70	**1.47**
Fe 239.6/Ca 315.9 axial	12.91	10.99	**0.82**	-	9.50	**1.26**
Fe 259.9/Ca 315.9 axial	44.56	6.05	**0.65**	14.43	7.98	**0.84**
Ti 334.9/Ca 315.9 axial	-	7.07	**1.34**	29.89	10.19	**0.78**
Ti 336.1/Ca 315.9 axial	-	21.77	**1.32**	-	11.56	**1.69**
Ti 337.3/Ca 315.9 axial	37.93	9.34	**1.48**	-	11.91	**1.82**

precisions for Mn/Ca (0.22% RSD) are obtained in Run 4 alongside the highest reported precisions on Mg/Ca and Sr/Ca values of ≤0.17% (RSD) (Table 3.9). In general, the best precisions on element ratios were obtained in Run 4 (see bold ratios in Table 3.9, with the "Twister" spray chamber and optimised integration times.

Ten replicate measurements of the Standard 2L (Table 3.7), characterised by trace element concentrations comparable to foraminiferal calcite (except for a slightly high Al concentration), consistently yield poorer precisions on trace element/calcium ratios than precisions obtained on ten replicate measurements of Standard 2 (Table 3.7), with higher trace element concentrations (Table 3.9). For example, in Standard 2, Al/Ca and Mn/Ca ratios are ≤0.22% (RSD), and Fe/Ca and Ti/Ca ratios are better than 0.85% (RSD) the same wavelength pairs in Standard 2L, yield precisions of ∼1% (RSD) and 12% (RSD), respectively.

TABLE 3.10: Comparison of relative standard deviations (%) on ratios determined using different viewing modes. The best precisions obtained on wavelength pairs are those determined simultaneously, i.e., in the same orientation, shown in bold. Data only shown from Run 4 for clarity.

	Run 4	
Interelement ratio	Std 2L	Std 2
Mg 279.5 (axial)/Ca 315.9 (axial)	**0.12**	**0.11**
Mg 279.5 (axial)/Ca 315.9 (radial)	0.24	0.23
Mg 279.5 (radial)/Ca 315.9 (radial)	0.31	0.30
Mg 279.5 (radial)/Ca 315.9 (axial)	0.42	0.37
Sr 421.5 (radial)/Ca 422.6 (radial)	**0.21**	**0.17**
Sr 421.5 (radial)/Ca 315.9 (radial)	0.31	0.37
Sr 421.5 (radial)/Ca 315.9 (axial)	0.44	0.53
Mn 259.4 (axial)/Ca 315.9 (axial)	**12.74**	**0.22**
Mn 259.4 (axial)/Ca 315.9 (radial)	12.76	0.23

Element emission wavelengths determined simultaneously consistently yield the highest precisions (Table 3.10), for example Mg 280.2 (axial)/Ca 315.9 (radial) has a precision of 0.24% (RSD), whereas simultaneous axial measurements of the same wavelength pair is 0.12% (RSD). Of course, identical integration times are not practical for all analytes because of the vastly different emission line sensitivities, as discussed above. Mg, Sr and Mn emission wavelengths are measured simultaneously with Ca, whereas less abundant elements and/or emission lines with lower sensitivities, e.g., Al, Fe and Ti, require a longer integration time and therefore these element measurements are not derived simultaneously with Ca.

3.3.4 Matrix Effects

The implications of a Ca matrix effect on elements is critical for accurate ratio determinations. The effect of the Ca matrix on element ratios was investigated using the certified reference material (CRM) ECRM 752-1 (limestone), which has a Mg/Ca ratio of 3.9 mmol/mol within the mid-range of typical foraminiferal calcite. ECRM 752-1 was dissolved in 0.075 M HNO_3 and then diluted to make seven solutions, each with the same element/calcium ratios but different [Ca] between 2 and 75 ppm. Calculated Al/Ca, Mn/Ca, Fe/Ca and Ti/Ca ratios in ECRM 752-1 are low (Table 3.11) but element/calcium ratios are still higher than the values observed in cleaned planktic foraminifera (Barker et al., 2003) and therefore suitable for testing Ca matrix effects on trace elements.

TABLE 3.11: Element/calcium ratios in mmol/mol for certified reference material ECRM 752-1 (limestone).

Reference material	Mg/Ca	Sr/Ca	Al/Ca	Fe/Ca	Mn/Ca	Si/Ca	Ti/Ca
ECRM 752-1	3.90	0.19	1.20	0.30	0.15	11.90	0.12

The matrix effect on the sensitivity of Mg and Sr emission lines was assessed using element/calcium ratios determined in this study (Fig. 3.1). The most sensitive Mg emission lines at 279.5 and 280.2 nm show evidence of pronounced matrix effects, with ∼6% decrease in emission line sensitivity with increasing [Ca] (Fig. 3.1a), whereas the least sensitive Mg emission line at 285.2 nm appears to show little evidence of matrix effects. It would therefore seem most sensible to measure Mg/Ca ratios using the least sensitive Mg emission line at 285.2 nm to generate accurate Mg/Ca data however, the relationship between Mg/Ca and [Ca] is not well constrained making any corrections to the calculated Mg/Ca ratio difficult and wavelength pairs using the Mg line at 285.2 nm consistently show lower precisions than obtained for other Mg emission lines (Table 3.9). The two Sr emission lines investigated in this study, at 407.7 and 421.5 nm, shown in Figure 3.1b, do not show a consistent behaviour below 10 ppm Ca but above 10 ppm Ca, both Sr emission lines show evidence of matrix effects with a 4 to 6% decrease in sensitivity with increasing [Ca].

Mg/Ca and Sr/Ca data are shown in Figures 3.2 and 3.3 respectively, as a function of [Ca] for the four separate instrument runs (Runs 1 to 4), to investigate the impact of different sample presentation systems and instrument settings on the accuracy, as a function of matrix effects, on the measured element/calcium ratios. In all four runs, Mg/Ca values show a similar decrease in sensitivity with increasing [Ca] (Figure 3.2a) but Run 4 consistently yields lower Mg/Ca values than Runs 1 to 3, closer to the reported Mg/Ca value for the CRM (Table 3.11). Sr/Ca ratios are less consistent (Fig. 3.3a), in Runs 1 through 3 ratios show a strong degree of line curvature, whereas in Run 4 there is little evidence of line curvature between [Ca] of 8 and 75 ppm. To quantify the nature of the matrix effects on Mg and Sr ratios, best fit lines were fitted to the Mg/Ca and Sr/Ca values determined in each run. Linear fits through the Mg/Ca and Sr/Ca ratios (Figs 3.2b-e and 3.3b-e) consistently yield lower correlation coefficient (R) values than exponential line fits. This finding is consistent with previous studies (De Villiers et al., 2002; Lear et al., 2002; Wara et al., 2003; Andreasen et al., 2006; Marchitto, 2006) indicating a significant exponential decrease in Mg/Ca and Sr/Ca values with increasing [Ca], particularly at low [Ca] using the ICP technique. Further investigation is required to more accurately quantify the relationship between increasing [Ca] and element ratios on this instrument and the optimum working [Ca] range.

Matrix effects on the elements Al, Mn, Fe and Ti in each of the instrument Runs 1 - 4 are shown in Figures 3.4, 3.5, 3.6 and 3.7. Solutions with low trace element concentrations,

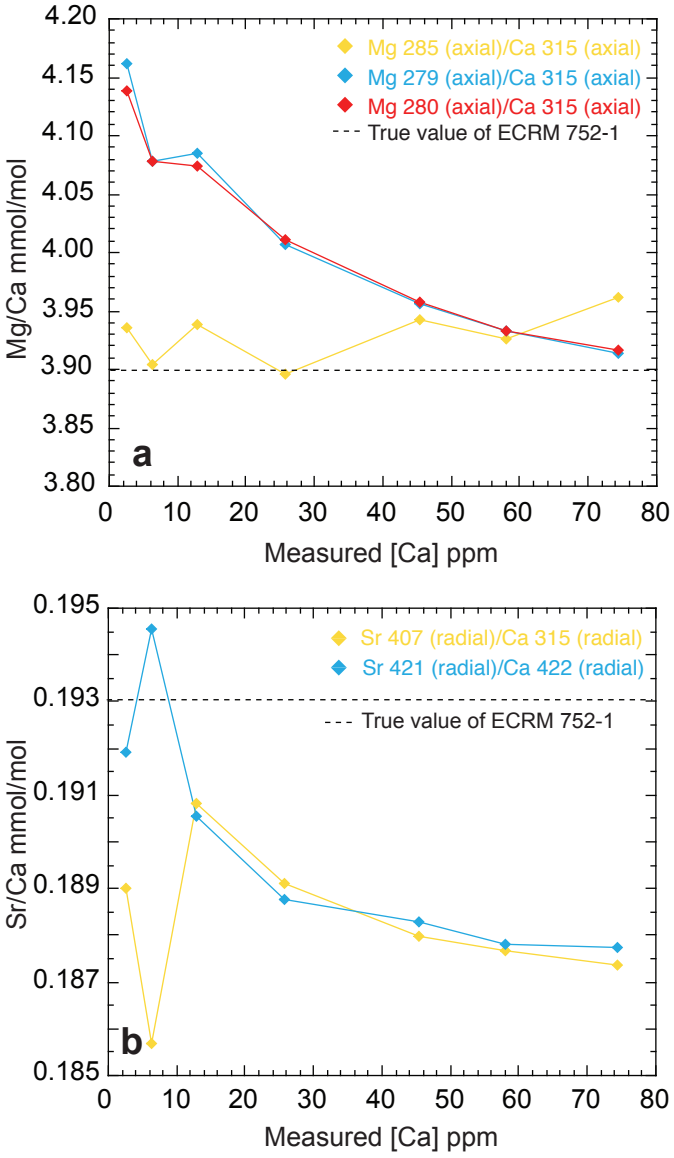

FIGURE 3.1: Matrix effects on measured Mg/Ca and Sr/Ca ratios as a function of [Ca]. All three elements show a decrease in emission line sensitivity of ∼6% with increasing [Ca] over the [Ca] range investigated. Data presented are from Run 4.

i.e., solutions with a [Ca] below 20 ppm, show increased 'noise' between instrument runs and between replicate measurements of the same solution, reflecting the different integration times employed in each instrument run and the difficulties accurately measuring trace elements at low concentrations. Al/Ca ratios shown in Figure 3.4, indicate a large degree of variability between the measured values in each of the runs reflecting the relatively poor determination of this element. Significant matrix effects are observed on Al/Ca ratios, shown in Figure 3.4b-e, with ∼20 - 25% decrease in the sensitivity of the Al emission line with increasing [Ca]. In Run 3 an even larger decrease in the sensitivity of the Al emission line is observed ∼65% (Fig. 3.4d). The large Ca matrix

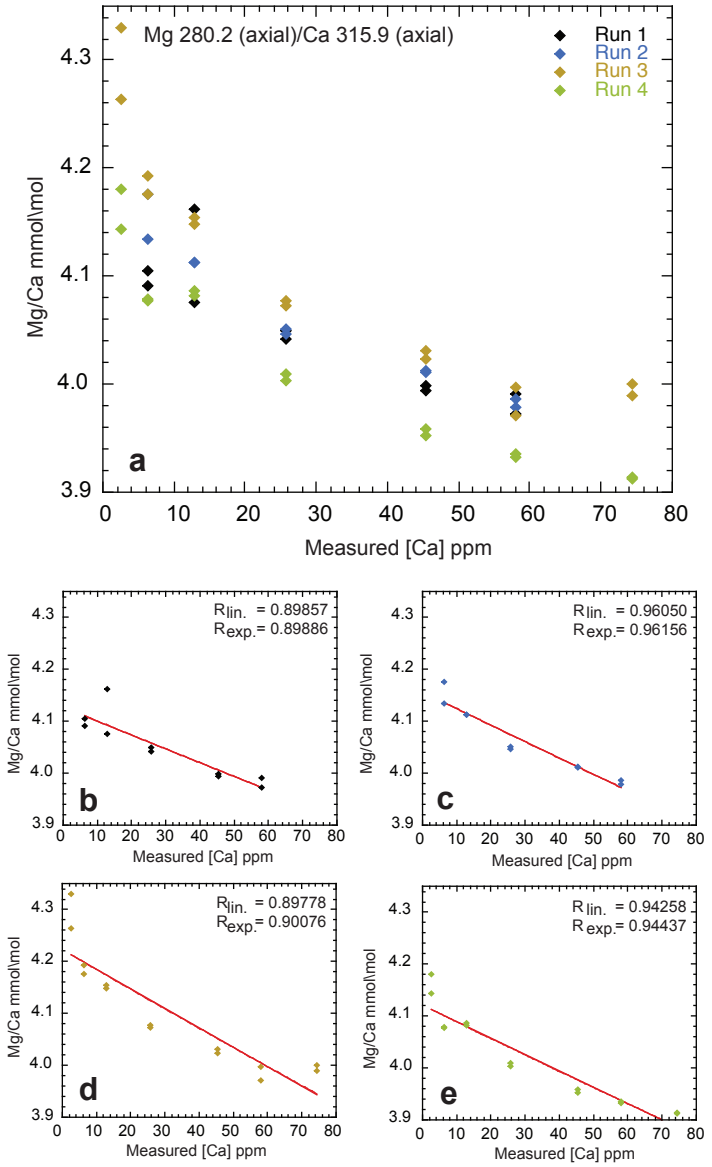

FIGURE 3.2: Mg/Ca ratios determined as a function of [Ca] in solutions derived from the certified reference material ECRM 752-1 in Runs 1 - 4. Solutions E0 and E6 were added in Runs 3 and 4. Panels b to e show the Mg/Ca data from each instrument run with best fit line shown in red, correlation coefficients for linear (R_{lin}) and exponential (R_{exp}) line fits to the data set in the top right corner of each panel.

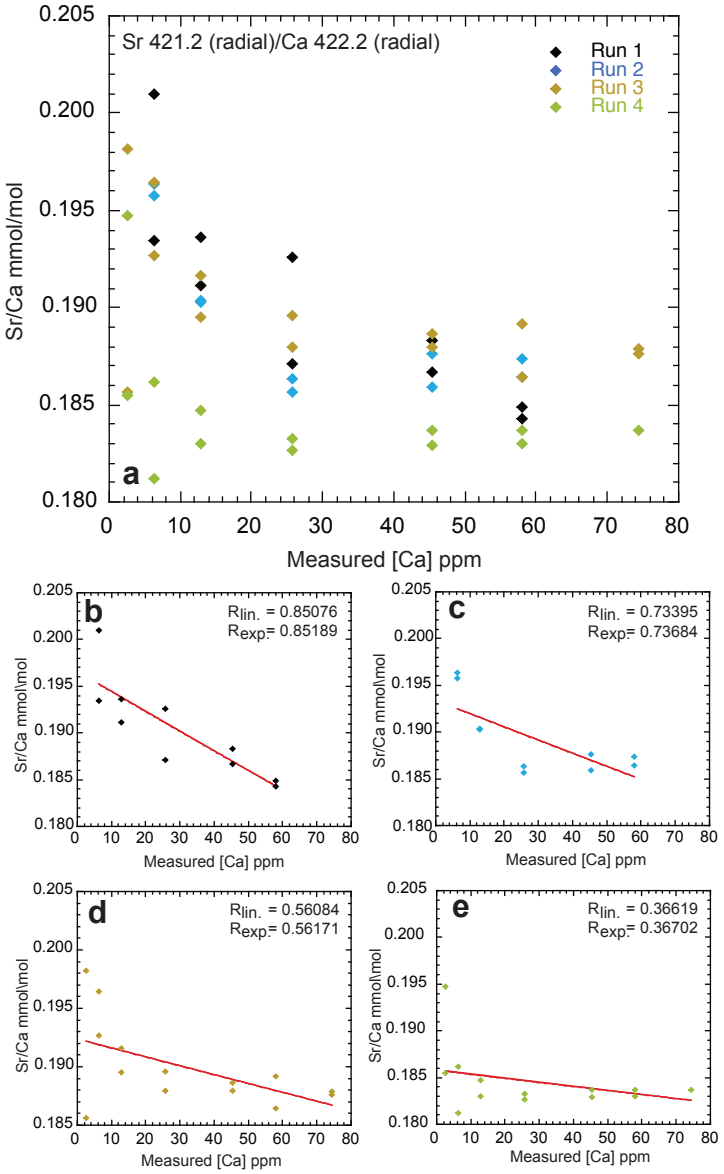

FIGURE 3.3: Sr/Ca ratios determined as a function of [Ca] in solutions derived from the certified reference material ECRM 752-1 in Runs 1 - 4. Solutions E0 and E6 were added in Runs 3 and 4. Horizontal dashed line is the reported Sr/Ca value for ECRM 752-1. Panels b to e show the Sr/Ca data from each instrument run with best fit line shown in red, correlation coefficients for linear (R_{lin}) and exponential (R_{exp}) line fits to the data set in the top right corner of each panel.

effect observed on Al, is the result of the very high sensitivity of Ca for determination by ICP-OES, which removes energy from the plasma reducing the amount of energy available to other elements, and the low sensitivity of Al for determination by ICP-OES. Measured Fe/Ca values show a similar matrix effect in Runs 2 - 4 over the [Ca] investigated, with decreasing sensitivity of between 10 and 45% (Fig. 3.5). Measured Ti/Ca ratios are very low and close to the detection limit of the instrument (Fig. 3.6). In general, a decrease in the sensitivity of Ti is observed above ∼10 - 20 ppm [Ca] but in Run 4 there is no significant variability above 10 ppm in the measured Ti/Ca value. Mn/Ca ratios show no significant matrix effects over the range of Ca investigated (Fig. 3.7). The reduced matrix effects observed for most element/calcium ratios in Run 4 are attributable in part to the substitution of the "Twister" spray chamber, which reduces instrument sensitivity and susceptibility to matrix effects, thus better linear calibration correlation coefficients are achieved in this run (see Section 3.3.1).

It is not possible to use ECRM 752-1 to assess the accuracy of the element values measured on the ICP-OES because the certified element concentrations are insufficiently precise for such a purpose, for example Mg/Ca ratios have a relative standard deviation of 6.8%. In addition, the CRM ECRM 752-1 contains a contaminant aluminosilicate component (Greaves et al., 2005) which can bias element/calcium ratios to higher values particularly Mg, Fe, and Al and introduce a source of variability.

3.3.5 Testing Ca matrix effects at low concentrations of [Ca] (1 to 5 ppm)

In light of the large Ca matrix effects observed on Mg/Ca and Sr/Ca ratios over the [Ca] range (2 to 75 ppm) investigated in this study (Figs 3.2 and 3.3), an experiment was designed to re-test the lack of matrix effects observed on Mg/Ca and Sr/Ca ratios over the 1 to 5 ppm [Ca] range on the same instrument by Green et al. (2003). Measurements were made on a set of five test solutions diluted to [Ca] of 1 to 5 ppm (Table 3.12) from the internal SOC standard (Mg/Ca of ∼5.0 mmol/mol and Sr/Ca ratio of ∼1.5 mmol/mol), with calibration standards tailored accordingly (Table 3.13), Figure 3.8 shows that Mg/Ca and Sr/Ca wavelength pairs, viewed axially and radially respectively, are consistent over the 1 to 5 ppm range of [Ca] investigated in the set of five solutions. The average value of the five points in each panel in Figure 3.8 is shown by the horizontal dashed line and fits through the errors bars ($\pm 1\sigma$) on all of the measurements, indicating that there is no significant matrix effect on the determination of Mg/Ca and Sr/Ca at these wavelengths over the [Ca] shown. Standard deviations were determined on the three replicate measurements of each solution and demonstrate that the best two pairs of emission wavelengths Sr 421.5 (radial)/Ca 422.7(radial) and Mg 280.3(axial)/Ca 317.9 (axial) have precisions of 0.25% and ∼1%, respectively.

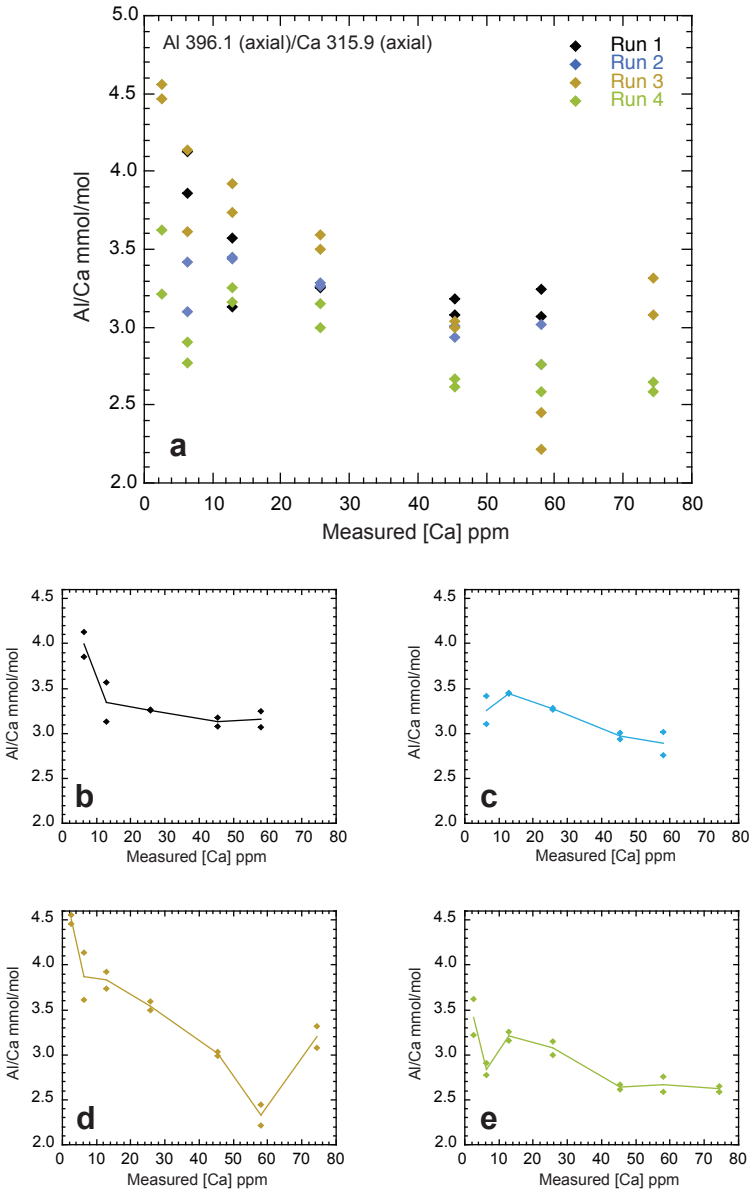

FIGURE 3.4: Al/Ca ratios determined as a function of [Ca] in solutions derived from the certified reference material ECRM 752-1 on Runs 1 - 4. All instrument runs were carried out over the course of one week with different instrument parameters for each (see Table 3.6). Large decrease in the sensitivity of Al ($\geq$20%) with increasing [Ca].

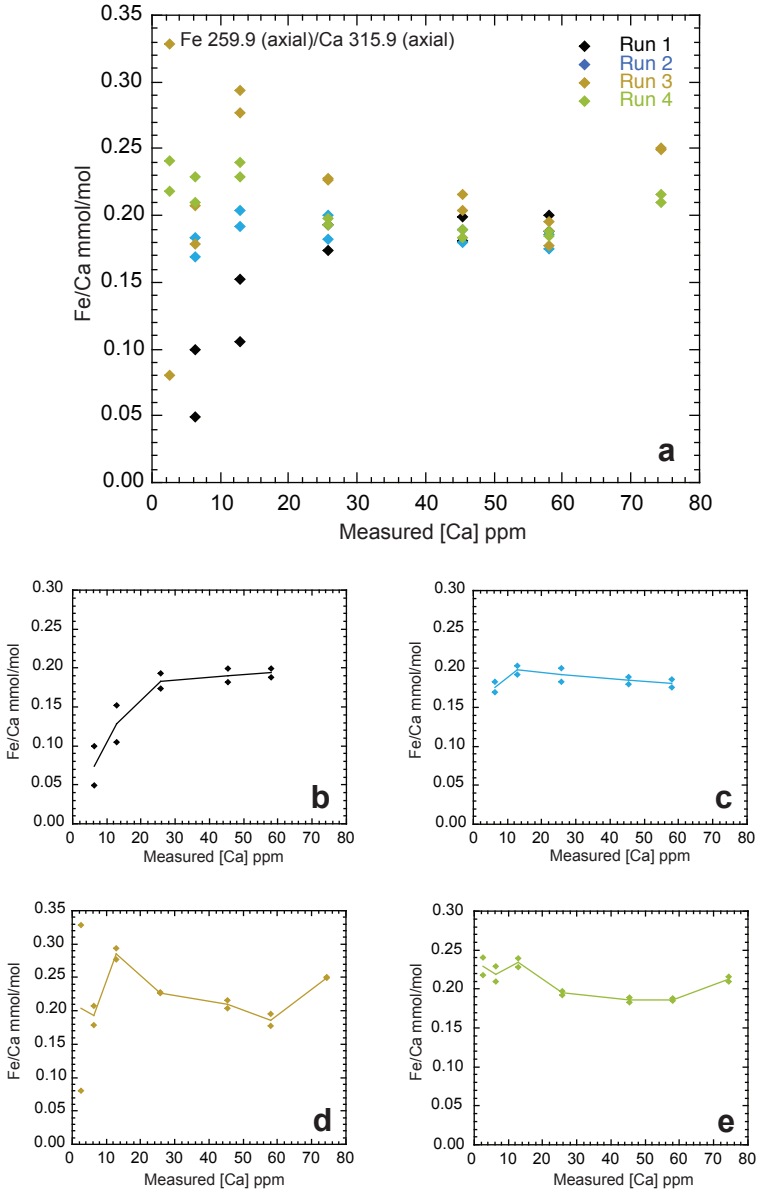

FIGURE 3.5: Fe/Ca ratios determined as a function of [Ca] in solutions derived from the certified reference material ECRM 752-1 on Runs 1 - 4. All instrument runs were carried out over the course of one week with different instrument parameters for each (see Table 3.6). The best two pairs of emission wavelengths Fe 259.9 (axial)/Ca 315.9 (axial) are shown. In Runs 2 - 4 significant matrix efects are observed on Fe/Ca ratios, $\geq$10% decrease in the sensitivity of Fe associated with increasing [Ca].

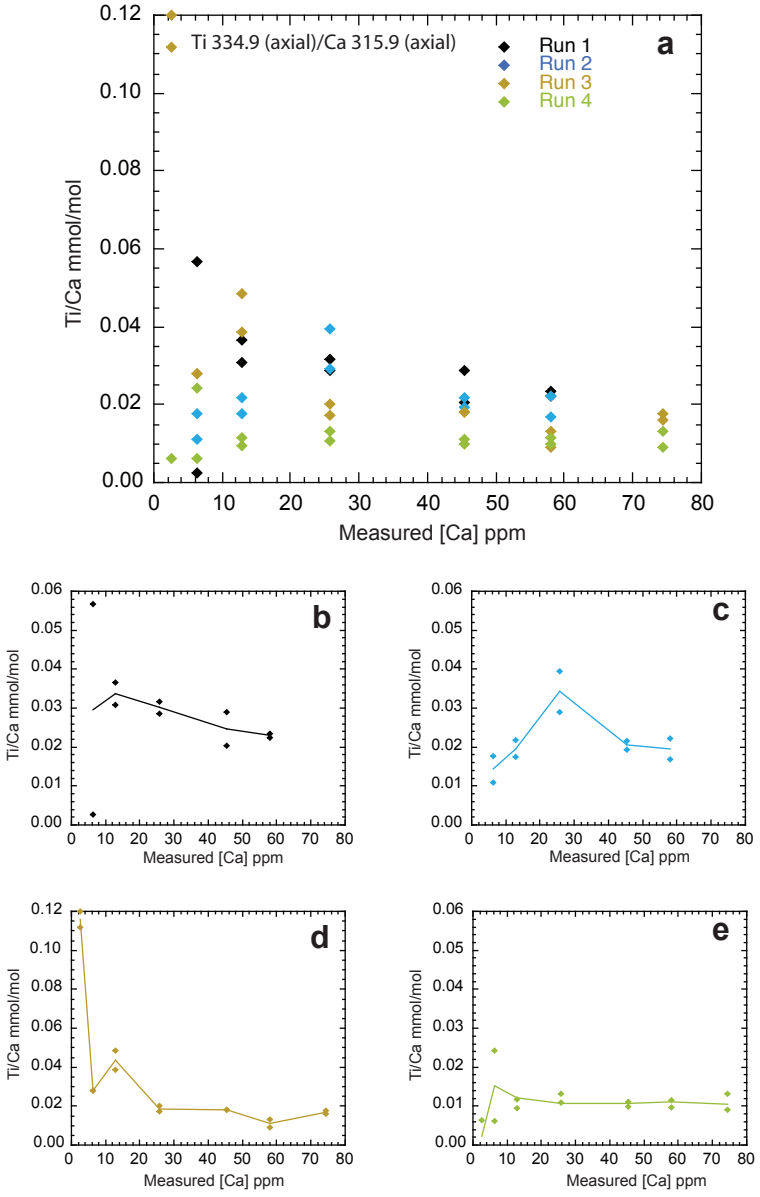

FIGURE 3.6: Ti/Ca ratios determined as a function of [Ca] in solutions derived from the certified reference material ECRM 752-1 on Runs 1 - 4. All instrument runs were carried out over the course of one week with different instrument parameters for each (see Table 3.6). The best two pairs of emission wavelengths Ti 334.9 (axial)/Ca 315.9 nm (axial) are shown.

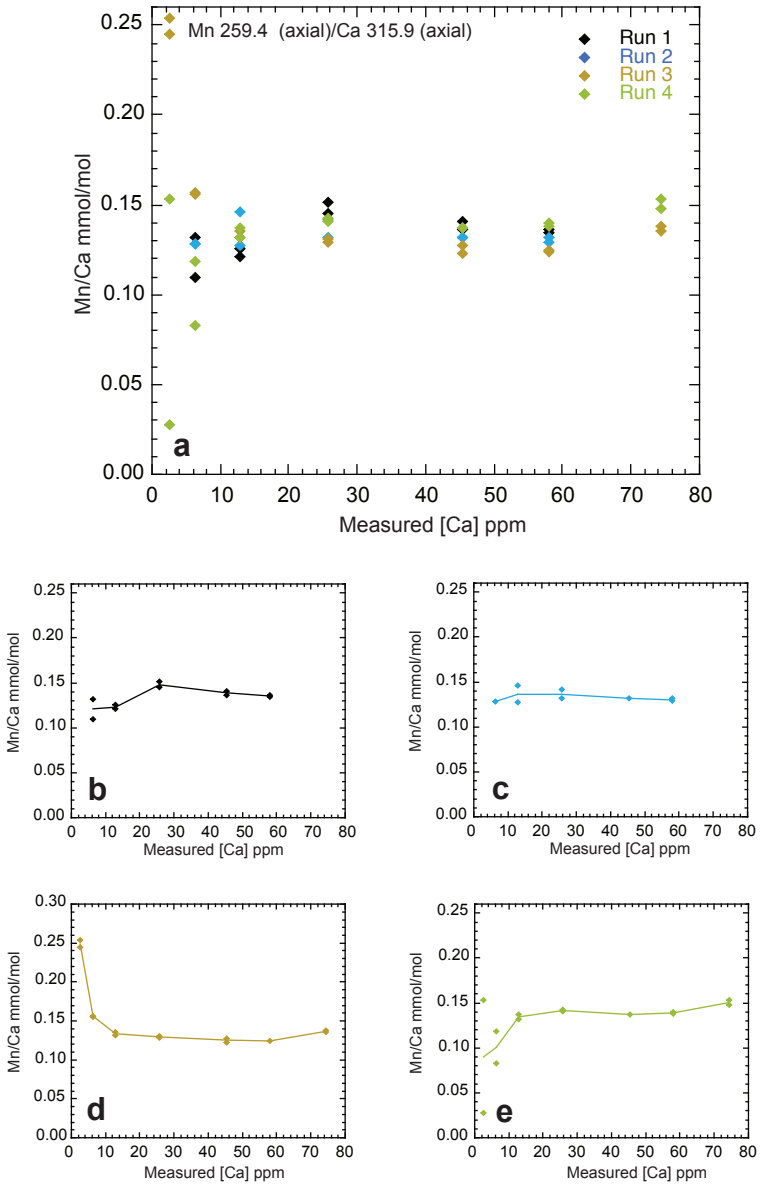

FIGURE 3.7: Mn/Ca ratios determined as a function of [Ca] in solutions derived from the certified reference material ECRM 752 on Runs 1 - 4. All instrument runs were carried out over the course of one week with different instrument parameters for each (see Table 3.6). The best two pairs of emission wavelengths Mn 259.4 (axial)/Ca 315.9 nm (axial) are shown. No significant matrix effects are observed on Mn/Ca ratios.

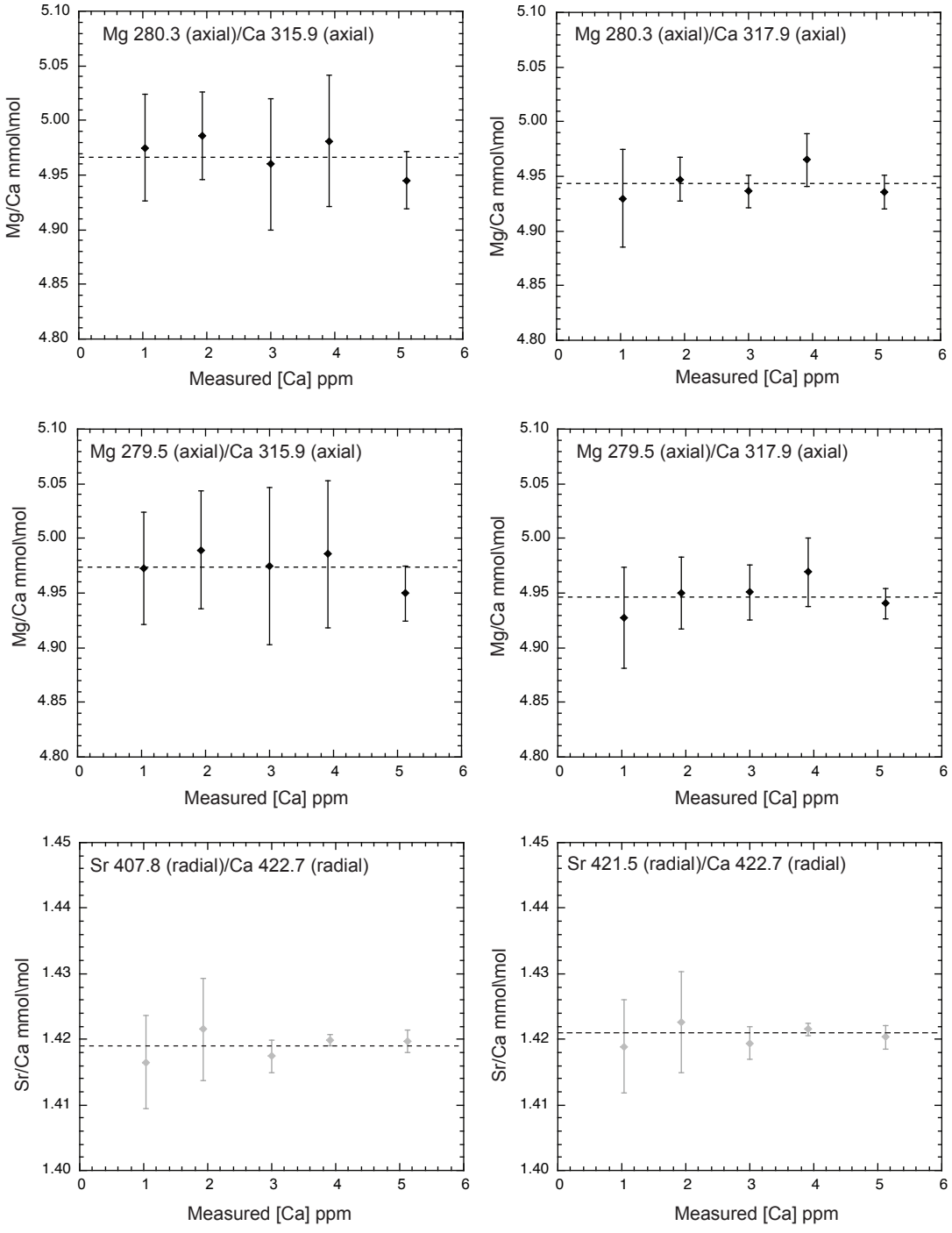

FIGURE 3.8: Mg/Ca and Sr/Ca ratios determined as a function of [Ca] in solutions with identical elemental ratios. The average element/calcium value determined from three replicate measurements of each solution is plotted. The standard deviation for each solution is calculated from the three original measurements. Horizontal dashed lines represent the mean of the five average Mg/Ca or Sr/Ca determinations, and fits through the 1σ indicating that there is no significant Ca matrix effect on element/-calcium ratios over this range of [Ca]. Note the different y-axis scales for Mg/Ca and Sr/Ca determinations.

TABLE 3.12: Concentrations of the solutions used to test Ca matrix effect on Mg/Ca and Sr/Ca ratios over the [Ca] of 1 to 5 ppm. The internal SOC standard was diluted to five different [Ca], therefore each solution possesses identical Ca:Mg:Sr ratios.

Test Solution	Ca (ppm)	Mg (ppb)	Sr (ppb)
SOC1	1.03	3.21	3.32
SOC2	1.93	6.00	6.21
SOC3	3.00	9.25	9.60
SOC4	3.91	12.14	12.53
SOC5	5.12	15.65	16.3

TABLE 3.13: Calibration standards used to derive calibration correlation coefficients.

Standard	Ca (ppm)	Mg (ppb)	Sr (ppb)
Std 1	0.98	1.79	1.88
Std 2	1.96	6.25	4.71
Std 3	3.16	9.62	10.10
Std 4	3.95	18.07	14.21
Std 5	4.85	31.36	37.64
Std 6	8.92	49.46	68.97
Std 7	15.33	50.68	110.88

3.4 Conclusions

The aim of this study was to develop a methodology at the National Oceanography Centre, Southampton (NOCS) for the determination of the trace metals with low concentrations in foraminiferal calcite (Al, Mn, Fe and Ti) simultaneously with desired Ca, Mg and Sr by ICP-OES. One of the preliminary findings of this investigation is that the low sensitivity of the ICP-OES technique to the elements Al, Mn, Fe and Ti and their relatively low concentrations in foraminiferal samples highlights that the currently established NOCS methodology (Green et al., 2003) is not suited to measurement of these trace elements. Thus, in this study optimum instrument parameters and settings for the determination of high-precision element/calcium ratios in foraminiferal calcite on a Perkin Elmer 4300 DV ICP-OES were evaluated. In particular, optimum emission wavelengths, plasma viewing orientation, detection and quantification limits, sample presentation system and detector measurement times were investigated. These key parameters are summarised in Table 3.14.

In samples with element ratios typical of foraminiferal calcite samples the precision on Al/Ca, Mn/Ca, Fe/Ca and Ti/Ca are typically better than 10% (RSD) which is sufficient for the purposes of screening data for contamination (precision could be improved if more targeted calibration standards were used). Much better precisions ($\leq$1%) can be obtained but only at element concentrations much higher than observed in foraminiferal

TABLE 3.14: Optimum instrument set-up and parameters for the determination of trace elements in foraminiferal calcite. Most sensitive element wavelength pairs for determination by ICP-OES selected. [1]Carrier gas flow rate adopted from Green et al. (2003). * represents sample solutions with trace elements concentrations significantly higher than observed in typical foraminiferal calcite samples. ** represents sample solutions at lower element concentrations more typical of foraminiferal calcite samples.

Analytical protocol component	Optimum protocol
Instrument:Perkin Elmer 4300 DV ICP-OES	
Nebulizer	Glass expansion "Conikal" (concentric)
Spray chamber	Glass expansion "Twister" (cyclonic)
Carrier gas flow rate	0.70 L/min[1]
Emission wavelength pairs	Mg/Ca:279.5 (Axial)/315.9 (Axial)
	Sr/Ca: 421.5 (Radial)/ 422.6 (Radial)
	Al/Ca: 396.1 (Axial)/315.9 (Axial)
	Mn/Ca: 259.4 (Axial)/315.9 (Axial)
	Fe/Ca: 259.9 (Axial)/315.9 (Axial)
	Ti/Ca: 334.9 (Axial)/ 315.9 (Axial)
Detector read time	10 secs
Detector integration times	Ca (Axial and Radial): 20 ms
	Mg (Axial): 20 ms
	Sr (Radial): 20 ms
	Mn (Axial): 20 ms
	Al (Axial): 2 secs
	Fe (Axial): 2 secs
	Ti (Axial): 2 secs
Precision	All element/calcium ratios $\leq$1%*
	All element/calcium ratios $\leq$10%**

calcite. As in Green et al. (2003) the best precisions are obtained when elemental measurements are derived truly simultaneously, e.g., Mg/Ca, Sr/Ca and Mn/Ca (see Table 3.14). Precisions of $\sim$0.13% (RSD) (based on ten replicate measurements of a single solution) can still be obtained on desired Mg/Ca and Sr/Ca ratios, but over the large range of [Ca] as investigated here (2 to 80 ppm) precision is typically lower $\sim$1 to 1.5% (including matrix effects) and is similar to precisions reported from other laboratories using ICP techniques to determine Mg/Ca.

Significant non-linear Ca matrix effects are observed on Mg/Ca, Sr/Ca, Al/Ca, Fe/Ca and Ti/Ca ratios over the large range of [Ca] (2 - 80 ppm) investigated in this study, reducing the accuracy of element/calcium ratios. Mn/Ca is the only element ratio that shows no significant evidence of matrix effects. Evidence of significant Ca matrix effects on element/calcium ratios in this study (Figs 3.2 - 3.6), indicates a need to constrain the [Ca] in sample solutions to a narrow working range, over which the matrix effect on element emission wavelengths is well constrained or absent. To measure the trace elements Al, Mn, Fe and Ti, requires that solutions are made to a [Ca] of at least 10 ppm

but preferably much higher, e.g., +40 ppm, and ideally over a [Ca] range where matrix effects are linear. Working over a narrow [Ca] range necessitates that each sample is run twice by ICP-OES. The sample [Ca] must be determined in an initial test run so that the sample can be prepared to fall within a narrow [Ca] range (as yet undefined) for a second run, during which the main analytical measurements are made. The main disadvantages of running each sample twice is that it is more time consuming, expensive and a larger initial sample size is required (Table 3.15). However, this is generally the standard practice in laboratories using ICP-OES to determine Mg/Ca and Sr/Ca ratios in biogenic calcite even without the added complication of measuring the trace elements Al, Mn, Fe and Ti (De Villiers et al., 2002).

TABLE 3.15: Estimated [Ca] in benthic foraminiferal samples; sample size constraints. Average benthic foraminiferal weight ∼39 μg for individuals in the 300 - 400μm size fraction (n = 60). Calculated [Ca] assume that there is no loss of material during the cleaning process and that the entire 500 μl of dissolved sample is used to make up the solution for analysis. 5 ml is the ideal sample size for easy handling by the autosampler and 3 ml is the smallest amount of solution that can be handled. Samples smaller than 3 ml must be run manually. Ideally 10 - 15 individuals (highlighted) from the 300 - 400 μm size fration are required for analysis if [Ca] ≥40 ppm required for analysis.

Number of benthic foraminifera used in analysis	Ca concentration (ppm) in solutions	
	500 μl in 5 ml	500 μl in 3 ml
2	6.2	10.3
3	9.3	15.4
5	15.4	25.7
10	30.9	**51.5**
15	**46.3**	77.2
20	61.8	102.9

It is important to note that despite apparent significant matrix effects on Mg/Ca values at low [Ca] (Fig. 3.2) that when a more targeted strategy is employed, i.e., calibration standards over a narrow 1 - 15 ppm range, no significant Ca matrix effects are observed on Mg/Ca and Sr/Ca ratios over the [Ca] range of 1 to 5 ppm (Fig. 3.8). Therefore, the high dilution methodology proposed by Green et al. (2003) is robust but trace element concentrations (Al, Mn, Fe and Ti) are too low to be measured over this [Ca] range.

3.5 Future work

Further work will involve (1) determination of the optimum [Ca] range to work over, (2) quantifying matrix effects (if any) on element ratios over this [Ca] range to correct measured ratio values, and (3) assessing the emission lines that show the most consistent matrix effects between instrument runs. This will be done using a series of synthetic multielement solutions with element concentrations similar to those found in typical

foraminifera prepared with [Ca] values within a set narrow working range. Calibration standards will be prepared with different element/calcium ratios and be closely matched to the sample concentrations to provide a good calibration curve.

The carrier gas flow rate significantly impacts the signal-to-noise ratios obtained for different emission lines, with higher flow rates associated with a shorter residence time in the plasma and a reduction in the proportion of elements excited and ionised. In this study, the flow rate was set at 0.7 L/min, the optimum gas flow rate for the most sensitive emission wavelengths of Mg determined by Green et al. (2003). In future, the optimum flow rate at which maximum signal-to-noise ratios are obtained for the most sensitive trace element emission wavelengths of Al, Mn, Fe and Ti should be investigated using the optimum sample presentation system determined in this study ("Conikal" nebulizer and "Twister" spray chamber). However, if the optimum gas flow rate for the trace elements differs significantly from that defined for optimum Mg and Sr measurements then it is not worthwhile adjusting this parameter if it involves sacrificing the integrity of the Mg/Ca data.

Chapter 4

No extreme bipolar glaciation during main Eocene calcite compensation shift

---

This chapter has been published as **Edgar, K. M.**, Wilson, P. A., Sexton, P. F. and Suganuma, Y. No extreme bipolar glaciation during the main Eocene calcite compensation shift. *Nature*, 448:908-911, 2007 and is presented here as it appeared in the journal but with the addition of subheadings (abstract, introduction, results, conclusions and methods) to aid the flow of the text.

4.1 Abstract

Major ice sheets were permanently established on Antarctica approximately 34 million years ago (Miller et al., 1991; Lear et al., 2000; Zachos et al., 2001), close to the Eocene/Oligocene boundary, at the same time as a permanent deepening of the calcite compensation depth in the worlds oceans (Coxall et al., 2005). Until recently, it was thought that Northern Hemisphere glaciation began much later, between 11 and 5 million years ago (Miller et al., 1991; Lear et al., 2000; Zachos et al., 2001; Holbourn et al., 2005). This view has been challenged, however, by records of ice rafting at high northern latitudes during the Eocene epoch (Moran et al., 2006; Eldrett et al., 2007) and by estimates of global ice volume that exceed the storage capacity of Antarctica (Tripati et al., 2005) at the same time as a temporary deepening of the calcite compensation depth ∼41.6 million years ago (Lyle et al., 2005). Here we test the hypothesis that large ice sheets were present in both hemispheres ∼41.6 million years ago using marine sediment records of oxygen and carbon isotope values and of calcium carbonate content from the equatorial Atlantic Ocean. These records allow, at most, an ice budget that

can easily be accommodated on Antarctica, indicating that large ice sheets were not present in the Northern Hemisphere. The records also reveal a brief interval shortly before the temporary deepening of the calcite compensation depth during which the calcite compensation depth shoaled, ocean temperatures increased and carbon isotope values decreased in the equatorial Atlantic decreased. The nature of these changes around 41.6 million years ago implies that the event may have common links, in terms of carbon cycling, with events at the Eocene/Oligocene boundary (Coxall et al., 2005) and possibly with with the hyperthermals of the Early Eocene climate optimum (Zachos et al., 2001, 2005; Lourens et al., 2005). Our findings help to resolve the apparent discrepancy between the geological records of Northern Hemisphere glaciation (Moran et al., 2006; Eldrett et al., 2007; Tripati et al., 2005) and model results (DeConto and Pollard, 2003, 2006), indicating that the threshold for continental glaciation was crossed earlier in the Southern Hemisphere than in the Northern Hemisphere.

4.2 Introduction

A striking feature of the composite (Zachos et al., 2001) Cenozoic δ^{18}O record in benthic foraminiferal calcite is the abrupt increase in values across the Eocene/Oligocene boundary, 34 Myr ago (Fig. 4.1a). Together with evidence from Southern Ocean records for the initiation of ice rafting (Zachos et al., 1992) and glacial weathering, and from sequence stratigraphic studies (Pekar et al., 2002) for a global sea level fall ($\sim$70 m apparent sea level), this δ^{18}O shift is widely interpreted to signify the onset of major Antarctic glaciation (Miller et al., 1991; Lear et al., 2000; Zachos et al., 2001, 1992) (Fig. 4.1a). The standard view (Miller et al., 1991; Lear et al., 2000; Zachos et al., 2001; Holbourn et al., 2005) is that substantial Northern Hemisphere glaciation occurred much later (Fig. 4.1a); recently, however, three lines of evidence have challenged this orthodoxy.

First, evidence now exists for ice rafting in the Arctic Ocean around 45 Myr ago (Moran et al., 2006) and in the Norwegian–Greenland Sea between 37 and 27 Myr ago (Moran et al., 2006; Eldrett et al., 2007) (Fig. 4.1a). Second, new records for the Eocene/Oligocene boundary from the equatorial Pacific Ocean (ODP Leg 199 of the Ocean Drilling Program) show (Coxall et al., 2005) that the amplitude of the δ^{18}O change ($\delta^{18}O_{benthic}$ = 1.5‰VPDB) is impossibly large to be attributed to Antarctic glaciation alone. The simplest explanation for this result is that some of the $\delta^{18}O_{benthic}$ signal must denote global cooling (Coxall et al., 2005). However, Mg/Ca records (Lear et al., 2000, 2004) provide little support for declining temperatures. This raises the possibility of ice growth beyond Antarctica or the operation of some factor (such as changes in seawater carbonate chemistry associated with increasing calcite compensation depth, (CCD) acting to mask the cooling signal in the Mg/Ca records (Coxall et al., 2005; Lear et al., 2004). Third, the δ^{18}O increase associated with the Eocene/Oligocene

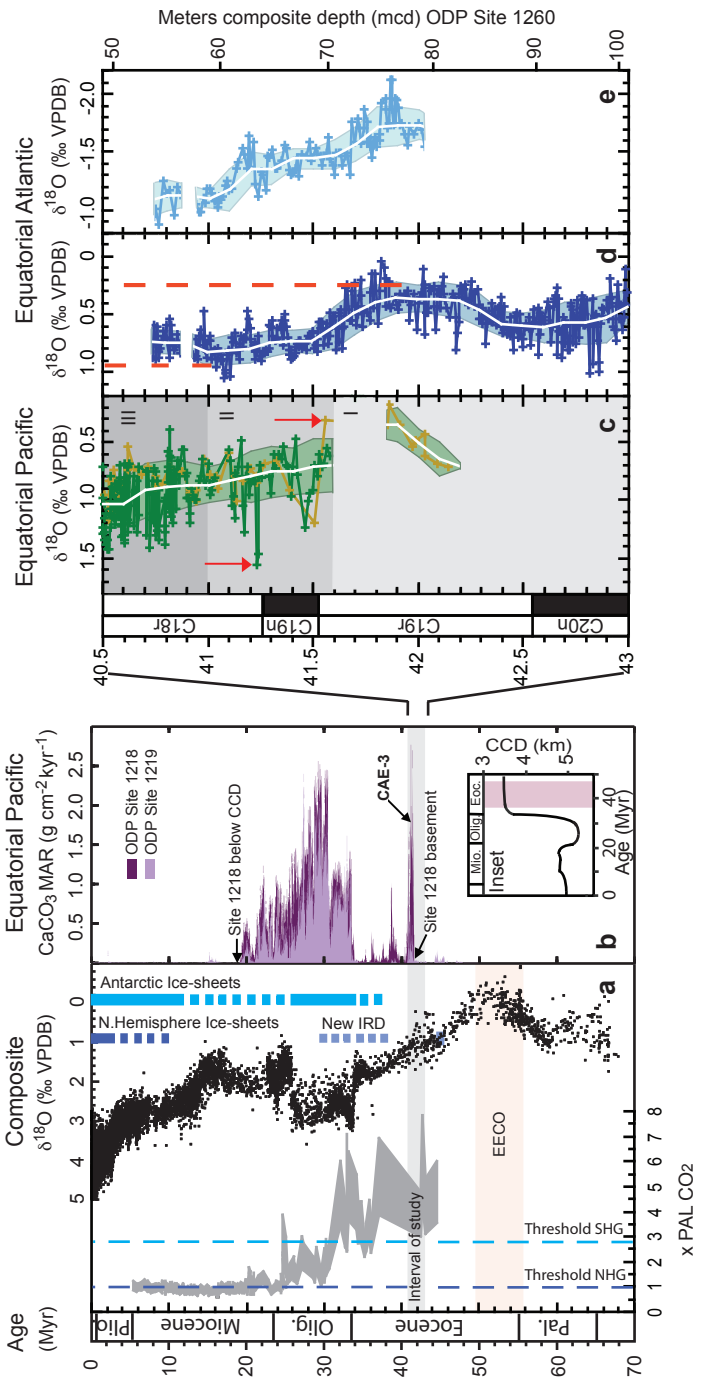

FIGURE 4.1: Palaeoceanographic records showing changes in ocean chemistry and global climate. a, Cenozoic atmospheric CO_2 levels ((Pagani et al., 2005)), grey shading defines the range of estimated CO_2 values as calculated in Pagani et al. (2005) relative to the pre-anthropogenic level (PAL). Vertical dashed blue lines are model-defined thresholds for large ice sheet initiation (DeConto and Pollard, 2003, 2006). SHG and NHG = Southern and Northern Hemisphere glaciation. Composite benthic $\delta^{18}O$ record (Zachos et al., 2001). Vertical blue bars show the standard view of the presence and extent of full scale/permanent ice sheets (solid bars) and those thought to have been partial/ephemeral (broken bars). Newly documented ice rafted debris (IRD) from the high northern latitudes is also shown (Moran et al., 2006; Eldrett et al., 2007). EECO, Early Eocene Climatic Optimum. b, $CaCO_3$ mass accumulation rate for the equatorial Pacific (Lyle et al., 2005; Pälike et al., 2006). The inset shows the classic CCD record for the equatorial Pacific 50 Myr ago to the present, with the pink-shaded zone indicating the interval of transient CCD events (Lyle et al., 2005). Epochs are indicated (abbreviated) to the left of a and in the inset. c, Benthic $\delta^{18}O$ record from ODP Site 1218 (the dark green data points are from Tripati et al. (2005) and yellow ones are from Lear et al. (2004)). The shaded grey zones are: I, pre-onset of CAE-3; II, onset-to-peak $CaCO_3$ mass accumulation rate during CAE-3; III, post-peak $CaCO_3$ mass accumulation rate during CAE-3. Red arrows denote data points defining (Tripati et al., 2005) a 1.2‰ amplitude of $\delta^{18}O$ increase ($\Delta\delta^{18}O$) and thus the hypothesized extreme bipolar glaciation. d, e, New benthic and planktic $\delta^{18}O$ records from ODP Site 1260. Median values (white lines) and 1σ variance (shaded envelopes) are shown in c, d and e. Vertical dashed red lines in d denote our smaller estimate of $\Delta\delta^{18}O$ (~0.6‰VPDB), derived from the maximum and minimum values in the 1σ envelope of the benthic record. Magnetochrons are indicated to the left of c.

boundary occurred in lock-step with permanent deepening of the CCD, possibly in response to glacioeustatic sea level fall and reduced shelf carbonate accumulation (Coxall et al., 2005). Thus, the discovery (Lyle et al., 2005; Shipboard Scientific Party, 2002b) of multiple intervals of temporary CCD deepening in the equatorial Pacific earlier in the Eocene (Fig. 4.1b) has prompted speculation of transient glaciations before the Eocene/Oligocene boundary. A recent study (Tripati et al., 2005) invokes three such glaciations including one extreme bipolar event (100−190 m apparent sea level change; ∼35−70 × 10^6 km^3 ice) coincident with the most prominent of the transient Eocene CCD deepening events (carbonate accumulation event CAE-3 ∼41.6 Myr ago; (Lyle et al., 2005) and Fig. 4.1b, c). Yet the idea that large ice sheets existed in both hemispheres at this time is at odds with contemporaneous warm polar ocean temperatures (Zachos et al., 2001; Sexton et al., 2006a), high atmospheric CO_2 levels (Pagani et al., 2005) (Fig. 4.1a) and the occurrence of (sub)tropical flora at mid- to high latitudes (Wolfe, 1985). Sequence stratigraphic records (Pekar et al., 2005) support the concept of early Cenozoic glaciations, but the ice sheets invoked are much more modest in size (∼10 to 45 m apparent sea level change; ∼40 to 65% of present East Antarctic ice sheet) and considered compatible with high-latitude warmth because of their restriction to the interior of Antarctica (Pekar et al., 2005).

Although the sensitivity to CCD change (Shipboard Scientific Party, 2002b) of the Pacific drill sites used to infer extreme bipolar Eocene glaciation is beneficial to understanding carbon cycling, it is detrimental to generating isotope records from calcareous microfossils whose occurrence and preservation are sensitive to changes in carbonate saturation state. Thus, further tests of bipolar Eocene glaciation are warranted.

4.3 Results

We generated high-resolution (∼4.5 kyr) monospecific stable isotope records for the interval spanning CAE-3 (Lyle et al., 2005) from the equatorial Atlantic Ocean (ODP Leg 207, Demerara Rise, Site 1260, 9° 16' N, 54° 33' W; palaeowater depth 2,500−3,000 m) (Shipboard Scientific Party, 2004). These sediments were deposited well above the local CCD for most of the study interval and are shallowly buried (Shipboard Scientific Party, 2004), favouring calcareous microfossil preservation (Sexton et al., 2006a). In Fig. 4.1c−e, we compare our new $\delta^{18}O$ records from the equatorial Atlantic with the record presented Tripati et al. (2005) from the equatorial Pacific in support of bipolar glaciation. $\delta^{18}O$ data from the equatorial Pacific show a considerable spread, and the amplitude of increase used to infer extreme bipolar glaciation relies on outliers in sparse data ($\Delta\delta^{18}O_{benthic}$ = 1.2‰VPDB, arrows, Fig. 4.1c). Our data from the Atlantic are more continuous and show less spread (Fig. 4.1d, e). Our benthic record (Fig. 4.1d) shows a well-defined minimum around the middle of magnetochron C19r followed by a shift to higher values attained by the onset of CAE-3 (zone I/II boundary, Fig. 4.1c).

Our planktic record shows a similar pattern (Fig. 4.1e). One interpretation of the correspondence between our planktic and benthic records is that it reflects an increase in the oxygen isotope composition of sea water ($\delta^{18}O_{seawater}$) and supports the notion of ice growth. Another interpretation, arguably more in keeping with the other palaeoclimate records (Pagani et al., 2005) and numerical modelling results (DeConto and Pollard, 2003, 2006) shown in Fig. 4.1a, is that our data are attributable to cooling of surface and bottom waters at Site 1260. Regardless, our estimate of the $\delta^{18}O_{benthic}$ signal associated with CAE-3 is about half that proposed (Tripati et al., 2005) from the Pacific (Fig. 4.1d versus Fig. 4.1c).

In Fig. 4.2 we show the relationship between measured $\Delta\delta^{18}O_{benthic}$ and global continental ice volumes for a range of values for mean $\delta^{18}O$ of stored ice ($\delta^{18}O_{ice}$). Horizontal dashed lines denote different values for $\delta^{18}O_{benthic}$, vertical solid lines correspond to different values assumed for $\delta^{18}O_{ice}$ and intersections yield the resulting estimated ice volumes (see 'isovol' lines). Lines a and b assume that the whole $\delta^{18}O_{benthic}$ signal is attributable to ice volume. Assuming that $\delta^{18}O_{ice}$ was as extreme as today (about 50‰ SMOW Coxall et al., 2005; Pekar et al., 2006), the $\Delta\delta^{18}O_{benthic}$ signal inferred in the Pacific study (Tripati et al., 2005) for CAE-3 (line a in Fig. 4.2) yields a global middle Eocene ice budget almost 1.5 times the present Antarctic ice volume (25.4×10^6 km^3) (Lythe et al., 2001). However, the latitudinal temperature gradient during the Eocene was less extreme than today, so it is likely that $\delta^{18}O_{ice}$ was also less extreme (conservatively, about 30‰ SMOW, Coxall et al., 2005; Pekar et al., 2006; Poulsen et al., 2007), yielding even larger ice budgets (almost 2.5 times the modern Antarctic budget). This ice volume is close to the global total estimated for the last glacial maximum (Fig. 4.2), when large ice sheets existed not only on Antarctica and Greenland but also over large areas of North America and Eurasia, and it implies an even greater global ice budget for the Eocene/Oligocene boundary when benthic $\delta^{18}O$ values were ~0.8‰ higher (Fig. 4.1a). Even larger ice volumes were invoked (Tripati et al., 2005) for CAE-3 in the Pacific study using the dual benthic Mg/Ca - $\delta^{18}O$ method ($\Delta\delta^{18}O_{seawater} = 1.5$‰). But we focus on the $\Delta\delta^{18}O_{benthic}$ signal alone because the presence of authigenic dolomite (Lear et al., 2004; Shipboard Scientific Party, 2002b) towards the base of the section at ODP Site 1218 means that the only potentially meaningful Mg/Ca data published for CAE-3 are for its termination (see Figure 3 of Tripati et al. 2005). By focusing on the $\Delta\delta^{18}O_{benthic}$ signal alone we adopt a conservative approach because the ice budgets calculated in this way in Tripati et al. (2005), although extreme (because the whole signal was attributed to ice growth with no associated cooling), are less extreme than those that were estimated by the dual benthic Mg/Ca - $\delta^{18}O$ method.

If we assume no cooling component associated with the smaller $\delta^{18}O_{benthic}$ signal seen in our new record (line b, Fig. 4.2), our revised estimate of the upper limit of possible ice growth associated with CAE-3 is correspondingly smaller, it need not require ice storage in the Northern Hemisphere and it is more in keeping with sequence stratigraphy records

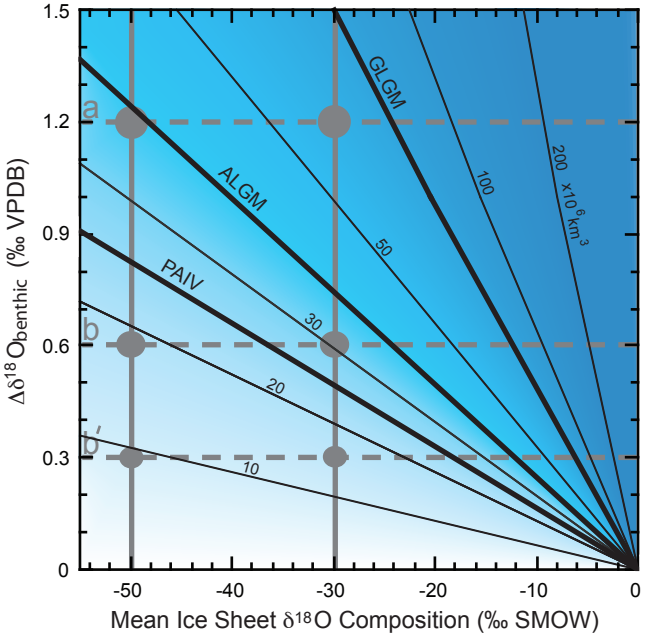

FIGURE 4.2: Measured increases in δ^{18}O in benthic foraminifera ($\Delta\delta^{18}O_{benthic}$) and resulting global continental ice volumes for a range of values for the mean δ^{18}O of stored ice ($\delta^{18}O_{ice}$). Horizontal dashed lines indicate different values for $\Delta\delta^{18}O_{benthic}$ (described in the text) and assume $\Delta\delta^{18}O_{benthic}$ = 100% ice volume (a, equatorial Pacific (Tripati et al., 2005); b, equatorial Atlantic, this study). Thick vertical lines correspond to different values of $\delta^{18}O_{ice}$ (estimated $\delta^{18}O_{ice}$ today at −50‰ and for the Middle Eocene at −30‰). Intersections yield resulting calculated ice volume shown by 'isovols' (values shown are $\times 10^6$ km^3). The horizontal dashed line labelled b' corresponds to $\Delta\delta^{18}O_{benthic}$ = 0.6‰, with 50% of that signal attributable to ice. Present Antarctic ice volume (PAIV) (Lythe et al., 2001), Antarctic ice volume at the Last Glacial Maximum (ALGM) (Huybrechts, 2002) and total global ice volume at the Last Glacial Maximum (GLGM) shown for reference. SMOW, standard mean ocean water.

(Pekar et al., 2005). On this basis, we cannot exclude the possible existence of small valley glaciers draining the uplands of Greenland around 41.6 Myr ago, particularly in light of dropstones recently discovered (Moran et al., 2006; Eldrett et al., 2007) in Eocene strata in the high northern latitudes. Nevertheless, we can rule out the existence of large ice sheets in the Northern Hemisphere and we therefore find no support for extreme Eocene bipolar glaciation. Based on work elsewhere (Pekar et al., 2006; Schrag et al., 2002) we might expect the $\Delta\delta^{18}O_{benthic}$ signal to be composed of at least equal parts ice volume and temperature (line b', Fig. 4.2). On this basis we calculate ice budgets that are easily accommodated on central Antarctica alone (∼0.4 to 0.6 times modern Antarctic budget). Under these circumstances, only by assuming an extremely high value for $\delta^{18}O_{ice}$ akin to the average for high altitude glaciers in the temperate zone today (≥15‰ SMOW) does the calculated ice volume exceed the modern budget for Antarctica (Fig. 4.2).

The main reason why the ice budgets of Tripati et al. (2005) are so large is because their

estimate of $\Delta\delta^{18}O_{benthic}$ was based on outlying data points and their isotope record is particularly sparse towards the top of magnetochron C19r (note the coring gap on the run up to CAE-3 and inferred glaciation, at the zone I/II boundary in Fig. 4.1c). To assess this interval in more detail we show an expanded version of our foraminiferal $\delta^{18}O$ series together with accompanying $\delta^{13}C$, lithological and bulk sediment records in Fig. 4.3. Excursions to lower values of $\delta^{18}O$ (by $\sim$0.4‰) and $\delta^{13}C$ (by 1.2−1.5‰) occur in both benthic and planktic records. These are accompanied by prominent decreases in bulk $\delta^{18}O$ (by 1.8‰) and $\delta^{13}C$ (by 1.1‰) within magnetochron C19r, across a 30 cm interval containing a highly dissolved foraminiferal assemblage and a well-developed red clay horizon where carbonate content falls sharply from $\sim$75 weight percent $CaCO_3$ to a minimum of $\sim$35 weight percent $CaCO_3$ (Fig. 4.3f). This event goes undetected in the equatorial Pacific record, presumably because it falls in the core gap at ODP Site 1218 (Fig. 4.1c) and therefore cannot explain the discrepancy between the two $\delta^{18}O_{benthic}$ signals shown in Fig. 4.1. On the other hand, our records show that, while ODP Site 1260 remained above the CCD for the vast majority of the study interval, shortly before the CCD deepened in the equatorial Pacific (CAE-3 in Fig. 4.1), it shoaled in the equatorial Atlantic sufficiently to be readily detectable at a water depth of about 3.0 to 2.5 km. In this respect, our records resemble those for the Eocene/Oligocene boundary where the CCD shoals sufficiently to completely eliminate $CaCO_3$ burial at ODP Site 1218 for $\sim$200 kyr immediately before the rapid two-step deepening associated with Antarctic glaciation (see Figure 1 of Coxall et al. 2005).

4.4 Conclusions

We cannot yet determine whether the C19r event is global in occurrence because of the coring gap at ODP Site 1218 and radiolarian clays and low sedimentation rates ($\leq$0.2 cm kyr) at other key drill sites in the Equatorial Pacific (Shipboard Scientific Party, 2002b) and on Shatsky Rise (Shipboard Scientific Party, 2002a). But it is distinct from the much longer-lived Middle Eocene Climate Optimum already documented at Site 1260 Sexton et al. (2006a) and it is more similar in expression to the well-known intervals of rapid carbon-cycle-led global warming and CCD shoaling in the early Palaeogene. The magnitude of the palaeoceanographic signals that we have documented for magnetochron C19r at Site 1260 is smaller than seen at the Palaeocene/Eocene boundary (Zachos et al., 2001, 2005) but at least as large as those marking the Eocene Thermal Maximum 2 ($\sim$53 Myr ago) (Lourens et al., 2005).

Our findings appear to highlight the instability of Eocene climate and to emphasize close coupling to the carbon cycle as expressed in oceanic carbonate saturation and $\delta^{13}C$. If the interval of CCD shoaling and isotopic shifts that we document is substantiated elsewhere, our results suggest that carbon-cycle-led instabilities akin to those documented in the early Eocene were not restricted to the Cenozoic climate optimum but also occurred

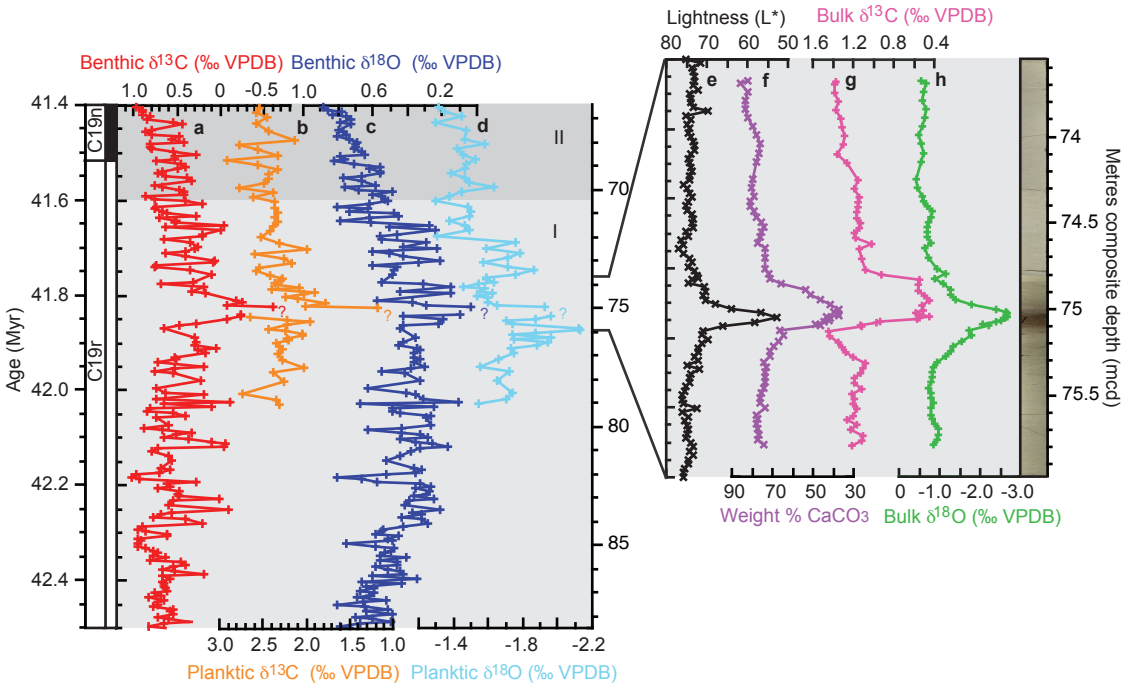

FIGURE 4.3: Palaeoceanographic records from ODP Site 1260 showing the run-up to CAE-3. We note the short-lived interval of CCD shoaling and ocean warming around 75 metres composite depth. a, Benthic δ^{13}C data. b, Planktic δ^{13}C data. c, Benthic δ^{18}O data. d, Planktic δ^{18}O data. e, Bulk sediment lightness (Shipboard Scientific Party, 2004). f, Bulk sediment weight %$CaCO_3$. g, Bulk sediment δ^{13}C. h, Bulk sediment δ^{18}O. Question marks in a–d denote absence of two to three samples because of the lack of suitable foraminifera for analysis in this interval. Grey shaded zones I and II as in Fig. 4.1.

millions of years later when the Earths baseline climate had cooled substantially and was poised much closer to the threshold of continental glaciation (Fig. 4.1a). Climate modelling experiments suggest (DeConto and Pollard, 2003, 2006) that this threshold would have been crossed earlier in the Southern Hemisphere than in the Northern Hemisphere (Fig. 4.1a) because of the fundamentally different land–ocean distributions at the two poles. Our work helps to re-align the geologic record with this view.

4.5 Methods

4.5.1 Chronology

We use the published (Suganuma and Ogg, 2006) palaeomagnetic reversal stratigraphy for ODP Site 1260, which we supplemented by analysing nearly 100 additional samples collected at approximately 20 to 30 cm intervals across each of the magnetic reversals

in the studied stratigraphic interval (magnetochrons C20r through C18r). Methods are as in Suganuma and Ogg (2006).

4.5.2 $CaCO_3$ and stable isotope data

All data were generated at the National Oceanography Centre, Southampton, UK. Bulk sediment weight $\%CaCO_3$ was measured on small (20−30 mg) discrete samples (1−5 cm spacing), by high-precision coulometry. Our foraminiferal stable isotope ($\delta^{18}O$ and $\delta^{13}C$) data were generated using species separates of the benthic and planktic foraminifera *Cibicidoides eoceanus* and *Morozovelloides lehneri*, respectively. Foraminifera were cleaned by ultrasonication before analysis. Benthics were picked from the size range 300−450 μm while planktics were picked from the 250−300 μm size fraction. Bulk stable isotope measurements were generated on splits of the same samples used for $CaCO_3$ data. All stable isotope measurements were determined using a Europa GEO 20−20 mass spectrometer equipped with an automatic carbonate preparation system. Results are reported relative to the Vienna Pee Dee Belemnite (VPDB) standard with an external analytical precision, based on replicate analysis of an in-house standard calibrated to NBS-19, better than 0.1‰ for $\delta^{18}O$ and $\delta^{13}C$. Benthic $\delta^{18}O$ values that we report from ODP Site 1260 have been adjusted to equilibrium by adding 0.28‰VPDB, the Palaeogene correction factor for *Cibicidoides*. We plot *Cibicidoides* data from ODP Site 1218 in the same way to aid comparison (Site 1218 data from *Nuttallides truempyi* are reported in the same way as in Tripati et al. 2005).

Chapter 5

Magnetic reversal stratigraphy of ODP Site 1051, Blake Nose

5.1 Introduction

5.1.1 Construction of the Geomagnetic Polarity Time Scale

The Geomagnetic Polarity Time Scale (GPTS) is the backbone of geological research, enabling stratigraphic correlation of rocks and sediments worldwide. The GPTS is based on the discovery that alternating intervals of magnetic polarity recorded by iron-bearing minerals in ocean basalts, correspond to reversals of Earth's magnetic field through time (Fig. 5.1) (Vine and Matthews, 1963). Recognition that this same pattern of magnetic reversals was also recorded simultaneously by iron oxides and other magnetic carriers in rocks and sediments worldwide, led to the development of magnetostratigraphy as a means of correlating sediments to the reference GPTS (Harrison and Funnell, 1964; Opdyke et al., 1966). At the present day the magnetic pole is in the Northern Hemisphere and the magnetic field is regarded as possessing a 'normal' polarity (Fig. 5.2), when the magnetic pole is in the Southern Hemisphere the magnetic field is said to possess a 'reversed' polarity.

The GPTS was constructed by determining the relative widths of Late Cretaceous and Cenozoic magnetic polarity intervals recorded in ocean basalts from marine magnetic anomaly profiles (Fig. 5.1). These profiles were primarily from the well documented, slow spreading South Atlantic mid ocean ridge (Heirtzler et al., 1968; Cande and Kent, 1992a), which has a long and continuous spreading history (Cande et al., 1988). Where necessary, finer scale information on magnetic polarity intervals was integrated into the South Atlantic spreading model from the marine magnetic profiles of faster spreading ridges ($\geq$50 mm/yr) in the Pacific and Indian Oceans (Cande and Kent, 1992a). The

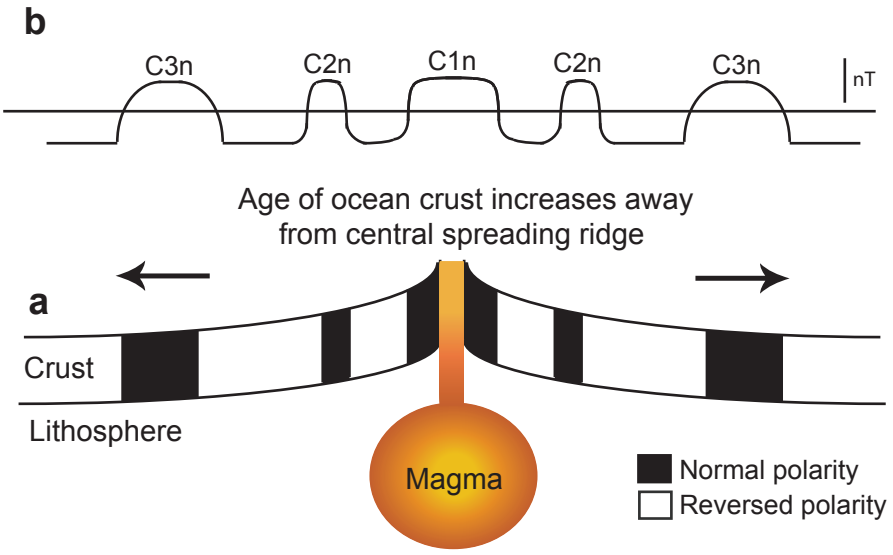

FIGURE 5.1: Magnetic reversals recorded in ocean crust. a) Magnetic 'stripes', represent alternating intervals of magnetic polarity or 'chrons' that run parallel to the spreading ridge and are symmetrical on both sides of the ridge. Polarity chrons are of varying widths because of changes in seafloor spreading rates and in the timing of magnetic polarity reversals. b) Schematic magnetic anomaly profile for the pattern of magnetic reversals shown in a. Polarity intervals in the Cenozoic and Late Cretaceous are numbered sequentially backwards from magnetochron C1 at the present day through to C34 in the Late Cretaceous. Normal geomagnetic polarity intervals are denoted by the suffix 'n' ,e.g., 34n, and 'r' is used to define the preceeding reversed-polarity interval (Ogg, 1995).

resulting composite magnetic polarity 'reference' sequence was then scaled and fitted onto a synthetic sea-floor spreading flow line in the South Atlantic.

Despite the large number of magnetic reversals recorded in the Late Cretaceous and Cenozoic, very few reliable radiometric ages exist to establish an absolute chronology for the magnetic reversal stratigraphy. This is largely attributable to difficulties in dating ocean basalts in which magnetic polarity intervals are recorded. In addition, an assumption of the seafloor spreading rate through time has to be made in order to interpolate between age control points. Unlike their predessors (Heirtzler et al., 1968), Cande and Kent (1992a) assumed that seafloor spreading rates were not constant through the Late Cretaceous and Cenozoic but varied (smoothly) with time. They therefore generated a time scale for the composite magnetic reversal sequence by fitting a cubic spline function to nine radiometric age calibration points and the zero-age ridge axis dating from the current magnetochron, C1n to the Cretaceous 'superchron' C34n (Cande and Kent, 1992a). However, of the nine radiometric ages used in Cande and Kent (1992a), only four fell within the Paleogene. Subsequent revision of age control points resulted in a revised GPTS in 1995, with the Cretaceous/Tertiary boundary revised from 66 to 65 Ma (Cande and Kent, 1995) and the first magnetochron ages based on

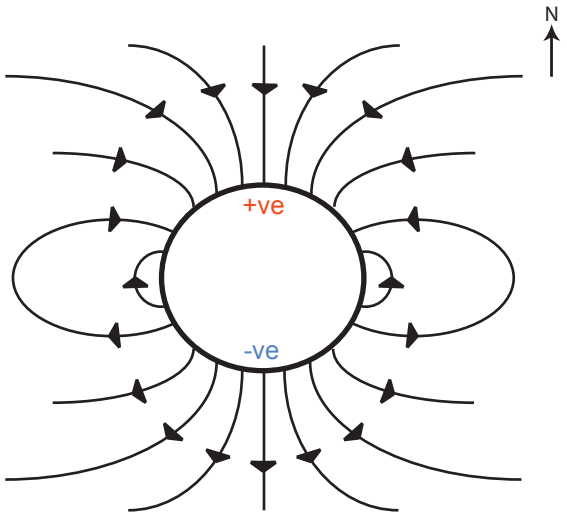

FIGURE 5.2: Schematic view of Earth's magnetic field lines at the present day. At the equator, the magnetic field lines are parallel to the Earth's surface therefore inclination, defined as the angle between the Earth's surface and the magnetic field, is 0°. At higher latitudes, inclination becomes progressively steeper until at the north magnetic pole, magnetic field lines are directed straight down into the Earth and inclination is 90°. During an interval of normal polarity, rocks and sediments in the Northern Hemipshere record a positive inclination and in the Southern Hemisphere a negative inclination. The opposite is true for an interval of reversed polarity.

astrochronology in the Plio-Pleistocene (Shackleton et al., 1990; Hilgen, 1991). In 2004, a new GPTS was proposed which revised the ages of magnetochrons from C6 in the earliest Miocene to C33 in the Cretaceous (Ogg and Smith, 2004). Modifications included astronomical tuning of the Neogene magnetic anomaly profile, estimated duration of Paleogene chrons from Milankovitch cyclicity, a new ridge spreading rate model and an increased number of radiometric age-control points available for spline fitting, of which twelve now fell in the Paleogene. The GPTS is in a constant state of flux and will continue to evolve as more precise magnetostratigraphic correlations are determined, new age control points are generated and as an astronomical timescale becomes available for the Paleogene.

The GPTS shows that complete reversals of magnetic polarity occur every 2 to 3 million years on average (Ogg, 1995). However, marine magnetic anomaly profiles from fast spreading mid ocean ridges, often show that intervals of constant polarity are punctuated by small amplitude, short frequency features termed 'tiny wiggles' (Fig. 5.3) (LaBrecque et al., 1977). There are two competing hypotheses as to the origin of these tiny wiggles. The first hypothesis suggests that tiny wiggles represent short magnetic reversals (Blakely and Cox, 1972; Gubbins, 1999; Roberts and Lewin-Harris, 2000). In fact, several tiny wiggles are now recognised as true magnetic reversals, these are the ∼10 kyr long normal polarity Cobb Mountain (Mankinen et al., 1978; Clement and Martinson, 1992) and Réunion subchrons (Chamalaun and McDougall, 1966) at ∼1.1 Ma

and ~2.1 Ma, respectively. The second hypothesis, is that the majority of tiny wiggles reflect large scale fluctuations in Earth's magnetic field intensity that are sometimes accompanied by palaeodirectional changes, termed palaeomagnetic 'excursions' (Cande and Kent, 1992b; Tauxe and Hartl, 1997; Bowles et al., 2003). However, the origin of many tiny wiggles in magnetic anomaly profiles remains uncertain. Consequently, Cande and Kent (1992a) refer to these tiny wiggles as 'cryptochrons' and exclude them from the GPTS because of complications in determining the origin and global significance of these short ≤30 kyr events. At least 54 tiny wiggles are identified from Cenozoic marine magnetic anomaly profiles but none are reported in the 20 million year interval between magnetochrons C15 in the Late Eocene and C24 in the Early Eocene (Cande and Kent, 1992a). Eocene marine magnetic anomaly profiles do show some evidence of tiny wiggles through this interval (Fig. 5.3) but these tiny wiggles are from widely spaced locations and the tiny wiggles are not reproducible between profiles (Cande and Kent, 1992a).

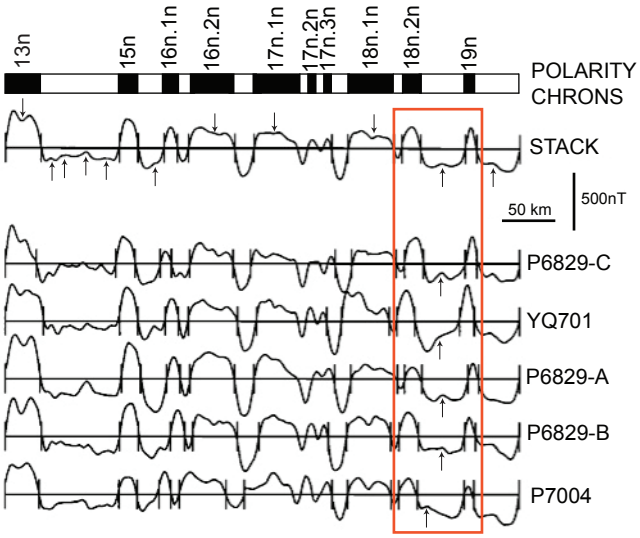

FIGURE 5.3: Magnetic anomaly profiles from the North Pacific used to constrain the fine detail within magnetic anomalies 15 to 20 in the Middle Eocene. Positive anomalies correspond to intervals of normal magnetic polarity and negative anomalies to reversed magnetic polarities. Black arrows indicate the position of tiny wiggles in the stacked anomaly record. The stacked records results in a smoothing of tiny wiggles reducing their apparent amplitude and the number of events because not all wiggles are uniformly resolved between the different profiles. Red box outlines the interval investigated at high resolution in this study and black arrows indicate the position of tiny wiggles in the individual profiles during this interval. Figure modified from Figure 20 in Cande and Kent (1992a).

In this chapter a new high-resolution magnetic reversal stratigraphy is presented from sediment cores of Eocene age recovered at Ocean Drilling Program (ODP) Site 1051 in the western North Atlantic. At Site 1051 a stratigraphically complete (to magnetochron level) Middle Eocene sedimentary succession was recovered with the highest deep-sea sedimentation rates (~4 cm/kyr) so far reported for this interval of time. The

Middle Eocene interval investigated here (magnetochrons C18 and C19) is a key target of chronostratigraphic studies for two main reasons. First, there are extremely few direct calibrations of calcareous plankton biostratigraphic datums to sections with reliable magnetostratigraphies in this interval (Berggren et al., 1985, 1995; Aubry and Van Couvering, 2005). Second, the interval in which magnetochrons C18 and C19 occur is palaeoclimatically important because it hosts the global warming event, the Middle Eocene Climatic Optimum (MECO) (Bohaty and Zachos, 2003; Sexton et al., 2006a; Agnini et al., 2007; Spofforth et al., 2008) and the so-called 'extreme bipolar glaciation' event hypothesized by Tripati et al. (2005) (see Chapter 4). The aims of this work are to refine the existing magnetic reversal stratigraphy at Site 1051, to help calibrate planktic foraminiferal datums at this site (datums refined in Chapter 6), to aid refinement of the integrated biomagnetochronologic scale (IBMS), to help constrain the nature and timing of palaeoclimatic events and to to determine the origin of tiny wiggles reported in magnetochron C18.

5.2 Geological setting and magnetostratigraphy of ODP Site 1051

During ODP Leg 171B, a depth transect of five sites were drilled on the Blake Nose plateau in the western North Atlantic (Sites 1049 - 1053) aimed at recovering shallowly buried Cretaceous and Paleogene sediments. Two holes, A and B, were drilled at Site 1051 (30°03'N; 76°21'W) (Fig. 5.4) in a water depth of ∼1980 mbsl. Site 1051 recovered an expanded and almost complete Late Paleocene to Late Eocene sedimentary sequence dominated by nannofossil and siliceous microfossil oozes, with ∼25 thin ash layers in the Eocene (Shipboard Scientific Party, 1998). The Middle Eocene is represented at Site 1051 by two main subunits; subunit IB, a thick yellow siliceous nannofossil ooze with foraminifers and clay (1051A, 2.98 - 73.96 metres composite depth, mcd;1051B, 4.80 - 74.05 mcd) and subunit IC, a grey green siliceous nannofossil ooze with foraminifers and clay (1051A, 73.96 - 129.98 mcd; 1051B, 74.05 - 146.06 mcd). The transition from subunit IB to IC is marked by a sharp yellow to green colour transition reflecting a change in the redox state of the sediment as observed at other Blake Nose Sites 1050, 1052 and 1053. A composite shipboard splice was constructed for the Middle Eocene by correlating GRAPE density and colour data between holes A and B, with 1051B forming the backbone of the splice (Shipboard Scientific Party, 1998).

Shipboard pass-through cryogenic magnetometer measurements made during Leg 171B, were made at ∼5 cm intervals on cores from both holes A and B, using alternating field (AF) demagnetisation (Chapter 2 for details of the method). Shipboard measurements yielded a relatively noisy polarity record from which it was difficult to accurately determine the boundaries of individual polarity intervals. Subsequently, 195 minicores from Hole 1051A, 2 samples per core section, were taken for shore based

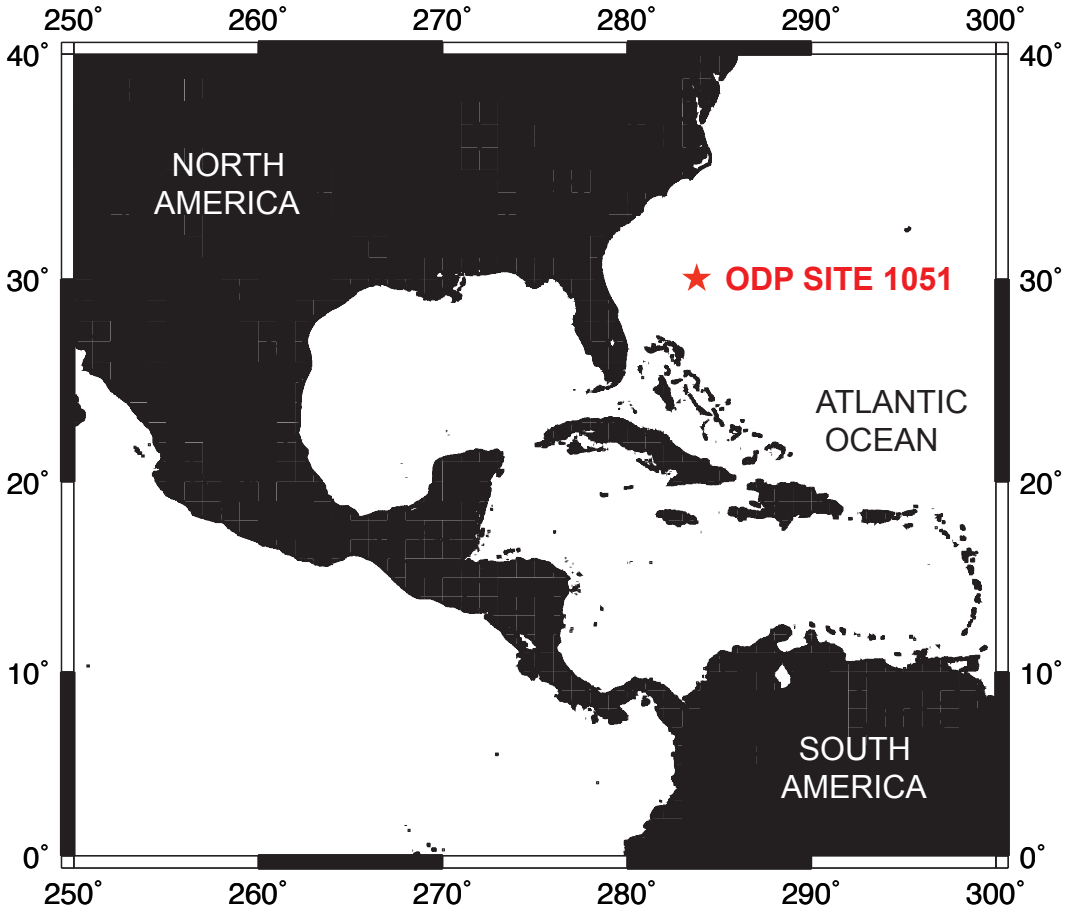

FIGURE 5.4: Location map showing the position of ODP Site 1051 on the Blake Nose Plateau.

work and treated using progressive thermal demagnetisation (Ogg and Bardot, 2001). These new measurements were integrated with the shipboard dataset enabling a more reliable magnetostratigraphy to be developed from magnetochron C28n through C16n (Shipboard Scientific Party, 1998; Ogg and Bardot, 2001).

5.3 Results

5.3.1 Magnetic behaviour and palaeomagnetic directions of sediments from ODP Site 1051

To generate a continuous high-resolution record of magnetic polarity from ODP Site 1051, continuous u-channels were taken between 1051A 7H-3 (66.15 mcd) and 1051B 15H-7 (146.43 mcd) following the shipboard splice, and measured at 1 cm (∼250 yr) resolution using progressive stepwise alternating field (AF) demagnetisation on a cryogenic

magnetometer (Chapter 2 for further details). The majority of the u-channel samples have weak magnetisations, in the range of 10^{-5} to 10^{-4} mA/M typical of carbonate rich sediments, which contain a low abundance of magnetic minerals. At Site 1051 the weak magnetisation potential of the sediments is further exacerbated by the high dilution of magnetic carriers by biogenic components, in particular radiolarians (Shipboard Scientific Party, 1998). Despite the weak magnetic signal recorded, the majority of u-channel samples have a stable and easy-to-interpret magnetic behaviour, demonstrated by demagnetisation directions that trend towards the origin of the vector component plot or Zidjerveld diagram (Fig. 5.5). Most of the analysed samples are characterised by the presence of a small, low-stability component with a steeply dipping normal inclination (blue dashed lines in Fig. 5.5c and e) which is interpreted to be an overprint from drilling. This magnetic overprint is successfully removed with peak AF fields of 20 mT isolating the characteristic remanent magnetism (ChRM) of each of the samples in the lower part of the core splice (108 - 146 mcd) between 20 and 50 mT, shown by the red dashed lines in Figure 5.5. Typical demagnetisation behaviour of u-channel samples is shown in Figure 5.5.

Towards the top of the core splice, 65 to 108 mcd, the demagnetisation behaviour of samples is progressively less stable, i.e., no clear ChRM component decaying towards the origin of the Zidjerveld diagram, and at demagnetisation steps above 20 mT behaviour often becomes erratic showing increasing magnetic intensities (Fig. 5.6a, b and c). Therefore, the ChRM in these samples is typically determined between the 5 and 20 mT demagnetisation steps (red dashed lines in Fig. 5.6a and b). Several u-channels record large jumps in the magnetisation intensity known as 'flux' jumps (Fig. 5.6e). These occur when the magnetometer is unable to count the large magnetic flux from 'strongly' magnetised samples fast enough and a non-reversable jump in magnetisation occurs (Roberts, 2006). Flux jumps render all of the data from that demagnetisation step useless and these data are removed from the dataset, reducing the number of data points that can be used to determine the sample's ChRM.

To determine the magnetic inclination and declination of the ChRM in each sample and the reliability of these calculated values, principal component analysis (PCA) was used to estimate the best least-squares regression line fit, along the demagnetisation paths plotted onto Zijderveld diagrams (Fig. 5.5 and described in Chapter 2) (Kirschvink, 1980). A minimum of three and a maximum of seven successive data points thought to represent the ChRM were manually selected for PCA of each sample. The precision of the best fit line was estimated by the maximum angular deviation (MAD). Lines with a MAD value of $\geq 15^{\circ}$ are thought to represent unstable magnetic behaviour and are generally excluded from palaeomagnetic studies, whereas those with a MAD value $\leq 10^{\circ}$ represent more reliable and stable magnetic behaviour, for example Figure 5.5 (Butler, 1992; McElhinny and McFadden, 2000). Following this orthodoxy, only data with a MAD value of $\leq 10^{\circ}$ are presented in this study. This practice results in a relatively

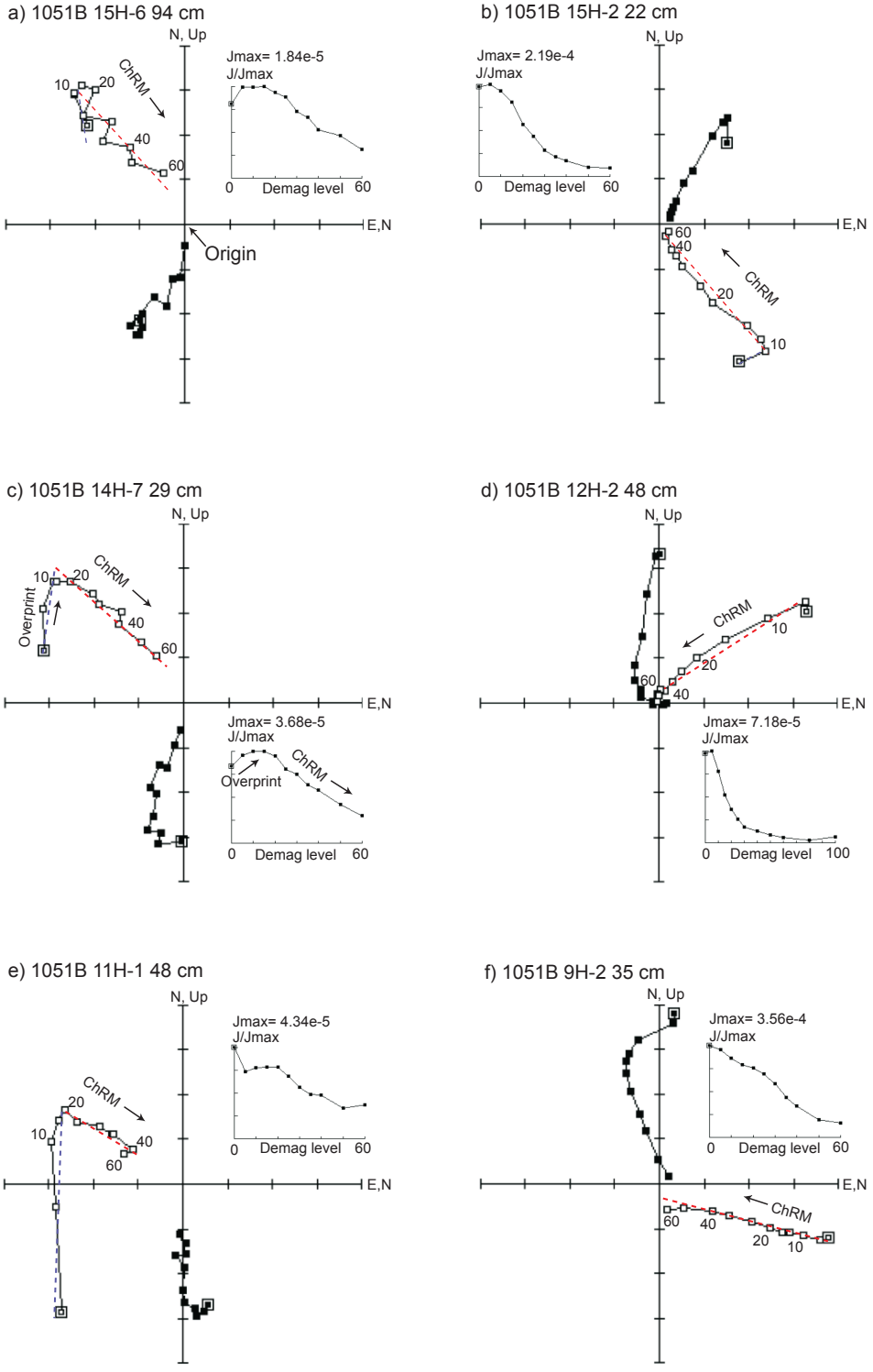

FIGURE 5.5: Typical alternating field (AF) demagnetisation profiles for 90 to 150 mcd from ODP Site 1051. For the Zidjerveld diagrams, open symbols represent projections on to the vertical plane (inclination - labelled with demagnetisation steps) and closed symbols on to the horizontal plane (declination). Magnetic polarity is determined using the inclination of samples. Dashed blue lines represent secondary natural remanent magnetism (NRM), i.e., the drilling overprint, not used to determine the sample polarity, and the red dashed lines show the characteristic remanent magnetism (ChRM) that is used to determine the polarity for each sample. Small figure insets show changes in NRM intensity during AF demagnetisation used to help assess the stability of demagnetisation behaviour and isolate the ChRM, Mmax is the maximum magnetisation measured in mA/M. MAD of all samples shown is $\leq 10°$.

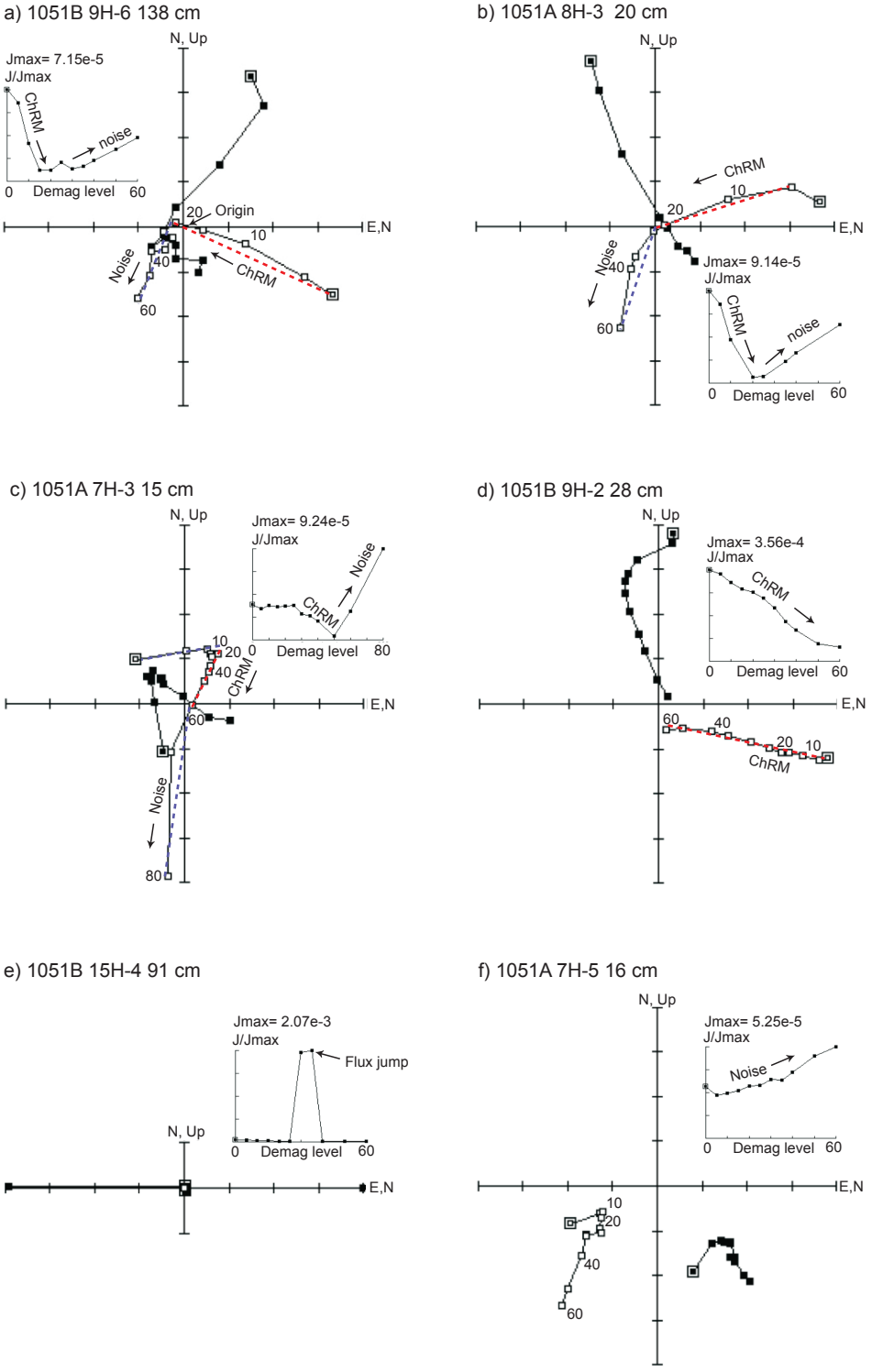

FIGURE 5.6: Typical alternating field (AF) demagnetisation profiles for 65 to 90 mcd from ODP Site 1051. For the Zidjerveld diagrams, open symbols represent projections on to the vertical plane (inclination - labeled with demagnetisation steps) and closed symbols onto the horizontal plane (declination). Dashed blue and red lines represents the secondary natural remanent magnetism (NRM), i.e., overprint,s and the characteristic remanent magnetism (ChRM) respectively. Insets show changes in NRM intensity during AF demagnetisation, Mmax is the maximum magnetisation measured in mA/M. Figures a) and b) ChRM interpreted between 5 and 20 mT, prior to intensity increase and spurious component decaying away from origin of plot, c) and d) clear ChRM component, e) flux jumps at 30 and 35 mT, data points must be removed from dataset prior to interpretation of ChRM, and f) sample not interpreted because shows an anomalous increase in intensity at progressively higher demagnetisation levels and no clear component decaying towards the origin of the plot.

continuous polarity record in the lower part of the core splice where ≥75% of data have MAD values ≤10° (Table 5.1) but in the topmost part of the core splice the polarity data are more sparse because only ∼50% of the data have a MAD value ≤10°.

TABLE 5.1: Summary of maximum angular deviation (MAD) values in the ODP Site 1051 core splice. Cores are presented in the order in which they appear in the 1051 core splice between 150 and 64 mcd. Higher percentage of 'good' (MAD ≤10°) data points are recovered in the lowermost part of the core splice where demagnetisation behaviour of samples is more stable (Fig. 5.5).

Site	Hole	Core	% MAD ≤10	% MAD ≥10
1051	B	15H	95.6	4.4
1051	A	15H	84.5	15.5
1051	B	14H	93.4	6.6
1051	A	14H	76.7	23.3
1051	B	13H	93.6	6.4
1051	A	13H	97.6	2.4
1051	B	12H	87.2	12.8
1051	A	12H	97.9	2.1
1051	B	11H	95.1	4.9
1051	A	11H	78.4	21.6
1051	B	10H	57.1	42.9
1051	B	9H	50	50
1051	A	9H	76.4	23.6
1051	B	8H	54.4	45.6
1051	A	8H	85.6	14.4
1051	A	7H	53.3	46.7

5.3.2 Reconstructing palaeointenstity variations of the geomagnetic field

Anhysteretic remanent magnetism (ARM) was imparted to all of the u-channels following measurement of NRM (Chapter 2 for details). These data were coupled with NRM data measured in the same sediments to generate a NRM/ARM record, a proxy for the palaeointensity of Earth's magnetic field used to help determine the origin of polarity shifts observed in the dataset. Low-field magnetic susceptibility was also measured on a sub set of u-channels to provide a second normalising parameter but the measured signal had a low signal to noise ratio and therefore a magnetic susceptibility record was not generated for the study interval.

5.4 Discussion

5.4.1 Magnetic reversal stratigraphy at ODP Site 1051

Following principal component analysis, measurements with an inclination $\geq$+80 degrees (assumed to be a steep drilling overprint) were removed from the dataset, as were data from the top and bottom 5 cm of each u-channel to avoid edge effects resulting from smoothing of magnetometer measurements over a 10 cm moving window (Roberts, 2006). Recognition of polarity intervals is based on the clustering of positive or negative inclinations, predominantly after the 20 mT demagnetisation step for the lower part of the core splice (108 - 150 mcd) and between 5 and 20 mT in the upper part of the data set (65 - 108 mcd). ODP Site 1051 has an estimated paleolatitude (λ) of $\sim$25°N in the Eocene (Ogg and Bardot, 2001), therefore positive inclinations correspond to normal polarity intervals and negative inclinations to reversed polarity intervals (Fig. 5.2). Planktic foraminiferal biostratigraphic datums and the pattern of polarity chrons are used to anchor the magnetic reversal stratigraphy to the GPTS. For consistency with the new Eocene planktic foraminiferal stratigraphy employed in this study (Berggren and Pearson, 2005), the numerical ages of the GPTS of Cande and Kent (1992a, 1995) are used. The main features of the polarity pattern at ODP Site 1051 are well resolved, providing a detailed record of magnetochrons C19r through C18n in the Middle Eocene (Figs 5.7, 5.8, 5.9, 5.10 and 5.11).

The short normal polarity interval between 138.42 and 143.53 mcd has a sharp square wave polarity pattern that is assigned to magnetochron C19n, with chron boundaries resolved by the new dataset to within $\pm$1 cm (magnetochron boundary defined as the point where inclination becomes 0°) (Fig. 5.11). The sharp ($\leq$20 cm) transition between polarity states indicates that magnetic reversals occurred rapidly (within 5 kyrs), and are accompanied by a collapse in the magnetic field intensity, inferred from the NRM/ARM record (horizontal grey bars in Fig. 5.12). Magnetic field intensity decreased by $\sim$70-80% reaching minimum values immediately prior to and during the transition from magnetochron C19r to C19n. There is an increase in the relative palaeointensity of the magnetic field following this transition before it collapses once again to lower values at the succeeding magnetochron C19n/C18r boundary. Good agreement between the position of magnetic reversals and magnetic field intensity variations in the dataset suggests that these records are robust.

The long reversed polarity interval between 90 and 138 mcd that follows magnetochron C19n is assigned to C18r (Fig. 5.9). Superimposed on magnetochron C18r are a number of previously unrecognised short-lived intervals during which the magnetic polarity reverses. These are referred to as polarity 'events' for the time being to avoid confusion with geomagnetic excursions and reversals and are discussed in more detail in subsection 5.4.3. The top of magnetochron C18r is not so well defined as its base because

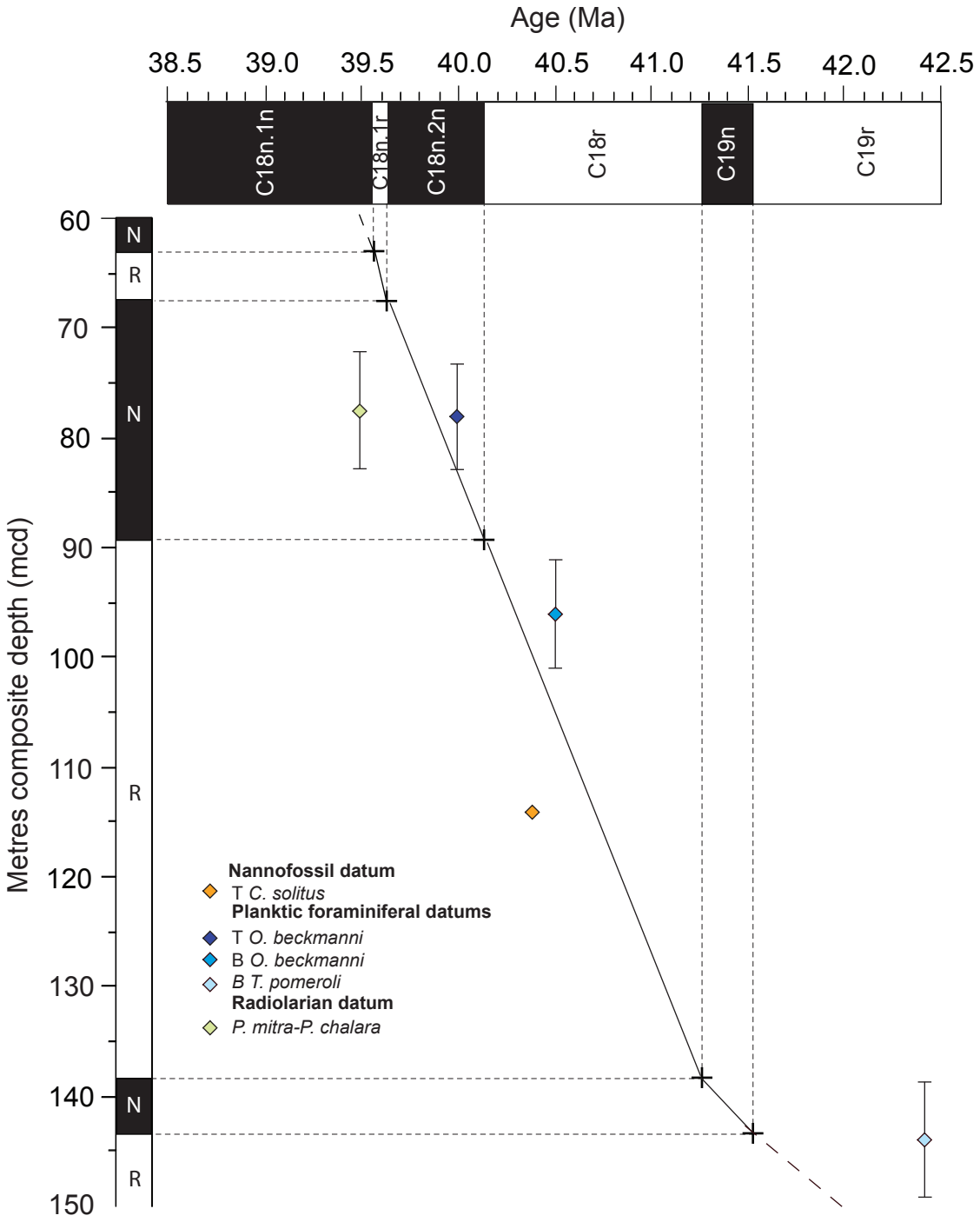

FIGURE 5.7: Correlation of the polarity sequence determined at ODP Site 1051 to the Geomagnetic Polarity Time Scale of Cande and Kent (1992a, 1995). Shipboard biostratigraphic datums are used to anchor assignment of magnetochrons to the polarity record (Shipboard Scientific Party, 1998). Polarity intervals marked 'R' have a reversed polarity and those marked 'N' have a normal polarity. T and B represent the last and first occurrence of a species, respectively.

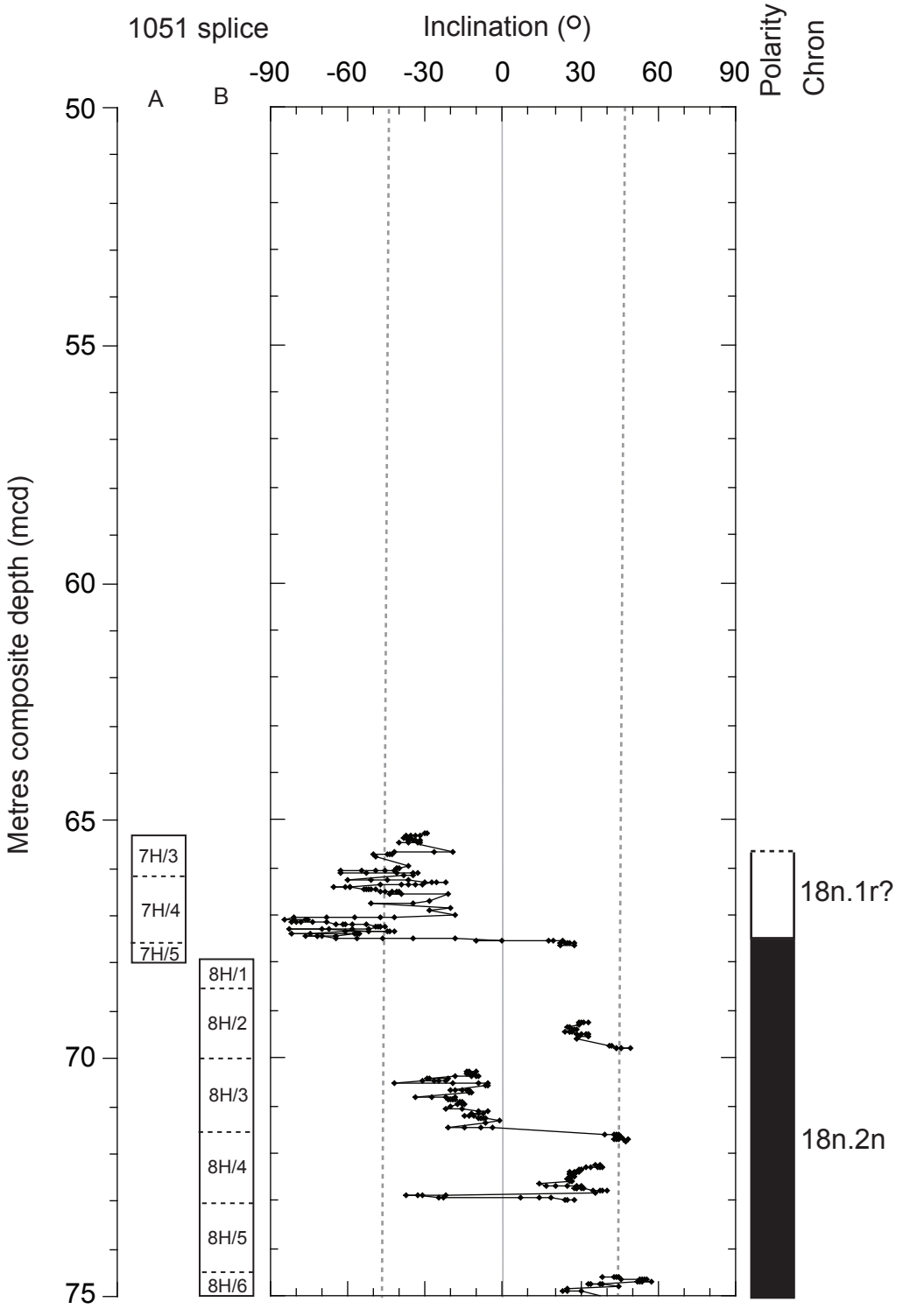

FIGURE 5.8: High resolution magnetic polarity data and magnetochron assignment between 50 - 75 mcd at ODP Site 1051. All maximum angular deviation values for these data are $\leq 10°$. Vertical grey dashed lines represent the expected inclination values (43° and -43°) calculated for Site 1051. Solid grey line denotes 0°. Gaps in the inclination record represent data removed because they have MAD values of $\geq 10°$ or are with an uninterpretable polarity.

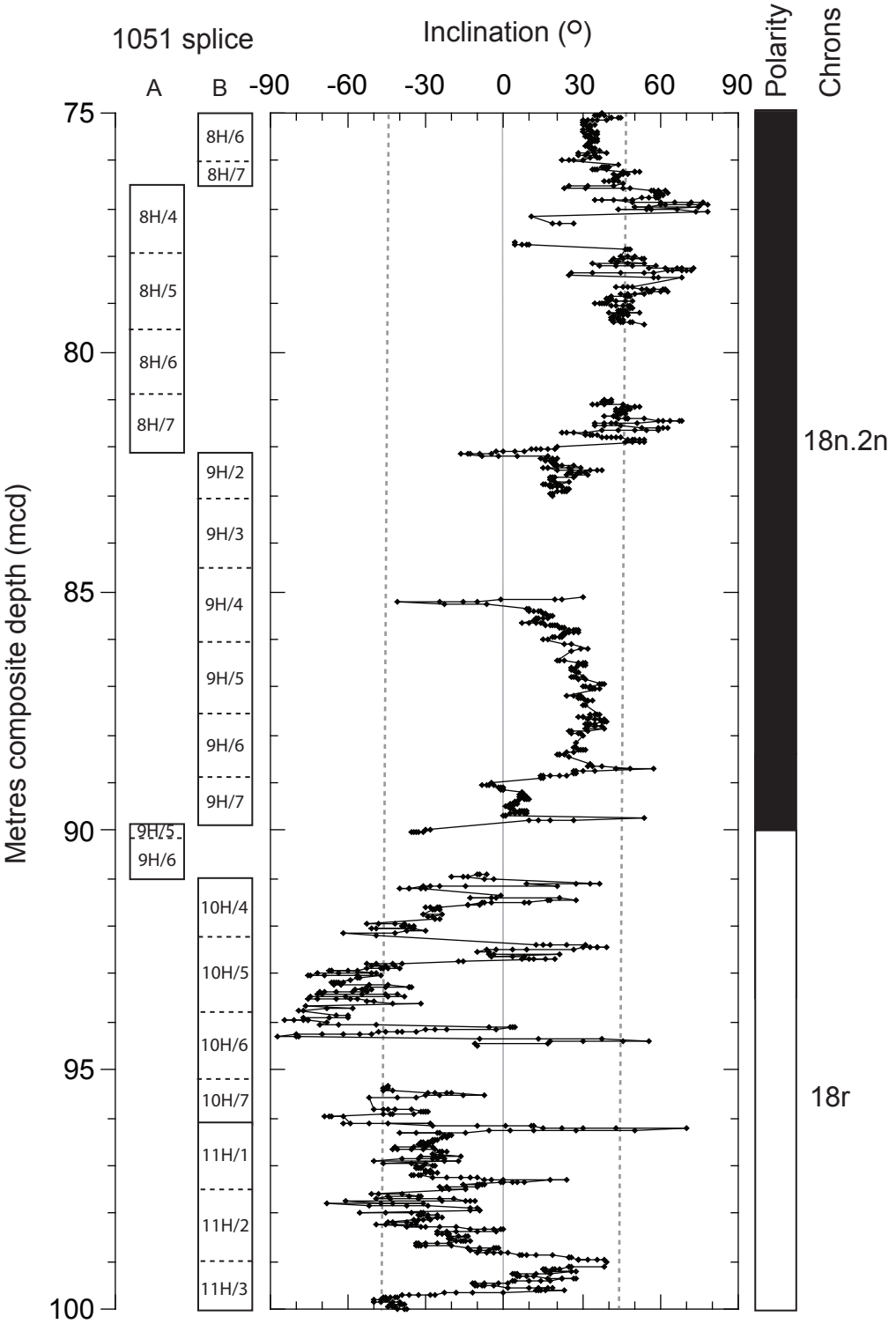

FIGURE 5.9: High resolution magnetic polarity data and magnetochron assignment between 75 - 100 mcd at ODP Site 1051. All maximum angular deviation values for these data are $\leq 10°$.Vertical grey dashed lines represent the expected inclination values (43° and -43°) calculated for Site 1051. Solid grey line denotes 0°. Gaps in the inclination record represent data removed because they have MAD values of $\geq 10°$ or are with an uninterpretable polarity.

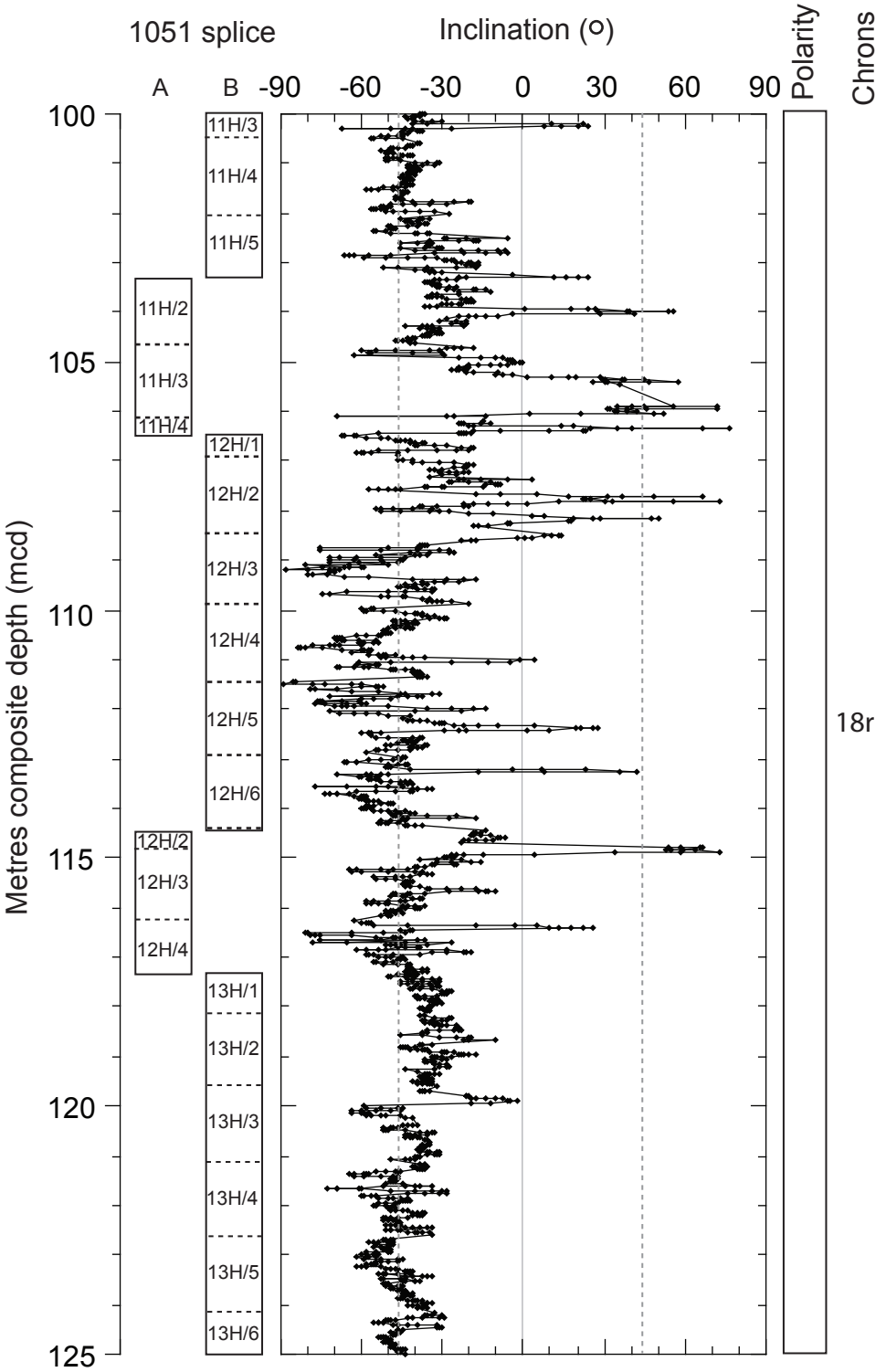

FIGURE 5.10: High resolution magnetic polarity data and magnetochron assignment between 100 - 125 mcd at ODP Site 1051. All maximum angular deviation values for these data are $\leq 10°$. Vertical grey dashed lines represent the expected inclination values (43° and -43°) calculated for Site 1051. Solid grey line denotes 0°.

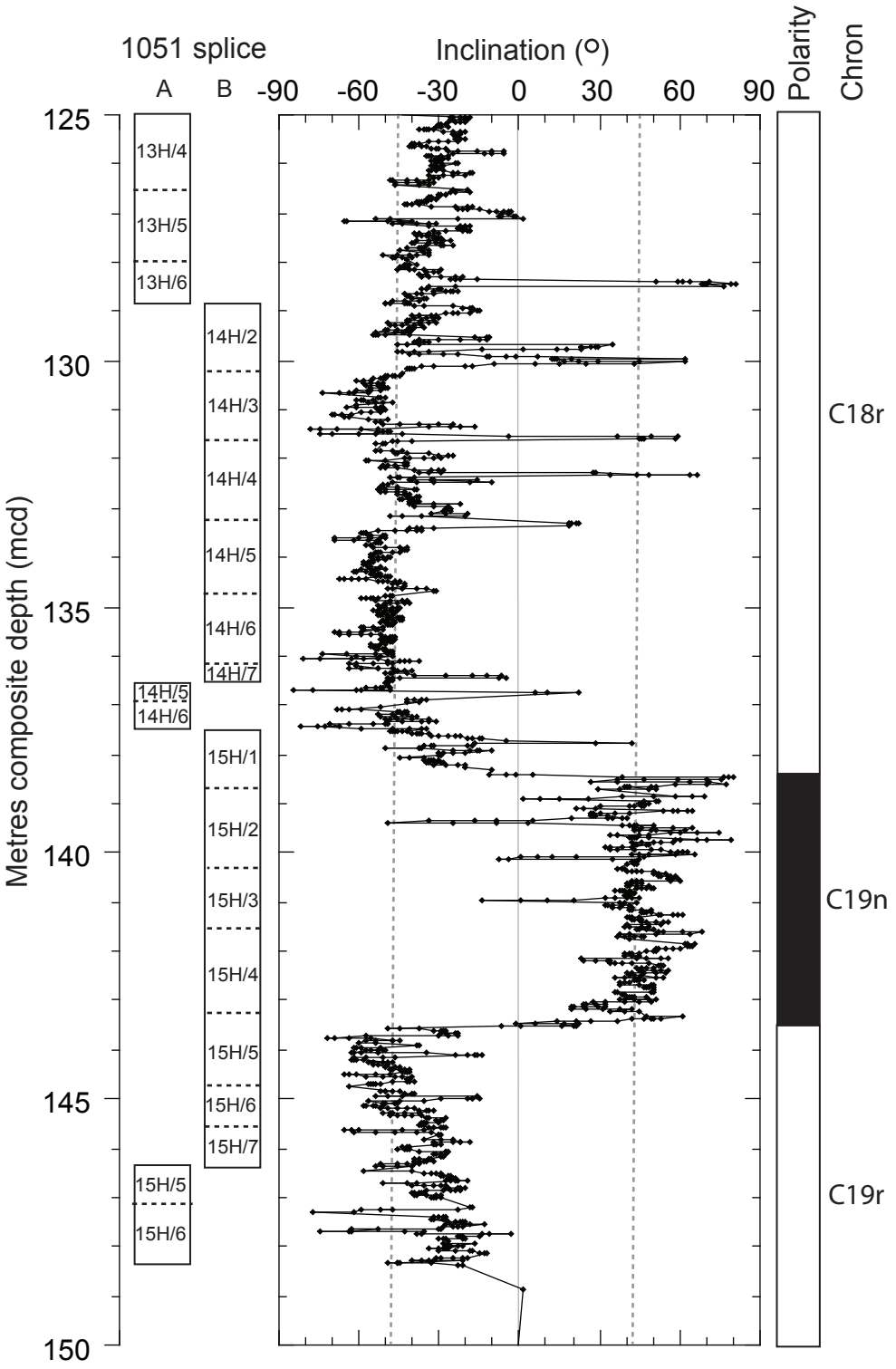

FIGURE 5.11: High resolution magnetic polarity data and magnetochron assignment between 125 - 150 mcd at ODP Site 1051. All maximum angular deviation (MAD) values for these data are $\leq 10°$.Vertical grey dashed lines represent the expected inclination values (43° and -43°) calculated for Site 1051. Solid grey line denotes 0°.

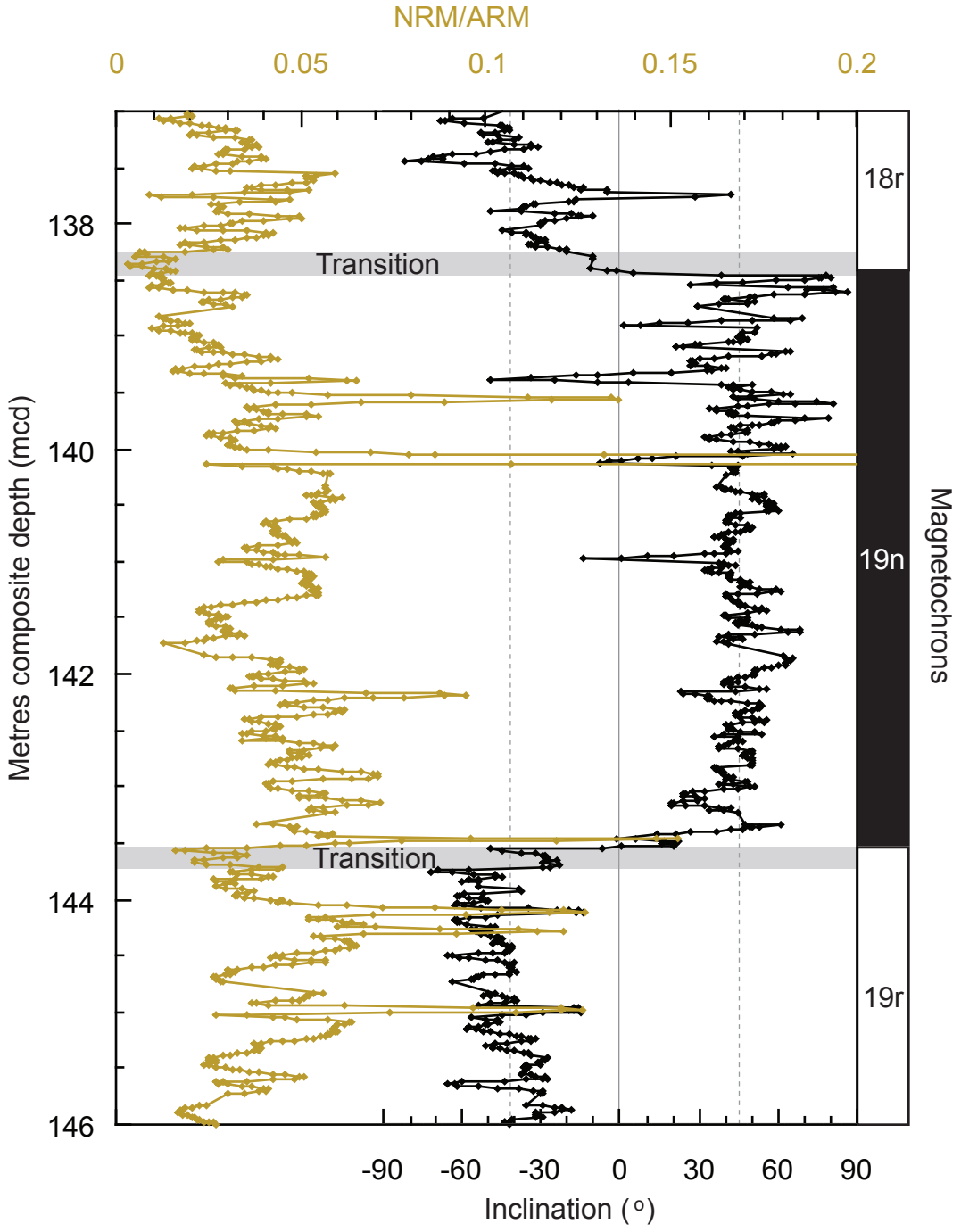

FIGURE 5.12: Relative palaeointensity of the geomagnetic field across magnetochron C19n. Natural remanent magnetism/anhysteretic remanent magnetism (NRM/ARM) after demagnetisation at 25 mT (all demagnetisation levels show the same pattern of change but only one shown for clarity). The NRM/ARM data show that the geomagnetic field collapsed immediately before and during the polarity transitions (shaded grey bars). Magnetic field strength recovered within magnetochron C19n before collapsing at the succeeding polartiy transition. Several high-intensity spikes in the NRM/ARM record are coincident with short lived polarity shifts.

there are several short excursions to more positive inclination values at 91 and 94 mcd prior to the reversal, and the magnetic reversal itself is only sparsely recorded because many of the samples from this interval lack a clear ChRM and therefore have a poor MAD value ($\geq$15°). A weak ChRM component may be attributable to the sustained interval of low magnetic field intensity that accompanies the magnetic reversal, i.e., only generating a weak magnetic signal (Figs 5.14 and 5.15) and be exacerbated by the weak magnetisation potential of the carbonate-rich sediments at Site 1051.

Within the succeeding polarity interval assigned to magnetochron C18n.2n, data is more sparse because of poorly defined ChRM in many samples and in two rare cases, the polarity of two entire core sections is uninterpretable (Fig. 5.6f). The deterioration in the stability of the magnetic signal recorded in sediments at Site 1051 above 85 mcd, appears to coincide with an increase in the frequency and amplitude of changes in the NRM/ARM record (Fig. 5.14). This may reflect instability of the geomagnetic field intensity through this interval but records from other deep sea sites show no evidence for this (Pares and Lanci, 2004; Florindo and Roberts, 2005; Jovane et al., 2007). It is more likely that the decrease in the magnetic signal stability reflects changes in the physical properties of the sediment or the magnetic signal recorders, that have modified the magnetic intensity. The most obvious explanation therefore, is the large change in sediment colour from yellow to green observed between subunits IB and IC at 74 mcd, which is coincident with the largest NRM/ARM variability. This colour change is attributed to a change in the redox state of the sediment and may have modified the magnetic character of the sediment. Otherwise, there are no other obvious physical property changes across this interval. Additional analysis of small discrete samples to determine any changes in the dominant magnetic carrier in the sediment upcore failed to identify the magnetic components in the sediment because the signal to noise ratio was too low.

At ~67 mcd there is a short-lived polarity reversal that has a relatively distinctive square wave polarity reversal. This polarity interval is interpreted as magnetochron C18n.1r, the short subchron within C18n. The NRM/ARM record also indicates a drop in the magnetic field palaeointensity associated with this magnetic reversal (Fig. 5.13). The succeeding reversal back to C18n.1n is not recovered within the u-channels sampled here but the low-resolution shore based work by Ogg and Bardot (2001) indicates a rapid return to a long polarity interval characterized by positive inclinations at ~60 mcd, consistent with magnetochron C18n.1n (Fig. 5.8).

Figure 5.18 shows the bimodal distribution of the ChRM inclination values that broadly coincide with the expected inclination (I_{exp}) ,~43°, of the geomagnetic field at Site 1051 (equation 5.1) suggesting that the magnetic polarity signal is robust for Site 1051. Short-lived polarity events observed in magnetochron C19n and C18r contribute to transitional values recorded in Figure 5.18. Inclination data generally show a good fit to the expected inclination particularly in the lower part of the core splice but measured inclinations

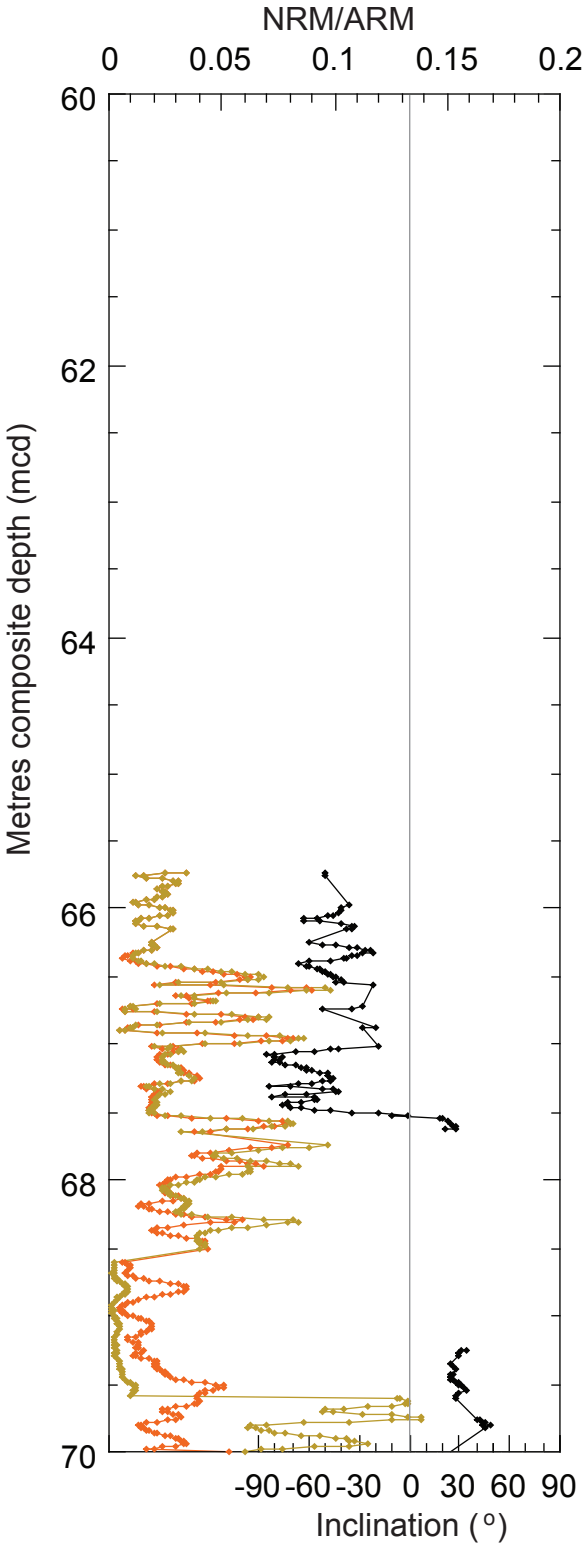

FIGURE 5.13: Palaeointensity and inclination data generated at Site 1051 between 60 and 70 mcd. Black diamonds are magnetic inclination data generated in this study. All data have maximum angular deviation (MAD) values of $\leq 10°$. Negative inclinations correspond to reversed polarity and positive inclinations to normal polarity intervals. Natural remanent magnetism/anhysteretic remanent magnetism (NRM/ARM), proxy for the palaeointensity of the geomagnetic field is shown for all samples. Orange and brown diamonds are NRM/ARM at 20 and 25 mT, respectively. Gaps in the inclination record represent data removed because they have MAD values of $\geq 10°$ or have an uninterpretable polarity.

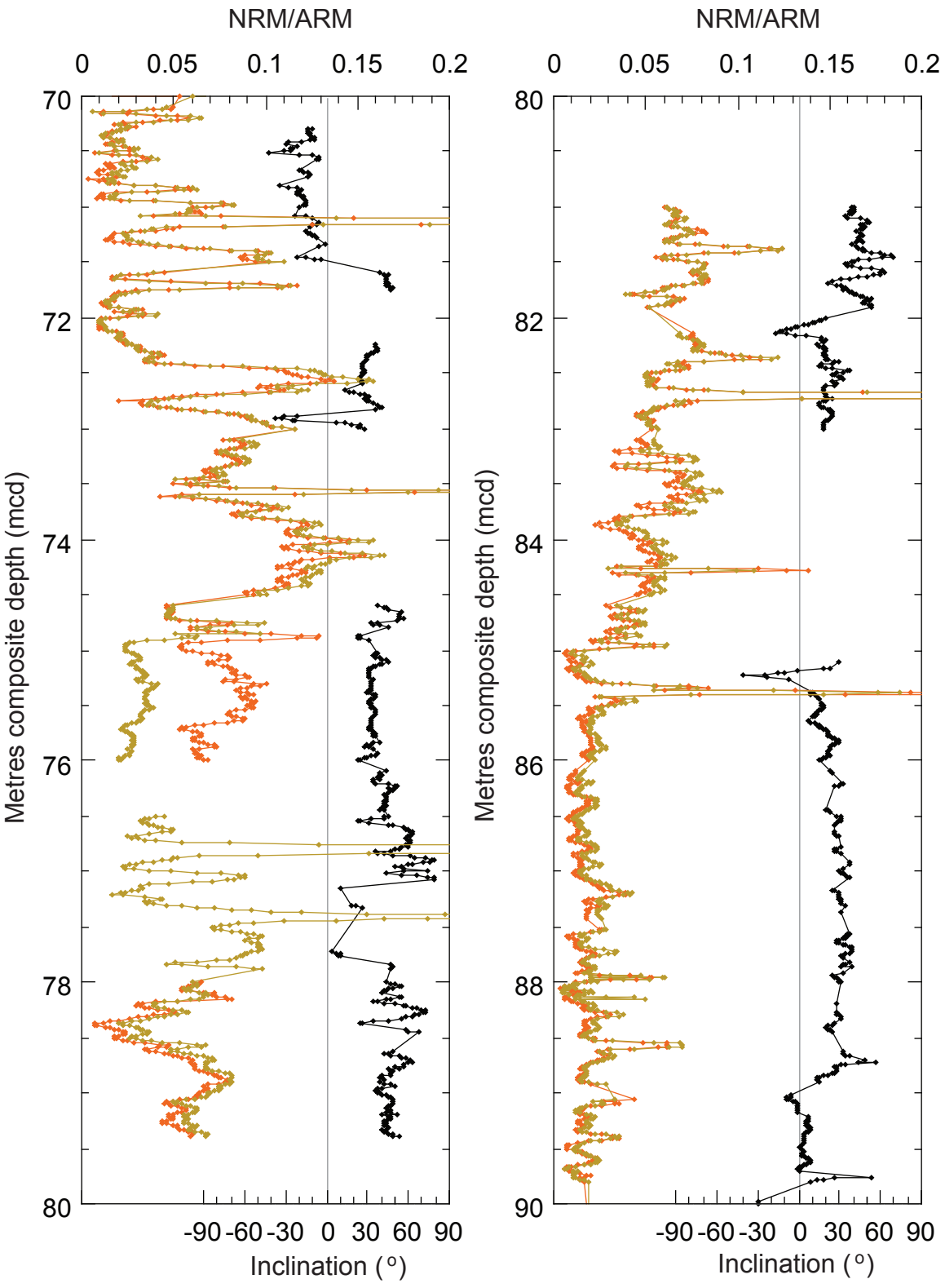

FIGURE 5.14: Palaeointensity and inclination data generated at Site 1051 between 70 and 90 mcd. Black diamonds are magnetic inclination data generated in this study. All data have maximum angular deviation (MAD) values of $\leq 10°$. Negative inclinations correspond to reversed polarity and positive inclinations to normal polarity intervals. Natural remanent magnetism/anhysteretic remanent magnetism (NRM/ARM), proxy for the palaeointensity of the geomagnetic field is shown for all samples. Orange and brown diamonds are NRM/ARM at 20 and 25 mT, respectively. Gaps in the NRM/ARM record reflect data removed because of flux jumps. Gaps in the inclination record represent data removed because they have MAD values of $\geq 10°$ or have an uninterpretable polarity.

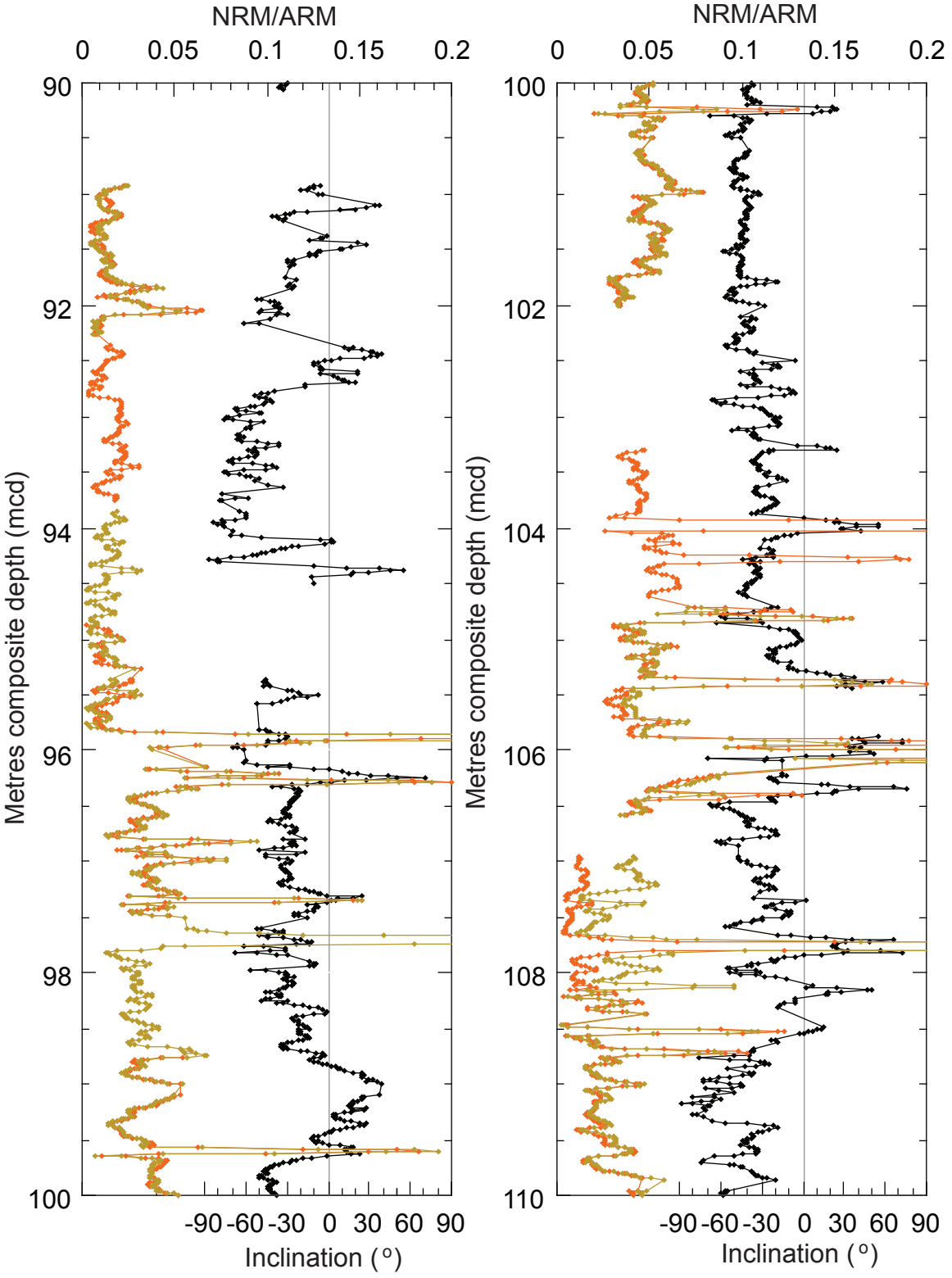

FIGURE 5.15: Palaeointensity and inclination data generated at Site 1051 between 90 and 110 mcd. Black diamonds are magnetic inclination data generated in this study. All data have maximum angular deviation (MAD) values of $\leq 10°$. Negative inclinations correspond to reversed polarity and positive inclinations to normal polarity intervals. Natural remanent magnetism/anhysteretic remanent magnetism (NRM/ARM), proxy for the palaeointensity of the geomagnetic field is shown for all samples. Orange and brown diamonds are NRM/ARM at 20 and 25 mT, respectively. Gaps in the NRM/ARM record reflect data removed because of flux jumps. Gaps in the inclination record represent data removed because they have MAD values of $\geq 10°$ or are have an uninterpretable polarity.

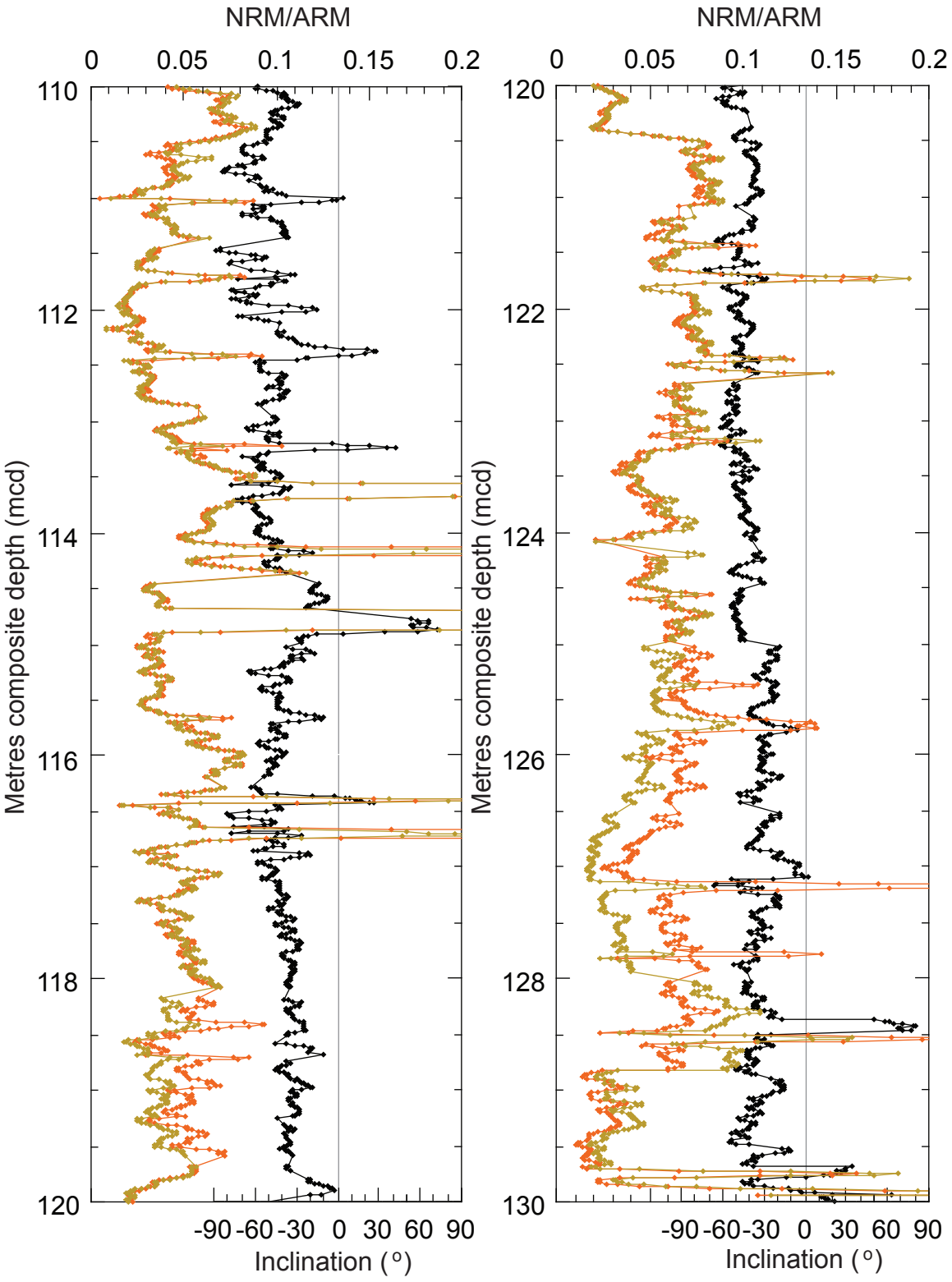

FIGURE 5.16: Palaeointensity and inclination data generated at Site 1051 between 110 and 130 mcd. Black diamonds are magnetic inclination data generated in this study. All data have maximum angular deviation (MAD) values of $\leq 10°$. Negative inclinations correspond to reversed polarity and positive inclinations to normal polarity intervals. Natural remanent magnetism/anhysteretic remanent magnetism (NRM/ARM), proxy for the palaeointensity of the geomagnetic field is shown for all samples. Orange and brown diamonds are NRM/ARM at 20 and 25 mT, respectively.

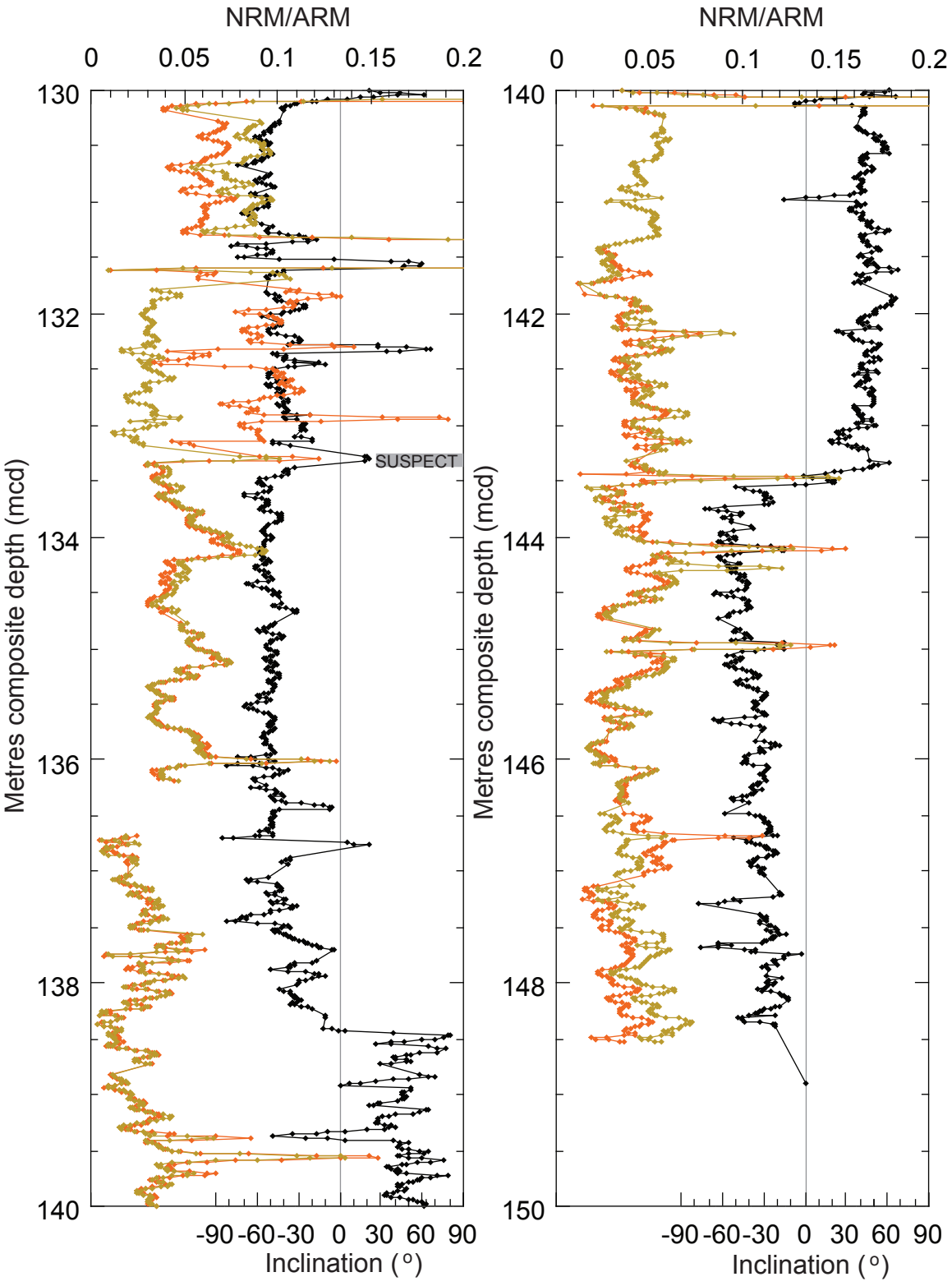

FIGURE 5.17: Palaeointensity and inclination data generated at Site 1051 between 130 and 150 mcd. Black diamonds are magnetic inclination data generated in this study. All data have maximum angular deviation (MAD) values of $\leq 10°$. Negative inclinations correspond to reversed polarity and positive inclinations to normal polarity intervals. Natural remanent magnetism/anhysteretic remanent magnetism (NRM/ARM), proxy for the palaeointensity of the geomagnetic field is shown for all samples. Orange and brown diamonds are NRM/ARM at 20 and 25 mT, respectively. Gaps in the NRM/ARM record reflect data removed because of flux jumps. Gaps in the inclination record represent data removed because they have MAD values of $\geq 10°$ or are have an uninterpretable polarity. Solid grey bar at 133.3 mcd indicates 'suspect' inclination excursion within 10 cm of the end of the u-channel.

appear to shallow at some depths, e.g., 98 mcd (Fig. 5.9). Inclination shallowing may be an artifact of the manual PCA method, in which the optimum demagnetisation steps were individually selected for each sample. Alternatively, shallowing may represent some variability in the degree of sediment compaction within the section, which is often related to changes in clay content of the sediment and/or depositional processes (Celaya and Clement, 1988; Arason and Levi, 1990; Kodama, 1997).

$$tanI = 2tan\lambda \tag{5.1}$$

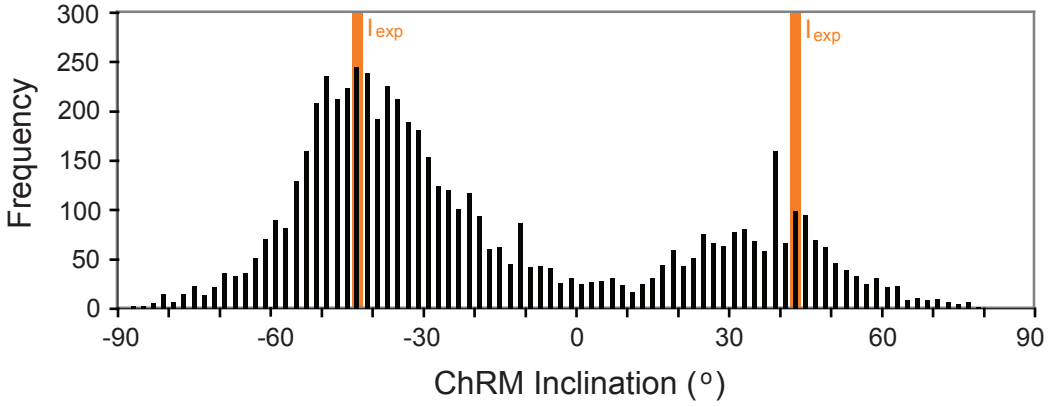

FIGURE 5.18: Histogram of characteristic remanent magnetisation (ChRM) inclinations for ODP Site 1051. The expected inclinations (I_{exp}) for the site are shown by the vertical orange bars. Data show a bimodal distribution of ChRM inclinations with the highest frequency of data around the I_{exp}.

5.4.2 Revising the shipboard magnetostratigraphy

Assignment of magnetochrons to polarity intervals identified at Site 1051 differs substantially between this study and Ogg and Bardot (2001) in the topmost part of the study interval, above ~65 mcd (Fig. 5.19). When correlating the pattern of polarity reversals to the GPTS, the shipboard party placed the greatest weight on calcareous nannofossil biostratigraphic datums (Fig. 5.20). The topmost metres of Site 1051 were consequently assigned to the Late Eocene, based on the first occurrence (FO) of the calcareous nannofossil species *Chiasmolithus oamauruensis*, that defines the base of biozone CP15 (Bukry, 1973, 1975). Therefore, the uppermost polarity interval identified in Hole 1051B and the core splice is interpreted as corresponding to magnetochron C16n, giving the top of the core splice an estimated age of 36.4 Ma (Shipboard Scientific Party, 1998; Ogg and Bardot, 2001). Several lines of evidence, listed below, have led to the re-interpretation of the shipboard magnetostratigraphy between 5 and 95 mcd.

- The polarity interval assigned to magnetochron C18n in the shipboard age model (Ogg and Bardot, 2001) appears relatively shortened compared to the reference scale of polarity chrons by Cande and Kent (1992a, 1995).

- In the shipboard age model, a large drop in the sedimentation rates, from 4.4 to 1.1 cm/kyr is calculated across the magnetochron C18r/C18n boundary (Fig. 5.20).

- At ODP Sites 1052 and 1053, which both recovered sediments of upper Eocene age, the base of calcareous nannofossil zone CP15 falls close to the base of magnetochron C17n.1n (∼37.9 Ma) coincident with the biomagnetostratigraphy of Berggren et al. (1995) and others. However, at ODP Site 1051, the base of zone CP15 is correlated to the base of magnetochron C16r at ∼36.6 Ma (Shipboard Scientific Party, 1998; Ogg and Bardot, 2001).

- Planktic foraminiferal assemblages identified in the top of Hole 1051A are consistent with assemblages found in planktic foraminiferal biozone P14 (now in biozone E13) (Berggren et al., 1995; Berggren and Pearson, 2005), yet the shipboard age model of (Ogg and Bardot, 2001) places biozone P14 within magnetochron C17n, not C18n to which it is assigned by Berggren et al. (1995); Berggren and Pearson (2005) - an offset of two million years.

- The last occurrence (LO) of the planktic foraminiferal species *Orbulinoides beckmanni* reported at ODP Site 1051 (see Chapter 6), which defines the top of the E12 biozone, is correlated to the base of magnetochron C17n and assigned an age of ∼38.1 Ma using the shipboard age model Ogg and Bardot (2001) - 2 million years younger than previously reported (Berggren et al., 1995; Berggren and Pearson, 2005).

Based on the points above, the long ranging normal polarity chron between ∼27.0 and 67.5 mcd in 1051A, is inferred to represent magnetochron C18n.1n, not C17n as assigned by Ogg and Bardot (2001) (Fig. 5.19). Furthermore, the apparently well-defined short polarity intervals at the top of Hole 1051B are tentatively re-assigned as magnetochrons C17r and C17n, rather than to C16r and C16n as by the Shipboard Scientific Party (1998). The revised age-depth plot for ODP Site 1051 based on the new interpretations in this study is shown in Figure 5.20 and results in more uniform sedimentation rates (∼3.5 cm/kyr) between 0 and 200 m than estimated by Ogg and Bardot (2001) (Fig. 5.20). Planktic foraminiferal and radiolarian datums appear to coincide well with the new magnetostratigraphy. Calcareous nannofossil datums below 100 mcd are generally in good agreement with the magnetostratigraphy although the assigned ages appear a little too young. However, the FO of the nannofossil species *Chiasmolithus oamaurensis* and *Dictyococcites bisectus* are significantly offset from the new magnetostratigraphy, by about a million years. It is worth noting that these two datums are also offset by several hundred thousand years from the shipboard magnetostratigraphy suggesting

that they require further calibration to the GPTS. Indeed, Aubry in Berggren et al. (1995) noted that the extremely low number of Middle Eocene sections with a reliable magnetostratigraphy means that nannofossil datums defining biozones NP15 through NP17 (37 - 40 Ma) are generally very poorly tied to magnetochronology.

TABLE 5.2: Depths of magnetic reversals at ODP Site 1051 and magnetochron assignments. Position of the magnetic reversal is taken as the point where the inclination is equal to 0°. Shipboard magnetic reversals (*) from Ogg and Bardot (2001) with the exception of the polarity chrons in the top of Hole 1051B not covered in additional work by Ogg and Bardot (2001) and estimated from Figure 24 in Shipboard Scientific Party (1998). Horizontal line refers to datum not determined in study. Ages according to Cande and Kent (1992a, 1995). mcd = metres composite depth.

	Shipboard data*		This study		
Magnetochron	top (mcd)	bottom (mcd)	top (mcd)	bottom (mcd)	Age (Ma)
Base 16n	∼14.5	-	-	-	36.341
Base 16r	∼27.4	-	-	-	36.618
Base C17n	60.35	65.00	∼14.50	-	38.113
Base C17r	68.00	71.00	∼27.40	-	38.426
Base C18n.1n	-	-	60.35*	65.55	39.552
Base C18n.1r	-	-	67.52	67.54	39.631
Base C18n.2n	85.96	90.46	88.90	90.00	40.130
Base C18r	135.78	139.88	138.41	138.43	41.257
Base C19n	142.88	145.88	143.52	143.54	41.521

5.4.3 Temporal variability of the geomagnetic field in the Middle Eocene

At Site 1051, a total of 29 short-lived polarity 'events' are recorded within magnetochrons C19n and C18r (Figs 5.9, 5.10 and 5.11). During these events the magnetic polarity appears to reverse, to varying degrees, for between 2 and 8 kyrs based on sedimentation rates determined in this study. However, marine magnetic anomaly profiles from the fast spreading North Pacific mid ocean ridge show evidence for only one or two tiny wiggles within magnetochron C18r (Fig. 5.3). This discrepancy may be a function of the much lower temporal resolution ∼20 kyrs obtained in marine magnetic anomaly profiles, significantly longer than the duration of the events estimated at Site 1051. The limitation of magnetic anomaly profiles to determine short-term variability in the geomagnetic field is demonstrated by the apparent absence of tiny wiggles during the Brunhes normal polarity chron (0.78 Ma to present), yet high resolution studies have recognised at least six globally correlatible magnetic excursions (5-10 kyrs duration) (Langereis et al., 1997), but perhaps as many as 14 (Lund et al., 1998) during this chron, suggesting that magnetic excursions are a frequent and intrinsic part of palaeomagnetic secular variability. High-resolution (≥5 kyrs) polarity reconstructions from Middle Eocene marine sediments at ODP Site 1220 (Pares and Lanci, 2004), ODP Site 690B (Florindo and Roberts, 2005) and the Contessa Section in Italy (Napoleone et al., 1983; Jovane

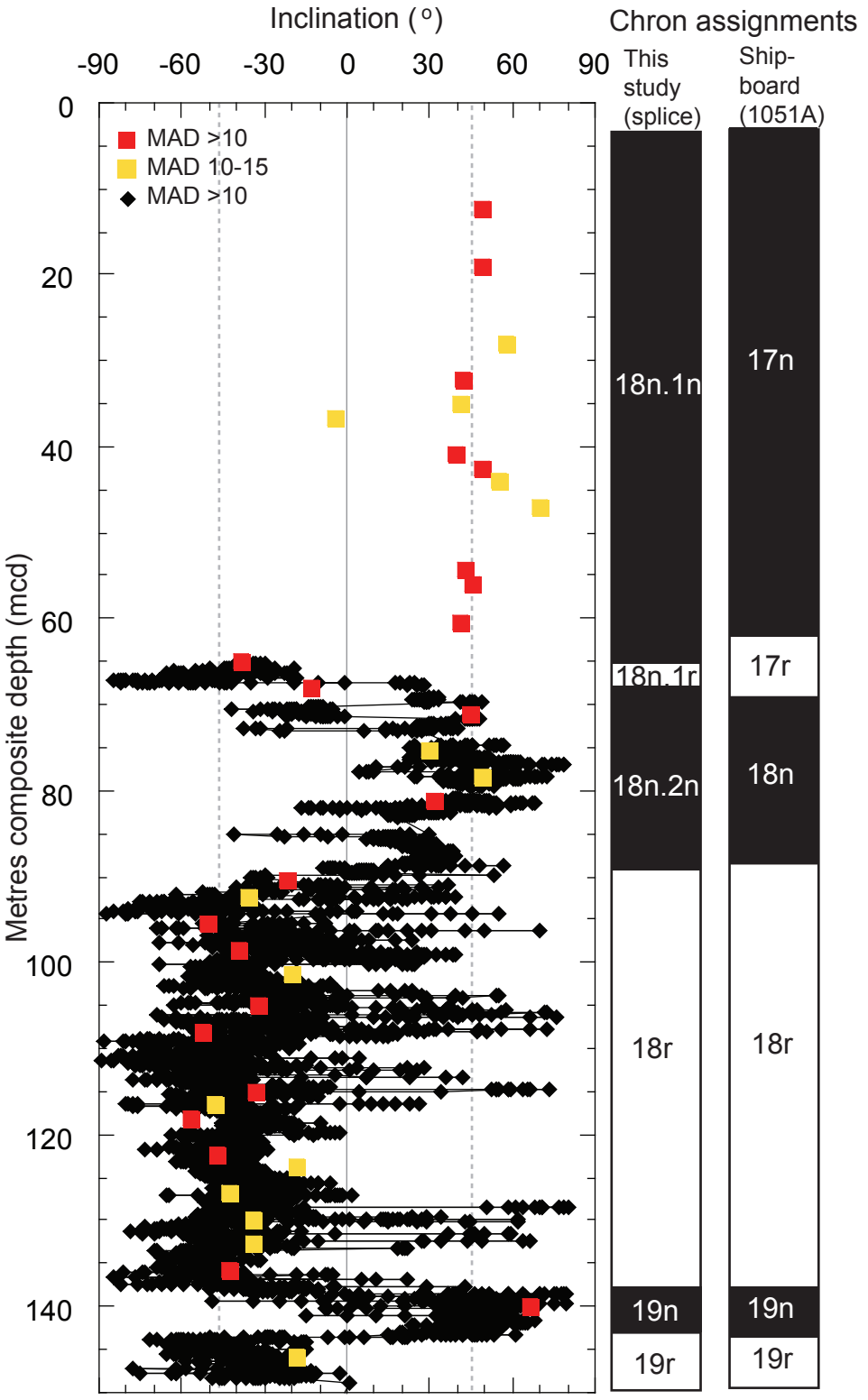

FIGURE 5.19: Comparison of shipboard polarity data and magnetochron assignments with this new study. Red and yellow squares are magnetic inclination data from Ogg and Bardot (2001) with maximum angular deviation (MAD) values of $\leq 10°$ and 10-15°, repectively. Black diamonds are magnetic inclinations generated in this study with MAD values of $\leq 10°$. Vertical grey dashed lines represent the expected inclination values (43° and -43°) for Site 1051. Solid vertical grey line denotes 0°. Note that Ogg and Bardot (2001) only conducted additional palaeomagnetic analysis of Hole 1051A but Hole 1051B contains slightly younger sediments and an additional pair of magnetic reversals are recorded above those observed in Hole 1051A. These were assigned to magnetochrons C16r and C16n but are now re-assigned to C17r and C17n shown on Figure 5.20.

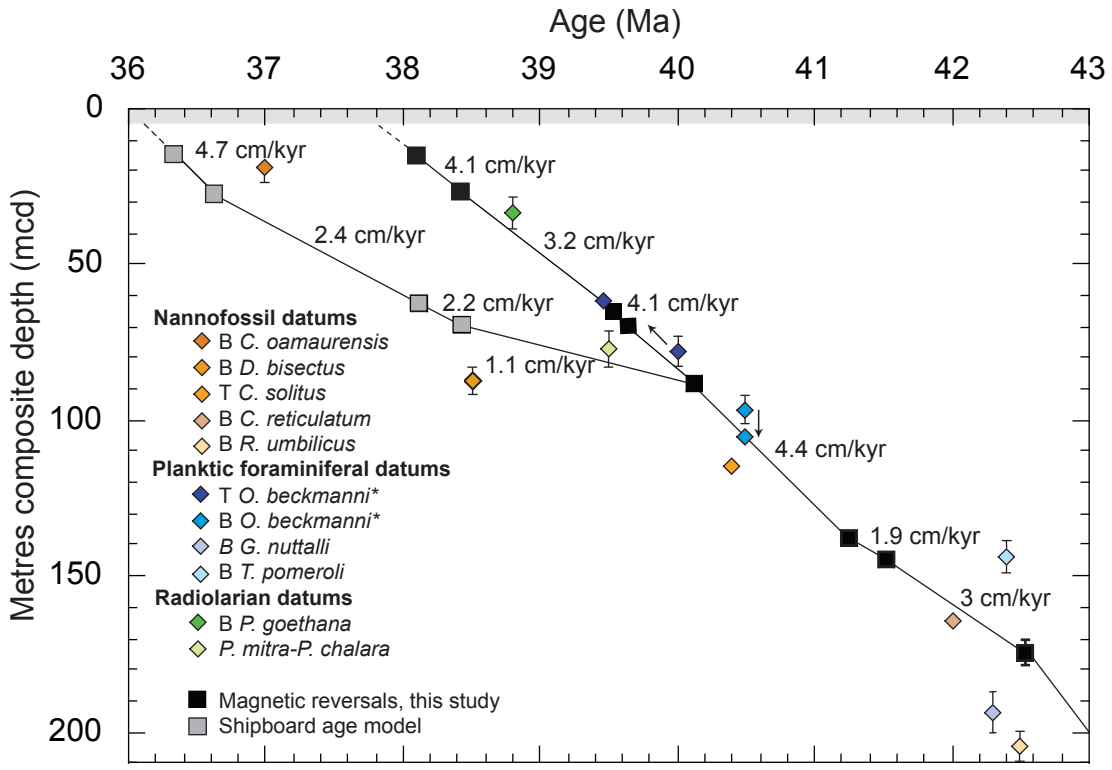

FIGURE 5.20: Sediment accumulation rates for ODP Site 1051. Grey squares indicate the assignment of magnetochrons by Shipboard Scientific Party (1998); Ogg and Bardot (2001) above 90 mcd. Black squares are the revised magnetostratigraphy in this study (Section 5.4.1). The base of the new E11 biozone defined by the last occurrence of *Guembelitriodes nuttalli* is added using the shipboard distribution chart of planktic foraminifera (Shipboard Scientific Party, 1998). Starred (*) biostratigraphic datums are revised in Chapter 6 and arrows indicate new placement of datums using revised magnetostratigraphy. B and T represent the first and last occurrence of a species, respectively. Numerical ages of magnetochrons are from Cande and Kent (1992a, 1995), calcareous nannofossil datums from Berggren et al. (1995), planktic foraminiferal datums from Berggren and Pearson (2005) and radiolarian datums from (Shipboard Scientific Party, 2002b). Horizontal grey bar indicates no core recovery between 0 and ∼5 m.

et al., 2007), fail to show evidence of the polarity events observed at Site 1051 in magnetochrons C18 and C19, suggesting that tiny wiggles in this interval must be the result of palaeointensity fluctuations or that magnetic reversals if present are less than 5 kyrs in duration. Therefore, the high-resolution (250 yrs) study of magnetic polarity at ODP Site 1051 in the Middle Eocene, which has the highest reported sedimentation rates for the deep-sea (∼3.5 cm/kyr) at this time, offers an excellent opportunity to determine the origin of the tiny wiggles observed in marine magnetic anomaly profiles and to assess the temporal variability of the geomagnetic field.

The key to discerning the origin of polarity events is to understand how the magnetic field intensity varied across these polarity shifts using the NRM/ARM record generated in this study. Full reversals of the geomagnetic field are accompanied by a collapse in

the magnetic field intensity prior to and during the magnetic reversal, a recovery of the field intensity within the chron before deceasing in intensity again at the succeeding reversal. This is clearly demonstrated across magnetochron C19n in Figure 5.12. In contrast, during a geomagnetic 'excursion' $\leq$2 kyrs in duration the magnetic field does not fully reverse polarity and palaeointensity records show a decline the magnetic field intensity but the field intensity fails to recover within the excursion. The NRM/ARM dataset shows that each of the polarity 'events' recorded in the u-channel dataset are coincident with large peaks in the NRM/ARM ratio, resulting from an increase in the measured NRM intensity. This renders the intensity data inconclusive and introduces some uncertainty into the authenticity of the polarity events. While u-channels are excellent for generating high-resolution and continuous measurements of magnetic polarity, one major drawback is that any large changes in the NRM intensity of the sediment can introduce spurious directional artifacts to the dataset (Weeks et al., 1993; Roberts et al., 1996) (Fig. 5.21). The lithology of the 1051 cores appears to be a relatively homogenous siliceous nannofossil ooze with no obvious lithological changes. Visual inspection of u-channels reveals no correlation to ash layers or gaps/cracks in the core, and interrogation of physical property records find no obvious changes that can be invoked to explain the spikes in NRM intensity. At present the observed polarity events can not be explained by physical changes in the properties of the sediment, but the tiny wiggles recorded in the magnetic anomaly profiles and high-resolution magnetic profiles in the Neogene that show evidence of frequent short term variability in the magnetic field (Langereis et al., 1997; Lund et al., 1998) suggests that at least some of these polarity events (especially those more than 20 cm from the core ends) may represent real variability in the geomagnetic field. Given the apparent very short duration of the majority of the polarity events ($\sim$2 kyrs) it seems most likely that they represent fluctuations in the magnetic field intensity, i.e., excursions rather than full magnetic reversals. To confirm the nature of these short-lived polarity events, it is necessary to generate new NRM and ARM records in continuous discrete samples from the intervals of high intensity because discrete samples are not subject to the same palaeodirectional artifacts that can arise in u-channel data as a function of the measurement process (see Section 5.6).

The short duration of the polarity events recorded at Site 1051 means that these events will probably be of little use stratigraphically because of the temporal resolution achievable in most deep sea sections and the feasibility of routinely carrying out high-resolution studies. However, determining the origin of these events will significantly contribute to our understanding of the temporal variability and the stability of the geomagnetic field through time, and the debate on the origin of tiny wiggles.

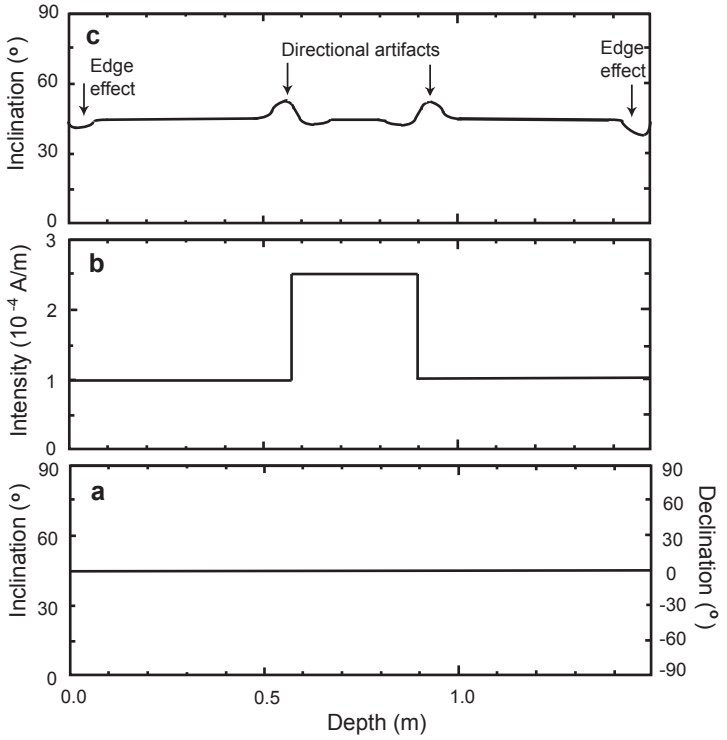

FIGURE 5.21: Simulated directional artifact introduced due to large changes in remanence intensity in a u-channel. a) True inclination profile, b) 2.5 fold increase in remanence intensity and c) change in remanence intensity causes a 10° inclination artifact at the top and base of intensity change. The larger the intensity change the larger the amplitude of the anomaly. Redrawn from Figure 6 in Roberts (2006).

5.5 Conclusions

ODP Site 1051 in the western North Atlantic recovered an expanded and stratigraphically complete, to magnetochron level, sedimentary section from magnetochrons C26n through C17n in the Middle Eocene. A revised magnetic reversal stratigraphy has yielded the following results:

1. High-resolution (∼250 yrs) magnetic polarity records generated between 65 and 155 mcd at ODP Site 1051, show a well resolved pattern of magnetic reversals that are assigned to magnetochrons C19r through C18n.1n. The new polarity records significantly improve upon the resolution available from the shipboard study, with the top and base of magnetochron C19n and the base of C18n.1r now constrained to ±1 cm, and the base of C18n.2n to ±55 cm.

2. Re-evaluation of planktic foraminiferal biostratigraphic information and the shipboard magnetic polarity sequence between 5 and 90 mcd has resulted in the reassignment of polarity chrons in the topmost part of the ODP Site 1051 core splice. Magnetochrons are reassigned compared to the shipboard magnetostratigraphy (s)

as follows; C18n (s) = C18n.1n, C17r (s) = C18n.1r, C17n (s) = C18n.2n, C16r (s) = C17r and C16n (s) = C17n.

3. The new polarity record indicates a number of hitherto unreported short-lived polarity 'events' within magnetochrons C18r and C19n. The nature and origin of these excursions is as yet unconfirmed but a number of lines of evidence suggest that these events may reflect real variability in the geomagnetic field in the Middle Eocene.

5.6 Future work

The expanded and continuous Paleogene section recovered at Blake Nose has great potential to help further refine the GPTS in the Middle Eocene. Future work will involve generating an astronomical time scale for ODP Site 1051 using physical property data (GRAPE and colour reflectance) generated during Leg 171B that show promising evidence of cyclicity. An astrochronology will enable an astronomical tuning of individual magnetochrons well resolved by this work (particularly magnetochron C19n) contributing towards refinement of the Paleogene GPTS, a more accurate estimation of the duration of planktic foraminiferal zone E12 determined at Site 1051 in Chapter 6, and the duration and timing of the MECO.

In order to discern the nature and origin of the polarity 'events' identified in the magnetic polarity record at ODP Site 1051, a series of discrete samples will be run on the 2-G cryogenic magnetometer at the National Oceanography Centre, Southampton. Discrete samples will be AF demagnetised and an ARM imposed using the same parameters as used on the u-channels in this study. If the polarity 'excursions' are authenticated by both a change in the polarity reversal (in the NRM dataset) and a collapse in relative palaeointensity (in the NRM/ARM dataset) across the polarity reversals, then these polarity excursions are likely to represent short magnetic reversals - the first recorded in the Middle Eocene. If these polarity 'events' are demonstrated to be instrumental artifacts, then the true inclination of these samples will be determined from the discrete samples and incorporated into a dataset with a much 'cleaner' polarity sequence. Furthermore, this would imply that the tiny wiggles observed in marine magnetic anomaly profiles in magnetochron C18 reflect changes in the palaeointensity of the geomagnetic field and not magnetic reversals.

Chapter 6

Refining planktic foraminiferal biozone E12

6.1 Introduction

Planktic foraminifera are a powerful tool in palaeoceanography, they are one of the primary means for determining the age of marine sediments and enabling regional and worldwide correlation of marine sediments. In addition, they are one of the key methods with which magnetic reversal stratigraphies generated in marine sediments are correlated to the Geomagnetic Polarity Time Scale (GPTS). Their importance is due to their often distinctive morphologies, relatively abundant occurrence (except where dissolution has removed carbonate from sediments), large geographic distribution and rapid evolutionary rates. During the Eocene many new and distinctive planktic foraminiferal genera made their first appearances *Clavigerinella, Hantkenina, Turborotalia, Globigerinatheka, Orbulinoides, Morozovelloides* and *Cribrohantkenina*, accompanied by the rapid evolution of existing genera *Morozovella* and *Acarinina*, enabling effective stratigraphic subdivision of the Eocene (Berggren, 1969; Blow, 1969, 1979; Toumarkine and Luterbacher, 1985; Berggren et al., 1995; Berggren and Pearson, 2005).

Planktic foraminiferal biostratigraphy was pioneered in the former Soviet Union (Subbotina, 1953) and in the Caribbean (Bolli, 1957a,b), intially for use in the petroleum industry but with the advent of the Deep Sea Drilling Project (DSDP) and its successors, the Ocean Drilling Program (ODP) and the Integrated Ocean Drilling Program (IODP) these biozonation schemes became widely applied. The Caribbean planktic foraminiferal biozonation scheme of Bolli (1957a,b) provides the basis for the modern low latitude zonal scheme because upon subsequent investigation it was demonstrated that this zonation scheme was generally applicable throughout the (sub)tropical regions worldwide (Berggren, 1969; Blow, 1969, 1979; Toumarkine and Luterbacher, 1985; Berggren and Miller, 1988; Berggren et al., 1995). However, the absence of many of

the low latitude biostratigraphic species at higher latitudes, meant that an alternative scheme had to be developed for these areas. Because high latitude assemblages are typically dominated by longer ranging foraminifera with smaller, less distinctive morphologies this results in a much coarser stratigraphic zonation scheme (Stott and Kennett, 1990; Huber and Quillévéré, 2005). To provide a time scale for the sequence of biostratigraphic events observed in marine sediments, Berggren et al. (1985) correlated the first and last occurrences (FO and LO) of the calcareous plankton to the independent chronometer, the GPTS. The chronology of the biostratigraphic datums was then estimated using linear interpolations between radiometric calibration tie-points and magnetostratigraphic boundaries, forming the first comprehensive Cenozoic integrated biomagnetochronologic scale (IBMS). Advances in radiometric dating, revision of the GPTS, and refinements of calcareous plankton biostratigraphy required a re-evaluation of the IBMS in 1995 (Berggren et al., 1995), which is still the most widely employed time scale in Cenozoic studies. In 2004, biostratigraphic datums from Berggren et al. (1995) were recalibrated against the new GPTS of Ogg and Bardot (2001) resulting in an updated IBMS. More recently, the Eocene (sub)tropical revised planktic foraminiferal zonation scheme was introduced (Berggren and Pearson, 2005) which includes a significant body of new work; modification of taxonomic genera/species concepts, taxa ranges and improved calibrations of many planktic foraminiferal datums to the earlier GPTS of Berggren et al. (1995). The new Eocene biozonation scheme adopts the prefix 'E' for biozones following the existing nomenclature available for the Neogene; with the prefixes 'M' (Miocene) and 'PL' (Pliocene) and 'PT' (Pleistocene) denoting foraminiferal biozones, as presented in Berggren et al. (1995). This revised Eocene zonal stratigraphy replaces the 13 planktic foraminiferal 'P' zones of Berggren et al. (1995) with 16 new 'E' zones.

Despite the vast amount of biostratigraphic data that has been collected, many Middle Eocene biostratigraphic datums are still poorly calibrated to the GPTS because of the extremely low number of high quality marine sections with good magnetostratigraphy of this age. In particular, the interval containing planktic foraminiferal zone E12, P13 in the biozonation scheme of Berggren et al. (1995), defined by the FO and LO of the short-lived tropical planktic foraminiferal species *Orbulinoides beckmanni*, is extremely poorly recovered hindering direct calibration of this biozone to the GPTS. A near global hiatus truncates the top of biozone E12 in many deep sea sections at ∼40.0 Ma, while other sites suffer from chert or condensation horizons, a lack of carbonate, magnetostratigraphic control or the absence of the biostratigaphic marker species *O. beckmanni* (Fig. 6.1). Consequently the low-resolution calibration of biozone E12 to the GPTS determined at Contessa, Italy (Lowrie et al., 1982) has subsequently been adopted in the IBMS of Berggren et al. (1985, 1995); Gradstein et al. (2004), with only a minor amendment to this calibration in the new scheme of Berggren and Pearson (2005) based on the restricted shipboard biostratigraphy determined at Site 1052, Blake Nose (Wade, 2004).

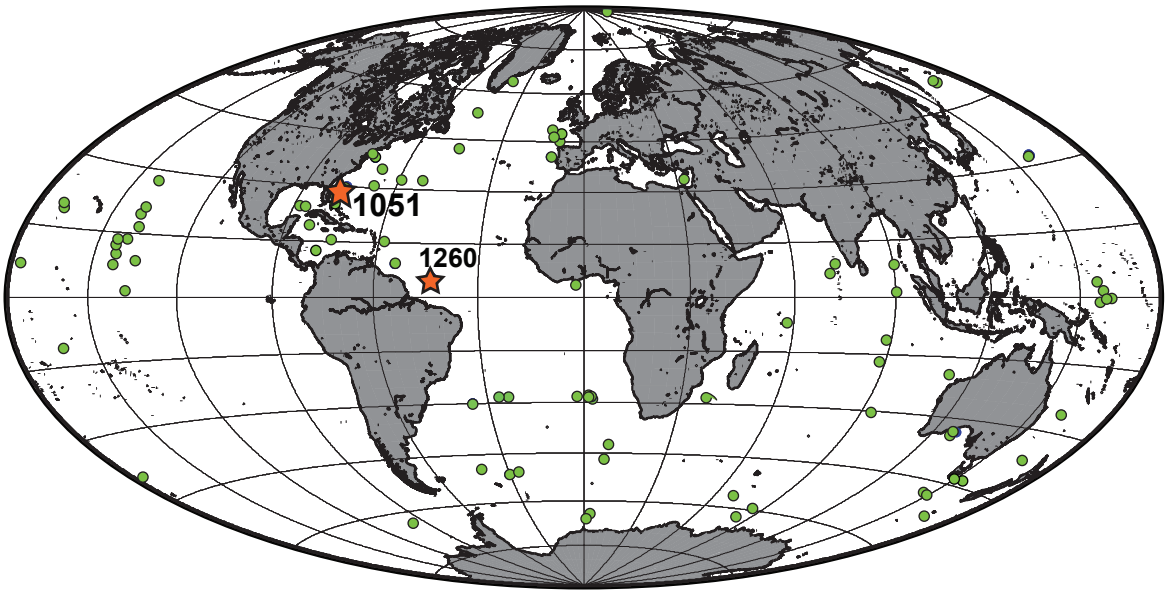

FIGURE 6.1: Location map. Green dots represent deep sea sites where Middle Eocene sediments have been recovered. Planktic foraminiferal biozone E12 is not identified at any of these deep sea sites because of either (1) no carbonate sediment was recovered, (2) non-deposition, (3) a sedimentary hiatus, (4) discontinuous sediment core recovery or (5) the low latitude marker species *Orbulinoides beckmanni* is absent (Data from http://www-odp.tamu.edu/). The red star labelled 1051 represents the most stratigraphically complete deep sea section containing planktic foraminiferal zone E12, with high sedimentation rates and good age control. Ocean Drilling Program (ODP) Site 1260 also marked by a red star is used here for comparison with Site 1051 but it is stratigraphically incomplete.

O. beckmanni is a particularly useful biostratigraphic marker because it divides what would otherwise be a very long ∼4 Myr biozone, the totality of biozones E11 through E13, between the LO of the planktic foraminifera *Guembelitriodes nuttalli* at 42.3 Ma and the LO of *Morozovelloides crassata* at 38.0 Ma. In addition, this interval of time is of palaeoclimatic significance because it hosts the global warming event, the Middle Eocene Climatic Optimum (MECO) (Bohaty and Zachos, 2003). Yet, no quantitative or high-resolution study of the relative abundance of *O. beckmanni* has ever been conducted to assess the reliability of the datums on which E12 is defined. In this chapter new high resolution quantitative records of the biostratigraphic marker species *O. beckmanni* are presented from ODP Sites 1051 and 1260. These are used to refine the existing biomagnetocalibration and assess the reliabilty of the bioevents that define planktic foraminferal biozone E12.

6.1.1 Stratigraphy of ODP Site 1051

ODP Site 1051 was drilled during Leg 171B on the Blake Nose Plateau in the western North Atlantic (Fig. 6.1), and comprises a stratigraphically complete (to magnetochron level) and expanded Middle Eocene sequence of siliceous nannofossil ooze, that includes a complete planktic foraminiferal E12 biozone. Estimated palaeowater depths for Site 1051 from benthic foraminiferal assemblages are 1500 - 2000 m (Shipboard Scientific Party, 1998) and the estimated palaeolatitude of the site is ∼25°N (Ogg and Bardot, 2001). A continuous shipboard splice was generated for the Middle Eocene at Site 1051. The high sedimentation rates (∼4 cm/kyr) and good magnetochronology at Site 1051 (see Chapter 5) allows high resolution calibration and a test of the reliability of the evolution and extinction of *Orbulinoides beckmanni* as markers for planktic foraminiferal biozone E12.

6.1.2 Stratigraphy of ODP Site 1260

Complimentary relative abundance records of *O. beckmanni* were generated at ODP Site 1260, at a palaeolatitude of 1°S (Ogg and Smith, 2004), in order to assess the synchrony of the FO of *O. beckmanni* between different sites in the Atlantic Ocean. ODP Site 1260 was drilled during ODP Leg 207, as part of a depth transect aimed at recovering expanded sequences of shallowly buried Cretaceous and Paleogene sediments on Demerara Rise in the tropical Atlantic (Fig. 6.1). Middle Eocene sediments are primarily composed of greenish gray nannofossil chalks with foraminifera and radiolarians. The Demerara plateau is thought to have reached water depths close to the present day, 2549 mbsf, at Site 1260 by the Late Cenomanian (Arthur and Natland, 1979). Palaeodepth interpretations based on the dominant benthic foraminifera in the assemblage at Demerara Rise are indicative of depths between 2500 and 3000 m, consistent with a palaeodepth close to the present during the Middle Eocene (Fig. 6.2). A continuous shipboard splice was generated for the Middle Eocene, except for a 1 m gap that was not recovered in holes A and B, at 57 mcd (Shipboard Scientific Party, 2004).

6.2 Results

6.2.1 Planktic foraminiferal biozone E12 at ODP Sites 1051 and 1260

High-resolution quantitative biostratigraphic analysis was carried out on the same sample splits ($\geq$ 300 μm size fraction) used to assess biotic turnover ∼40.0 Ma in Chapter 7. At ODP Site 1051, planktic foraminifera were counted between 61.40 and 102.20 mcd with a sampling resolution of between 10 and 30 cm equivalent to 3 - 9 kyrs resolution respectively, based on sedimentation rates determined for Site 1051 in Chapter 5 (Fig.

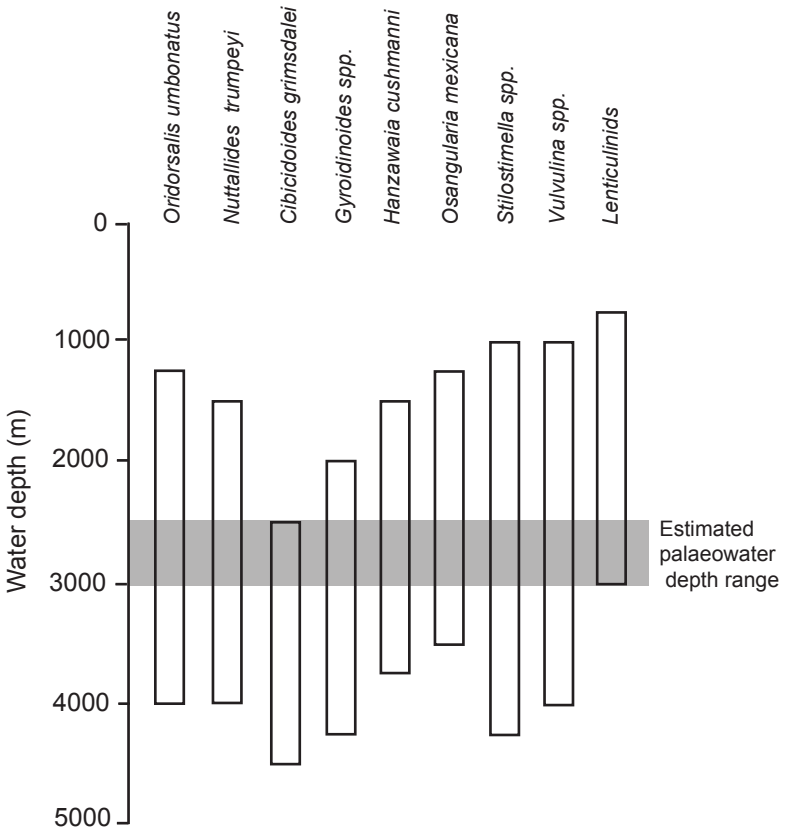

FIGURE 6.2: Reconstruction of palaeowater depth from benthic foraminiferal assemblages at ODP Site 1260 in the Middle Eocene. Grey bar indicates estimated palaeowater depth range at Site 1260 based on the dominant components of the benthic foraminiferal assemblage. Benthic foraminiferal taxonomy and the palaeowater depth estimates for each species or genera follow that of Tjalsma and Lohmann (1983).

5.20). At ODP Site 1260, samples were counted between 38.27 and 60.27 mcd at 30 cm spacing, equivalent to ∼12 kyr resolution (Fig. 6.7). The main bioevents recorded within the study interval are the evolution and extinction of the short-lived planktic foraminiferal species *Orbulinoides beckmanni* (Saito, 1962), whose total range defines planktic foraminiferal biozone E12 (Berggren and Pearson, 2005). *O. beckmanni* typically has a large (≥500 μm) and almost spherical test with an embracing final chamber that comprises more than 50% of the total foraminiferal test. At the base of the final chamber are multiple small secondary sutural apertures and numerous spiral supplementary apertures in the early whorls, some individuals may also possess areal apertures in the the (pen)ultimate chambers (Saito, 1962). In contrast, *O. beckmanni's* closest ancestor *Globigerinatheka euganea*, from which *O. beckmanni* evolves (Fig. 6.3), is distinguished by the presence of three chambers in the final whorl that may increase rapidly in size, a compact and spherical test with fewer and larger secondary apertures (typically 2 - 4), rarely recorded apertures in the inner spire and absent areal apertures (Proto Decima and Bolli, 1970).

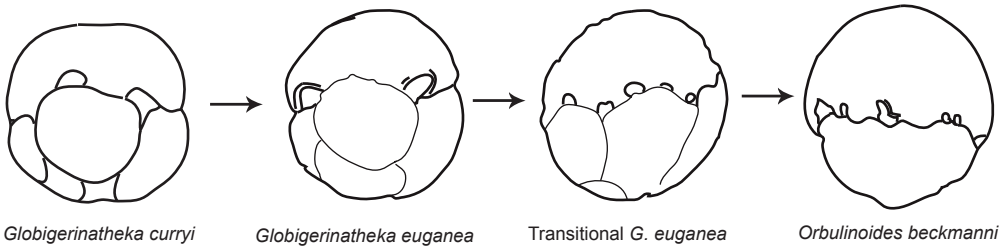

FIGURE 6.3: Evolutionary lineage between *Globigerinatheka curryi* - *Globigerinatheka euganea* - *Orbulinoides beckmanni*. Within this lineage there is a trend towards increasing sphericity of the foraminiferal test as the final chamber becomes progressively larger and more encompassing of the earlier chambers. At the same time sutural apertures become smaller and more abundant, and the sutures between the earlier chambers become less pronounced (Proto Decima and Bolli, 1970).

The samples studied contained a relatively diverse planktic foraminiferal assemblage typical of (sub)tropical environments in the Middle Eocene (Berggren, 1978; Keller et al., 1992; Sexton et al., 2006b). Samples are dominated by the genera *Acarinina, Morozovelloides, Globigerinatheka, Subbotina* and *Turborotalia* with subordinate *Orbulinoides* and *Hantkenina* (described in detail in Chapter 7). Planktic foraminiferal assemblages are characteristic of planktic foraminiferal biozones E11 through E13 (P12 through P14 in previous biozonation scheme of Berggren et al. 1995). Planktic foraminifera show evidence of recrystallisation, i.e., are not glassy, but are free of carbonate infilling and overgrowths based on observation under the binocular light microscope.

Figure 6.4 is a compilation of available data from deep sea drill sites (DSDP, ODP and IODP) and exposed marine sections, to evaluate the palaeobiogeographic distribution of *O. beckmanni*. This map is constructed using the standard presence/absence mapping method applied in biological and ecological studies (Miller, 2004). Sites labelled 'absent' have recovered carbonate sediments of the appropriate Middle Eocene age, i.e., covering the biozone E12 interval, but *O. beckmanni* is not present (solid yellow circles in Fig. 6.4). Sites where erosion has removed the E12 biozone interval or carbonate sediments are absent have been excluded from this reconstruction. Where available, the paleolatitude of the site is used. Where an estimated paleolatitude is not already available it has been estimated using the present day location of the site and the paleolatitude of surrounding sites. Figure 6.4 provides a good first order approximation of the palaeogeographic distribution of *O. beckmanni*, indicating that it is present in all Eocene ocean basins, with the exception of the high latitude Southern and Arctic Oceans. In fact, *O. beckmanni* appears to only be present at sites between ~30°S and 45°N, supporting previous interpretations that it is restricted to tropical and warm mid-latitudes (Bolli, 1972; Premoli-Silva et al., 2006).

O. beckmanni is present at both ODP Sites 1051 and 1260 and its relative abundance in the total planktic foraminiferal assemblage is shown in Figures 6.5 and 6.6 alongside the

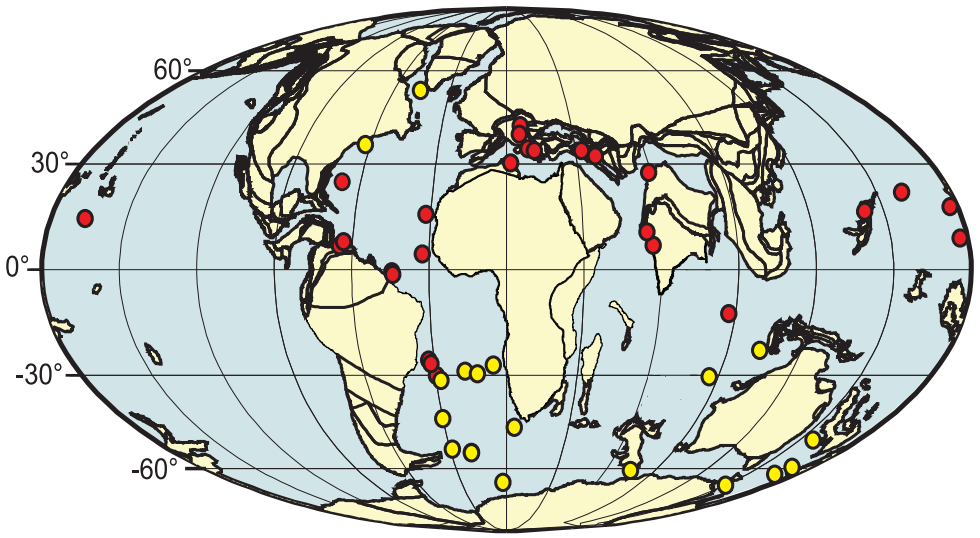

FIGURE 6.4: Palaeobiogeographic reconstruction of planktic foraminiferal species *Orbulinoides beckmanni*. Solid red and yellow circles indicate the presence and absence of *O. beckmanni*, respectively. Data are compiled from deep sea drill sites (DSDP, ODP and IODP) and exposed marine sections, that have recovered Middle Eocene carbonate sediments that encompass the time interval in which the biozone E12 occurs. To prevent introducing bias, sites where the *O. beckmanni* is not found because of hiatuses, dissolution, lack of carbonate sediments or non-recovery of this interval, are excluded from the map. Deep sea drill site data available from http://www-odp.tamu.edu/. Exposed marine sections containing *O. beckmanni* from Beckmann (1953); Bolli (1957b); Saito (1962); Cordey (1968); Samanta (1970); Mohan and Soodan (1970); Salaj; Lowrie et al. (1982); Warraich and Nishi (2003); BouDagher-Fadel and Clark (2006); Babić et al. (2007). Palaeogeographic base map for 40 Myr ago generated at www.odsn.de/odsn/serices/paleomap/paleomap.html.

shipboard assignment of bioevents, also outlined in Table 6.1. At Site 1051 the FO of *O. beckmanni* occurs at 106.45 mcd and at Site 1260 at 58.87 mcd. Figures 6.5 and 6.6 show that *O. beckmanni* has a low relative abundance ($\leq$0.5 %) and sporadic occurrence in the lowermost part of its stratigraphic range in magnetochron C18r at both sites.

At Site 1051 the relative abundance of *O. beckmanni* remains low in the bottom ~20 m of the study interval. From 86.80 mcd, *O. beckmanni* is consistently present in every sample until close to the top of its range at 63.30 mcd. It is therefore possible to define a first and last common occurrence (FCO and LCO) of *O. beckmanni* at Site 1051 that may, upon further investigation, prove to be stratigraphically or palaeoceanographically significant. Indeed, Raffi et al. (2006) suggest that use of species common occurrence or acme intervals as a means for defining biozones, may in some cases be more reliable than using the FO and LO of the same species. At 86.70 mcd there is a large and abrupt increase in the relative abundance of *O. beckmanni* from 0.5 to ~3 - 6% within $\leq$30 cm. Relative abundance of *O. beckmanni* in the foraminiferal assemblage then gradually decreases from the highest relative abundances at ~86.70 mcd through to 61.40 mcd, in a series of steps at 80, 71 and 63 mcd, at which mean relative abundance

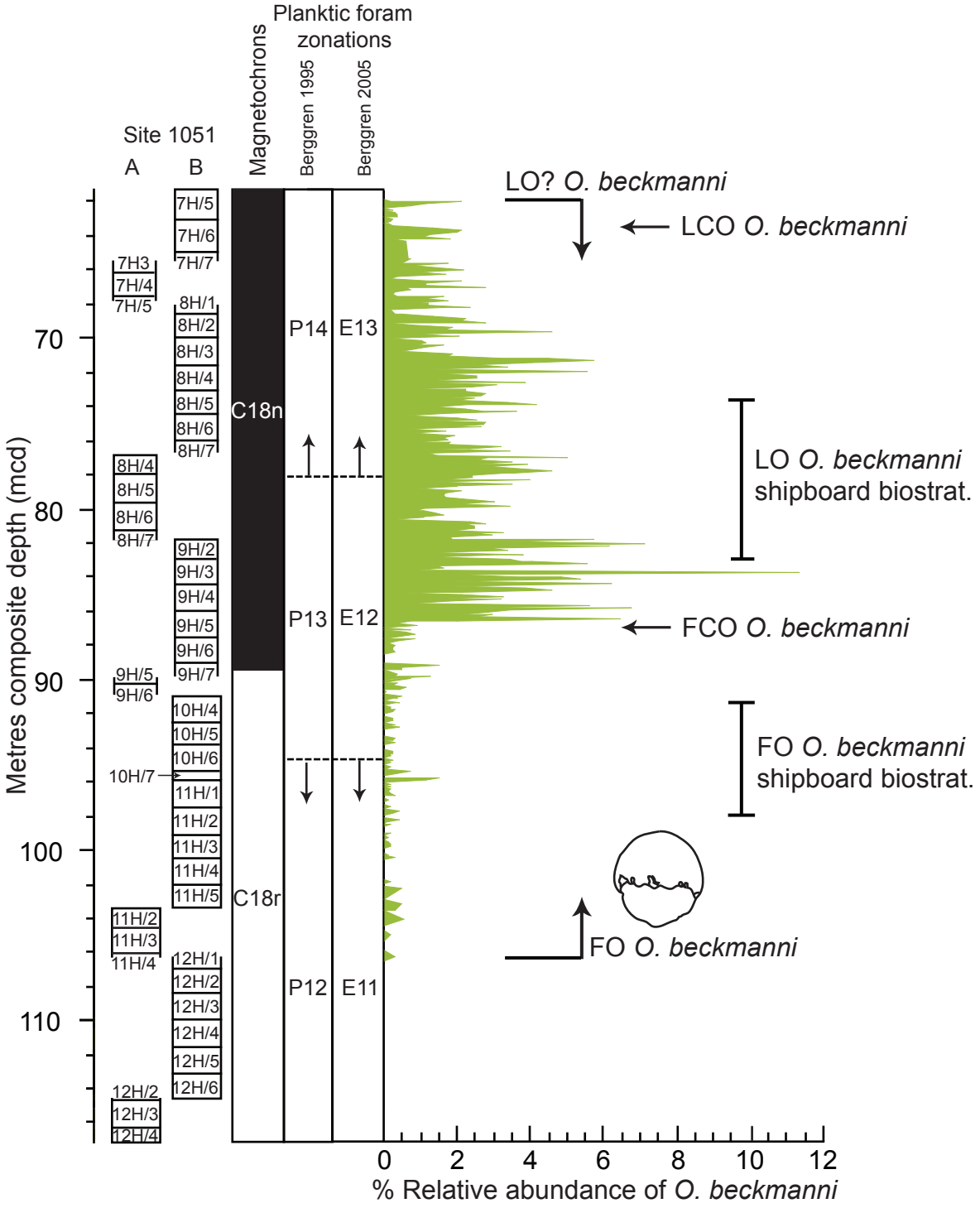

FIGURE 6.5: Relative abundance of *Orbulinoides beckmanni* at ODP Site 1051 plotted against depth. Site 1051 core splice through the study interval is shown. Data presented as % relative abundance of total planktic foraminiferal assemblage. Magnetostratigraphy determined in Chapter 5. Planktic foraminiferal 'P' zones of Berggren et al. (1995) shown against new 'E' zones of Berggren and Pearson (2005). Biozone boundaries are based on shipboard biostratigraphic assignment of the first and last occurrence, FO and LO respectively, of *O. beckmanni* (Shipboard Scientific Party, 1998), new relative abundance counts of *O. beckmanni* indicate the need to revise the position of these boundaries (see arrows).

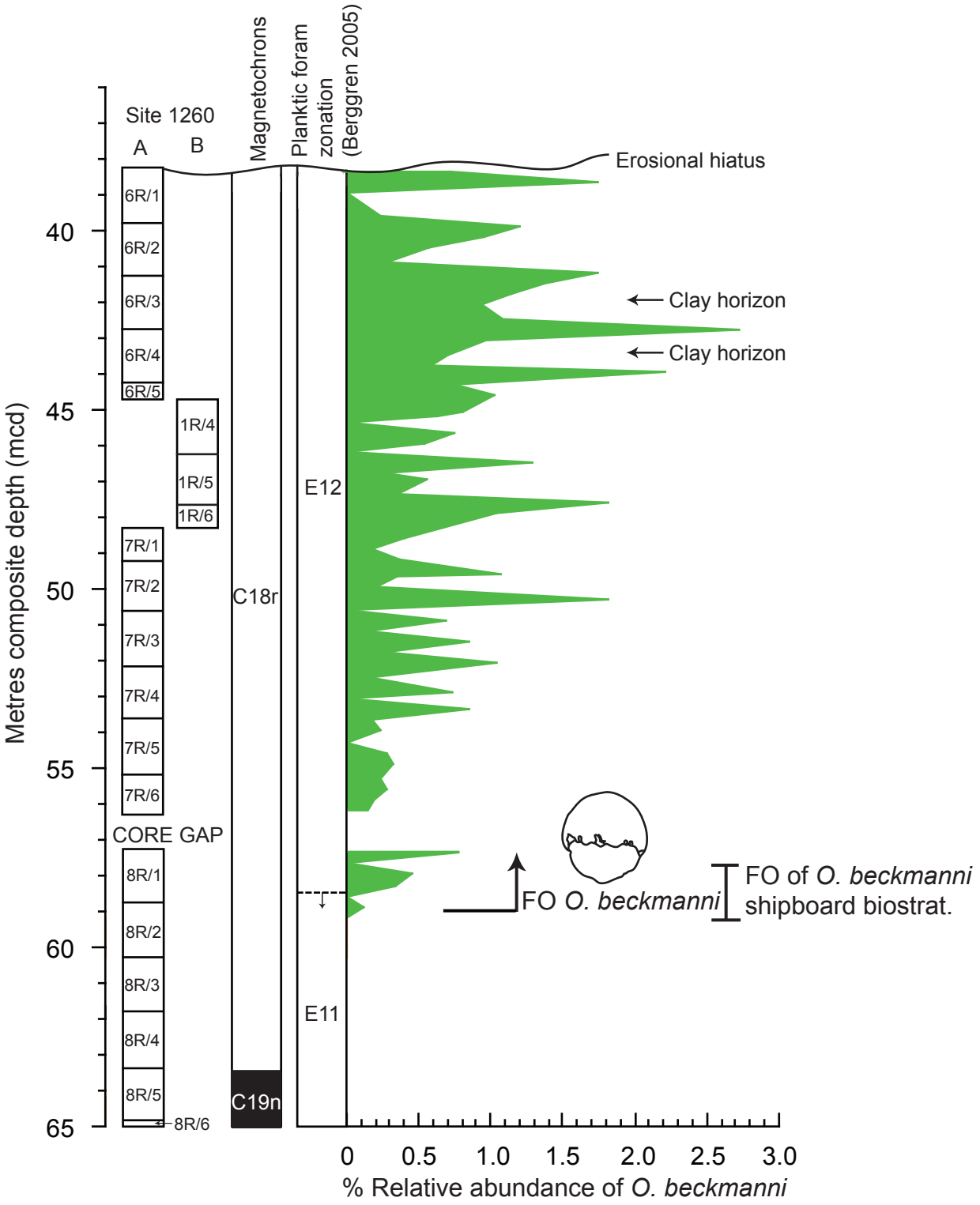

FIGURE 6.6: Relative abundance of *Orbulinoides beckmanni* at ODP Site 1260 plotted against depth. Site 1051 core splice through the study interval is shown. Data presented as % relative abundance of total planktic foraminiferal assemblage. Magnetostratigraphy from (Ogg and Bardot, 2001; Y. Suganuma, written pers. comm., 2007). Planktic foraminiferal zone assignment following Berggren and Pearson (2005), new relative abundance counts of *O. beckmanni* indicate the need to revise the position of these boundaries (see arrow). Shipboard biostratigraphic datums from Shipboard Scientific Party (2004).

decreases, superimposed on this trend are cyclical variations in relative abundance. From 63.30 mcd, *O. beckmanni* becomes progressively less abundant and appears in several pulses each separated by several samples where *O. beckmanni* is absent. The LO of *O. beckmanni* at Site 1051 is determined at 61.90 mcd because *O. beckmanni* is absent in the top five samples in the study interval. Frequently, high-resolution studies of marine plankton indicate several pulses in species separated by intervals where it is absent, prior to its final occurrence (Backman, 1986; Raffi et al., 1993; Gibbs et al., 2005).

At Site 1260, *O. beckmanni* has a low relative abundance (0.5 to 2.5%) and discontinuous presence throughout the study interval which appears to correlate to the low abundance zone observed in magnetochron C18r at Site 1051, between the FO and FCO of *O. beckmanni* (Fig. 6.6). The subsequent trend in the data set is towards increasing relative abundances of *O.beckmanni* from ≤0.5 to 2.5% up splice, with the highest relative abundances of *O. beckmanni* recorded at ∼42.80 mcd. *O.beckmanni* is still present in in the topmost sample of the Site 1260 core splice preventing identification of the LO of *O.beckmanni* and indicating that the E12 biozone is not complete at this site. At 36.1 mcd, the sedimentary succession is interrupted by a hiatus that spans approximately five million years of geological time (Shipboard Scientific Party, 2004). The top of magnetochron C18r and the whole of C18n are absent from Site 1260, making it impossible to test whether the abrupt increase in the relative abundance of *O.beckmanni* observed in the base of magnetochron C18n, at Site 1051 is repeated at Site 1260. Two clay horizons observed in core photos and physical property records at Site 1260 coincide with minor decreases in the relative abundance and preservation of *O.beckmanni* at ∼41.80 and 43.60 mcd. Coincident clay horizons are not present at Site 1051 presumably because it is significantly shallower (∼1 km) site.

6.3 Interpretation

6.3.1 Calibration of planktic foraminiferal biozone E12

The lowermost part of the study interval at Sites 1260 and 1051 corresponds to planktic foraminiferal zone E11 of Berggren and Pearson (2005). The biozone E11/E12 boundary defined by the FO of *Orbulinoides beckmanni* falls in the topmost part of magnetochron C18r and is assigned an age of 40.5 Ma (Berggren et al., 1995). Using the new age model developed for ODP Site 1051 in this study (Fig. 5.20), and assuming a constant linear sedimentation rate between magnetic reversals, the base of biozone E12 as determined in this study occurs at ∼40.5 Ma, in good agreement with the existing (sub)tropical calibration (Berggren et al., 1995; Berggren and Pearson, 2005).

Assigning an age to the base of the E12 biozone at Site 1260 is complicated by the presence of a hiatus. While magnetochrons C20n through C19n are recovered and well

resolved, the top of magnetochron C18r (Shipboard Scientific Party, 2002b) and the top of planktic foraminiferal biozone E12 are absent at Site 1260. Supplementary investigation to determine the LO of the calcareous nannofossil species *Chiasmolithus solitus*, which defines the base of biozone CP14b and is assigned an age of 40.4 Ma (Berggren et al., 1995), at Site 1260 was unsuccessful because *C. solitus* is still present in the topmost sample of the core splice at this site and therefore could not be employed as an age control point.

In principle, three different methods can be employed to calculate the age of the FO of *O. beckmanni* at Site 1260. First, if we assume that the calibrated age of 40.5 Ma for the base of the *O. beckmanni* biozone is correct, this corresponds to a fourfold decrease in the sedimentation rate from 2 to ∼0.6 cm/kyr between the top of magnetochron C19n and the FO of *O. beckmanni*, followed by a rapid increase in excess of 6 cm/kyr for the top 20 m of the core splice (A in Fig. 6.7). Such large and rapid shifts in sedimentation rate seem unrealistic. A second method assumes that the calibration of the LO of *C. solitus* to the GPTS is robust and that the absence of this datum at Site 1260 can be used to constrain sedimentation rates in the topmost of the core splice, i.e., sediments can not be younger than 40.4 Ma. Employing the LO of *C. solitus* as an age control point results in sedimentation rate estimates of ≥3.2 cm/kyr and an age estimate for the FO of *O. beckmanni* older than 41.1 Ma (B in Fig. 6.7). Given the poor calibration of calcareous nannofossil datums to the GPTS during the Middle Eocene, use of this datum as an age control point may not be appropriate (Berggren et al., 1995). A third method utilises the absence of the top of magnetochron C18r calibrated to 40.13 Ma (Berggren et al., 1995) as a relative age control point to constrain sedimentation rates. This provides a more realistic estimate of sedimentation rate, ∼2.5 cm/kyr for the topmost part of the core splice (C in Fig. 6.7) consistent with previous sedimentation rates inferred between older magnetic reversals. Although, this method still yields an age for the FO of *O. beckmanni* of 41.0 Ma, significantly older than previously reported or estimated at Site 1051 in this study.

The LO of *O. beckmanni* is calibrated by Berggren et al. (1995) to the base of magnetochron C18n.2n, corresponding to an age of 40.1 Ma. More recently, the LO of *O. beckmanni* was reassigned to 40.0 Ma by Wade (2004) using the shipboard biostratigraphy already generated at ODP Site 1052 (Shipboard Scientific Party, 1998). If the astronomical timescale generated at ODP Site 1052 by Pälike et al. (2001) is employed this assigns an even younger age to the top of the E12 biozone of 39.7 Ma. At ODP Site 1051 the LO of *O. beckmanni* occurs at 61.85 mcd and falls in the lowermost part of magnetochron C18n.1n, giving an age of 39.4 Ma. This is 600 kyrs earlier than previously reported. In addition, this leads to an estimated duration of the E12 biozone of 900 kyrs - almost double previous estimates of the zones duration but more realistic than the even younger age and two million year duration inferred using the shipboard age model. The much younger LO of *O. beckmanni* reported here is attributed to the

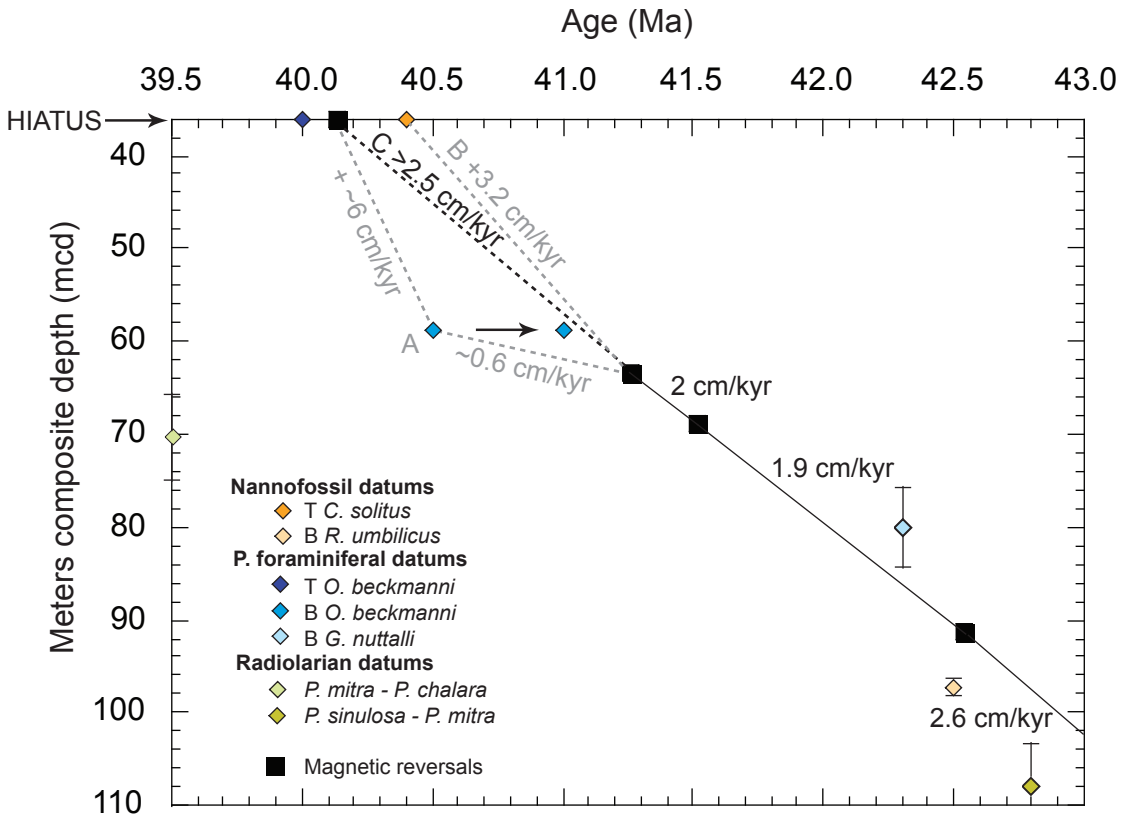

FIGURE 6.7: Revised sediment accumulation rates for ODP Site 1260. Biostratigraphic datums from the Shipboard Scientific Party (2004) except for the first occurrence of *Orbulinoides beckmanni*, and presence of *Chiasmolithus solitus* determined in this study. Refined magnetic reversal stratigraphy from Y. Suganuma, written pers. comm. (2007). Ages are reported on the time scale of Cande and Kent (1992a, 1995). The top of magnetochron C18r, planktic foraminiferal zone E12 and nannofossil zone CP14a are absent because of the hiatus at ∼36 mcd. Lines labelled A through C represent different datums employed to constrain sedimentation rates in the top of the core splice. Line C is considered to be the best estimate (discussed in Section 6.3.1). B and T represent the first and last occurrence of a species, respectively.

typically poor recovery and ambiguous age control at the top of this biozone at deep sea sites, that has hindered previous recognition of its true age. Further investigation of this datum is required to assess the reliability of the new age assigned to the top of biozone E12.

6.3.2 Diachroneity of the of *Orbulinoides beckmanni*

There is a significant temporal offset by ∼500 kyrs in the estimated age of the FO of *Orbulionoides beckmanni* between the two sites investigated in this study, that has not been previously documented. Diachrony is commonly reported for biostratigraphic

TABLE 6.1: Revised planktic foraminiferal biostratigraphic data for biozone E12. Abbreviations used are F(C)O and L(C)O = first and last (common) occurrence respectively, T and B = top and bottom, and mcd = metres composite depth. Starred (*) top and bottom of datum are from the Shipboard Scientific Party (2004) and (**) ages are from Berggren and Pearson (2005). Revised ages are calculated using the age models outlined in this study (Figs 5.20 and 6.7) and are reported relative to the time scale of Cande and Kent (1992a, 1995).

Datum	T - B (mcd)*	T - B (mcd)	Age (Ma)**	Rev. age (Ma)
ODP Site 1051				
LO? *O. beckmanni*	73.26 - 82.95	61.80 - 61.90	40.0	39.4
LCO *O. beckmanni*	-	63.20 - 63.30	-	39.5
FCO *O. beckmanni*	-	86.80 - 86.90	-	40.1
FO *O. beckmanni*	91.45 - 101.35	106.15 - 106.45	40.5	40.5
ODP Site 1260				
FO *O. beckmanni*	57.80- 59.30	58.77 - 59.07	40.5	41.0

datums in the geological record but caution is warranted, temporal discrepancies can reflect a number of factors, and it is therefore important to distinguish between *apparent* diachrony and genuine *geological* diachrony. Apparent diachrony can arise in four main ways. Firstly through sampling artifacts, biostratigraphic analysis is typically conducted on widely spaced samples, ∼5 - 10 m spacing at deep sea sites, resulting in poor temporal and stratigraphic resolution of bioevents introducing potential offsets to bioevents correlated between sites (Raffi, 1999). Second, while species extinctions are often unambiguous and easily recognisable datums, the FO of a species can be more difficult to accurately identify. Particularly, if the datum is defined by a gradual transition between two morphospecies, e.g., *Globigerinatheka euganea* and *O. beckmanni*, which will be placed in subtly different places by different workers, imparting a degree of uncertainty to the calibration of this datum (Pearson and Chaisson, 1997). Indeed, in a global survey of Neogene planktic foraminiferal datums, Spencer-Cervato et al. (1994) indicate greater, by ∼ 200 kyr, error on reported FO compared to LO of species. It is therefore important that all workers adopt a strict species taxonomic concept to enable accurate inter-site comparisons. Third, ambiguous or lack of magnetostratigraphy at a number of sites limits the accuracy of the calibration of biostratigraphic datums to the GPTS. Fourth, unrecognised hiatuses and unconformities in sampled sections can distort species apparent ranges and produce patterns that mimic diachrony (Aubry and Van Couvering, 2005).

The 500 kyr offset in the FO of *O. beckmanni* between Sites 1260 and 1051 reported here exceeds the variability expected from methodological or age model inconsistencies and is therefore interpreted to represent a genuine case of geological diachrony within the Atlantic Ocean. The oldest FO of *O. beckmanni* is recorded at Site 1260 at 41.0 Ma, this suggests that *O. beckmanni* may have had its evolutionary first appearance in equatorial waters, at least in the Atlantic, and later expanded its biogeographic range (FO at Site 1051, 40.5 Ma). Examples of latitudinal diachrony are relatively common among datums

defined by the FO of a species in all the marine plankton; diatoms (Spencer-Cervato et al., 1994), radiolarians (Moore et al., 1993), calcareous nannofossils (Raffi et al., 1993) and planktic foraminifera (Spencer-Cervato et al., 1994; Kucera and Kennett, 2000), typically with the oldest FO of a species recorded in the equatorial regions/lower latitudes and a lag of up to several hundred thousand years before that species appears at higher latitudes (but in extreme cases several million years). This finding is consistent with studies that document the highest rates of speciation, i.e., evolutionary first appearances, amongst the marine plankton, particularly planktic foraminifera, in the tropics (Allen and Gillooly, 2006). Mechanisms that are invoked to explain latitudinal diachrony include the gradual migration of a species and/or expansion of its geographic range due to changing environmental conditions or gradual evolutionary adaptation of the species through 'adaptive immigration' (Spencer-Cervato et al., 1994).

6.3.3 Environmental change associated with the evolution and extinction of *Orbulinoides beckmanni*

Intriguingly, *Orbulinoides beckmanni's* stratigraphic range broadly coincides with the global warming event, the Middle Eocene Climatic Optimum (MECO) ∼40.0 - 40.5 Ma (Bohaty and Zachos, 2003; S. Bohaty, written pers. comm. 2007), leading to the possibility that the MECO may have played a role in the evolution and extinction of *O. beckmanni*. The MECO is associated with a gradual 1‰ increase in δ^{18}O values (Fig. 6.8) generated in bulk carbonate and benthic foraminiferal calcite, coincident with a small shift to more positive δ^{13}C values, inferred to represent carbon cycle-led warming of surface and deep waters of ∼4°C (assuming no ice volume contribution to the δ^{18}O signal) (Bohaty and Zachos, 2003). Minimum δ^{18}O values, i.e., warmest inferred temperatures at ∼40.0 Ma are associated with a small 0.5‰ short lived negative δ^{13}C excursion (Bohaty and Zachos, 2003). The end of the MECO is characterised by an increase in δ^{13}C and δ^{18}O values.

In Figure 6.8 new benthic foraminiferal δ^{18}O ($\delta^{18}O_{benthic}$) records from ODP Sites 1260 and 1051 generated in this study are presented with published $\delta^{18}O_{benthic}$ records from ODP Site 748 in the Southern Ocean (Bohaty and Zachos, 2003) on a new agescale (see Chapter 7) against the relative abundance records of *O. beckmanni* generated here. These data show that the FO of *O. beckmanni* at Site 1260 predates the large shift in benthic foraminiferal $\delta^{18}O_{benthic}$ values (see arrows in Fig. 6.8) used to define the onset of the MECO by several hundred thousand years suggesting that the evolution of *O. beckmanni* may not be related to the onset of MECO. However, changes in the composition of the planktic foraminiferal assemblage at Site 1260, discussed in Chapter 7, indicate that environmental changes in the surface waters predate the shift in $\delta^{18}O_{benthic}$ values and inferred deep water warming. It is also worth noting, as shown in Figure 6.8, that only the onset of the MECO is recovered at Site 1260, the peak and recovery

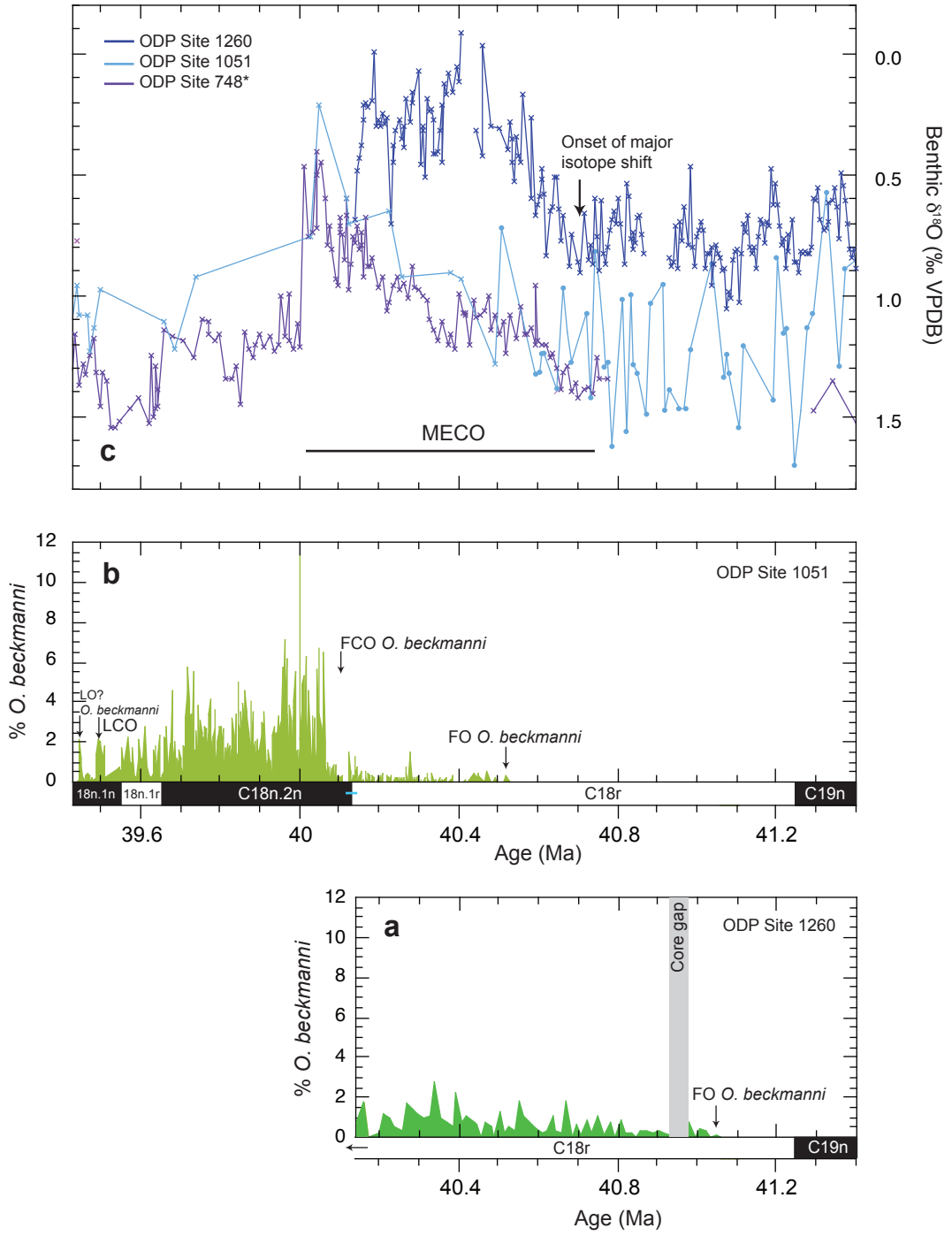

FIGURE 6.8: The Middle Eocene Climatic Optimum (MECO) and *Orbulinoides beckmanni*. a and b) Relative abundance records of *O. beckmanni* at ODP Sites 1260 and 1051, respectively. c) Benthic foraminiferal δ^{18}O records from ODP Sites 1051 and 1260 generated in *Cibicidoides eoceanus* in this study (crosses) and by Hindley (2003) (solid circles). Data from ODP Site 748 generated in *Cibicidoides* spp. from Bohaty and Zachos (2003) and shown on revised age scale (see Figure 7.4). The low resolution δ^{18}O data from Site 1051 shows a shift towards higher δ^{18}O values broadly synchronous with other records. Duration of the MECO marked by horizontal line. At Site 1260 the FO of *O. beckmanni* precedes the large increase in δ^{18}O values observed at this site (see arrow) whereas at Site 1051 this species FO appears to occur shortly after the onset of the MECO. LO of *O. beckmanni* at Site 1051 postdates the MECO. Error on magnetochron boundaries at ODP Sites 1051 and 1260 shown by horizontal blue bar. δ^{18}O values adjusted to equilibrium using the correction factors of Katz et al. (2003).

of the event are not captured because of the hiatus at ∼36 mcd. At ODP Site 1051, the FO of *O. beckmanni* occurs at 40.5 Ma shortly after the onset of MECO. The coincidence between the FO of *O. beckmanni* and the onset of the MECO suggests that the poleward expansion of warm surface waters inferred to have accompanied the MECO at ∼40.5 Ma may have created more favourable conditions for this species and enabled *O. beckmanni* to migrate to the subtropics, e.g, Site 1051. Indeed, the highest relative abundances of *O. beckmanni* recorded at Site 1051 do appear to broadly coincide with minimum δ^{18}O values in stable isotope records shown in Figure 6.8 and more importantly with published bulk stable isotope records (not shown here) (Bohaty and Zachos, 2003; Spofforth et al., 2008), i.e., highest inferred temperatures, coupled with the restricted palaeobiogeographic distribution of *O. beckmanni* shown in Figure 6.4, this strongly suggests that sea surface temperature is the dominant control on *O. beckmanni's* biogeographic distribution.

The relative abundance data from Site 1051 indicate a gradual decline of *O. beckmanni* from peak abundances at ∼39.9 Ma, prior to its extinction ∼600 kyrs after MECO (Fig. 6.8) ruling out an abrupt extinction mechanism such as a killer virus (Emiliani, 1982, 1993) or comet impact (Raup, 1986). If temperature is the dominant control on *O. beckmanni's* distribution as suggested it seems most likely that the gradual decline and eventual extinction of *O. beckmanni* is related to global cooling that follows the MECO (Zachos et al., 2001; Bohaty and Zachos, 2003), because either it had only a narrow environmental tolerance or the ecological niche that it occupied was disrupted or destroyed by cooling (Norris, 2000).

6.4 Conclusions

At ODP Site 1051 in the western North Atlantic, an expanded and stratigraphically complete, to magnetochron level, sedimentary section through planktic foraminiferal biozone E12 was recovered. Sediments host moderately to well preserved planktic foraminifera with an assemblage containing *Orbulinoides beckmanni*, and a highly resolved magnetostratigraphy generated in Chapter 5. High-resolution quantitative biostratigraphic analysis of *O. beckmanni* calibrated to a high-resolution magnetostratigraphy has yielded the following results:

1. High-resolution relative abundance records of the planktic foraminiferal species *O. beckmanni* from ODP Site 1051 show that the FO of *O. beckmanni* occurs in the top of magntochron C18r and is assigned an age of 40.5 Ma, consistent with previous work. However, the FO of *O. beckmanni* determined at ODP Site 1260 in the equatorial Atlantic occurs in the bottom of magnetochron C18r and is assigned an age of 41.0 Ma, 500 kyrs older than previously reported. This large temporal

discrepancy in the FO of *O. beckmanni* between the two sites is most likely an example of latitudinal diachrony.

2. *O. beckmanni* is inferred to have had its evolutionary first appearance in equatorial waters as recorded at Site 1260, and subsequently migrated to the subtropics as recorded at Site 1051, with the poleward expansion of warm surface waters inferred to have accompanied the MECO ∼40.5 Ma.

3. *O. beckmanni* is a short-lived species that is an important biostratigraphic marker and can still be employed as such but caution must be applied when using the FO of *O. beckmanni* to assume an age, in these cases it may be more appropriate to employ a regional rather than a global calibration scheme to this datum.

4. The LO of *O. beckmanni* at Site 1051 occurs in magnetochron C18n.2n and is assigned an age of 39.4 Ma, 600 kyrs younger than previously reported. This revised age for the top of biozone E12 is attributed to the typically discontinuous recovery of sediments and poor age control across this biozone in earlier work.

5. The total range of *O. beckmanni* recorded at ODP Site 1051 indicates that the E12 biozone is 900 kyrs in duration, not 500 kyrs as suggested by the IBMS.

6. The mapped palaeobiogeographic distribution (Fig. 6.4) and the diachrony of the stratigraphic FO of *O. beckmanni* associated with the MECO implies that sea surface temperature plays an important role in controlling its distribution.

6.5 Future work

This study clearly highlights the importance of generating multiple quantitative records of key species abundances at a number of sites to assess the reliability and the degree of synchrony/diachrony of biostratigraphic datums. Further work will involve generating additional quantitative records of *Orbulinoides beckmanni* at other deep sea sites to validate the conclusions and hypotheses of this study. For instance, are the highest relative abundances of *O. beckmanni* coincident with the peak of the MECO (and inferred peak warmth) at other deep sea sites? Is the LO of *O. beckmanni* also latitudinally diachronous? Is the FO of *O. beckmanni* similarly diachronous in other ocean basins?

Further work will include the development of astronomical age models for Sites 1051 and 1260 using physical property data. This will enable a more accurate assessment of the age of the bioevents identified in this study and the degree of diachrony, avoiding the circularity inherent to calibrating biostratigraphic datums to magnetostratigraphic time scales, i.e., assigning magnetochrons using the biostratigrapic datums and subsequently determining the age of biostratigraphic datums from the magnetostratigraphy.

To determine if the LO of *O. beckmanni* defined at Site 1051 in this study is valid, the count record will be extended for this species.

Observation of planktic foraminif eral samples at ODP Site 1051 appears to indicate an increase in the size and sphericity of *O. beckmanni* coincident with its abrupt increase in relative abundance observed in the base of magnetochron C18n, and the 'peak' of the MECO (Fig. 6.5). A pilot study will be conducted to determine the diameter and sphericity of individuals throughout *O. beckmanni's* stratigraphic range in order to test this observation and investigate any potential link between morphological variation and environmental change.

Chapter 7

Planktic foraminiferal response to the Middle Eocene Climatic Optimum

7.1 Introduction

Superimposed on the long-term Eocene cooling trend is a transient ∼600 thousand year (kyr) long warming event (Fig. 7.1), the Middle Eocene Climatic Optimum (MECO) (Bohaty and Zachos, 2003) across the magnetochron C18r/C18n boundary (S. Bohaty written pers. comm., 2007) ∼40 million years ago (Ma) based on the timescale of Cande and Kent (1992a, 1995). The MECO was originally reported as occurring at 41.5 Ma (Bohaty and Zachos, 2003) based on nannofossil biostratigraphic datums (the last occurrence (LO) of *Chiasmolithus solitus* at 40.4 Ma and the first occurrence (FO) of *Reticulofenestra umbilica* at 43.7 Ma Berggren et al., 1995) but its timing has since been revised in light of new stable isotope records with better age models (Bohaty written pers. comm., 2007). The MECO was first identified in stable isotope records from the Southern Ocean at ODP Sites 689, 738 and 748 (Fig. 7.2) but has now been identified in stable isotope records from other localities - ODP Site 1260, Demerara Rise (Sexton et al., 2006a) and in the Alano di Piave (Agnini et al., 2007; Spofforth et al., 2008) and Contessa sections in Italy (Jovane et al., 2007) (Fig. 7.2), indicating that the MECO was global in nature, and represented a significant climatic reversal in the Earth's long-term cooling trend. Stable isotope records generated in benthic foraminiferal calcite (Bohaty and Zachos, 2003; Sexton et al., 2006a) and bulk sediment (Bohaty and Zachos, 2003; Agnini et al., 2007; Spofforth et al., 2008) show a gradual shift of 1‰ to lower δ^{18}O values over ∼600 kyrs, followed by a rapid (∼10 kyrs) decline and then equally rapid increase in δ^{18}O signalling the end of the MECO (Fig. 7.1). Continental ice sheets at this time were most likely small ($\leq$ 50% of the modern Antarctic ice volume, Chapter 4) and

thus, at most, have the potential to account for only approximately half of the decrease in δ^{18}O values associated with the onset of the MECO. Thus, at least ∼0.5‰ of the δ^{18}O signal must reflect warming of bottom and surface waters by at least 2°C. The MECO is terminated by rapid cooling. Coincident with minimum δ^{18}O values, i.e. the peak of the MECO, is a short-lived negative δ^{13}C excursion (Fig. 7.1) that may reflect a brief injection of isotopically light carbon to the ocean-atmosphere system associated with bottom water warming (Bohaty and Zachos, 2003). A shift to more positive δ^{13}C values across the onset of the MECO rules out the input of isotopically exogenic carbon to the ocean-atmosphere system as a mechanism to explain the inferred warming. Instead, a transient rise in the partial pressure of carbon dioxide (pCO_2) in the atmosphere as a result of increased volcanic outgassing due to either North Atlantic rifting and/or metamorphic decarbonation reactions associated with the collision of India and Asia have been invoked (Bohaty and Zachos, 2003). Although existing pCO_2 reconstructions indicate high pCO_2 levels ∼1000 - 2000 ppm for the Eocene (Pearson and Palmer, 2000; Pagani et al., 2005), they are of insufficient resolution and agreement across this interval of the Middle Eocene to provide a reliable test of this hypothesis.

Coincident with the MECO is a significant shoaling of the carbonate compensation depth (CCD) in the Pacific (Lyle et al., 2005) and Atlantic Oceans (Tripati et al., 2005) and a near global hiatus that truncates many deep-sea sedimentary sections around the magnetochron C18r/C18n boundary (∼40 Ma) indicating either an interval of non-deposition or erosion of material by more vigorous ocean circulation or corrosive bottom waters.

Little is known about biotic turnover during this interval of the Middle Eocene because previous work has focussed on only long term multi-million year faunal transition characterised by the successive replacement of tropical fauna and flora by sub-tropical or temperate taxa through the Middle Eocene to Early Oligocene (Kennett, 1977; McGowran, 1977; Berggren, 1978; Keller et al., 1992). Yet several lines of evidence indicate that the MECO may be associated with changes in marine plankton assemblages. First, the new placement of the MECO at the magnetochron C18r/C18n.2n boundary and the ∼500 kyr duration of the event is coincident with the placement of planktic foraminiferal biozone E12 (Berggren and Pearson, 2005). Biozone E12 is defined by the FO and LO of the low latitude planktic foraminifera, *Orbulinoides beckmanni* which shares several striking similarities with the so-called Palaeocene-Eocene thermal maximum (PETM) 'excursion' taxa (Kelly et al., 1996, 1998; Cramer et al., 2000). These similarities include the distinctive morphology of *O. beckmanni* and its anomolously short stratigraphic range (∼500 kyrs), which, based on the existing biozonation scheme (Berggren and Pearson, 2005), appears coincident with the duration of the MECO (Fig. 7.1). Second, faunal assemblages in the Indian Ocean indicate invasion of warm water taxa to higher latitudes in planktic foraminiferal biozone E12 (McGowran, 1977). Third, a large number

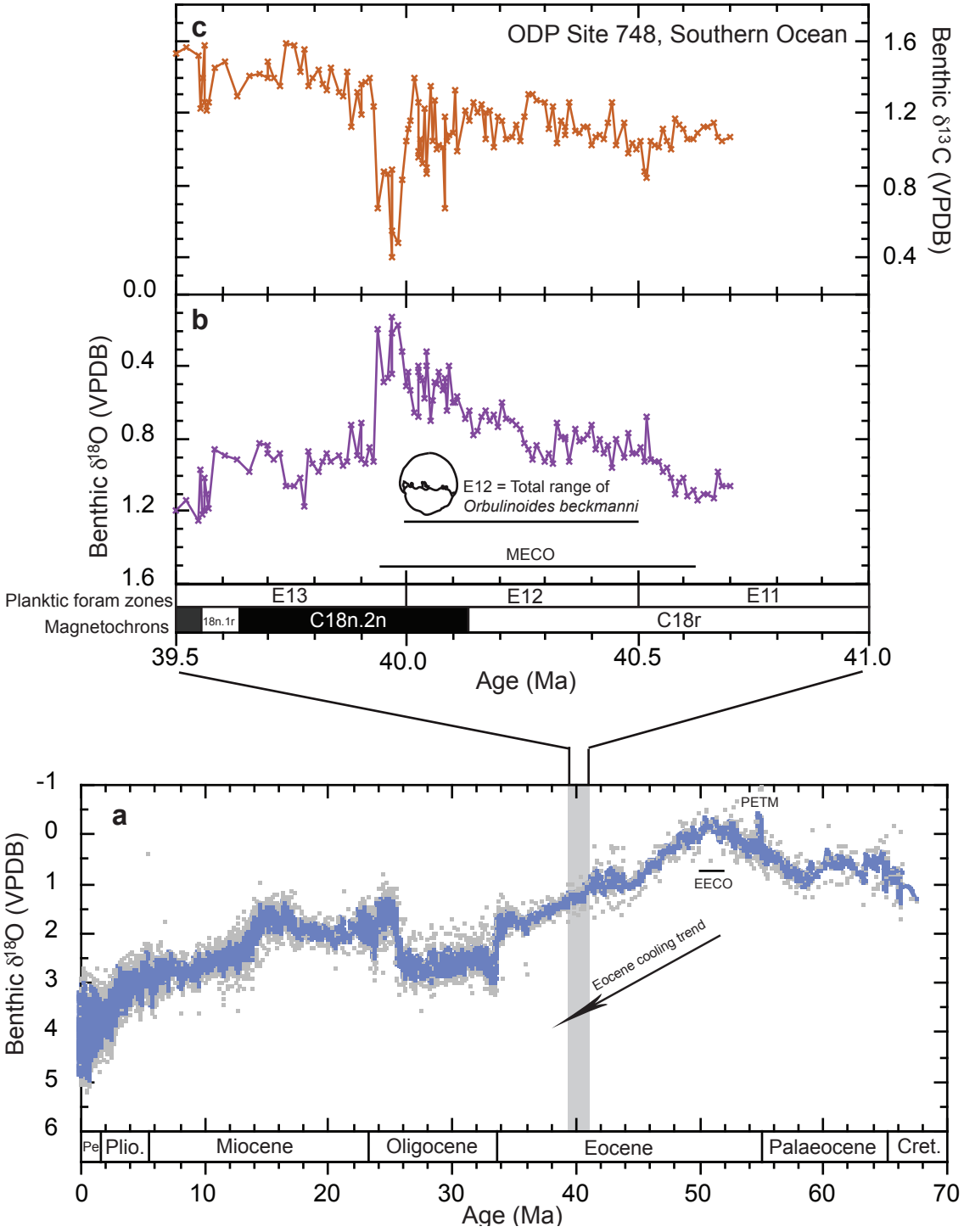

FIGURE 7.1: Benthic stable isotope curves for the Cenozoic and the Middle Eocene Climatic Optimum (MECO). a) Composite oxygen isotope record generated in benthic foraminiferal calcite redrawn from Zachos et al. (2001). Blue line represents 5 point running mean through data set. Cret. = Cretaceous, Plio. = Pliocene and Pe = Pleistocene. PETM = Palaeocene-Eocene thermal maximum and EECO = Early Eocene climatic optimum. b) and c) benthic foraminiferal δ^{18}O and δ^{13}C records across the MECO generated in *Cibicidoides* spp. from Bohaty and Zachos (2003) on the revised age scale of S. Bohaty, written pers. comm (2007). δ^{18}O values adjusted to equilibrium as in Shackleton and Opdyke (1973). Horizontal line in panel b represents the stratigraphic range of *Orbulinoides beckmanni* based on the most recent biostratigraphic zonation scheme of Berggren and Pearson (2005).

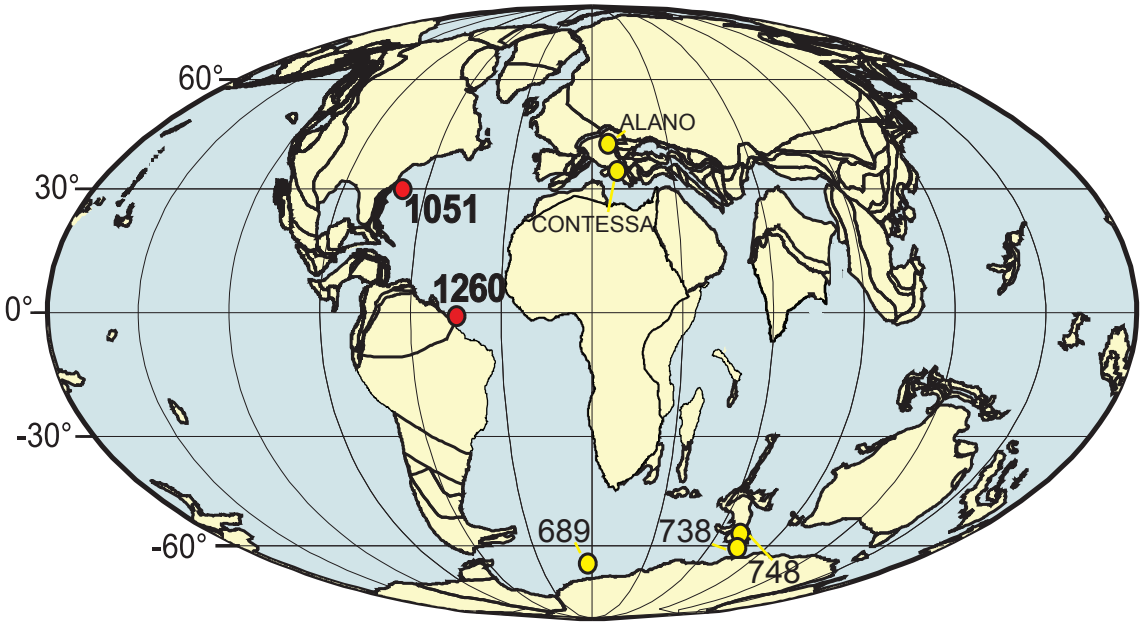

FIGURE 7.2: Palaeogeographic reconstruction at 40 Ma showing location of sites where MECO has been reported (Bohaty and Zachos, 2003; Sexton et al., 2006a; Agnini et al., 2007; Edgar et al., 2007; Spofforth et al., 2008). Solid red circles indicate ODP Site 1051 and 1260 used in this study. Base map generated at www.odsn.de/odsn/serices/paleomap/paleomap.html.

of stratigraphic FO and LO of Eocene planktic foraminifera are recorded during biozone E12 based on stratigraphic range charts in Pearson et al. (2006).

The impact of global warming events on biotic assemblages is poorly understood but concern over the fate of the marine biosphere in response to anthropogenically forced increases in pCO_2 means that this sort of information has never been more pertinent. To date, the PETM ∼55 Ma has been the major focus of Paleogene biotic studies and major shifts in both the marine and terrestrial biota have been identified, e.g., Tjalsma and Lohmann (1983), Maas et al. (1995), Hooker (1996), Kelly et al. (1996), Bralower (2002), Gibbs et al. (2006). In the marine realm, the benthic foraminifera suffer their largest extinction of the past 90 Myr with 30 to 50% of benthic foraminiferal species becoming extinct at the onset of the PETM (Tjalsma and Lohmann, 1983; Speijer et al., 1996; Thomas and Shackleton, 1996). In surface waters, PETM warming triggered a rapid diversification among the shallow dwelling planktic foraminifera and calcareous nannoplankton giving rise to several short-lived species or so-called 'excursion' taxa thought to be confined to the PETM (Kelly et al., 1996, 1998; Cramer et al., 2000). The marine plankton also demonstrate an expansion of low latitude marine taxa to higher latitudes (Bujak and Brinkhuis, 1998; Bralower, 2002; Kelly, 2002; Sluijs et al., 2006) and significant shifts in assemblage composition (Kelly et al., 1996, 1998; Kelly, 2002; Gibbs et al., 2006; Petrizzo, 2007). However, the MECO differs from the PETM in several

ways. First, the PETM is characterised by an initial large, abrupt ≤10 kyr shift to more negative δ^{13}C (by ∼3‰ in marine carbonate) and δ^{18}O values (by ∼1 to 2‰), followed by a gradual recovery (≥100 kyrs) to near pre-excursion stable isotope values (Kennett and Stott, 1991; Norris and Röhl, 1999; Zachos et al., 2003, 2005). The isotope profile of the MECO is very different. The onset of the MECO is defined by a gradual shift to heavier δ^{13}C and lighter δ^{18}O values over ∼500 kyrs and rapid (≤10 kyrs) recovery of isotope values following the peak of the event (Bohaty and Zachos, 2003). However, there is a short-lived negative δ^{13}C excursion at the peak of the MECO superimposed on the longer term trend towards more positive δ^{13}C values. Second, the PETM is estimated most recently to be ∼170 - 220 kyrs in duration (Farley and Eltgroth, 2003; Röhl et al., 2007), significantly shorter than the ∼600 kyr long duration inferred for the MECO (Bohaty and Zachos, 2003). Third, Earth's baseline climate was much warmer at the PETM than the MECO (Zachos et al., 2001).

The main aim of this study is to present high-resolution quantitative records documenting the response of the planktic foraminifera to the MECO. Changes in the relative abundance of the dominant groups of planktic foraminifera reflect changes in the physical and biological character of the environment in which they live and can therefore be used to examine the relationship between environmental changes and planktic foraminiferal assemblage changes. To construct a continuous faunal assemblage record across the MECO, ODP Site 1051 in the western North Atlantic (Fig. 7.2) was utilised. The sedimentary section recovered at Site 1051 comprises an essentially continuous, at least to magnetochron and biozone level, Middle Eocene sedimentary section of pale green/-grey, siliceous nannofossil oozes with excellent magnetostratigraphic age control refined in Chapter 5. Site 1051 was located at a subtropical latitude ∼25°N from the Aptian through Eocene (Ogg and Bardot, 2001). To assess any similarities and/or differences in the plankton response at lower latitudes, an additional planktic foraminiferal assemblage record was generated at ODP Site 1260 (Fig. 7.2) situated at a palaeolatitude of ∼2°S in the Eocene (Ogg and Smith, 2004). ODP Site 1260 contains an expanded Middle Eocene sedimentary section comprised of predominantly light greenish grey foraminifera and nannofossil oozes but is interrupted by a hiatus at the top of magnetochron C18r, so the MECO is not fully recovered at this site (Shipboard Scientific Party, 2004).

7.2 Results

7.2.1 Stable isotope stratigraphy of the MECO at ODP Site 1051

A low resolution benthic foraminiferal stable isotope stratigraphy was generated at ODP Site 1051 to identify the MECO at this site (Fig. 7.3a and d). The age model for this site assumes constant linear sedimentation rates between the well constrained magnetic reversal stratigraphy generated at Site 1051 presented in Chapter 5. Included with

the benthic stable isotope record generated in this study (crosses in Fig. 7.3) are data generated during a University of Southampton undergraduate project from the interval between 40.6 and 41.0 Ma (circles in Fig. 7.3) (Hindley, 2003). Benthic foraminifera have a relatively sporadic occurrence and low abundance in the majority of samples at Site 1051 making it difficult to generate a continuous high-resolution, monospecific stable isotope record across this interval. Therefore, three different benthic foraminiferal species, *Cibicidoides eoceanus, Nuttallides truempyi* and *Oridorsalis umbonatus*, were utilised. The stable isotope record generated in benthic foraminiferal calcite shows a ∼1‰ shift towards more negative δ^{18}O values (Fig. 7.3a) approximately coincident with a ∼0.5 ‰ increase in δ^{13}C (Fig. 7.3d) in the top half of magnetochron C18r at ∼40.7 Ma. Minimum δ^{18}O values are recorded in all three benthic species at the base of magnetochron C18n.2n at ∼40.0 Ma and are associated with a large negative ∼0.8‰ δ^{13}C excursion recorded in *C.eoceanus* and *N. treumpyi* (Fig. 7.3a). Thereafter, δ^{18}O and δ^{13}C values rapidly recover to more positive values. At present the benthic foraminiferal stable isotope record at Site 1051 is of insufficient resolution to determine whether recovery from minimum δ^{18}O values was as rapid as inferred from published Southern Ocean records (Fig. 7.1).

The planktic foraminiferal stable isotope stratigraphies for Site 1051 are shown in Figure 7.3b, c, e and f. Stable isotope records were generated across the onset, peak and recovery of the MECO in the planktic foraminifera *Acarinina praetopilensis* and *Subbotina angiporoides* because these are the most continuously abundant species in the study interval, and are inferred to be surface and thermocline dwellers respectively (Sexton et al., 2006a; Pearson et al., 2006). The planktic δ^{18}O stratigraphies differ from the benthic isotope stratigraphies (Fig. 7.3) in that both of the planktic species record a broad minimum in δ^{18}O values in the top half of magnetochron C18r (∼40.3 Ma), δ^{18}O values then increase by 0.5‰ around 40.2 Ma (most clearly in the *A. praetopilensis* record). Coincident with minimum δ^{18}O values in the benthic isotope stratigraphy is a short-lived, rapid decrease in δ^{18}O values of about 0.5‰ in the planktics in the base of magnetochron C18n.2n. δ^{18}O values increase immediately following this minimum and continue to trend towards more positive values. The δ^{18}O record generated in planktic foraminiferal calcite at Site 1051 differs from the isotopic profile recorded in the δ^{18}O of benthic foraminiferal calcite at this site (Fig. 7.3) and at other deep-sea sites in the Southern Ocean (Bohaty and Zachos, 2003) (Fig. 7.4). However, it is worth noting that at Site 1051 the MECO appears to coincide with the appearance of anomolously heavily calcified planktic foraminifera (horizontal grey bar in Fig. 7.4d), this phenomenon is most pronounced in the surface dwelling genera *Acarinina* and *Morozovelloides* but is also noticeable in the genus *Globigerinatheka* (P. F. Sexton, oral pers. comm., 2007) (discussed further in Section 7.3.2). Yet, in these new stable isotope records *S. angiporoides* a deeper-dwelling taxon, also records a shift to heavier δ^{18}O values. The genera *Acarinina* and *Morozovelloides* may show the most pronounced thickening of calcite because the carbonate pustules or 'muricae' on their test surfaces act as nucleation points

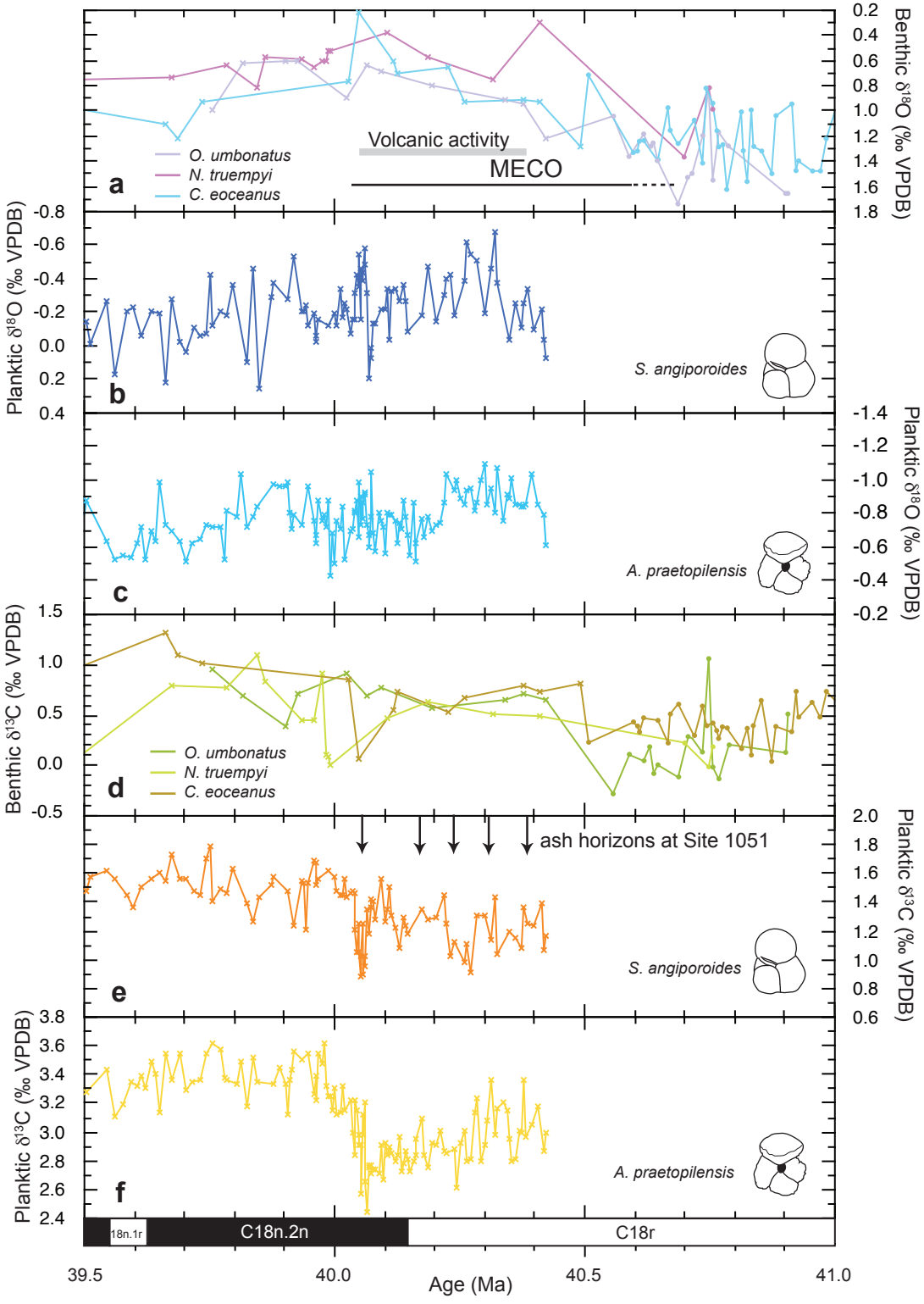

FIGURE 7.3: Foraminiferal stable isotope records from ODP Site 1051 across the MECO. a) and d) stable isotope data generated in monospecific benthic foraminiferal calcite. Crosses indicate data generated in this study and circles by Hindley (2003). Species employed are *Oridorsalis umbonatus, Cibicidoides eoceanus* and *Nuttallides truempyi*. Stable isotope values are adjusted to equilibrium using the values shown in Table 7.1. b-c) and e-f) oxygen and carbon stable isotope data, respectively generated on monospecific samples using the planktic foraminifera *Subbotina angiporoides* in panels b and e and *Acarinina praetopilensis* in panels c and f. Absolute ages are relative to the GPTS of Cande and Kent (1992a, 1995). Horizontal grey bar in panel a represents interval of volcanic activity inferred from the presence of ash horizons identified at Site 1051, shown by arrows in panel e (Shipboard Scientific Party, 1998) and discussed in Section 7.4.

for recrystallisation, whereas test thickening in *Subbotina* may be more difficult to detect under the binocular light microscope.

The δ^{13}C records generated in planktic foraminiferal calcite shown in Figure 7.3 c and d, show more clearly defined isotopic trends. The *S. angiporoides* δ^{13}C record (Fig. 7.3e) shows some variability in values in the top half of magnetochron C18r between 40.4 and 40.1 Ma superimposed on a general trend towards increasing δ^{13}C values. In contrast, the *A. praetopilensis* δ^{13}C record shows a pronounced decrease in the δ^{13}C values over the same interval. These gradual changes in δ^{13}C are punctuated in the base of magnetochron C18n.2n at ∼40.0 Ma by a short-lived negative δ^{13}C excursion of ≥0.6‰ similar to that recorded in the benthic isotope stratigraphy and coincident with the brief decrease in δ^{18}O values. Following the negative δ^{13}C excursion, δ^{13}C values in both species recover rapidly within 200 kyrs to high δ^{13}C values that remain relatively stable for the remainder of the record.

TABLE 7.1: Stable isotope adjustment factors to 'equilibrium calcite' in Eocene benthic foraminifera. All values determined on paired species isotope analysis relative to *Oridorsalis umbonatus* by Katz et al. (2003).

Species	δ^{18}O	δ^{13}C
Cibicidoides spp.	+0.28	-0.72
Nuttallides truempyi	+0.36	-0.46
Oridorsalis umbonatus	-	-

7.2.2 Benthic foraminiferal stable isotope stratigraphy of the MECO at ODP Site 1260

The benthic foraminiferal stable isotope stratigraphy for ODP Site 1260, Demerara Rise is shown in Figure 7.5. Ages were determined by assuming constant linear sedimentation rates between magnetic reversals refined by Y. Suganuma written pers. comm. (2007) and numerical ages were assigned as in Cande and Kent (1992a, 1995) (see Chapter 6 for further details).

Figure 7.5 shows stable isotope data generated from the benthic foraminifera *Cibicidoides eoceanus*. The δ^{18}O record from Site 1260 shows a gradual decrease of 0.8‰ in magnetochron C18r between 40.7 and 40.4 Ma and δ^{18}O values plateau between ∼40.4 and 40.1 Ma. Associated with decreasing δ^{18}O is a 0.6‰ shift to more positive δ^{13}C values in magnetochron C18r between 40.8 and 40.4 Ma that appears to lead the δ^{18}O shift by ∼100 kyrs.

These new stable isotope records reveal the existence of two short-lived (∼40 kyrs) negative 0.8‰ δ^{13}C excursions in magnetochron C18r superimposed on the gradual shift to more positive δ^{13}C values across the MECO. These excursions henceforth referred to

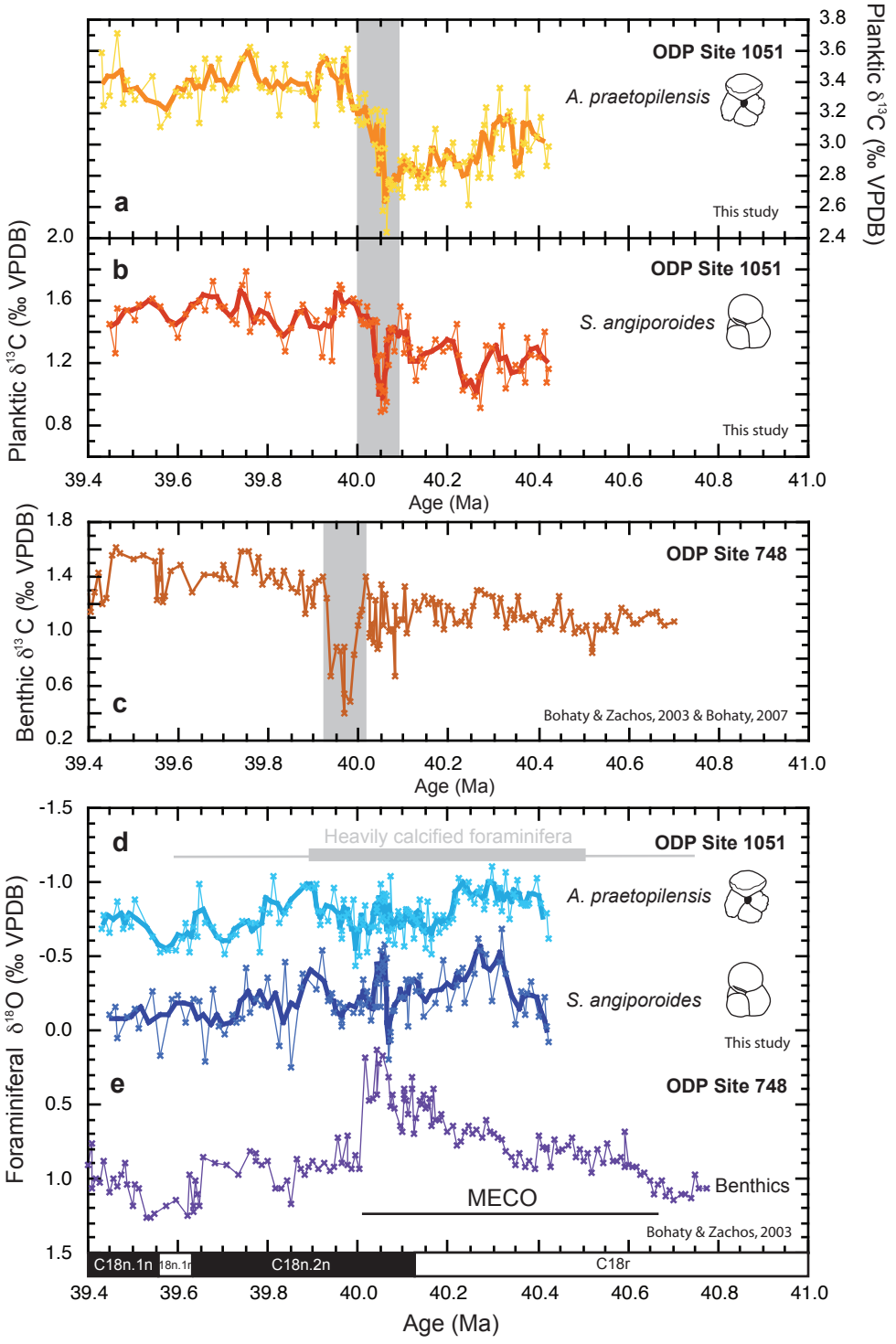

FIGURE 7.4: Correlating stable isotope records from ODP Site 1051 in the North Atlantic to ODP Site 748 in the Southern Ocean. a) and b) monospecific planktic δ^{13}C records generated in *Acarinina praetopilensis* and *Subbotina angiporoides* in this study. Both records show a shift to more negative δ^{13}C values at ~40.05 Ma in the base of magnetochron C18n.2n. c) Stable isotope record generated in benthic foraminiferal calcite at ODP Site 748 from Bohaty and Zachos (2003) on revised time scale provided by S. Bohaty, written pers. comm. (2007). Large negative δ^{13}C excursion appears in all three records a to c (shown by vertical grey shaded area) it is therefore possible to correlate the Site 748 record to Site 1051 by simply aligning this δ^{13}C excursion. d) Planktic foraminiferal δ^{18}O records generated in this study. Horizontal grey bar in panel d marks interval of anomolously heavily calcified planktic foraminifera (P.F. Sexton, oral pers. comm., 2007). e) Benthic δ^{18}O record from Bohaty and Zachos (2003) shown on new timescale determined in this study.

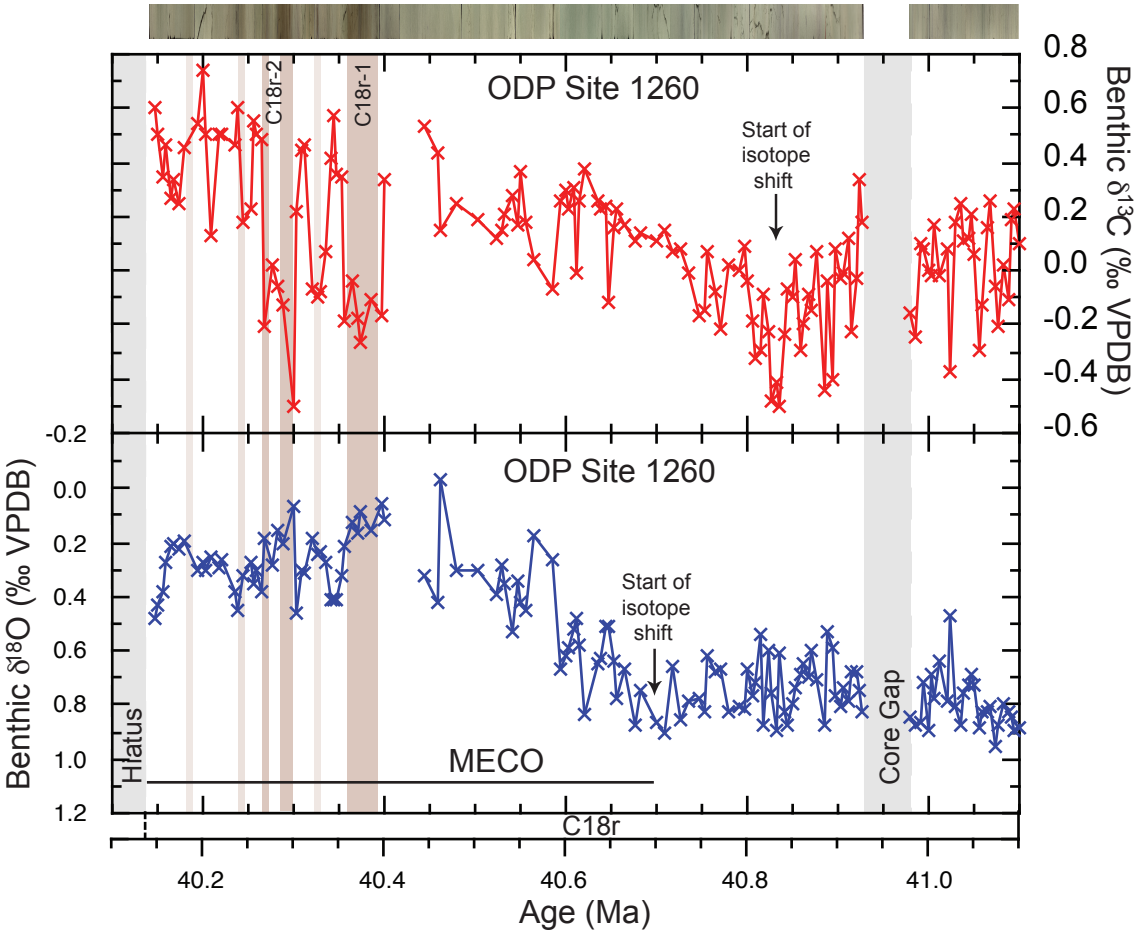

FIGURE 7.5: Benthic foraminiferal carbon and oxygen stable isotope records from ODP Site 1260 across the onset of the MECO. Data generated on the benthic foraminifera *Cibicidoides eoceanus*. Stable isotope values are normalised to 'equilibrium calcite' according to Katz et al. (2003) (Table 7.1). Vertical brown bars correspond to clay horizons visible in the core photos, paler brown bars relate to less prominent clay horizons. Absolute ages are relative to the GPTS of Cande and Kent (1992a, 1995). Core photos downloaded from *http://www-odp.tamu.edu/database/*.

as δ^{13}C-C18r-1 and -C18r-2 (Fig. 7.5) have not been identified in previous studies and are not time equivalent to the negative δ^{13}C excursion already documented at the peak of the MECO in the base of magnetochron C18n.2n by Bohaty and Zachos (2003). The δ^{13}C excursions seen at Site 1260 have a distinctly symmetrical profile and are coincident with minimum δ^{18}O values and brown clay horizons up to 30 cm thick (Fig. 7.5). The upper δ^{13}C excursion (C18r-2) has a double peak, with each of the δ^{13}C excursions coincident with a distinct clay horizon (Fig. 7.5). The position of these δ^{13}C excursions in the top of magnetochron C18r at Site 1260 suggests that these excursions may be stratigraphically correlative to smaller negative δ^{13}C excursions identified in the planktic δ^{13}C records generated in this study at Site 1051 (Fig. 7.6). It is uncertain at present if the C18r-1 and C18r-2 δ^{13}C excursions are global in nature because they

are not observed in the benthic foraminifera stable isotope record generated at Site 1051 because of low sampling resolution (∼1 sample every 32 kyrs) and may not be seen in the Southern Ocean records because of low sedimentation rates (∼0.4 cm/kyr) at the drill sites investigated (Bohaty and Zachos, 2003). A number of thinner and less prominent clay horizons are also present at Site 1260 across the onset of the MECO and correspond to less pronounced δ^{13}C minima. A hiatus at Site 1260 prevents recovery of the peak of the MECO (Shipboard Scientific Party, 2004).

7.2.3 Planktic foraminiferal assemblage character across the MECO at ODP Sites 1051 and 1260

Faunal abundance counts at Site 1051 were carried out on 459 samples using sample splits of the ≥300 μm size fraction at 10 cm sampling resolution (∼3 kyr temporal resolution) throughout the MECO. Sample spacing was increased to 30 cm across the long gradual onset of the MECO. At Site 1260 a total of 70 samples were counted from the interval spanning the onset of the MECO at 30 cm sample spacing (∼12 kyr temporal resolution). Samples contain a relatively diverse planktic foraminiferal assemblage typically comprising more than 20 species and of which the genera *Acarinina, Morozovelloides, Turborotalia, Globiogerinatheka, Hantkenina* and *Subbotina* comprise over 90% of the assemblage (Table 7.2) typical of (sub)tropical environments in the Middle Eocene (Berggren, 1978; Keller et al., 1992; Sexton et al., 2006b). The planktic foraminifera species *Orbulinoides beckmanni* was also counted because the FO and LO of this species is stratigraphically important and may be useful for palaeoclimatic reconstructions based on the findings in Chapter 6. All other planktic foraminifera were counted as 'planktic other', which comprises a number of different Middle Eocene genera including *Dentoglobigerina, Catapsydrax, Globoturborotalia* and *Parasubbotina*. Qualitative estimates of radiolarian abundance were also made by visual approximation of the percentage of radiolarians from the total number of particles present in the sample split to provide qualitative information on siliceous bioproductivity during the MECO.

High-resolution sampling of Middle Eocene sediments at ODP Sites 1051 and 1260 provides detailed records that reveal that the planktic foraminiferal assemblage underwent marked changes in abundance across the MECO (Figs 7.7 and 7.8). Key findings include the following: (1) The genera *Acarinina* dominate pre-MECO assemblages with an accompanying diverse non-*Acarinina* fraction comprising the genera *Globigerinatheka*, *Turborotalia*, *Morozovelloides*, *Hantkenina* and *Subbotina*. Samples are characterised by low equitability values (Fig. 7.9) throughout this interval (∼0.5). (2) Increases in the relative abundance of the genera *Globigerinatheka* and *Morozovelloides* across the onset of the MECO lead to an increase in equitability values (≥0.5). (3) Several abrupt changes in the assemblage occur during the MECO and are coincident with the highest equitability values (0.8) observed in the record (Fig. 7.9) representing an increase in the

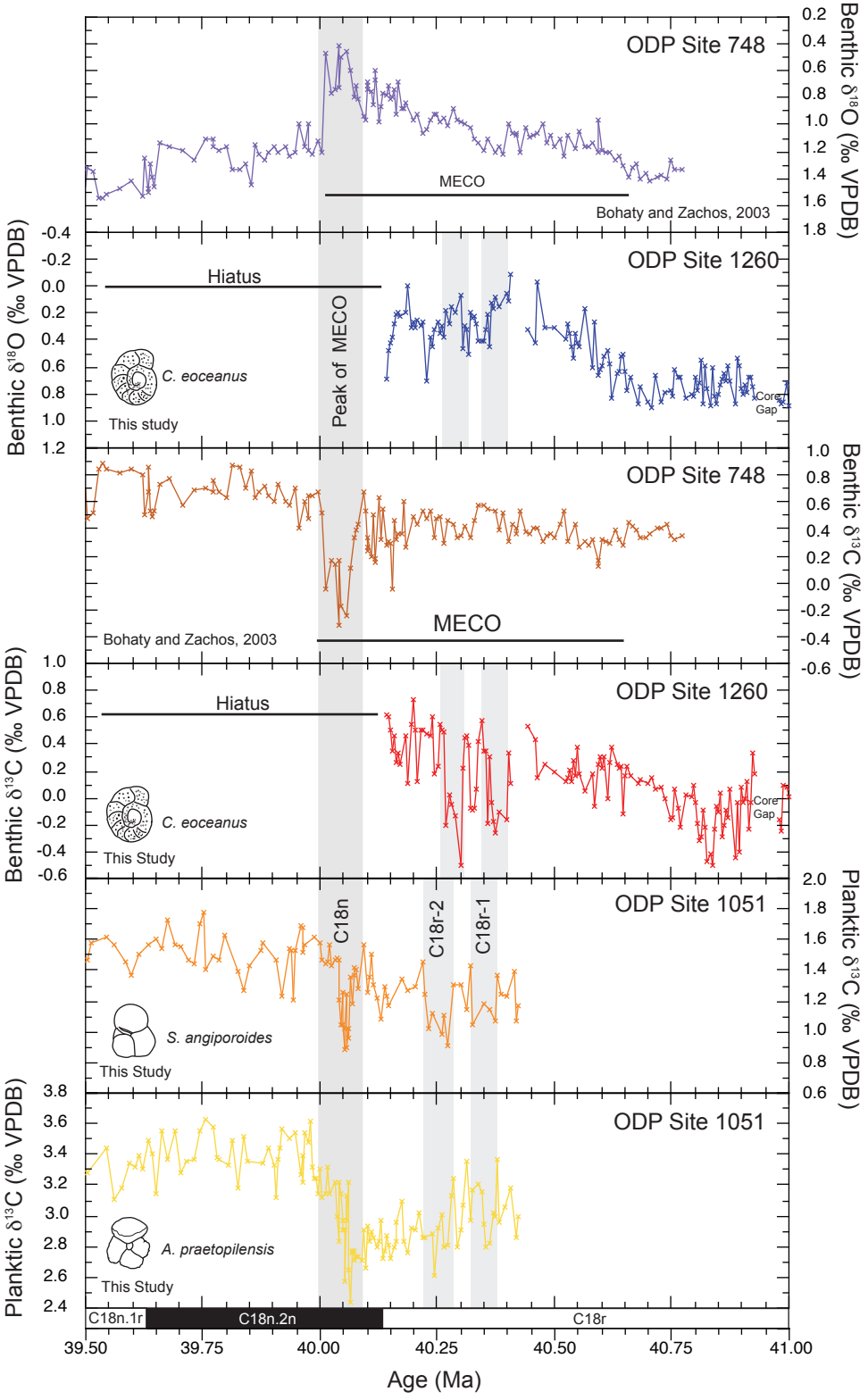

FIGURE 7.6: Transient carbon cycle perturbations superimposed on the MECO. Stable isotope records generated at ODP Sites 1051 and 1260 reveal the existence of two hitherto unreported negative δ^{13}C excursions during the MECO in magnetochron C18r at 40.4 and 40.3 Ma and henceforth are labeled C18r-1 and C18r-2. A third δ^{13}C excursion is recorded in the base of magnetochron C18n.2n at ~4.0 Ma at Site 1051 and is correlative to a negative δ^{13}C excursion recorded in δ^{13}C records from ODP Site 748 (Bohaty and Zachos, 2003). Benthic stable isotope records are corrected to equilibrium calcite using Katz et al. (2003).

TABLE 7.2: Dominant planktic foraminiferal genera in assemblages at ODP Site 1051. Genera counted in study comprise over 90% of the planktic foraminiferal assemblage at any one time. All other planktic foraminifera were counted as 'planktic other' with the exception of the biostratigraphic marker species *Orbulinoides beckmanni* which was also counted but typically comprised ≤3% of the total planktic foraminiferal assemblage.

Genera	Pre-MECO	MECO	Post-MECO
% *Acarinina*	52.3	22.3	15.6
% *Subbotina*	13.6	13.0	14.6
% *Morozovelloides*	10.4	9.9	1.5
% *Globigerinatheka*	8.7	27.6	31.7
% *Turborotalia*	4.9	18.3	27.8
% *Hantkenina*	2.7	3.6	0.8
% Total	91.6	94.7	92.1

evenness of the assemblage prior to the peak of the MECO. The *Hantkenina* and the *Radiolaria* have a relative abundance maxima prior to the peak of the MECO but have relatively low abundances (or are absent) across the peak and recovery of the MECO. The *Turborotalia* increase in relative abundance during the MECO and remain high for the remainder of the study interval. (4) Significant increases and decreases occur in the relative abundances of several of the surface dwelling taxa at the peak of the MECO in the base of magnetochron C18n.2n. Coincident with the peak of the MECO and the lightest δ^{13}C values is an abundance minimum in the large acarininids concomitant with an abrupt increase in the relative abundance of *O. beckmanni*. There are no significant changes in equitability values during this interval. (5) Following the peak of the MECO the relative abundance of the *Morozovelloides* decreases abruptly coincident with recovery of the *Acarinina*. (6) The remainder of the study interval is characterised by relatively stable foraminiferal assemblage.

While the overall pattern of assemblage change is very similar prior to and across the onset of the MECO at the two sites, there are a number of differences in both the assemblage composition and foraminiferal response. First, the stratigraphic FO of *O. beckmanni* occurs in the base of magnetochron C18r (∼41.0 Ma) at Site 1260 but occurs ∼500 kyrs later in the top half of magnetochron C18r at Site 1051 (see Chapter 6 for further details). Second, at Site 1260 the *Morozovelloides* and *Globigerinatheka* increase in relative abundance approximately coincident with one another but at Site 1051 the two are decoupled and the rise in the globigerinathekids is not accompanied by an increase in the *Morozovelloides*. Third, increases in the relative abundances of the *Morozovelloides* and *Globigerinatheka* at Site 1260 precede the onset of the MECO defined by the bulk of the shift in benthic foraminferal δ^{18}O values (Fig. 7.8). Fourth, the timing of the major changes in abundance are offset from one another based on the age models currently available for the two sites (see Fig. 7.9). Fifth, there is a higher relative abundance of turborotaliids at Site 1260 prior to the MECO compared to Site 1051. Finally, the

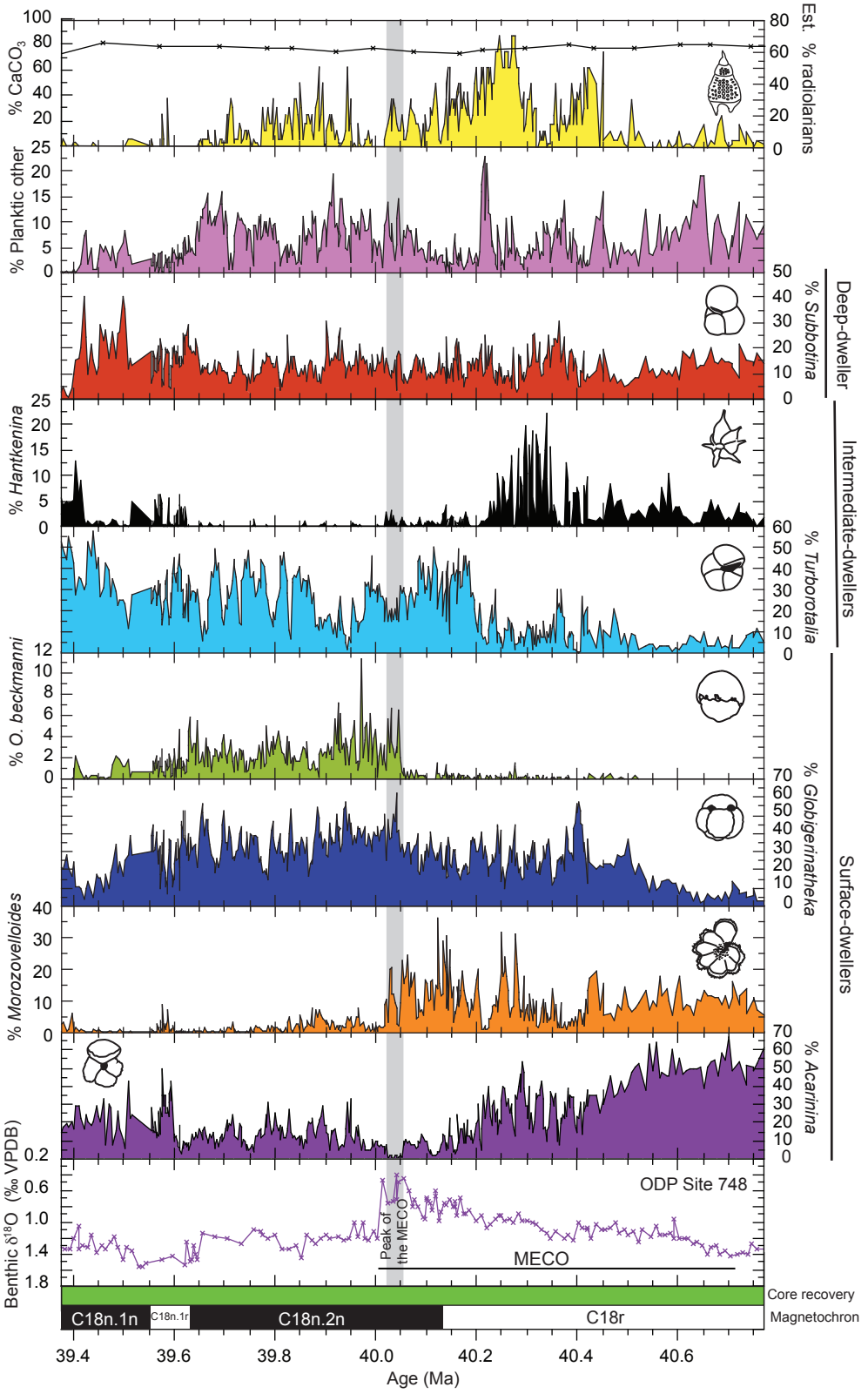

FIGURE 7.7: Compositional changes in the planktic foraminiferal assemblage across the MECO at ODP Site 1051. Schematic representations of each genera illustrated. Surface, intermediate and deep refers to the relative position in the water column that genera are thought to have occupied based on stable isotope studies, morphology and ecology (Pearson et al., 2001; Sexton et al., 2006a). Oxygen isotope stratigraphy from ODP Site 748 (Bohaty and Zachos, 2003) shown on revised agescale determined in this study (Fig. 7.4). Wt% $CaCO_3$ from Shipboard Scientific Party (1998). Core recovery indicated by green bar.

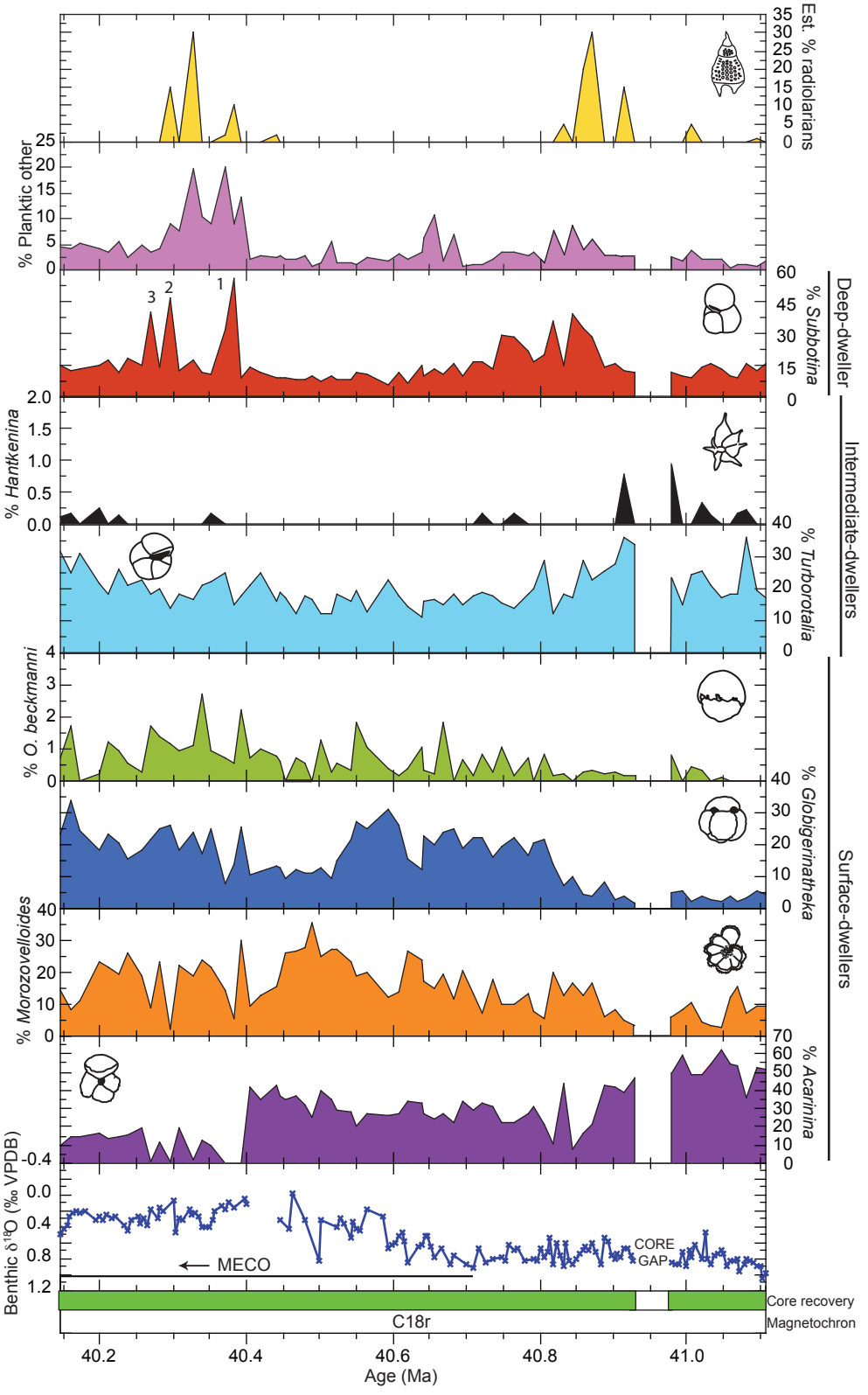

FIGURE 7.8: Relative abundance records for planktic foraminifera at ODP Site 1260. Peaks in the relative abundance of *Subbotina* labelled 1 - 3 are coincident with clay rich horizons, see Figure 7.5. Schematic representations of each genera counted illustrated. Core recovery indicated by green bar. Surface, intermediate and deep refers to the relative position in the water column that genera are thought to have occupied based on stable isotope studies, morphology and ecology (Pearson et al., 2001; Sexton et al., 2006a).

hantkeninids and radiolarians are virtually absent throughout the entire study interval at Site 1260 in contrast to Site 1051.

To help extract the dominant signals associated with the MECO, principal component analysis (PCA) was performed on each of the planktic foraminiferal datasets. PCA of the datasets reveals that ≥87% of the total variance in both of the datasets can be explained by just a few principal components (Tables 7.3 and 7.4). High loadings on *Acarinina* in the first principal component at Sites 1051 and 1260 accounts for ∼50% of the total variance in the datasets (Tables 7.3 and 7.4) thus, the decline in relative abundance of the *Acarinina* is the dominant signal associated with these assemblages during the MECO At Site 1051, high loading of *Acarinina* is accompanied by intermediate negative loading for *Turbortotalia* illustrating the opposite trends shown by these genera prior to and across the onset of the MECO. The dominant components for the second and third principal components differ between the two sites because the assemblage record from Site 1260 is half the length of that at Site 1051 and does not cover the peak of the MECO or post-MECO interval. At Site 1051 the second principal component shows a high positive loading for *Globigerinatheka* and intermediate negative loading for *Turborotalia* indicating the opposite behaviour of these genera at the beginning and end of the assemblage record. Whereas, at Site 1260 the second principal component shows intermediate negative loadings for *Globigerinatheka* and *Morozovelloides* reflecting the similar long term (∼800 kyrs) behaviour of these two genera and positive loading for *Subbotina* indicating the opposite behaviour of these two groups. At Site 1051, the third principal component shows a high negative loading for *Morozovelloides*. At Site 1260, the third principal component shows high positive loading on *Globigerinatheka* and negative loading on *Morozovelloides* because of the covarying behaviour of these two genera on short timescales (≤100 kyrs).

TABLE 7.3: Loadings of planktic foraminiferal genera onto the first three principal components in the analysis of relative abundance data from ODP Site 1051. % variability refers to the percentage of the variation in the data explained by each of the principal components. Values in the table are 'loadings', these represent the relationship between the principal components and the original variables. Highlighted loadings represent the variables that contribute most strongly to the variance.

	Principal component loadings		
Genera	PC1	PC2	PC3
Subbotina	0.040	-0.132	0.193
Hantkenina	-0.267	0.032	-0.064
Turborotalia	**0.569**	**-0.596**	-0.267
Orbulinoides	0.203	0.087	0.174
Globigerinatheka	0.284	**0.712**	0.123
Acarinina	**-0.621**	-0.293	0.335
Morozovelloides	-0.310	0.159	**-0.855**
Variability	49%	18%	15%

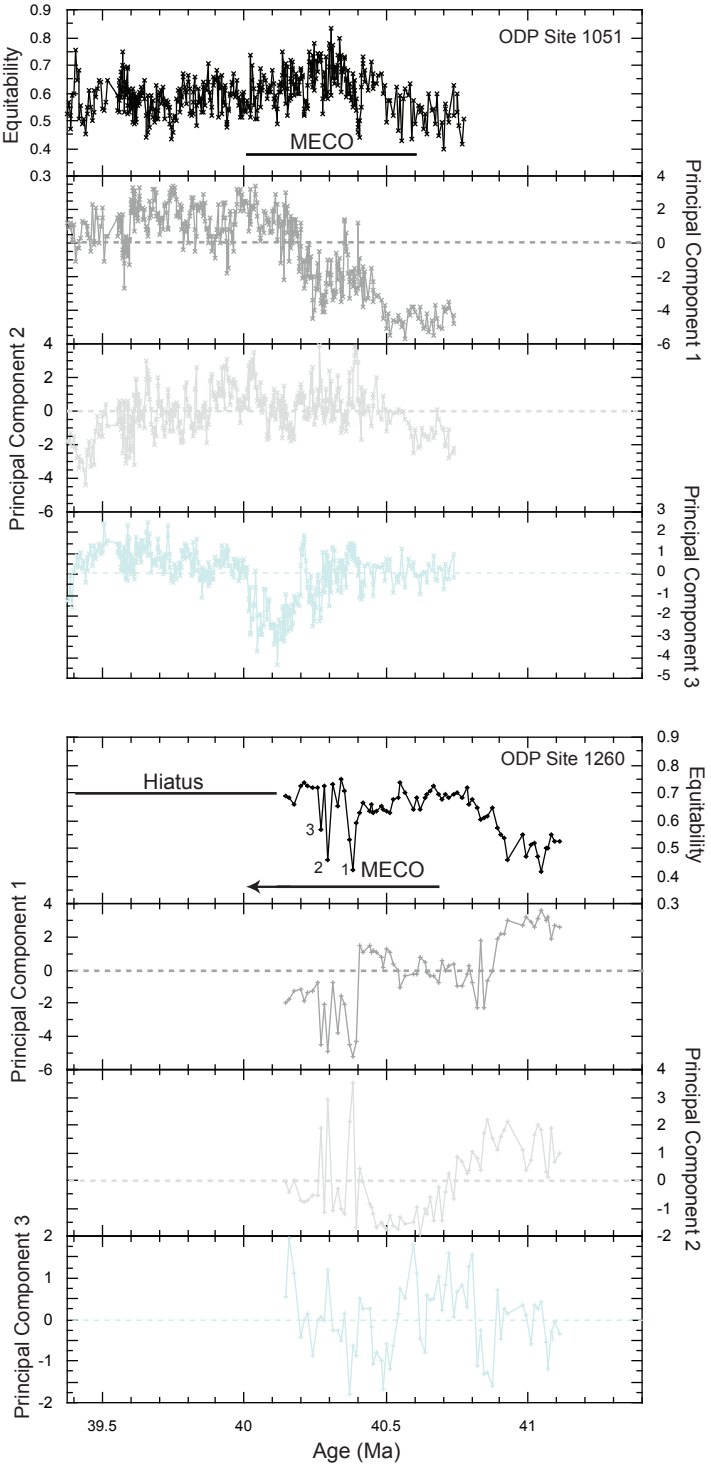

FIGURE 7.9: Sample scores along principal component (PC) axes and equitability for ODP Sites 1051 and 1260. Equitability describes the evenness with which abundance is distributed amongst the different genera, e.g., Pre-MECO samples have low equitability values because they are dominated by the genus *Acarinina*. Note the similarity between PC1 shown here and the relative abundance of *Acarinina* in Fig. 7.7. During the MECO equitability values become higher and reach peak values as the *Acarinina* decrease in abundance and other taxa increase in abundance. The shift to higher equitability values occurs at ∼40.9 Ma at Site 1260 and ∼40.5 Ma at Site 1051. Equitability values remain relatively stable (∼0.6) from several hundred kyrs prior to the peak of the MECO and throughout the post-MECO interval indicating little change in the evenness of the assemblage.

TABLE 7.4: Loadings of planktic foraminiferal genera onto the first three principal components in the analysis of relative abundance data from ODP Site 1260. % variability refers to the portion of the total variation explained by each of the principal components. Values in the table are 'loadings', these represent the relationship between the principal components and the original variables. Highlighted loadings represent the variables that contribute most strongly to the variance.

	Principal component loadings		
Genera	PC1	PC2	PC3
Subbotina	-0.281	**0.555**	-0.114
Hantkenina	0.019	0.036	0.043
Turborotalia	0.039	0.181	0.122
Orbulinoides	-0.101	-0.088	0.067
Globigerinatheka	-0.398	**-0.469**	**0.715**
Acarinina	**0.858**	-0.144	0.207
Morozovelloides	-0.119	**-0.640**	**-0.641**
Variability	58%	24%	9%

Plots of individual sample scores along these principal components for Sites 1051 and 1260 (Figs 7.10 and 7.11) demonstrate the presence of several closely spaced 'clusters' comprised of stratigraphically adjacent samples that reflect the gradual evolution of the assemblage. At Site 1260, two distinct clusters occur distinct from the main foraminiferal assemblage (Fig. 7.11). Closer inspection of the samples that comprise these clusters indicate that these samples fall within clay-rich horizons at Site 1260, in magnetochron C18r at ∼40.25, 40.30 and 40.40 Ma (Fig. 7.5) and correspond to abrupt short-lived changes in the faunal assemblage, negative δ^{13}C excursions (C18r1-2 and C18n on Fig. 7.6) and abrupt decreases in equitability (Fig. 7.9). Within the assemblage, the clay-rich horizons correspond to abrupt increases in the relative abundance of the genus *Subbotina* (labeled 1-3 in Fig. 7.8) coincident with abrupt short-lived decreases in the abundance of *Morozovelloides, Acarinina* and *O. beckmanni*. This finding is consistent with the hypothesis that dissolution has modified the planktic foraminiferal assemblage at Site 1260 within the clay-rich layers, with dissolution susceptible forms particularly the *Morozovelloides* being preferentially removed. Previous studies have also documented that it is the warm mixed-layer dwellers that are frequently the first to be removed from assemblages by dissolution rather than the more heavily calcified deeper dwelling forms (Savin et al., 1975; Erez, 1979; Wu and Berger, 1989). Although, this is not consistently the case (Petrizzo, 2007).

7.2.4 Cyclicity in planktic foraminiferal abundance patterns

In addition to the longer term trends in planktic foraminiferal relative abundance that are described above, the high resolution abundance record shown in Figure 7.7 shows evidence of genera abundances fluctuating in a quasi-periodic manner around longer term

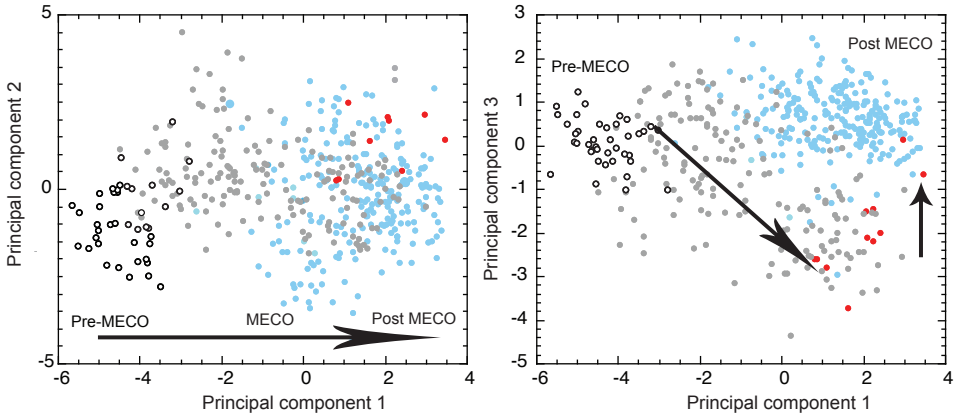

FIGURE 7.10: Distribution of sample scores from ODP Site 1051 along the first three principal component axes. These axes alone account for over 87% of the faunal variation in the dataset. Black open circles = Pre-MECO samples, Solid grey circles = MECO samples, Solid red circles = Peak of the MECO samples and solid blue circles = Post-MECO samples. Black arrows indicate the direction in which the assemblage develops.

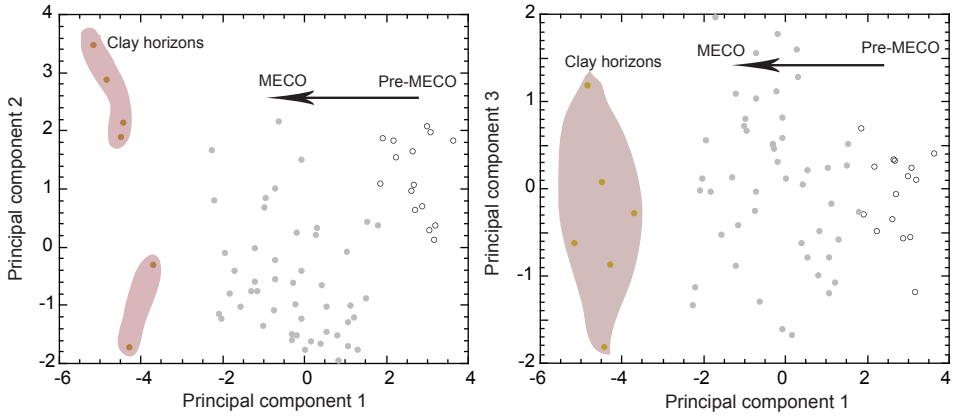

FIGURE 7.11: Distribution of sample scores from ODP Site 1260 along the first three principal component axes. These axes alone account for 91% of the faunal variation in the dataset. Two major clusters, corresponding to Pre-MECO (open black circles) and MECO (solid grey circles) assemblages can be distinguished among the samples. The clusters labeled 'clay horizons' represent samples where dissolution has overwritten the original faunal composition.

mean values. This variability differs between genera in both its amplitude and apparent duration. Spectral analysis of this data set (Fig. 7.12) reveals spectral peaks in the dominant genera, e.g., *Acarinina, Turborotalia, Morozovelloides* and *Globigerinatheka*, that generally fall between the 40 and 29 kyr obliquity cycles with average durations of ∼29 - 31 kyrs and ∼35 - 38 kyrs. Higher frequency cyclicities observed are generally a few thousand years shorter than the 19 kyr precession cycle. None of the taxa in this study show significant peaks with frequencies similar to eccentricity. The radiolarians show significant peaks in the precessional band. Slight offsets in the estimated cycle duration from expected orbital frequencies probably reflects assumptions of constant sedimentation rates between widely spaced magnetic datums in the age model employed

(see Chapter 5).

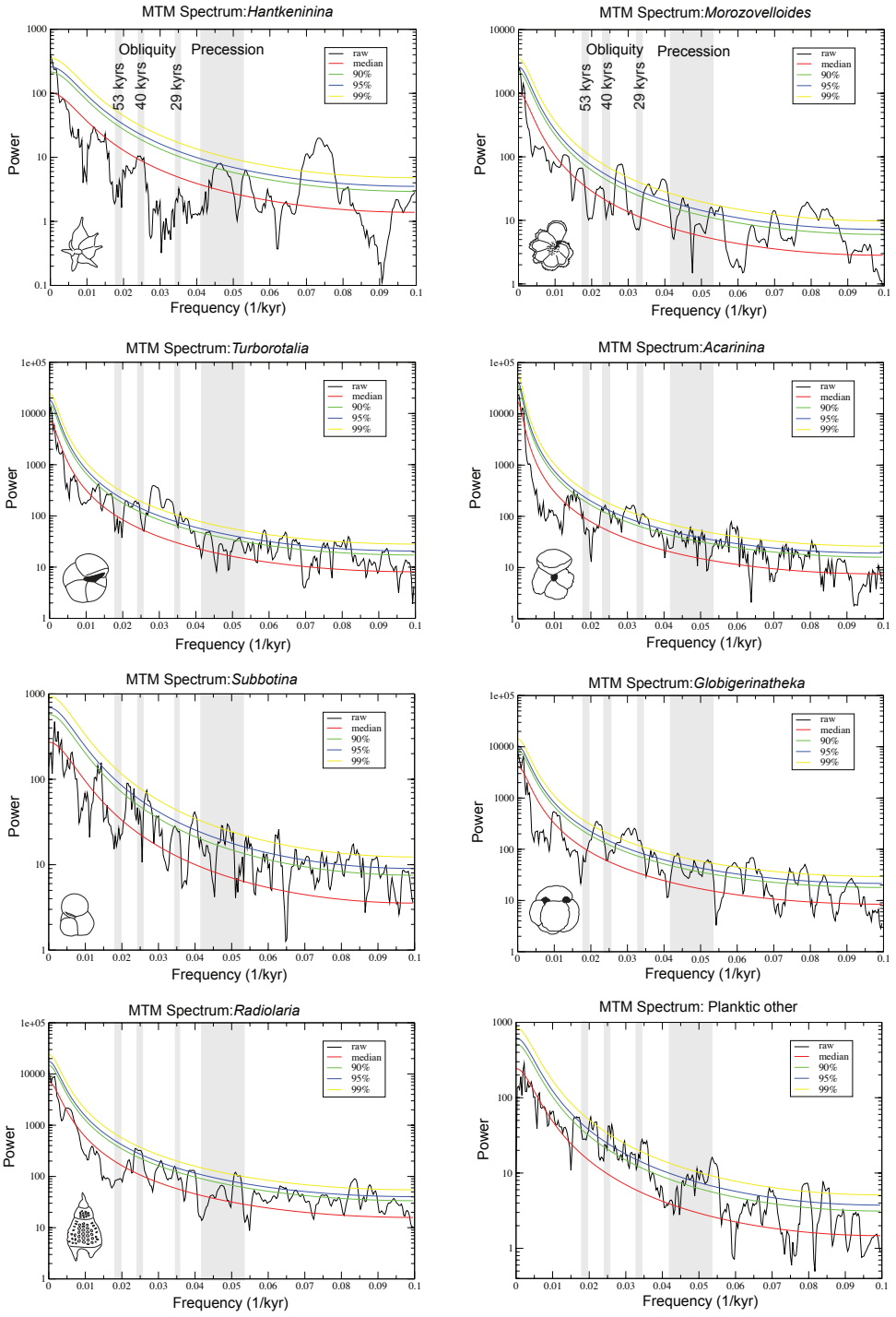

FIGURE 7.12: Spectral analysis (multitaper method) of planktic foraminiferal relative abundance records from ODP Site 1051. Settings - resolution = 2, tapers = 3. Grey shaded areas indicate frequencies that correspond to obliquity and precessional cyclities.

7.3 Discussion

7.3.1 Environmental significance of planktic foraminiferal assemblage variations during the MECO

All of the taxa investigated in this study are extinct thus, interpretations of palaeoecology are deduced from the palaeobiogeography of taxa, stable isotope compositions of foraminferal tests and by analogy to modern species where appropriate. In Table 7.5 the palaeoecologies of key Middle Eocene genera that occur across the MECO are summarised. Palaeoecological affinities of genera are then used to infer palaeonvironmental changes in surface waters from the biotic shifts observed in the dataset. Similarities in the planktic foraminiferal assemblage response and composition before and during the MECO between Sites 1051 and 1260 imply that similar biotic responses and palaeoenvironmental shifts occurred in the open ocean throughout the (sub)tropical Atlantic. Overall, the pattern of environmental change across the MECO inferred from planktic foraminiferal assemblages suggests a shift from warm, oligotrophic surface waters to warmer, more mesotrophic conditions (Fig. 7.13).

Prior to the MECO, the assemblage is dominated by *Acarinina* a characteristic component of most mid-low latitude assemblages in the Middle Eocene (Keller, 1982, 1983; Boersma et al., 1987) and inferred to favour warm, oligotrophic surface water environments (see Table 7.5). Warm, nutrient depleted background conditions prior to the onset of the MECO (Fig. 7.13a) are supported by low relative abundances of the cooler water-favouring planktic foraminifera genera, *Turborotalia* and *Subbotina*, and radiolaria at both sites (see Table 7.5). By analogy to the modern ocean (Ravelo and Fairbanks, 1992; Andreasen and Ravelo, 1997), the dominance of photosymbiotic foraminifera ($\geq$70%) in the assemblage at these sites may also indicate a lack of seasonal variation in nearsurface hydrography, i.e. stable mixed layer, and the presence of a deep nutrient depleted mixed layer.

During the early stages of the MECO, the warm water-favouring genera *Morozovelloides*, *Globigerinatheka* and *Hantkenina* (Table 7.5) exhibit increasing abundances inferred to reflect gradual warming of surface-waters (Fig. 7.13b). The accompanying increase in equitability, i.e., the evenness of the assemblage (Fig. 7.9), may represent increased ecological niche availability at this time (Fig. 7.13b) consistent with inferred warming. At Site 1260, where a high resolution stable isotope stratigraphy is available, the increase of the warm-water genera *Morozovelloides* and *Globigerinatheka* precedes the onset of the MECO and inferred bottom water warming by $\sim$200 kyrs (Fig. 7.8) suggesting that surface and bottom water warming, at least at this site, were decoupled from one another or that another environmental variable such as nutrient availability was more important in controlling foraminiferal abundances than generally recognised. In contrast to the apparent warming inferred by other warm-water favouring genera (Table 7.5),

Genus	Palaeoecology
Acarinina	Mixed layer dweller[1−5]. Photosymbiotic[2,3,7] genus based on test size related variations in δ^{13}C similar to modern photosymbiotic taxa[3]. Larger tests host to more symbionts and thus, greater fractionation by symbionts [7,8]. Photosymbiosis considered adaptation to nutrient depleted water masses[3,9,10]. Inferred photosymbiotic taxa show similar diversity trends in the Palaeogene to inferred oligotrophic benthic foraminifera[10]. *Acarinina* are inferred to prefer warm and oligotrophic surface waters. One of dominant taxa in Late Palaeocene through Middle Eocene low and mid-latitude assemblages[11−15].
Globigerinatheka	Mixed layer dweller[1,2,4,5]. Probably photosymbiotic, no published stable isotope data currently available with ecology similar to the modern photosymbiotic genus *Globigerinoides*[16]. Globigerinathekids cosmopolitan but most common at mid-to-low latitudes[1,16]. Several species have highest abundances at high latitude, e.g., *G. index* and *G. subconglobata*[1,16,17]. Often found in high abundances at gyre margins characterised by eutrophic conditions and vigorous current flow but not always with high radiolarian abundances thus, assumed that high current vigour is favourable similar to modern globoquadrinids[17].
Hantkenina	Gradual shift in preferred depth habitat from cold, deep possibly sub-thermocline waters[1,4,18] associated with eutrophic conditions in the early Middle Eocene to near surface, oligotrophic waters in the Late Eocene. Change in ecology accompanied by change in morpohology of genus from elongate chambers with tubulospines to more globular chambers with tubulospines[18].Nearly all species are restricted to the low latitudes[11,19]. Not found at high latitudes except for brief intervals in the Eocene that may reflect global warming events[19]. Asymbiotic genus[18].
Morozovelloides	Mixed layer dweller[1−5]. Photosymbiotic genus based on test size related variation in δ^{13}C similar to modern photosymbiotic taxa[3,6,20]. Restricted to (sub)tropics[21]. Used as warm water indicator. Highly ornamented test morphology typical of low latitude forms, considered an ecological specialist[1,17]. Similar to Late Palaeocene and Early Eocene genus *Morozovella* which dominates low latitude assemblages[13,14,22].
*Orbulinoides**	Palaeoecology poorly constrained, no published stable isotope data. Found at tropical and warm mid latitudes (Fig. 6.4). Diachronous first occurrence (see Chapter 6) also implies sea surface temperature control on distribution. Shows similar pattern of abundance change to the globigerinathekids (Fig. 7.7). Inferred to occupy similar ecological niche by analogy to its ancestors the globigerinathekids.
Subbotina	Cosmopolitan, deep thermocline dwelling taxa [1,2,4,5,24]. Dominates high latitude assemblages in the Late Palaeocene to Middle Eocene[1,1116,25]. Most abundant in cooler and more eutrophic waters[1,11,13,25,26]. Asymbiotic genus [2,3].
Turborotalia	Upper thermocline habitat[2,4,5,24]. Cosmopolitan, abundant in low to mid-latitude assemblages[1]. Probably adapted to more eutrophic waters. Asymbiotic genus [20].
Radiolaria	Highest abundances in eutrophic, upwelling water masses[27,28]. In the absence of carbonate dissolution in deep sea sediments, likely reflects an increase in biosiliceous productivity.

TABLE 7.5: Palaeoecology of selected Middle Eocene genera. *Orbulinoides** is a monospecific genus comprising only *O. beckmanni*. 1) Boersma et al. (1987) , 2) Pearson et al. (1993), 3) Norris (1996), 4) Pearson et al. (2001), 5) Sexton et al. (2006b), 6) D'Hondt et al. (1994), 7) Spero and Williams (1988), 8) Spero (1992), 9) Hallock (1985), 10) Hallock et al. (1991), 11) Berggren (1978), 12) Boersma and Premoli-Silva (1983), 13) Premoli-Silva and Boersma (1989), 14) Kelly et al. (1996), 15 Pearson et al. (2006), 16) Premoli-Silva et al. (2006), 17) Premoli-Silva and Boersma (1988), 18) Coxall et al. (2000), 19) Coxall and Pearson (2006), 20) Wade et al. (2007), 21) Pearson and Berggren (2006), 22) Petrizzo (2007), 23) Berggren et al. (1995), 24) Poore and Matthews (1984), 25) Kelly (2002), 26) Keller (1982), 27) Scopelliti et al. (2004), 28) Armstrong and Brasier (2005).

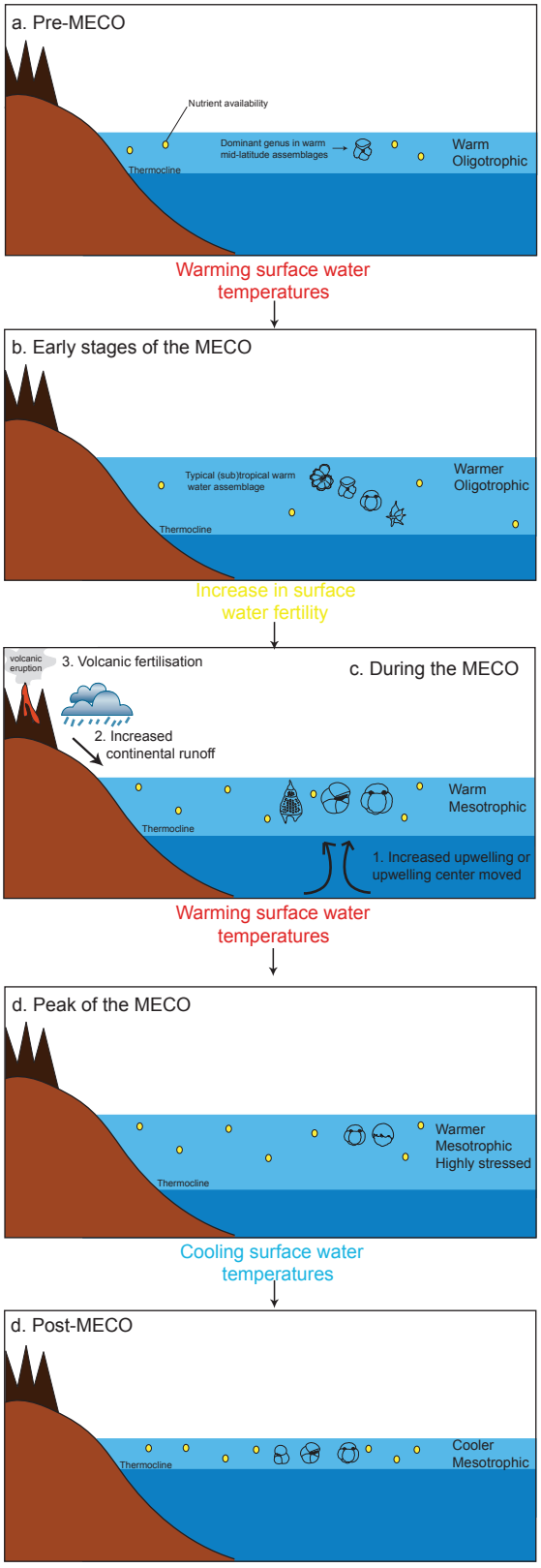

FIGURE 7.13: Environmental reconstruction for the MECO based on biotic shifts. Schematic illustration of taxa used to infer palaeoenvironmental changes during the MECO, for identification see Figure 7.7). Solid yellow points represent nutrient availiabilty in surface waters, i.e., the higher the number of points = higher fertility. a) Warm, oligotrophic surface waters inferred prior to the MECO. b) Inferred surface water warming and expansion of the warm mixed layer. c). Biotic shift implies an increase in surface water fertility. Possible mechanisms that could increase surface water fertility are shown and discussed in Section 7.4.3. d) Short-lived rapid warming inferred during the peak of the MECO. e) Rapid cooling of surface waters inferred following the MECO.

the acarininids show a *decrease* in abundance suggesting that some aspect of *Acarinina* palaeoecology was not favoured by increasing surface water temperatures inferred for the MECO (see Section 7.3.3 for further discussion). Certainly, the acarininids appears to have found environmental conditions unfavourable because they decline in abundance in the low (herein) and mid latitudes (Nocchi et al., 1988) and also appear to undergo a size reduction, both features observed during a number of other global warming events in the Late Cretaceous and Cenozoic (Kelly, 2002; Abramovich and Keller, 2003; Keller, 2005).

Between $\sim$ 40.15 and 40.25 Ma, the pattern of environmental change is more complex. The warm-water indicators, the *Morozovelloides* and *Hantkenina*, show no further increase in abundance and a decline, respectively, at the same time as short-lived increases in the abundance of the cool, eutrophic surface water indicators (Table 7.5), the radiolaria and the *Dentoglobigerina* (included in planktic other), and a longer-term increase in *Turborotalia* (Fig. 7.7). Given the relatively high abundance of the warm, mesotrophic genus *Globigerinatheka*, an increase in surface water nutrient availability rather than cooling during the MECO explains the biotic pattern (Fig. 7.13c). Superimposed on the shift to more mesotrophic conditions is a brief ($\leq$100 kyrs) interval of more 'extreme' conditions during which there may have been cooling as well as elevated nutrients in surface waters accompanied by a reduction in watermass stratification as evidenced by the transient rise in the radiolarians and deeper-dwelling planktic foraminifera. The overall inferred shift to more fertile surface waters during the MECO would also have been detrimental to the *Acarinina* and compounded the environmental stress already observed during inferred initial surface water warming, and perhaps contributed to the decline of the acarininids from their pre-MECO abundances.

The peak of the MECO between $\sim$40.02 and 40.06 Ma (Fig. 7.7), is accompanied by an abrupt assemblage change amongst the shallow mixed-layer dwelling foraminifera (Fig. 7.7), *Acarinina, Globigerinatheka* and *Orbulinoides beckmanni*. The ecological affinities of *O. beckmanni* are not well known but currently a number of lines of evidence (Table 7.5) indicate an affinity for warm surface waters. The coupled increases in *O. beckmanni* and *Globigerinatheka* relative abundance may therefore reflect an increase in sea surface temperatures at the peak of the MECO and/or increased ecological space availability again linked to possible warming. The coincident relative abundance increases in *O. beckmanni* and *Globigerinatheka* also suggests that these genera were able to thrive in warm, mesotrophic surface waters. The acarininids reach their minimum abundances during this interval of inferred peak warmth.

Following the MECO, the abrupt decline in the abundance of the warm-water genus *Morozvelloides* (Table 7.5) at $\sim$40.0 Ma is inferred to indicate rapid ($\leq$10 kyrs) cooling of surface waters (Fig. 7.13e). This interpretation is consistent with the subsequent return of the large acarininids, perhaps excluded from the assemblage during the peak

of the MECO at Site 1051, and indicating that surface-water conditions once again became favourable. A rapid drop in sea-surface temperatures in planktic foraminiferal biozone E12 is also consistent with other low-resolution planktic foraminiferal studies that demonstrate abrupt faunal changes to cooler-water taxa in the South Atlantic and Indian Oceans (Keller, 1982). Subsequent increases in the percentage of the cool water-favouring intermediate and deep-dwelling genera (Table 7.5), the subbotinids and turborotaliids, around 39.6 Ma are coincident with further decline in the percentage of the warm water taxa in the assemblage, e.g., the globigerinathekids and *O. beckmanni*, (Fig. 7.7) implying continued cooling of surface waters. Decreasing sea-surface temperatures following the MECO may have been accompanied by shoaling of the thermocline and decreasing water column stratification, detrimental to mixed layer-dwelling foraminifera by reducing habitat and niche availability.

Overall, the pattern of change observed in the dominant foraminiferal genera illustrate similarities across the MECO at low latitudes regions in the Atlantic Ocean. In terms of inferring a global biotic patterns at the MECO, outside of the low latitudes it is perhaps reasonable to expect that faunal assemblages will also respond to changes in ocean temperature during the MECO, but to varying amounts depending on latitude, i.e., largest biotic response to warming expected at higher latitudes, and that those biogeographic shifts inferred herein could be tracked. Low abundance of the warm water-favouring genera *Acarinina* and *Morozovelloides* during the MECO observed in this study is inferred to represent the migration of these genera to higher latitudes as the surface ocean warmed and (sub)tropical regions likely expanded to higher latitudes. Equally, abrupt cooling following the MECO was presumably accompanied by the equatorward contraction of these same zones. This inferred pattern of expansion and contraction of (sub)tropical biogeographic provinces is similar to that observed for other global warming events such as the PETM (Kelly et al., 1996; Kelly, 2002; Gibbs et al., 2006; Petrizzo, 2007) and during the Cretaceous (Abramovich and Keller, 2003; Keller, 2005).

7.3.2 Evidence for surface water warming during the MECO

The overall interpretation here of surface water warming at Sites 1051 and 1260 during the MECO is supported by faunal assemblage changes and stable isotope signals at other sites. First, the invasion of the warm water favouring taxa *Hantkenina alabamensis* and *Acarinina spinuoinflata* in magnetochron C18r at ~40.5 Ma has been recorded at ODP Site 1090, 44°S in the South Atlantic (Galeotti et al., 2002). Second, warm temperatures during E12 are inferred from the widespread deposition of carbonate shelf facies, the southward migration of tropical taxa and the presence of large and abundant *Morozovelloides* and *Globigerinatheka* in assemblages in the Indo-Australasian region (McGowran, 1977; McGowran et al., 1997). Third, incursions of the tropical genus *Hantkenina* to high northern latitudes (≥50°N) have been documented towards the top

of calcareous nannofossil biozone NP16 in the top half of magnetochron C18r (Shipboard Scientific Party, 1987).

Somewhat paradoxically, the planktic foraminiferal $\delta^{18}O$ records generated herein at Site 1051 (Fig. 7.3) show an increase in $\delta^{18}O$ suggesting at least 2°C of surface water *cooling* during the MECO (assuming that half of the $\delta^{18}O$ signal accounts for the loss of small continental ice sheets from Antarctica at this time). This contrasts with existing bulk stable isotope records across the same interval (Bohaty and Zachos, 2003; Spofforth et al., 2008; Ivany et al., 2008), including the original records which inferred surface-water warming (Bohaty and Zachos, 2003). On the one hand, this discrepancy could be explained by the presence of diagenetically altered foraminiferal calcite, i.e., shifting foraminiferal calcite to heavier $\delta^{18}O$ values. In fact, at Site 1051 the shift towards heavier $\delta^{18}O$ values in the MECO is coincident with an interval of anomolously heavily calcified planktic foraminifera supporting this hypothesis (Fig. 7.4). However, this hypothesis is inconsistent with an unpublished bulk $\delta^{18}O$ record generated at Site 1051 (S. Bohaty, written pers. comm., 2007) which implies surface water warming and is more in-keeping with published stable isotope records (Bohaty and Zachos, 2003; Spofforth et al., 2008; Ivany et al., 2008). This finding raises the question - why are stable isotope records recording surface-water changes at ODP Site 1051 decoupled from one another?

7.3.3 Photosymbiosis and *Acarinina* during the MECO

Acarinina is a well established mixed layer dweller that is inferred to be a strongly photosymbiotic taxa (see Table 7.5) this palaeoecological interpretation is supported by the range of stable isotope values generated for *Acarinina praetopilenis* in this study (Fig. 7.14). [Note that if the $\delta^{18}O$ of planktic foraminiferal tests at Site 1051 are overprinted by secondary calcite this would only lead to heavier $\delta^{18}O$ values and therefore an underestimation of surface water temperatures and a deepening of the acarininids depth ranking in the water column]. At Site 1051 the decrease in the relative abundance of the large acarininids is coincident with a shift to more negative $\delta^{13}C$ values in *A. praetopilensis* across the MECO (Fig. 7.15). In contrast, all other existing $\delta^{13}C$ records, derived in benthic and planktic foraminiferal calcite and bulk sediment, available across this interval show a trend towards more positive $\delta^{13}C$ values during the MECO, e.g., this study (Fig. 7.3), Southern (Bohaty and Zachos, 2003) and Tethyan Oceans (Jovane et al., 2007; Spofforth et al., 2008).

One hypothesis for this observation is that at Site 1051 the apparent reduction of the $\delta^{13}C$ gradient in the water column (Fig. 7.3) may reflect a decrease in the efficiency of the biological pump across the MECO, i.e., reduced primary productivity and carbon cycling in the deep ocean. A decrease in primary productivity during the MECO is inconsistant with biotic evidence for increased surface water fertility at this time (Section 7.3.1). Alternatively, a shift to progressively lighter $\delta^{13}C$ values during the MECO by

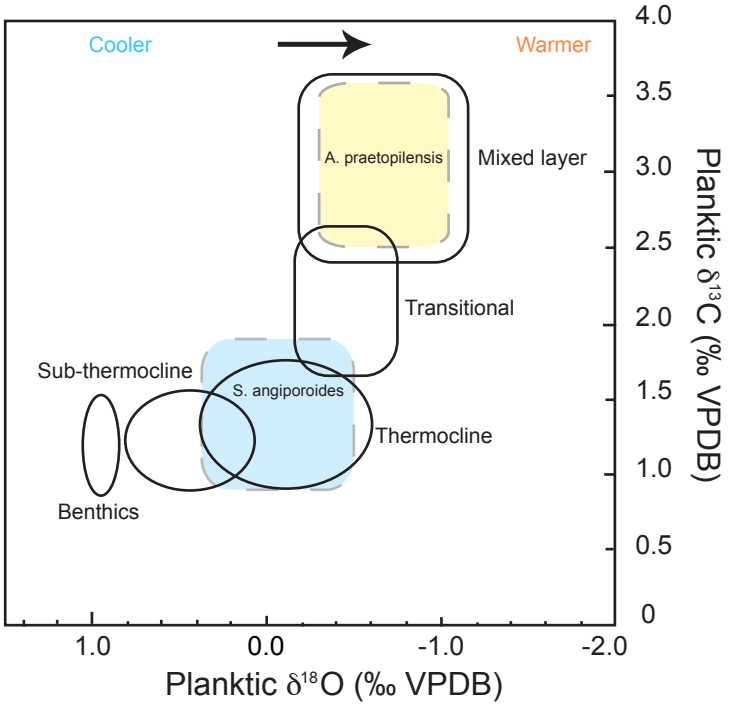

FIGURE 7.14: Model for the interpretation of the palaeoecology of planktic foraminifera in the Middle Eocene (modified from Sexton et al. (2006b)). Shaded areas represent the range of δ^{18}O values recorded by *Acarinina praetopilensis* in yellow and *Subbotina angiporoides* in blue, generated in this study. Stable isotope values are consistent with previous interpretations (Pearson et al., 1993; Sexton et al., 2006b) of these species palaeoecology.

A. praetopilensis may reflect the transient migration of this species to deeper subsurface waters based on depth ranking of stable isotopes in which the heaviest δ^{13}C values are recorded by planktic foraminifera calcifying in surface waters and lighter δ^{13}C values by deeper dwelling foraminifera (Fig. 7.14). However, δ^{18}O values for *A. praetopilensis* are consistent with a surface layer habitat throughout the MECO (Fig. 7.14). The hypothesis favoured here, therefore, is that the *A. praetopilensis* δ^{13}C record can best be explained by the transient loss or inhibition of photosymbiont activity during the MECO. Photosymbionts preferentially take up ^{12}C leaving the ambient water enriched in ^{13}C (Spero and DeNiro, 1987; Spero and Williams, 1988) resulting in the ^{13}C enrichment of the foraminiferal test relative to ambient seawater (Erez, 1978). Thus, a decline in photsymbiotic activity will lead to a reduction in the fractionation of carbon and lighter δ^{13}C values will be recorded in foraminiferal tests. The breakdown of this ecological strategy would have hindered the success of the acarininids by affecting foraminiferal nutrition, reproduction and calcification (Bé et al., 1982). Competition for the same resources with other surface-dwelling genera, particularly the successful globigerinathekids, would have exacerbated this enivronmental stress thereby, accounting for the rapid decrease in relative abundance of the acarininids. Further support for this hypothesis is derived from the large (1.2‰) amplitude of the recovery in δ^{13}C following the negative δ^{13}C

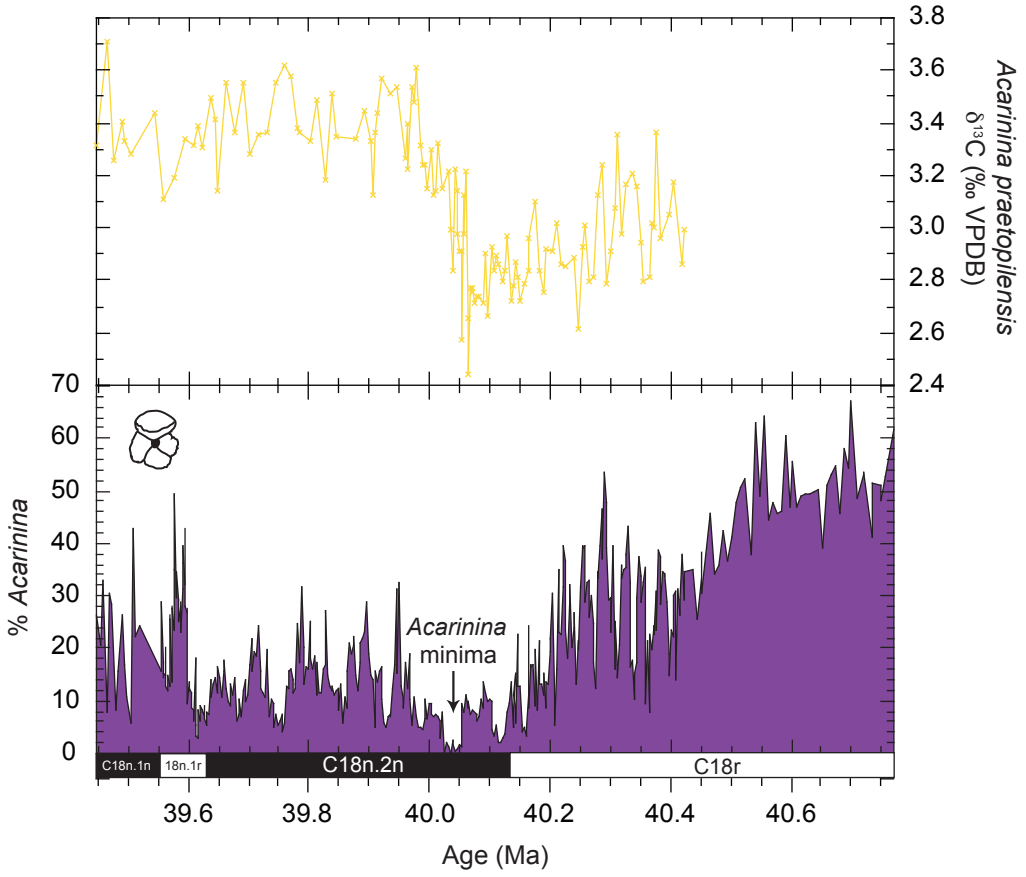

FIGURE 7.15: Correlation between δ^{13}C values and the relative abundance of *Acarinina*.

excursion (labeled C18n in Fig. 7.6) at the peak of the MECO, almost twice the amplitude of the δ^{13}C recovery recorded by *Subbotina angiporoides* (Fig. 7.3). The amplified δ^{13}C signal during recovery from the MECO may reflect both sequestration of isotopically light carbon and recovery of the photosymbiotic relationship. Overamplification of δ^{13}C signal in photosymbiotic planktic foraminifera relative to asymbiotic taxa is also recorded at the PETM (Kennett and Stott, 1991).

The short-term or permanent loss of photosymbionts or 'bleaching' in photosymbiotic organisms, e.g., corals and planktic foraminifera, has been documented both in the modern oceans in response to extremes of temperature (Hallock and Schlager, 1986; Gates et al., 1992; Fitt et al., 2001; Norris, 2007) and eutrophication (Hallock and Schlager, 1986; Edinger and Risk, 1994) in surface waters. Examples of symbiont bleaching can also be found in the geological record. For example, at the PETM, global warming was rapid and severe enough to completely eliminate symbiosis in symbiont bearing planktic foraminifera for a ~40 kyr long interval (Norris, 2007). During the MECO, the onset of the decline in the relative abundance of the acarninids precedes the inferred shift to more nutrient rich surface waters and the acarininid minimum is not associated with

any large shifts in the relative abundance of the eutrophic or cold water favoured taxa (Fig. 7.7). Thus, at the MECO, it is inferred that it is high surface water temperatures that may have promoted bleaching. The loss or decline in photosymbiotic activity in acarininids across the MECO is a relatively straightforward hypothesis to test and will be investigated as part of future work (Section 7.6).

7.3.4 Evolutionary effects of the MECO?

So-called 'excursion' taxa are of interest in evolutionary studies for a number of reasons including determination of the rate of evolutionary response to climatic events and the magnitude or type of event needed to prompt an evolutionary response in the marine plankton. The high-resolution abundance data generated here for *Orbulinoides beckmanni* (a potential 'excursion' taxa) indicates that, while the FO of *O. beckmanni* at Site 1051 appears to occur during the early stages of the MECO, its LO is recorded more than 600 kyrs after the MECO (Fig. 7.7). This finding clearly indicates that *O. beckmanni* is not an 'excursion' taxa although the MECO likely played a role in its biogeographic distribution once it evolved (Chapter 6). To fully evaluate any potential effects of the MECO on the evolutionary response of the planktic foraminifera would require documentation of turnover in individual species beyond the scope of the current study.

In terms of assessing any long-term evolutionary impacts of the MECO on the planktic foraminferal assemblage, the record after the MECO is $\geq$600 kyrs long, sufficient to suggest that the Post-MECO planktic foraminiferal assemblage did not return to its pre-MECO composition. Instead a new assemblage was established characterised by cooler water favouring planktic foraminifera. This pattern of change appears to be superimposed on the long term faunal trend from tropical to subtropical taxa that occurs in the Eocene indicative of a progressive shift to cooler surface waters and rather than being gradual, this transition was comprised of a series of steps accompanied by the successive replacement of tropical flora and fauna by subtropical or temperate species (Kennett, 1977; McGowran, 1977; Berggren, 1978; Keller et al., 1992). The new high-resolution biotic records presented here indicate that rapid cooling at the end of the MECO centered on biozone E12 in the base of magnetochron C18n.2n at approximately 40 Ma may represent one of these cooling 'steps'.

As a final note, one might speculate that the MECO may have had long-term effects on planktic foraminifera by contributing to the extinction of the *Morzovelloides* and the large acarininids. Both the *Morozovelloides* and large acarininids become extinct shortly after the MECO at ~38 Ma, in magnetochron C17n.3n but their abundance began to decline at least 500 kyrs prior to their extinction (Wade, 2004). The extinction of the *Morozovelloides* and *Acarinina* is frequently linked to cooling surface waters in the Late Eocene (Berggren, 1969; Keller, 1983; Boersma and Premoli-Silva, 1991; Keller et al.,

1992; Pearson, 1996), however, more recent studies have demonstrated that the extinction event itself does not coincide with any significant fall in sea surface temperatures (Wade, 2004). An alternative explanation invokes the decline of the photosymbiont relationship either through the expulsion of symbionts or the inhibition of photosynthesis associated with eutrophication and/or the decline of niche availability, which may have been a consequence of cooling sea surface temperatures (Wade, 2004; Wade et al., 2007). The loss of symbionts would remove the *Morozovelloides* competitive advantage in nutrient depleted environments and have led to considerable ecological stress. New data from Wade et al. (2007) document a 1.5 million year deterioration of the photosymbiotic relationship based on a reduction in the δ^{13}C-test size gradient of *Morozovelloides crassatus* between ~39.5 Ma and 38.0 Ma. The abundance of the *Morozovelloides* at Site 1051 decreases in the base of magnetochron C18n.1n at ~40.0 Ma, 500 kyrs prior to the study interval of Wade et al. (2007) suggesting that, the photosymbiotic relationship may have begun to break-down even earlier. Thus, the low abundance of the *Morozovelloides* ($\leq$5%) for at least 600 kyrs after the MECO at Site 1051 may imply that surface water temperatures declined below some critical threshold for the first time following this event below which temperatures were detrimental to the *Morozovelloides* and/or their symbionts. Alternatively, the MECO may have disrupted the foraminiferal ecology sufficiently to promote bleaching eventually leading to the demise of the *Morozovelloides*.

7.4 Mechanisms of palaeoenvironmental change during the MECO

The following section proposes a possible mechanism for global warming during the MECO based on the new data presented in this study and its links to short-term carbon cycle perturbations such as the magnetochron C18r-1 and 2 excursions identified in stable isotope records. Several hypotheses to are also presented to try and explain the inferred increase in the nutrient availability in surface waters that accompanied surface water warming during the MECO.

7.4.1 Mechanisms of global warming during the MECO

Volcanic CO_2 is a powerful driver of climate change on multi-million year (Tarduno et al., 1991; Eldholm and Thomas, 1993; Larson and Erba, 1999) through to decadal timescales (Crowley et al., 1993; Robock, 2000). ODP Leg 165 scientists documented a major episode of explosive volcanism in the Mid- to Late Eocene (~45 to 35 Ma) based on ash horizons found in Caribbean deep sea sediments that have been linked to ignimbrite forming eruptions in Central America and Mexico (Sigurdsson et al., 2000). Thus, the discovery here that there are a number of distinctive ash horizons (and volcanic glass identified in sediments) coincident with the MECO (Fig. 7.3) may imply a

causal link. It is easy to infer from this apparent coincidence that large volumes of CO_2 and other greenhouse gases released during these eruption events may have contributed towards global warming at this time. This is consistent with Bohaty and Zachos (2003) who propose that volcanic degassing of CO_2 may have been one means of driving global warming during the MECO. In fact, volcanically degassed CO_2, from circum-Caribbean volcanism (Bralower et al., 1997) and/or the emplacement of the North Atlantic Igneous Province (Eldholm and Thomas, 1993; Schmitz et al., 2004; Storey et al., 2007), is hypothesized to have been a potential cause of global warming at the PETM and may have triggered the carbon isotope excursion (Bralower et al., 1997). However, it is important to note that the record of volcanism based on ash horizons from Blake Nose appears to post-date the initiation of warming inferred from the shift in benthic foraminiferal calcite $\delta^{18}O$ (Fig. 7.3) which may imply that these volcanic events are not the primary cause of the initial warming but it does not rule out the possibility of other eruptions that may not have been expressed at this location. It is important to consider the scale of these eruption events and whether they were large enough to have contributed to and sustained global warming on the timescales of the MECO (∼600 kyrs). The amount of CO_2 injected into the atmosphere from single eruption events is relatively tiny compared to the scale of the atmospheric and oceanic 'surficial' carbon reservoir exchange and thus, unlikely to impact global climate on long timescales. However, because of the long residence time of CO_2 in the 'surficial' reservoirs before being sequestered in to the geological 'rock' reservoir, the cumulative effects of successive closely spaced large eruptions could be significant (Kerrick, 2001).

7.4.2 A volcanic trigger for short-lived carbon isotope excursions in the Eocene?

Individual ash horizons at Site 1051 appear to broadly coincide with the onset of negative $\delta^{13}C$ excursions recorded at ODP Sites 1051 and 1260, which may imply a volcanic trigger for these events. The distinctive symmetrical $\delta^{13}C$ profile recorded (Figs 7.3 and 7.5), indicates the equally rapid input and sequestration of isotopically light carbon to the ocean-atmosphere system. However, the $\delta^{13}C$ of volcanic CO_2 is only approximately -6 ±2‰ VPDB (Faure and Mensing, 2005) and thus, unrealistically large amounts of this carbon (≥20,000 Gt C) would be required to create the observed 1‰ shift recorded in the stable isotope records. It may be that volcanically released CO_2 'conditioned' the Earth's system and resultant warming may have triggered the subsequent abrupt release of isotopically light carbon from another carbon reservoir in the system, a hypothesis again invoked for the PETM interval (Eldholm and Thomas, 1993; Bralower et al., 1997). The clay-rich horizons coincident with $\delta^{13}C$ excursions at Site 1260 indicate that the CCD shoaled repeatedly to at least 2.5 - 3.0 km depth in the tropical Atlantic supporting the suggestion of the input of a large quantity of carbon to the system at this time. [Note that no clay horizons are visible at Site 1051 because the site is situated at

water depths ∼1 km shallower than Site 1260]. The events described here may therefore be akin to additional smaller magnitude 'hyperthermal' events recently reported in the Paleogene, e.g., the Early Palaeocene Dan-C2 event (Quillévéré et al., 2008), Early Eocene, ETM-2 (Lourens et al., 2005), 'X' horizons (Röhl et al., 2004) and the H2, I1 and I2 events (Cramer et al., 2003; Nicolo et al., 2007) and the Middle Eocene C19r event (Edgar et al., 2007). These events are characterised by prominent shifts in δ^{13}C values of up to ∼2‰, δ^{18}O values up to 1.5‰ and are accompanied by a shift to more clay-rich lithologies, but are smaller than the the isotopic signals documented at the PETM at 55 Ma. The most frequently invoked carbon source to explain the negative δ^{13}C excursion at the PETM is methane hydrate which has a very light δ^{13}C value, ∼-60‰ , and therefore far less carbon is required to create the δ^{13}C excursion recorded here, ∼400 GtC based on analogy to the PETM (Dickens et al., 1995, 1997; Zachos et al., 2005). However, this hypothesis would imply multiple, closely spaced coupled warming-gas hydrate release events which would require a rapid refill of the hydrate resevoir. Estimates of the amount of biogenic methane that could have been stored in seafloor sediments during the Paleogene and the long 'refill' time of this reservoir have raised doubts about the viability of this mechanism (Buffett and Archer, 2004).

The PETM is accompanied by a long recovery phase during which carbon is re-sequestered (Zachos et al., 2005). The absence of a long recovery phase associated with multiple smaller Paleogene 'hyperthermal' events has led to the alternative hypothesis that these events may be related to the astronomically paced release of carbon within the 'surficial' carbon reservoirs (Quillévéré et al., 2008). Certainly, 'hyperthermal' events appear to be a pervasive part of the Paleogene climate system, suggesting a common trigger mechanism that permits the repeated injection of isotopically light carbon into the ocean-atmosphere system. However, the mechanism and source of the carbon remains elusive.

From a biotic viewpoint, despite the high resolution biotic records generated in this study, the planktic foraminiferal assemblage at Site 1051 shows no consistent pattern of change across the negative δ^{13}C excursions recorded. [Note that at Demerara Rise, the original faunal composition appears to have been overprinted by dissolution (Fig. 7.11) and therefore only the assemblage records from Blake Nose which was situated in water depths approximately 1 km shallower than Site 1260 in the Middle Eocene are considered]. This implies one of a number of things: (i) that there was a biotic response but it was over an interval of less than ∼3 kyrs, (ii) there is a threshold level of environmental perturbation below which no biotic response is invoked and/or (iii) that the foraminifera were insensitive to the environmental changes that accompanied these δ^{13}C excursions.

7.4.3 Driving productivity changes in surface waters

At the present day, ODP Site 1051 on the Blake Nose plateau is an open-ocean site that sits close to the western boundary current the Gulf Stream, a high velocity surface water current that transports heat from the tropics to the high latitudes. Changes in the position of the Gulf Stream across the plateau in response to global climate changes (Kaneps, 1979; Pinet et al., 1981) can lead to significant temperature fluctuations in surface waters of up to 8°C over short distances. Stable isotope studies of the Eocene palaeoceanography of Blake Nose during planktic foraminiferal biozones E13 and E14, i.e., in sediments younger than 40 Ma, indicates significant variability in surface water conditions that are attributed to temperature shifts of up to 10°C on relatively short, orbital timescales as a result of either changes in the position of the Gulf Stream across the Blake Nose Plateau or large variability in ocean up-welling intensity at Blake Nose (Wade et al., 2001; Wade and Kroon, 2002). Modeling studies indicate that changes in wind driven upwelling and continental run-off on a precessional time scale in the North Atlantic can account for (seasonal) temperature variability of up to 8°C at 29°N (Huber et al., 2002). However, stable isotope records generated at ODP Site 1051 in this study indicate maximum temperature fluctuations of 3°C, significantly less than previously documented at Blake Nose (Wade and Kroon, 2002) and may indicate more stable surface water conditions during planktic foraminiferal biozone E12 than recorded in younger sediments (Wade et al., 2001; Wade and Kroon, 2002). Apparent cyclical changes in the relative abundances of planktic foraminifera at frequencies similar to obliquity and precession (Fig. 7.12) support previous interpretations of the dominant orbital frequencies recorded in sedimentary and geochemical records at this site (Wade et al., 2001). Spectral peaks consistent with precessional frequencies are typical of low latitude insolation effects on surface water conditions affecting abundances (Fig. 7.12) and obliquity related signals in the faunal dataset may reflect upwelling of waters sourced from higher latitudes.

The MECO at Site 1051 was marked by gradual warming of sea surface temperatures over ∼600 kyrs superimposed on shorter term (probably orbitally) driven changes in temperature and/or nutrient availability. The foraminiferal assemblage data herein suggests that this warming was accompanied by a shift to more mesotrophic/eutrophic surface water conditions. In principle, nutrient-enhanced surface-waters at Blake Nose during the MECO could be explained by a number of processes. Firstly, increased upwelling of bottom waters during the MECO may have been one means of increasing the nutrient concentration in surface waters. Blake Nose is thought to be sensitive to upwelling in the Eocene because of large variations in surface water temperatures that periodically approach deep water temperatures (Wade et al., 2001; Wade and Kroon, 2002), a relatively high abundance of radiolarians found at this site (Shipboard Scientific Party, 1998) and high sensitivity of the Blake Nose region to upwelling in modeling studies (Huber et al., 2002). A near global hiatus that occurs approximately at the magnetochron C18r/C18n

boundary may also point towards more vigorous ocean circulation at this time. Increased upwelling might be represented by a decrease in water column stratification that might manifest in the faunal record by an increase in the deeper-dwelling foraminiferal taxa at the expense of the shallow-dwelling taxa but this is not observed (except perhaps for a brief interval at ∼40.2 Ma prior to the peak of the MECO, see Section 7.3.1). A second and perhaps more likely hypothesis is that global warming at the MECO lead to an intensification of the hydrological cycle promoting chemical weathering and continental run-off, and hence the delivery of terrestrially-sourced nutrients to the surface ocean at this time. This mechanism is invoked to explain observed increased productivity patterns during other intervals of elevated global warmth such as the PETM (Bains et al., 2001; Ravizza et al., 2001; Pagani et al., 2006; Gibbs et al., 2006). Finally, nutrient levels, at least on a regional scale may have been briefly enhanced by volcanic fallout inputing biolimiting nutrients (P, Fe, Si and Mn) into surface waters from the dissolution of ash particles. At Site 1051 five distinctive ash horizons were identified (Shipboard Scientific Party, 1998) spaced approximately 100 kyrs apart from one another within the MECO (Fig. 7.3), a frequency consistent with large explosive volcanic events similar to the Toba-size eruption at 75 ka (Sigurdsson et al., 2000). However, laboratory experiments that investigate the impact of nutrient fertilisation on marine biota indicate that the bulk of the nutrients are released from dissolved ash within the first day of contact with seawater (Frogner et al., 2001; Duggen et al., 2007) and it may be that the marine biota respond on an equally short timescale (Martin et al., 1994; Frogner et al., 2001). Therefore, while the timescales over which this mechanism operates and the duration for which it maintains elevated rates of primary production remain unclear (Boyd and Law, 2001), it seems unlikely that increased nutrient concentrations in seawater could be sustained over the timescales discussed in this study, i.e., ∼500 kyrs, unless accompanied by an additional source such as submarine volcanism or increased hydrothermal activity (Leckie et al., 2002). An additional source of nutrients to the ocean at this time could have come from submarine volcanism related to North Atlantic rifting, which was still occurring above 60°N around Greenland (Storey et al., 2007), and could have led to the sustained release of nutrients into the water column. Thus, the interaction of the two volcanic provinces in central America and the North Atlantic may have contributed to elevated productivity during the MECO. Certainly, a similar hypothesis has been invoked to explain elevated levels of primary productivity during various ocean anoxic events (OAEs) in the Cretaceous (Bralower et al., 1994; Sinton and Duncan, 1997; Leckie et al., 2002; Turgeon and Creaser, 2008).

7.5 Conclusions

New high-resolution records generated in this study provide the first insight into the impact of the MECO on planktic foraminiferal assemblages. Similarities in the planktic

foraminiferal response to the MECO at Sites 1051 and Site 1260 implies that similar oceanographic conditions persisted throughout the (sub)tropical Atlantic at this time. The overall assemblage shift suggests a change from warm, relatively oligotrophic surface waters to warmer, more nutrient rich surface waters during the MECO. The most rapid and 'extreme' environmental changes are inferred to occur during a brief 40 kyr long interval indicated by abrupt shifts in the mixed-layer dwelling assemblages most likely attributable to high sea surface temperatures. Following the MECO, typical warm water genera are replaced by cooler water genera indicating surface water cooling consistent with existing low-resolution records that document a similar pattern of long term faunal turnover through the Middle and Late Eocene. Hypotheses to explain the inferred increase in surface water nutrient availability during the MECO include an increase in continental runoff at this time resulting from an intensified hydrological cycle associated with global warming, more vigorous ocean circulation and upwelling and/or the addition of volcanically sourced nutrients to the system.

Although the MECO is a relatively short-lived event, it may have had long-term effects on planktic foraminifera, contributing to the extinction of the *Morozovelloides* and the large acarininids in the late Middle Eocene. The short-term evolutionary effects, if any, of the MECO on planktic assemblages are difficult to assess with the current dataset but certainly *O. beckmanni* is not an 'excursion' taxa. The findings here suggest that climatic and environmental changes associated with the MECO were sufficient to provoke a response in planktic assemblages at low latitudes and further work is needed to reveal its impact on the other marine plankton and at higher latitudes.

One of the major surprises arising from the new stable isotope records was that superimposed on the 'transient' warming event the MECO are three prominent negative δ^{13}C excursions around the magnetochron C18r/C18n boundary that are coincident with CCD shoaling and increasing ocean temperatures akin to 'hyperthermal' events reported in the early Paleogene (Fig. 7.6). The rapid injection and sequestration of isotopically light carbon to the ocean-atmosphere system during these events in the MECO may have been triggered by volcanically driven bottom water warming.

7.6 Future work

To test the hypothesis that it was the demise of the photosymbiotic relationship in *Acarinina* that led to the decline in their abundance during the MECO, monospecific size segregated δ^{13}C data will be collected across the MECO. In photosymbiotic foraminifera δ^{13}C values increase with test size, whereas asymbiotic taxa, e.g., subbotinids, show no size related δ^{13}C trends. Therefore, if the photosymbiotic relationship with the acarninids broke down during the MECO a decrease in the size-related δ^{13}C trend should be observed.

Thus far, the globgerinathekids have been assumed to host photosymbionts based on the similarity of the 'isotopic niche' that they occupy to that of the modern photosymbiotic genus *Globigerinoides* (Pearson et al., 1993). Yet no size fraction δ^{13}C data has been published on the globigerinathekids. Future work may involve a study of globigerinathekid palaeoceology using stable isotope data.

Future work will involve extending the planktic foraminifera assemblage record at Site 1051 to cover the same interval of time as the record generated at Site 1260. This new record will aid inter-site comparisons and allow assessment of whether the genus *Morozovelloides* shows an increase in abundance prior to the onset of the MECO at ~40.9 Ma as observed at Site 1260 (Fig. 7.8).

A low resolution stable isotope record in planktic foraminiferal calcite will be generated at Site 1260 across the onset of the MECO to discern whether surface water warming preceded bottom water warming as currently inferred (Fig. 7.8).

A pilot study will be conducted to examine changes in the size of different genera in the planktic foraminiferal assemblage throughout the MECO. This study will predominantly focus on the surface dwelling genera *Acarinina, Morozovelloides*, and *Globigerinatheka* and species *O. beckmanni* which show the most pronounced response to the MECO.

Extension of the foraminiferal assemblage record at Site 1051 into the late Middle Eocene to examine the decline of the *Morozovelloides* and the *Acarinina* in a quantitative manner might help to shed light on the mechanisms of extinction and address the following questions. (1) Do the *Morozovelloides* abundances remain consistently low following the peak of the MECO until they become extinct in the late Middle Eocene? (2) Is there a decrease in the test size of the genera *Acarinina* and *Morozovelloides* prior to the their extinction in the late Middle Eocene? (3) Do the *Acarinina* and *Morozovelloides* show the same pattern of decline prior to the extinction implying a common cause?

Chapter 8

Conclusions

In this thesis, new palaeoceanographic and faunal records are presented from Ocean Drilling Program (ODP) sediments drilled during Legs 171B and 207 for the interval between magnetochrons C18 and C19 (∼39 - 43 Ma) in the Middle Eocene. These records shed new light on the nature, timing and consequences of carbon cycle perturbations of the Middle Eocene. In this final chapter the scientific aims posed in Chapter 1 that motivated this work are addressed, the main achievements and findings of this thesis are summarised, and future directions for palaeoceanographic studies are proposed.

1) Develop a methodology for measuring trace metals with low concentrations in foraminiferal calcite by inductively coupled plasma-optical emission spectrometry.

This investigation represents the first step towards the development of a new inductively coupled plasma-optical emission spectrometer (ICP-OES) technique capable of measuring Al, Mn, Fe and Ti in foraminiferal samples to screen Mg/Ca and Sr/Ca data for contamination. Initial results indicate that the current methodology employed at the National Oceanography Centre, Southampton (NOCS) to determine Mg/Ca and Sr/Ca values in foraminiferal calcite is unsuited to the simultaneous determination of the elements Al, Mn, Fe and Ti. These elements generally have low concentrations in foraminiferal calcite samples and the ICP-OES technique is less sensitive to them than to Ca, Mg and Sr and thus, the existing NOCS methodology requires modification.

The main conclusions of this study are that to quantitatively measure the elements Al, Fe, Mn and Ti in association with the desired elements Mg, Ca and Sr by ICP-OES requires the following: (1) sample [Ca] is $\geq$10 ppm, to ensure sufficient element concentrations for quantitative measurements on the ICP-OES. (2) The ICP-OES must be configured to view the plasma axially to increase the instrument sensitivity to the elements Al, Mn, Fe and Ti. (3) Longer integration times should be employed to measure Al, Fe and Ti than for the more abundant or for elements Mg, Ca, Sr and Mn that are more sensitive for determination by ICP-OES, so to increase the number of

photons counted during each measurement and therefore increase the precision of the measurement. (4) A sample presentation system comprising a "Conikal" nebulizer coupled to a "Twister" spray chamber should be employed to increase the sensitivity of the instrument to the elements Al, Mn, Fe and Ti.

The best analytical precisions obtained during this investigation were better than 1% for Mg/Ca and Sr/Ca values and ≤10% for other trace element/calcium ratios, which is sufficient to detect any contamination that may be present in samples. The large [Ca] range investigated in this study highlights what appears to be significant matrix effects on the majority of elements measured. Thus, future work should target a sample protocol with a narrow [Ca] range to negate or correct for matrix effects. Working within a narrow range of [Ca] will enable the use of more tightly bracketed element concentrations in calibration standards. This will also allow the use of extended integration times and should lead to a significant increase in the precision of measurements. Ultimately, this work contributes towards the development of a new ICP-OES methodology for generating trace element data in foraminiferal calcite that will increase confidence in the authenticity of data.

2) Evaluate the hypothesis that large transient continental ice sheets were present in both hemispheres close to the top of magnetochron C19r (∼41.6 Ma) in the Middle Eocene.

New monospecific high-resolution stable isotope records generated at ODP Site 1260, are used to test the hypothesis that large continental ice sheets developed in the Northern Hemisphere, ∼30 Myrs earlier than the standard view, towards the top of magnetochron C19r at ∼41.6 Ma in the Middle Eocene. The amplitude of the $\delta^{18}O$ shift recorded in benthic foraminiferal calcite ($\delta^{18}O_{benthic}$) at Site 1260 is almost half the amplitude of that reported from the Pacific and used to formulate the bipolar glaciation hypothesis. Therefore, even if the whole of the new $\delta^{18}O_{benthic}$ shift recorded at Site 1260 is attributed to the growth of ice sheets at this time, the estimated ice budget can be accommodated on Antarctica alone and does not require contemporaneous ice growth in the Northern Hemisphere to be invoked. Furthermore, if the $\delta^{18}O_{benthic}$ signal from Site 1260 comprises ∼50 % global cooling as inferred for previous ice building events such as the Eocene-Oligocene boundary and the last glacial cycle then even smaller ice volume estimates are calculated (∼40 - 60% of the present day Antarctic ice volume) more inkeeping with existing climate and sequence stratigraphy records. These records do not rule out the possible existence of small isolated ice sheets or mountain glaciers draining the uplands of Greenland at this time, particularly in light of dropstones recently discovered in Eocene strata at high northern latitudes (Moran et al., 2006; Eldrett et al., 2007). Nevertheless, we can rule out the existence of large continental ice sheets in the Northern Hemisphere at this time in the Middle Eocene. This finding implies that large continental ice sheets would not have developed in the Northern Hemisphere

until much later when Earth's baseline climate was significantly cooler and poised closer to the threshold for glaciation.

3) Document the link between transient carbon cycle perturbations and global climate change in magnetochrons C18 and C19.

New high-resolution foraminiferal and bulk stable isotope records generated in this thesis from ODP Sites 1051 and 1260 document the first short-lived (∼40 kyrs) carbon cycle-led warming events in the Middle Eocene. These events are characterised by prominent negative δ^{13}C excursions of ∼1‰ , a decrease in δ^{18}O inferred to represent an increase in ocean temperatures and are accompanied by a decrease in wt% carbonate and/or prominent clay rich horizons suggestive of coincident carbonate compensation depth (CCD) shoaling. The magnitude of the palaeoceanographic signals documented here are smaller than those seen during the well-known Palaeocene-Eocene thermal maximum (PETM) (Kennett and Stott, 1991; Zachos et al., 2001, 2005) but are similar to multiple 'hyperthermal' events recently reported in the early Paleogene such as the Eocene Thermal Maximum 2 (Lourens et al., 2005) and Dan C2 events (Quillévéré et al., 2008).

The first of the newly described carbon cycle events occurs towards the top of magnetochron C19r at ∼41.8 Ma, thus entitled the C19r event, and is superimposed on a transient ∼600 kyr reversal in the Eocene long-term cooling trend. It is not possible to determine at present whether the C19r event is global in nature. The next three events identified (Chapter 7) occur in close proximity to one another in the top of magnetochron C18r and the base of C18n at 40.4, 40.3 and 40 Ma (C18r-1, C18r-2 and C18n-1 events, respectively) and are superimposed on an interval of longer-term warming - the Middle Eocene Climatic Optimum (MECO). All of the magnetochron C18 events that have so far been identified can be correlated between two separate deep sea sites at present and may prove to be global in nature.

The significance of these findings are threefold. First, so-called 'hyperthermals' are not restricted to the Early Eocene 'greenhouse' but also occur millions of years later when Earth's baseline climate had cooled substantially. This implies that 'hyperthermal' events are a pervasive part of the early Paleogene climate system. Secondly, the similar palaeoceanographic signals observed during multiple 'hyperthemal' events implies the operation of some common, but as yet unknown, carbon cycling process that allows repeated rapid injection and sequestration of isotopically light carbon within the ocean-atmosphere system. Thirdly, the majority of hyperthermal events thus far identified are confined to the Palaeocene and Early Eocene with only a small number identified in the Middle Eocene superimposed on reversals in the long term Eocene cooling trend. This finding if substantiated may imply the presence of some 'critical', possibly thermal, threshold in the Earth's system.

In a broader context, there are similarities in terms of carbon cycling between events reported in this study during magnetochron C19 (∼41.6 - 41.0 Ma) and those at the Eocene-Oligocene boundary. Both intervals are characterised by a brief interval of CCD shoaling prior to a large (≥700 m) deepening of the CCD that persisted for ∼500 kyrs in magnetochron C19 but was permanent at the Eocene-Oligocene boundary. This implies the operation of some common carbon-cycling mechanism between the two intervals in the Paleogene.

4) Refine and re-evaluate the existing magnetic stratigraphy at ODP Site 1051 between magnetochrons C17 and C19 (39.5 to 42.0 Ma).

New high-resolution (∼1 sample every ∼250 yrs) magnetic polarity records generated at ODP Site 1051 show a well resolved pattern of magnetic reversals between 65 and 150 metres composite depth (mcd) that are assigned to magnetochrons C19r through C18n.1n. Magnetochron boundaries are resolved to ±1 cm across the top and base of magnetochron C19n and base of C18n.1r and ±55 cm across the magnetochron C18r/C18n boundary. New high-resolution magnetostratigraphy and and careful evaluation of existing shipboard and new biostratigraphic information generated in this thesis (Chapter 6), has led to the re-interpretation of the shipboard magnetostratigraphy between 5 and 95 mcd. The resulting new age model for Site 1051 results in the top of the core splice being assigned to magnetochron C17n and an age of ∼37.8 Ma, about 2 million years younger than previously suggested. The new age model yields a more realistic sedimentation rate history of ∼3.5 cm/kyr for the core splice between 150 and 5 mcd and is more inkeeping with biostratigraphic controls. Thus, Site 1051 offers an excellent opportunity to improve the existing integrated biomagnetochronologic time scale and contribute towards the development of a more reliable time scale for the Middle Eocene.

The new polarity record indicates a number of hitherto unreported short-lived polarity (≤8 kyr) 'events' within magnetochrons C18r and C19n. The nature and origin of these events is, as yet, unconfirmed but a number of lines of evidence suggest that at least some of these events may reflect true variability in the geomagnetic field in the Middle Eocene. Even if subsequent work shows that this is not the case, the unprecedented temporal resolution of these new polarity records generated will also contribute to the debate on the origin of tiny wiggles observed in marine magnetic anomaly profiles in the Middle Eocene by enabling us to distinguish between the competing hypotheses that they represent either full magnetic reversals or magnetic excursions.

5) Assess the reliability of the datums defined by Orbulinoides beckmanni *and improve their calibration to the geomagnetic polarity time scale.*

In this thesis, the first high-resolution and quantitative abundance records of the biostratigraphic marker species *Orbulinoides beckmanni* that defines planktic foraminiferal biozone E12 are generated from an expanded sedimentary section at ODP Site 1051, which has a good magnetic stratigraphy (Chapter 5). Assuming that the reliability of a datum can be considered to be an evaluation of the relative synchrony of a biotic event, the records presented here strongly suggest that the first occurrence (FO) of *O. beckmanni* is diachronous, at least within the Atlantic. *O. beckmanni* had its evolutionary first appearance in equatorial waters in the base of magnetochron C18r at ∼41.0 Ma, approximately 500 kyrs older than previously documented. However, *O. beckmanni* is not recorded at Site 1051 in the subtropics until much later, in the top half of magnetochron C18r at ∼40.5 Ma in agreement with earlier biostratigraphic calibrations. The resulting expansion of *O. beckmanni's* geographic range may have been associated with the poleward expansion of warm surface waters that accompanied the MECO. Given *O. beckmanni's* latitudinally restricted distribution (∼40°N to 30°S) it seems reasonable to infer that sea surface temperature may have played a strong role in controlling *O. beckmanni's* biogeography. The stratigraphic last occurrence (LO) of *O. beckmanni* (also recorded at Site 1051) occurs in magnetochron C18n.2n and is assigned an age of 39.4 Ma, 600 kyrs younger than previously reported. This revised age for the top of biozone E12 is attributed to the typically discontinuous recovery of sediments and poor age control across this biozone in earlier work. Based on the revised FO and LO of *O. beckmanni*, the continuous record generated at ODP Site 1051 indicates that the E12 biozone is ∼900 kyrs in duration almost twice as long as previously thought.

The results of this study clearly highlight a number of important points. First, the importance of working at deep sea sites with a reliable high-resolution magnetic stratigraphy with which to calibrate biotic events and the need to further test the reliability of other Middle Eocene biostratigraphic datums. Second, the application of a strict taxonomic concept for biostratigraphic marker species is essential to prevent comparisons of the stratigraphic occurrences of biotic events producing misleading interpretations. Third, the need to better understand the environmental and ecological controls on the biological species that are used to define biostratigraphic datums.

6) Document the ecological, environmental and evolutionary signals associated with the MECO using planktic foraminifera.

New high-resolution records generated in this study provide the first insight into the impact of the MECO on planktic foraminiferal assemblages. Planktic foraminiferal assemblages at ODP Sites 1051 and 1260 are sensitive to environmental changes that are inferred to have occurred in the surface waters during the MECO as evidenced by a series of successive assemblage changes across the event. Similar biotic responses at the two sites during the initial stages of the MECO implies similar environmental forcing

throughout the (sub)tropical Atlantic at this time. The major assemblage shift suggests a change from warm, oligotrophic surface waters to warmer, more productive conditions. The most abrupt assemblage changes occur among the mixed-layer dwelling genera at the peak of the MECO indicating a brief interval of significant environmental stress in surface waters at this time, most likely attributable to high sea surface temperatures. The findings suggest that climatic and environmental changes associated with the MECO were sufficient to provoke a response in planktic assemblages at low latitudes and thus, it is likely that further work will also reveal its impact at higher latitiudes and on the other marine plankton. Following the MECO, genera associated with warmer waters were gradually replaced by cooler water-favouring genera indicating surface water cooling inkeeping with existing low-resolution records that document a similar pattern of turnover through the Middle and Late Eocene. Competing hypotheses to explain the inferred increased in nutrient availability in surface waters during the MECO are an increase in continental runoff resulting from an intensified hydrological cycle, increased rates of upwelling and/or volcanically sourced nutrients.

8.1 Future perspectives

Our understanding of Eocene climate dynamics has increased dramatically since the early 1990's, in most part because of the increased recovery of more continuous and expanded deep sea sediments enabling the generation of palaeoceanographic records for the Eocene at temporal resolutions that in the past were rarely obtained beyond the Plio-Pleistocene. As atmospheric pCO_2 and global mean temperature continue to rise in response to anthropogenic forcing it becomes increasingly important that we understand the nature and causes of climatic variability and its impact on the environment during previous globally warm, high pCO_2 intervals.

Despite recent advances in our understanding of Eocene climatic behaviour some fairly significant gaps persist in our knowledge of short-term climate variability, the mechanisms responsible and impacts of climate change on the environment. This is primarily still attributable to a dearth of appropriate sediments available on which to work for some intervals of the Paleogene. Thus, future drilling initiatives should continue to target shallowly buried and expanded sedimentary sections from poorly recovered time intervals of the Paleogene and from ocean basins where few records are available. Ideally sites with well preserved foraminifera, i.e., shallowly buried and/or clay rich sections, should be targeted to facilitate the generation of reliable palaeoclimate records. One of the first steps should be to target drilling at high northern latitudes, e.g., in the northern North Atlantic and Arctic Ocean (the Arctic has no carbonate sediments before the Neogene but non-carbonate based proxies can be employed), because there is a deficit of continuous Paleogene sections with which to address current palaeoclimatic topics of interest such as the timing of the onset and the magnitude of continental ice sheets

in the Northern Hemisphere at present. Another 'hot' topic in palaeoceanography at present that could be addressed with new drill sites in the Southern Ocean is the location and timing of the onset of continental ice-sheets in the Late Cretaceous and Cenozoic. Renewed scientific interest in this topic has been prompted by several studies which invoke the onset of transient ice-sheets, at least on Antarctica, much earlier than widely thought. In fact, one study even proposes transient ice sheets on Antarctica during the Late Cretaceous - the warmest interval in the last 95 million years of Earth's history. If substantiated this finding has serious implications for the fate of continental ice-sheets in the coming centuries. Thus, it is essential that we gain a better understanding of the boundary conditions and triggers for ice growth, and the volume of ice sheets in the past. Intervals of time that are poorly resolved and recovered include the interval of the Middle Eocene between ~43 and 49 Ma which is still only known at relatively coarse $\geq$100 kyrs resolution. Yet, this interval is of key importance because it comprises the first interval of rapid global cooling following the Early Eocene climatic optimum and thus, warrants investigation.

References

S. Abramovich and G. Keller. Planktic foraminiferal response to the latest Maastrichtian abrupt warm event: a case study from South Atlantic DSDP Site 525A. *Marine Micropaleontology*, 48:225–249, 2003.

C. Agnini, D. J. Spofforth, E. Fornaciari, I. Giusbert, L. Lanci, V. Luciani, G. Muttoni, H. Pälike, and D. Rio. Is the Middle Eocene Climatic Optimum (MECO) recorded in the central western Tethys? In *EOS Transactions of the American Geophysical Union*, volume 88, Fall Meeting Abstract OS11A-0188, San Francisco, 2007.

A. P. Allen and J. F. Gillooly. Assessing latitudinal gradients in speciation rates and biodiversity at the global scale. *Ecology Letters*, 9:947–954, 2006.

D. A. Andreasen, S. Soisdan, S. Perron-Cashman, C. H. Lear, T. deGaridel Thoron, P. Field, and Y. Rosenthal. Fidelity of radially viewed ICP-OES and magnetic-sector ICP-MS measurement of Mg/Ca and Sr/Ca ratios in marine biogenic carbonates: Are they trustworthy together? *Geochemistry, Geophysics, Geosystems*, 7: doi:10.1029/2005GC001124, 2006.

D. J. Andreasen and A. C. Ravelo. Tropical Pacific Ocean thermocline depth reconstructions for the last glacial maximum. *Paleoceanography*, 12:395–413, 1997.

P. Arason and S. Levi. Compaction and inclination shallowing in deep sea sediments from the Pacific Ocean. *Journal of Geophyscial Research*, 95:4501–4510, 1990.

H. A. Armstrong and M. D. Brasier. Radiozoa (Acantharia, Phaeodaria and Radiolaria) and Heliozoa. In *Microfossils*, pages 188–199. Blackwell Publishing Ltd, Oxford, second edition, 2005.

M. A. Arthur and J. H. Natland. Carbonaceous sediments in the North and South Atlantic: The role of salinity in stable stratification of Early Cretaceous basins. In M. E. A. Talwani, editor, *Deep Drilling Results in the Atlantic Ocean: Continental Margins and Paleoenvironment*, volume 3 of *Maurice Ewing Series*, pages 375–401. American Geophysical Union, 1979.

M.-P. Aubry and J. A. Van Couvering. Buried Time: Chronostratigraphy as a Research Tool. In E. A. M. Koutsoukos, editor, *Applied Stratigraphy*, pages 23–53. Springer, Netherlands, 2005.

L. Babić, M. H. Kuŭenjak, S. Ćoric, and J. Zupanic. The middle Eocene age of the supposed late Oligocene sediments in the flysch of the Pazin Basin (Istria, Outer Dinarides). *Croatian Natural History Museum*, 16:83–103, 2007.

J. Backman. Late Paleocene to middle Eocene calcareous nannofossil biochonology from the Shatsky Rise, Walvis Ridge and Italy. *Palaeogeography, Palaeoclimatology, Palaeoecology*, 57:43–59, 1986.

S. Bains, R. D. Norris, R. M. Corfield, and K. L. Faul. Termination of global warmth at the Palaeocene/Eocene boundary through productivity feedback. *Nature*, 407:171–174, 2001.

S. Barker and H. Elderfield. Core-top Calibrations of Foraminiferal Mg/Ca From a North Atlantic Transect: Refining Mg/Ca Paleothermometry. In *EOS Transactions of the American Geophysical Union*, volume 82, Fall Meeting Abstract PP12A-68, San Francisco, 2001.

S. Barker, M. Greaves, and H. Elderfield. A study of cleaning procedures used for foraminiferal Mg/Ca paleothermometry. *Geochemistry, Geophysics, Geosystems*, 4: doi:10.1029/2003GC000559, 2003.

E. Barrera and B. T. Huber. Paleogene and Early Neogene oceanography of the Southern Indian Ocean: Leg 119 Foraminifer Stable Isotope Results. In J. Barron, B. Larson, et al., editors, *Proceedings of the Ocean Drilling Program, Scientific Results*, volume 119, pages 693–717. (Ocean Drilling Program), College Station, Texas, 1991.

E. J. Barron. Explanations of the Tertiary global cooling trend. *Palaeogeography, Palaeoclimatology, Palaeoecology*, 50:45–61, 1985.

E. J. Barron. Eocene equator-to-pole surface ocean temperature: A significant climate problem? *Paleoceanography*, 2:729–739, 1987.

E. J. Barron, W. H. Peterson, L. G. Thompson, and D. Pollard. Past climate and ocean the role of ocean heat transport: model simulations for the Cretaceous. *Paleoceanography*, 8:785–798, 1993.

A. W. H. Bé, H. J. Spero, and O. R. Anderson. Effects of symbiont elimination and reinfection on the life processes of the planktonic foraminifer *Globigerinoides sacculifer*. *Marine Biology*, 70:73–86, 1982.

J.-P. Beckmann. Die Foraminiferen der Oceanic Formation (Eocaen-Oligocaen) von Barbados, kl. Antillen. *Eclogae Geologicae Helvetiae*, 46:301–412, 1953.

B. E. Bemis, H. J. Spero, J. Bijima, and D. W. Lea. Reevaluation of the oxygen isotopic composition of planktonic foraminifera: Experimental results and revised paleotemperature equations. *Paleoceanography*, 13:150–160, 1998.

W. A. Berggren. Rates of evolution in some Cenozoic planktonic foraminifera. *Micropaleontology*, 15:351–365, 1969.

W. A. Berggren. Recent advances in Cenozoic planktonic foraminiferal biostratigraphy, biochronology, and biogeography: Atlantic Ocean. *Micropaleontology*, 24:337–370, 1978.

W. A. Berggren, D. V. Kent, and J. J. Flynn. Paleogene geochronolgy and chronostratigraphy. In N. J. Snelling, editor, *The Chronology of the Geological Record: Geological Society of London Memoir*, volume 10, pages 141–195. Geological Society of London, 1985.

W. A. Berggren, D. V. Kent, C. C. Swisher III, and M.-P. Aubry. A Revised Cenozoic Geochronology and Chronostratigraphy. In W. A. Berggren, D. V. Kent, M.-P. Aubry, and J. Hardenbol, editors, *Geochronology, Time Scales and Global Stratigraphic Correlation, SEPM Special Publication*, volume 54, pages 129–213. SEPM (Society for Sedimentary Geology), Tulsa, Oaklohoma, 1995.

W. A. Berggren and K. G. Miller. Paleogene tropical planktonic foraminiferal biostratigraphy and magnetobiochronology. *Micropaleontology*, 34:362–380, 1988.

W. A. Berggren and P. N. Pearson. A revised tropical to subtropical planktonic foraminiferal zonation of the Eocene and Oligocene. *Journal of Foraminiferal Research*, 35:279–298, 2005.

R A. Berner and Z. Kothavala. GEOCARB III: A revised model of atmospheric CO_2 over Phanerozoic time. *American Journal of Science*, 301:182–204, 2001.

R. A. Berner, A. C. Lasaga, and R. M. Garrels. The carbonate-silicate geochemical cycle and its effect on atmospheric carbon dioxide over the past 100 million years. *American Journal of Science*, 283:641–683, 1983.

K. L. Bice, C. R. Scotese, D. Seidov, and E. J. Barron. Quantifying the role of geographic change in Cenozoic ocean heat transport using uncoupled atmosphere and ocean models. *Palaeogeography, Palaeoclimatology, Palaeoecology*, 161(295-310), 2000.

K. Billups and D. P Schrag. Paleotemperatures and ice volume of the past 27 Myr revisisted with paired Mg/Ca and $^{18}O/^{16}O$ measurements on benthic foraminifera. *Paleoceanography*, 17:doi:10.1029/2000PA000567, 2002.

K. Billups and D. P Schrag. Application of benthic foraminiferal Mg/Ca ratios to questions of Cenozoic climate change. *Earth and Planetary Science Letters*, 209:181–195, 2003.

R. J. Blakely and A. Cox. Evidence for short geomagnetic polarity intervals in the early Cenozoic. *Journal of Geophysical Research*, 77:7065–7072, 1972.

W. H. Blow. Late middle Eocene to Recent planktonic foraminiferal biostratigraphy. In P. Brönnimann and H. H. Renz, editors, *Proceedings of the First International Conference on Planktonic Microfossils*, volume 1, pages 199–422, Geneva, 1969. E. J. Brill, Leiden.

W. H. Blow. *The Cainozoic Globigerinida*. E. J. Brill, Leiden, 1979.

A. Boersma and I. Premoli-Silva. Paleocene planktonic foraminiferal biogeography and the paleoceanography of the Atlantic Ocean. *Micropaleontology*, 29:355–381, 1983.

A. Boersma and I. Premoli-Silva. Distribution of Paleogene planktonic foraminifera - analogies with the recent? *Palaeogeography, Palaeoclimatology, Palaeoecology*, 83: 29–48, 1991.

A. Boersma, I. Premoli-Silva, and N. J. Shackleton. Atlantic Eocene planktonic foraminiferal paleohydrographic indicators and stable isotope paleoceanography. *Paleoceanography*, 2:287–331, 1987.

S. M. Bohaty and J. C. Zachos. Significant Southern Ocean warming in the late middle Eocene. *Geology*, 31:1017–1020, 2003.

H. M. Bolli. The genera *Globigerina* and *Globorotalia* in the Paleocene-Lower Eocene Lizard Springs Formation of Trinidad. *Bulletin of the United States National Museum*, 215:61–81, 1957a.

H. M. Bolli. Planktonic foraminifera from the Eocene Navet Formation in Trinidad, B. W. I. In A. R. Jr. Loeblich et al., editors, *Studies in Foraminifera: Bulletin of the United State Museum*, volume 215, pages 155–172. 1957b.

H. M. Bolli. The genus *Globigerinatheka* Brönnimann. *Journal of Foraminiferal Research*, 2:109–136, 1972.

M. BouDagher-Fadel and G. N. Clark. Stratigraphy, paleoenvironment and paleogeography of Maritime Lebanon: a key to Eastern Mediterranean Cenozoic history. *Stratigraphy*, 3:81–118, 2006.

J. Bowles, L. Tauxe, J. Gee, D. McMillan, and S. C. Cande. Source of tiny wiggles in Chron C5: A comparison of sedimentary relative intensity and marine magnetic anomalies. *Geochemistry, Geophysics, Geosystems*, 4:1049, 2003.

P. W. Boyd and C. S Law. The Southern Ocean Iron RElease Experiment (SOIREE) - introduction and summary. *Deep-Sea Research Part II: Topical Studies in Oceanography*, 48:2425–2438, 2001.

E. A. Boyle. Cadmium, zinc, copper and barium in foraminifera tests. *Earth and Planetary Science Letters*, 53:11–35, 1981.

E. A. Boyle. Manganese carbonate overgrowths on foraminifera tests. *Geochemica et Cosmochimica Acta*, 47:1815–1819, 1983.

E. A. Boyle. Cadmium: Chemical tracer of deepwater paleoceanography. *Paleoceanography*, 3:471–489, 1988.

E. A. Boyle and L. D. Keigwin. Comparison of Atlantic and Pacific paleochemical records for the last 215,000 years: Changes in deep ocean circulation and chemical inventories. *Earth and Planetary Science Letters*, 76:135–150, 1985.

T. J. Bralower. Evidence of surface water oligotrophy during the Paleocene-Eocene thermal maximum: Nannofossil assemblage data from Ocean Drilling Program Site 690, Maud Rise, Weddell Sea. *Paleoceanography*, 17:doi:10.1029/2001PA000662, 2002.

T. J. Bralower, M. A. Arthur, R. M. Leckie, W. V. Sliter, D. J. Allard, and S. O. Schlanger. Timing and paleoceanography of oceanic dysoxia/anoxia in the late Barremian to early Aptian. *Palaois*, 9:335–369, 1994.

T. J. Bralower, D. J. Thomas, J. C. Zachos, M. M. Hirschmann, U. Röhl, H. Sigurdsson, E. Thomas, and D. L. Whitney. High-resolution records of the late Paleocene thermal maximum and circum-Caribbean volcanism: Is there a causal link? *Geology*, 25: 963–966, 1997.

B. Buffett and D. Archer. Global inventory of methane clathrate: sensitivity to changes in the deep ocean. *Earth and Planetary Science Letters*, 227:185–199, 2004.

J. P. Bujak and H. Brinkhuis. Global warming and dinocyst changes across the Paleocene-Eocene boundary. In M.-P. Aubry, S. G. Lucas, and W. A. Berggren, editors, *Late Paleocene-Early Eocene Climatic and Biotic Events in the Marine and Terrestrial Records*, pages 277–295. Columbia University Press, New York, 1998.

D. Bukry. Low-latitude biostratigraphic zonation. In N. T. Edgar, J. B. Saunders, et al., editors, *Initial Reports of the Deep Sea Drilling Project*, volume 15, pages 685–703. U.S. Government Printing Office, Washington D. C., 1973.

D. Bukry. Coccolith and silicoflagellate stratigraphy, northwest Pacific Ocean, Deep Sea Drilling Project Leg 32. In R. L. Larson, R. Moberly, et al., editors, *Initial Reports of the Deep Sea Drilling Project*, volume 32, pages 677–701. U.S. Government Printing Office, Washington, D. C., 1975.

R. F. Butler. *Paleomagnetism: Magnetic Domains to Geological Terranes.* Blackwell Scientific Publications, 1992.

S. C. Cande and D. V. Kent. A new geomagnetic polarity time scale for the Late Cretaceous and Cenozoic. *Journal of Geophysical Research*, 97:13197–13951, 1992a.

S. C. Cande and D. V. Kent. Ultrahigh resolution marine magnetic anomaly profiles: a record of continuous paleointensity variations? *Journal of Geophysical Research*, 97: 15075–15083, 1992b.

S. C. Cande and D. V. Kent. Revised calibration of the geomagnetic polarity timescale for the Late Cretaeous and Cenozoic. *Journal of Geophysical Research*, 100:6093–6095, 1995.

S. C. Cande, J. L. LaBrecque, and W. F. Haxby. Plate kinematics of the South Atlantic: Chron C34 to present. *Journal of Geophysical Research*, 93:13479–13492, 1988.

M. A. Celaya and B. M. Clement. Inclination shallowing from deep-sea sediments from the North Atlantic. *Journal of Geophyscial Research*, 15:52–55, 1988.

F. H. Chamalaun and I. McDougall. Dating geomagnetic polarity epochs in Réunion. *Nature*, 210:1212, 1966.

G. V. Chilingar. Dependence on temperature of Mg/Ca ratio of skeletal structures of organisms and direct chemical precipitates out of sea water. *Bulletin of South California Academy of Science*, 61:45–61, 1962.

B. M. Clement and D. G. Martinson. A quantitative comparison of two paleomagnetic records of the Cobb Mountain subchron from North Atlantic deep-sea sediments. *Journal of Geophysical Research*, 97:1735–1752, 1992.

T. B. Coplen, C. Kendall, and J. Hopple. Comparison of stable isotope reference samples. *Nature*, 302:236–238, 1983.

W. G. Cordey. Morphology and Phylogeny of *Orbulinoides beckmanni* (Saito 1962). *Paleontology*, 11:371–375, 1968.

H. K. Coxall and P. N. Pearson. Taxonomy, biostratigraphy, and phylogeny of the Hantkeninidae (*Clavigerinella, Hantkenina*, and *Cribrohantkenina*). In P. N. Pearson, R. K. Olsson, B. T. Huber, C. Hemleben, and W. A. Berggren, editors, *Atlas of Eocene Planktonic Foraminifera*, volume 41, pages 213–256. Cushman Foundation Special Publication, 2006.

H. K. Coxall, P. N Pearson, N. J. Shackleton, and M. A. Hall. Hantkeninid depth adaptation: An evolving life strategy in a changing ocean. *Geology*, 28:87–90, 2000.

H. K. Coxall, P. A. Wilson, H. Palike, C. H. Lear, and J. Backman. Rapid stepwise onset of Antarctic glaciation and deeper calcite compensation in the Pacific Ocean. *Nature*, 433:53–57, 2005.

H. Craig. The measurement of oxygen isotopes paleotemperatures. In E. Tongiorgi, editor, *Proceedings Spoleto Conference on Stable Isotopes in Oceanographic Studies and Paleotemperatures*, volume 3, pages 3–24. Pisa, 1965.

B. S. Cramer, K. G. Miller, M.-P. Aubry, R. K Olsson, J. D. Wright, D. V. Kent, and J. V. Browning. The Bass River section: An exceptional record of the LPTM event in a neritic setting. *Bulletin de la Société Géologique de France*, 170:883–897, 2000.

B. S. Cramer, J. D. Wright, D. V. Kent, and M-P. Aubry. Orbital climate forcing of δ^{13}C excursions in the Late Paleocene - Early Eocene (chrons C24n - C25n). *Paleoceanography*, 18:doi:10.1029/2003PA000909, 2003.

T. J. Crowley, T. A. Christie, and N. R. Smith. Reassessment of Crete (Greenland) ice core acidity/volcanism link to climate change. *Geophysical Research Letters*, 20: 209–212, 1993.

S. De Villiers, M. Greaves, and H. Elderfield. An intensity ratio calibration method for the accurate determination of Mg/Ca and Sr/Ca of marine carbonates by ICP-AES. *Geochemistry, Geophysics, Geosystems*, 3:doi:10.1029/2001GC000169, 2002.

R. M. DeConto and D. Pollard. Rapid Cenozoic glaciation of Antarctica induced by declining atmospheric CO_2. *Nature*, 421:245–249, 2003.

R. M. DeConto and D. Pollard. Northern Hemisphere Glaciation in the Early Cenozoic? In *EOS Transactions of the American Geophysical Union*, volume 87, Fall Meeting Abstract PP21B-1678, San Francisco, 2006.

P. S. Dekens, D. W. Lea, D. K. Pak, and H. J. Spero. Core top calibration of Mg/Ca in tropical foraminifera: Refining paleotemperature estimation. *Geochemistry, Geophysics, Geosystems*, 3:doi:10.1029/2001GC000200, 2002.

R. V. Demicco, T. K. Lowenstein, and L. A. Hardie. Atmospheric pCO_2 since 60 Ma from records of seawater pH, calcium, and primary carbonate mineralogy. *Geology*, 31:793–796, 2003.

S. D'Hondt, J. C. Zachos, and G. Schultz. Stable isotopic signals and photosymbiosis in Late Paleocene planktic foraminifera. *Paleobiology*, 20:391–406, 1994.

G. R. Dickens, M. Castillo, and J. Walker. A blast of gas in the latest Paleocene: simulating first-order effects of massive dissociation of oceanic methane hydrate. *Geology*, 25:259–262, 1997.

G. R. Dickens, J. R. O'Neil, D. K. Rea, and R. M. Owen. Dissociation of oceanic methane hydrate as a cause of the carbon isotope excursion at the end of the Paleocene. *Paleoceanography*, 10:965–971, 1995.

L. Diester-Haass and R. Zahn. Eocene-Oligocene transition in the Southern Ocean: History of water mass circulation and biological productivity. *Geology*, 24:163–166, 1996.

S. Duggen, P. Croot, U. Schacht, and L. Hoffman. Subduction zone volcanic ash can fertilize the surface ocean and stimulate phytoplankton growth: Evidence from biogeochemical experiments and satellite data. *Geophysical Research Letters*, 34:doi: 10.1029/2006GL027522, 2007.

K. M. Edgar, P. A. Wilson, P. F. Sexton, and Y. Suganuma. No extreme Eocene bipolar glaciation during main Eocene calcite compensation shift. *Nature*, 448:908–911, 2007.

E. N. Edinger and M. J. Risk. Oligocene-Miocene extinction and geographic restriction of Carribean corals: roles of turbidity, temperature, and nutrients. *Palaios*, 9:576–598, 1994.

D. Ekart, T. E. Cerling, I. P. Montanez, and N. J. Tabor. A 400 million year carbon isotope record of pedogenic carbonate: Implications for paleoatmospheric carbon dioxide. *American Journal of Science*, 299:805–827, 1999.

H. Elderfield and G. Ganssen. Past temperature and δ^{18}O of surface ocean waters inferred from foraminiferal Mg/Ca ratios. *Nature*, 405:442–445, 2000.

O. Eldholm and E. Thomas. Environmental impact of volcanic margin formation. *Earth and Planetary Science Letters*, 117:319–329, 1993.

J. Eldrett, I. C. Harding, P. A Wilson, E. Butler, and A. P. Roberts. Continental ice in Greenland during the Eocene and Oligocene. *Nature*, 446:176–179, 2007.

C. Emiliani. Extinctive evolution: extinctive and competitive evolution combine into a unified model of evolution. *Journal of Theoretical Biology*, 97:13–33, 1982.

C. Emiliani. Viral extinctions in deep-sea species. *Nature*, 366:217–218, 1993.

S. Epstein, R. Buchsbaum, H. A. Lowenstam, and H. C. Urey. Revised carbonate-water isotopic temperature scale. *Geological Society of America Bulletin*, 64:1315–1325, 1953.

S. Epstein and T. K. Mayeda. Variations of the $^{18}O/^{16}O$ ratio in natural waters. *Geochemica et Cosmochimica Acta*, 4:213, 1953.

J. Erez. Vital effect on stable-isotope composition seen in foraminifera and coral skeletons. *Nature*, 273:199–202, 1978.

J. Erez. Modification of oxygen isotope records in deep sea cores by Pleistocene dissolution cycles. *Nature*, 281:535–538, 1979.

J. Erez and B. Luz. Experimental paleotemperature equation for planktonic foraminifera. *Geochimica et Cosmochimica Acta*, 47:1025–1031, 1983.

K. A. Farley and S. F. Eltgroth. An alternative age model for the Paleocene-Eocene thermal maximum using extraterrestrial ^{3}He. *Earth and Planetary Science Letters*, 208:135–148, 2003.

G. Faure and T. M. Mensing. *Isotopes, Principles and Applications*. John Wiley and Sons, Inc, Hoboken, New Jersey, third edition, 2005.

W. F. K. Fitt, B. E. Brown, M. E. Warner, and R. P. Dunne. Coral bleaching: interpretation of thermal tolerance limits and thermal thresholds in tropical corals. *Coral Reefs*, 20:51–65, 2001.

F. Florindo and A. P. Roberts. Eocene-Oligocene magnetobiochronology of ODP Sites 689 and 690, Maud Rise, Weddell Sea, Antarctica. *Geological Society of America Bulletin*, 117:46–66, 2005.

P. Frogner, S. Reynir Gíslason, and N. Óskarsson. Fertilizing potential of volcanic ash in ocean surface water. *Geology*, 29:487–490, 2001.

S. Galeotti, R. Coccioni, and R. Gersonde. Middle-Eocene-Early Pliocene Subantarctic planktic foraminiferal biostratigraphy of Site 1090, Agulhas Ridge. *Marine Micropaleontology*, 45:357–387, 2002.

R. D. Gates, G. Baghdasarian, and L. Muscatine. Temperature stress causes host cell displacement in symbiotic Cnidarians: implications for coral bleaching. *The Biological Bulletin*, 182:324–332, 1992.

S. J. Gibbs, T. J. Bralower, P. R. Bown, J. C. Zachos, and L. M. Bybell. Shelf and open-ocean calcareous phytoplankton assemblages across the Paleocene-Eocene Thermal Maximum: Implications for global productivity gradients. *Geology*, 34:233–236, 2006.

S. J. Gibbs, J. R. Young, T. J. Bralower, and N. J. Shackleton. Nannofossil evolutionary events in the mid-Pliocene: an assessment of the degree of synchrony in the extinctions of *Reticulofenestra pseudoumbilicus* and *Sphenolithus abies*. *Palaeogeography, Palaeoclimatology, Palaeoecology*, 217:155–172, 2005.

F. Gradstein, J. G. Ogg, and A. G. Smith. *A Geologic Time Scale 2004*. Cambridge University Press, Cambridge, New York, Melbourne, 2004.

D. W. Graham, M. L. Bender, D. F. Williams, and L. D. Keigwin. Strontium calcium ratios in Cenozoic planktonic foraminifera. *Geochimica et Cosmochimica Acta*, 46: 1281–1292, 1982.

M. Greaves, S. Barker, C. Daunt, and H. Elderfield. Accuracy, standardization, and interlaboratory calibration standards for foraminiferal Mg/Ca thermometry. *Geochemistry, Geophysics, Geosystems*, 6:doi:10.1029/2004GC000790, 2005.

D. R. H. Green, M. J. Cooper, C. R. German, and P. A. Wilson. Optimization of an inductively coupled plasma-optical emission spectrometry method for the rapid determination of high-precision Mg/Ca and Sr/Ca in foraminiferal calcite. *Geochemistry, Geophysics, Geosystems*, 4:doi:10.1029/2002GC000488, 2003.

D. R. Greenwood and S. L. Wing. Eocene continental climates and latitudinal temperature gradients. *Geology*, 23:1044–1048, 1995.

D. Gubbins. The distinction between geomagnetic excursions and reversals. *Geophysical Journal International*, 137:1–3, 1999.

D. Gubbins and E. Herrero-Bervera. *Encyclopedia of Geomagnetism and Paleomagnetism*. Springer-Verlag, Berlin, Heidelberg, New York, 2007.

P. Hallock. Why are larger Foraminifera large? *Paleobiology*, 11:195–208, 1985.

P. Hallock, I. Premoli-Silva, and A. Boersma. Similarities between planktonic and larger foraminiferal evolutionary trends through paleoceanographic changes. *Palaeogeography, Palaeoclimatology, Palaeoecology*, 83:49–64, 1991.

P. Hallock and W. Schlager. Nutrient excess and demise of coral reefs and carbonate platforms. *Palaios*, 1:389–398, 1986.

D. A. T. Harper. *Numerical Palaeobiology: Computer-based Modelling and Analysis of Fossils and their Distributions*. John Wiley and Sons, New York, 1999.

C. G. Harrison and B. M. Funnell. Relationship of paleomagnetic reversals and micropaleontology in two late Cenozoic cores from the Pacific Ocean. *Nature*, 204:566, 1964.

J. R. Heirtzler, G. O. Dickson, E. M. Herron, W. C. Pitman, and X. Le Pichon. Marine magnetic anomalies, geomagnetic field reversals, and motions of the ocean floor and continents. *Journal of Geophysical Research*, 73:2119–2136, 1968.

F. Hilgen. Extension of an astronomically calibrated (polarity) time scale to the Miocene/Pliocene boundary. *Earth and Planetary Science Letters*, 107:349–368, 1991.

A. E. Hindley. New high-resolution Middle Eocene palaeoceanographic records from benthic foraminifera: ODP Site 1051 [MSc thesis]. *Southampton, UK, University of Southampton*, 54 pp, 2003.

J. Hoefs. *Stable Isotope Geochemistry*. Springer-Verlag, Berlin, fourth edition, 1997.

A. Holbourn, W. Kuhnt, M. Schulz, and H. Erlenkeuser. Impacts of orbital forcing and atmospheric carbon dioxide on Miocene ice-sheet expansion. *Nature*, 438:483–487, 2005.

B. T. Huber, R. D. Norris, and K. G. MacLeod. Deep-sea paleotemperature record of extreme warmth during the Cretaceous. *Geology*, 30:123–126, 2002.

B. T. Huber and F. Quillévéré. Revised Paleogene planktonic foraminiferal biozonation for the Austral Realm. *Journal of Foraminiferal Research*, 35:299–314, 2005.

M. Huber, H. Brinkhuis, C. E. Stickley, K. Döös, A. Sluijs, J. Warnaar, S. A. Schellenberg, and G. L. Williams. Eocene circulation of the Southern Ocean: Was Antarctica kept warm by subtropical waters? *Paleoceanography*, 19:doi:10.10292004PA001014, 2004.

P. Huybrechts. Sea-level changes at the LGM from ice-dynamic reconstructions of the Greenland and Antarctic ice sheets during the glacial cycles. *Quaternary Science Reviews*, 21:203–231, 2002.

L. C. Ivany, K. C. Lohmann, F. Hasiuk, D. B. Blake, A. Glass, R. B. Aronson, and R. M. Moody. Eocene climate record of high southern latitude continental shelf: Seymour Island, Antarctica. *Geological Society of America Bulletin*, 120:659–678, 2008.

L. Jovane, F. Florindo, R. Coccioni, J. Dinares-Turell, A. Marsili, S. Monechi, A. P. Roberts, and M. Sprovieri. The middle Eocene climatic optimum event in the Contessa Highway section, Umbrian Apennines, Italy. *Geological Society of America Bulletin*, 119:413–427, 2007.

A. G. Kaneps. Gulf Stream: Velocity fluctuations during the late Cenozoic. *Science*, 204:515–527, 1979.

A. Katz. The interaction of magnesium with calcite during crystal growth at 25 - 90°c and one atmosphere. *Geochimica et Cosmochimica Acta*, 37:1563–1586, 1973.

M. E. Katz, D. R. Katz, J. D. Wright, K. G. Miller, D. K. Pak, N. J. Shackleton, and E. Thomas. Early Cenozoic benthic foraminiferal isotopes: Species reliability and interspecies correction factors. *Paleoceanography*, 18:doi:10.1029/2002PA000798, 2003.

M. E. Katz, K. G. Miller, J. D. Wright, B. S. Wade, J. V. Browning, B. S. Cramer, and Y. Rosenthal. Stepwise transition from the Eocene greenhouse to the Oligocene icehouse. *Nature Geoscience*, 1:329–334, 2008.

G. Keller. Biochronology and paleoclimatic implications of middle Eocene to Oligocene planktonic foraminiferal faunas. *Marine Micropaleontology*, 7:463–482, 1982.

G. Keller. Paleoclimate analyses of middle Eocene through Oligocene planktic foraminiferal faunas. *Palaeogeography, Palaeoclimatology, Palaeoecology*, 43:73–94, 1983.

G. Keller. Biotic effects of late Maastrichtian mantle plume volcanism: implications for impacts and mass extinctions. *Lithos*, 79:317–341, 2005.

G. Keller, N. MacLeod, and E. Barrera. Eocene-Oligocene faunal turnover in planktic foraminifera, and Antarctic glaciation. In D. R. Prothero and W. A. Berggren, editors, *Eocene-Oligocene Climatic and Biotic Evolution*, pages 218–244. Princeton University Press, New Jersey, 1992.

D. C. Kelly. Response of Antarctic (ODP Site 690) planktonic foraminifera to the Paleocene-Eocene thermal maximum: Faunal evidence for ocean/climate change. *Paleoceanography*, 17:doi:10.1029/2002PA000761, 2002.

D. C. Kelly, T. J. Bralower, and J. C. Zachos. Evolutionary consequences of the latest Paleocene thermal maximum for tropical planktonic foraminifera. *Palaeogeography, Palaeoclimatology, Palaeoecology*, 141:139–161, 1998.

D. C. Kelly, T. J. Bralower, J. C. Zachos, I. Premoli-Silva, and E. Thomas. Rapid diversification of planktonic foraminifera in the tropical Pacific (ODP Site 865) during the late Paleocene thermal maximum. *Geology*, 24:423–426, 1996.

J. P. Kennett. Cenozoic evolution of Antarctic glaciation, the circum-Antarctic ocean, and their impact on global paleoceanography. *Journal of Geophysical Research*, 82: 3843–3859, 1977.

J. P. Kennett and L. D. Stott. Abrupt deep-sea warming, palaeoceanographic changes and benthic extinctions at the end of the Palaeocene. *Nature*, 353:225–229, 1991.

D. M. Kerrick. Present and past nonanthropogenic CO_2 degassing from the solid Earth. *Review of Geophysics*, 39:565–585, 2001.

S.-T. Kim and J. R. O'Neil. Equilibrium and non-equilibrium oxygen isotope effects in synthetic carbonates. *Geochimica et Cosmochimica Acta*, 61:3461–3475, 1997.

J. L. Kirschvink. The least-squares line and plane and line analysis of palaeomagnetic data. *Geophysical Journal of the Royal Astronomical Society*, 62:699–718, 1980.

K. P. Kodama. A successful rock magnetic technique for correcting paleomagnetic inclination shallowing: Case study of the Nacimiento Formation, New Mexico. *Journal of Geophyscial Research*, 102:5193–5025, 1997.

M. Kucera and J. P Kennett. Biochronology and evolutionary implications of Late Neogene California margin planktonic foraminiferal events. *Marine Micropaleontology*, 40:67–81, 2000.

J. L. LaBrecque, D. V. Kent, and S. C. Cande. Revised magnetic polarity time scale for Late Cretaceous and Cenozoic time. *Geology*, 330-335, 1977.

C. G. Langereis, M. J. Dekkers, G. J. de Lange, M. Paterne, and P. J. M. van Santvoort. Magnetostratigraphy and astronomical calibration of the last 1.1 myr from an eastern Mediterranean piston core and dating of short events in the Brunhes. *Geophysical Journal International*, 129:75–94, 1997.

R. L. Larson and E. Erba. Onset of the mid-Cretaceous greenhouse in the Barremian-Aptian: Igneous events and the biological, sedimentary, and geochemical responses. *Paleoceanography*, 14:663–678, 1999.

D. W. Lea. Elemental and Isotopic Proxies of Past Ocean Temperatures. In H. Elderfield, editor, *The Oceans and Marine Geochemistry*, volume 6, pages 365–390. Elsevier-Pergamon, Oxford, 2004.

D. W. Lea, T. A. Mashiotta, and H. J. Spero. Controls on magnesium and strontium uptake in planktonic foraminifera determined by live culturing. *Geochimica et Cosmochimica Acta*, 63:2369–2379, 1999.

C. H. Lear, T. R. Bailey, P. N Pearson, H. K. Coxall, and Y. Rosenthal. Cooling and ice growth across the Eocene-Oligocene transition. *Geology*, 36:251–254, 2008.

C. H. Lear, H. Elderfield, and P. A Wilson. Cenozoic deep-sea temperatures and global ice volumes from Mg/Ca in benthic foraminiferal calcite. *Science*, 287:269–272, 2000.

C. H. Lear, H. Elderfield, and P. A Wilson. A Cenozoic seawater Sr/Ca record from benthic foraminiferal calcite and its application in determining global weathering fluxes. *Earth and Planetary Science Letters*, 208:69–84, 2003.

C. H. Lear, Y. Rosenthal, H. K. Coxall, and P. A. Wilson. Late Eocene to early Miocene ice sheet dynamics and the global carbon cycle. *Paleoceanography*, 19: doi:10.109/2004PA001039, 2004.

C. H. Lear, Y. Rosenthal, and N. Slowey. Benthic foraminiferal Mg/Ca-paleothermometry: A revised core-top calibration. *Geochimica et Cosmochimica Acta*, 66:3375–3387, 2002.

M. R. Leckie, T. J. Bralower, and R. Cashman. Oceanic anoxic events and plankton evolution: Biotic response to tectonic forcing during the mid-Cretaceous. *Paleoceanography*, 17:doi:10.1029/2001PA000623, 2002.

L. J. Lourens, A. Sluijs, D. Kroon, J. C. Zachos, E. Thomas, U. Röhl, J. Bowles, and I. Raffi. Astronomical pacing of late Paleocene to early Eocene global warming events. *Nature*, 435:1083–1087, 2005.

W. Lowrie, W. Alvarez, G. Napoleone, K. Perch-Nielson, I. Premoli-Silva, and M. Toumarkine. Paleogene magnetic stratigraphy in Umbrian pelagic carbonate rocks: The Contessa sections, Gubbio. *Geological Society of America Bulletin*, 93:414–432, 1982.

S. P. Lund, G. Acton, B. Clement, M. Hastedt, M. Okada, and R. Williams. Geomagnetic field excursions occurred often during the last million years. *EOS, Transactions of the American Geophysical Union*, 79:178–179, 1998.

D. Lüthi, M. Le Floch, B. Bereiter, T. Blunier, J-M. Barnola, U. Siegenthaler, D. Raynaud, J. Jouzel, H. Fischer, K. Kawamura, and T. F. Stocker. High-resolution carbon dioxide concentration record 650,000-800,000 years before present. *Nature*, 435:379–382, 2008.

M. Lyle, A. Olivarez Lyle, J. Backman, and A. Tripati. Biogenic Sedimentation in the Eocene Equatorial Pacific - The Stuttering Greenhouse and Eocene Compensation Depth. In P. A. Wilson, M. Lyle, and J.V. Firth, editors, *Proceedings of the Ocean Drilling Program, Scientific Results*, volume 199, page doi:10.2973/odp.proc.sr.199.219.2005. College Station, Texas (Ocean Drilling Program), 2005.

M. B. Lythe, D. G. Vaughan, and BEDMAP consortium. BEDMAP: A new ice thickness and subglacial topographic model of Antarctica. *Journal of Geophysical Research*, 106: 11,335–11,351, 2001.

S. Maestre, T. Mora, J. L. Todoli, and A. Canals. Evaluation of several commercially available spray chambers for use in inductively coupled plasma atomic emission spectrometry. *Journal of Analytical Atomic Spectrometry*, 14:61–67, 1999.

A. E. Magguran. *Ecological diversity and its measurement.* Croom Helm, London, 1988.

E. A. Mankinen, J. M. Donnelly, and C. S. Gromme. Geomagnetic polarity event recorded at 1.1 m. y. B. P. on Cobb Mountain, Clear Lake volcanic field, California. *Geology*, 6:653–656, 1978.

T. M. Marchitto. Precise multielemental ratios in small foraminiferal samples determined by sector field ICP-MS. *Geochemistry, Geophysics, Geosystems*, 7: doi:10.1029/2005GC0010186, 2006.

P. J. Markwick. Fossil crocodilians as indicators of Late Cretaceous and Cenozoic climates: Implications for using palaeontological data in reconstructing palaeoclimate. *Palaeogeography, Palaeoclimatology, Palaeoecology*, 137:205–271, 1998.

J. H. Martin, K. H. Coale, K. S. Johnson, S. E. Fitzwater, R. M. Gordon, S. J. Tanner, C. N. Hunter, V. A. Elrod, J. L. Nowicki, T. L. Coley, R. T. Barber, S. Lindley, A. J. Watson, K. Van Scoy, C. S. Law, M. I. Liddicoat, R. Ling, T. Stanton, J. Stockel, C. Collinc, A. Anderson, R. Bidigare, M. Ondruesk, M. Latasa, F. J. Millero, K. Lee, W. Yao, J. Z. Zhang, G. Friedrich, C. Sakamoto, F. Chavez, K. Buck, Z. Kolber, R. Greene, P. Falkowski, S. W. Chisholm, F. Hoge, R. Swift, J. Yungel, S. Turner, P. Nightingale, A. Hatton, P. Liss, and N. W. Tindale. Testing the iron hypothesis in ecosystems of the equatorial Pacific Ocean. *Nature*, 371:399–404, 1994.

P. A. Martin and D. W. Lea. A simple evaluation of cleaning procedures on fossil benthic foraminiferal Mg/Ca. *Geochemistry, Geophysics, Geosystems*, 3: doi:10.1029/2001GC000280, 2002.

D. P Mattey. Gas source mass spectrometry: isotopic composition of lighter elements. In R. Gill, editor, *Modern Analytical Geochemistry: An Introduction to Quantitative Chemical Analysis Techniques for Earth, Environmental and Material Scientists.*, pages 154–170. Longman, Harlow, 1997.

J. M. McCrea. On the isotopic chemistry of carbonates and a paleotemperature scale. *Journal of Chemistry and Physics*, 18:849–853, 1950.

M. W. McElhinny and P. Z. McFadden. *Paleomagnetism Continents and Oceans*, volume 73 of *International Geophysics Series*. Academic Press, San Diego, 2000.

B. McGowran. Maastrichtian to Eocene foraminiferal assemblages in the northern and eastern Indian Ocean region: Correlations and historical patterns. In J. R. Heirtzler et al., editors, *Indian Ocean geology and biostratigraphy*, pages 417–458. American Geophysical Union Special Publication, Washington, D. C., 1977.

B. McGowran, Q. Li, and G. Moss. Cenozoic neritic record in southern Australia: The biogeohistorical framework. In *SEPM (Society for Sedimentary Geology) Special Publication*, volume 56, pages 185–203. 1997.

G. A. Meehl, T. F. Stocker, W. D. Collins, P. Friedlingstein, A. T. Gaye, J. M. Gregory, A. Kitoh, R. Knutti, J. M. Murphy, A. Noda, S. C. B. Raper, I. G. Watterson, A. J. Weaver, and Z. C. Zhao. Global Climate Projections. In S. Solomon, D. Qin, M. Manning, Z. Chen, M. Marquis, K. B. Averyt, M. Tignor, and H. L. Miller, editors, *Climate Change 2007: The Physical Science Basis. Contribution of Working Group I to the Fourth Assessment of the Intergovernmental Panel on Climate Change*. Cambridge University Press, Cambridge and New York, 2007.

C. B. Miller. *Biological Oceanography*. Blackwell Science Ltd, London, 2004.

K. G. Miller, R. G. Fairbanks, and G. S. Mountain. Tertiary oxygen isotope synthesis, sea level history, and continental margin erosion. *Paleoceanography*, 2:1–19, 1987.

K. G. Miller, J. D. Wright, and R. G. Fairbanks. Unlocking the Ice House: Oligocene-Miocene Oxygen Isotopes, Eustasy, and Margin Erosion. *Journal of Geophysical Research*, 96:6829–6848, 1991.

M. Mohan and K. S. Soodan. Middle Eocene planktonic foraminiferal zonation of Kutch, India. *Micropaleontology*, 16:37–46, 1970.

T. C. Moore, N. J. Shackleton, and N. G. Pisias. Paleoceanography and the diachrony of radiolarian events in the eastern equatorial Pacific. *Paleoceanography*, 8:567–586, 1993.

K. Moran, J. Backman, H. Brinkhuis, S. C. Clemens, T. Cronin, G. R. Dickens, F. Eynaud, J. Gattacceca, M. Jakobsson, R. W. Jordan, M. Kaminski, J. King, N. Koc, A. Krylov, N. Martinez, J. Mattheissen, D. McInroy, T. Moore, J. Onodera, M. O'Regan, H. Pälike, B. Rea, D. Rio, T. Sakamoto, D. C. Smith, K. Stein, R. St John, I. Suto, N. Suzuki, K. Takahashi, M. Watanabe, M. Yamamoto, J. Farell, M. Frank, P. Kubik, W. Jokat, and Y. Kristoffersen. The Cenozoic palaeoenvironment of the Arctic Ocean. *Nature*, 441:601–605, 2006.

G. Napoleone, I. Premoli-Silva, F. Heller, P. Cheli, S. Corezzi, and A. Fischer. Eocene magnetic stratigraphy at Gubbio, Italy, and its implications for Paleogene geochronology. *Bulletin of the Geological Society of America*, 94:181–191, 1983.

M. Nicolo, G. R. Dickens, C. Hollis, and J. C. Zachos. Multiple early Eocene hyperthermals: Their sedimentary expression on the New Zealand continental margin and in the deep sea. *Geology*, 35:699–702, 2007.

M. Nocchi, G. Parisi, P. Monaco, S. Monechi, and M. Madile. Eocene and early Oligocene micopaleontology and paleoenvironments in SE Umbria, Italy. *Palaeogeography, Palaeoclimatology, Palaeoecology*, 67:181–244, 1988.

R. D. Norris. Symbiosis as an evolutionary innovation in the radiation of Paleocene planktic foraminifera. *Paleobiology*, 22:461–480, 1996.

R. D. Norris. Pelagic species diversity, biogeography, and evolution. In D. H. Erwin and S. L. Wing, editors, *Deep Time: Paleobiology's Perspective*, pages 236–258. The Paleontological Society, Lawrence, KS, 2000.

R. D. Norris. Bleaching of Symbiotic Foraminifera During Extreme Global Warming at the Paleocene-Eocene Boundary. *EOS Transactions of the American Geophysical Union*, 88, Fall Meeting Abstract OS14A-07, 2007.

R. D. Norris and U. Röhl. Carbon cycling and chronology of climate warming during the Palaeocene/Eocene transition. *Nature*, 401:775–778, 1999.

D. Nürnberg, J. Bijima, and C. Hemleben. Assessing the reliabilty of magnesium in foraminiferal calcite as a proxy for water mass temperatures. *Geochemica et Cosmochimica Acta*, 60:803–814, 1996.

J. G. Ogg. Magnetic Polarity Time Scale of the Phanerozoic. In T. J. Ahrens, editor, *Global Earth Physics: A Handbook of Physical Constants*, volume 1 of *AGU Reference Shelf*, pages 240–270. American Geophysical Union, Washington, D. C., 1995.

J. G. Ogg and L. Bardot. Aptian through Eocene Magnetostratigraphic correlation of the Blake Nose Transect (Leg 171B), Florida Continental Margin. In D. Kroon, R. D. Norris, and A. Klaus, editors, *Proceedings of the Ocean Drilling Program, Scientific Results*, volume 171B, page doi:10.2973/odp.proc.sr.171b.104.2001. College Station, Texas (Ocean Drilling Program), 2001.

J. G. Ogg and A. G. Smith. The geomagnetic polarity time scale. In F. Gradstein, J. G. Ogg, and A. G. Smith, editors, *A Geologic Time Scale 2004*, pages 63–86. Cambridge University Press, Cambridge, 2004.

J. R O'Neil, R. N. Clayton, and T. K. Mayeda. Oxygen isotope fractionation in divalent metal carbonates. *Journal of Chemistry and Physics*, 51:5547–5558, 1969.

N. D. Opdyke, B. Glass, J. D. Hays, and J. Foster. Paleomagnetic study of Antarctic deep-sea cores. *Science*, 154:349–357, 1966.

M. Pagani, K. Caldeira, D. Archer, and J. C. Zachos. An Ancient Carbon Mystery. *Science*, 314:1556–1557, 2006.

M. Pagani, J. C. Zachos, K. H. Freeman, B. Tipple, and S. M. Bohaty. Marked Decline in Atmospheric Carbon Dixoide Concentration During the Paleogene. *Science*, 309: 600–603, 2005.

H. Pälike and F. Hilgen. Rock clock synchronization. *Nature Geoscience*, 1:282, 2008.

H. Pälike, R. D. Norris, J. O Herrle, P. A. Wilson, H. K. Coxall, C. H. Lear, N. J. Shackleton, A. Tripati, and B. S. Wade. The Heartbeat of the Oligocene Climate System. *Science*, 314:1894–1898, 2006.

H. Pälike, N. J. Shackleton, and U. Röhl. Astronomical forcing in late Eocene marine sediments. *Earth and Planetary Science Letters*, 193:589–602, 2001.

J. M. Pares and L. Lanci. A Middle Eocene-Early Miocene Magnetic Polarity Stratigraphy in Equatorial Pacific Sediments (ODP Site 1220). In *Timescales of the Paleomagnetic Field*, volume 145, pages 131–140. American Geophysical Union Monograph, 2004.

R. Park and S. Epstein. Carbon isotope fractionation during photosynthesis. *Geochimica et Cosmochimica Acta*, 21:110–126, 1960.

P. N. Pearson. Cladogenetic, extinction and survivorship patterns from a lineage phylogeny: the Paleogene planktonic foraminifera. *Micropaleontology*, 42:179–188, 1996.

P. N. Pearson and W. A. Berggren. Taxonomy, biostratigraphy, and phylogeny of *Morozovelloides* n. gen. In P. N Pearson, R. K Olsson, B. T. Huber, C. Hemleben, and W. A. Berggren, editors, *Atlas of Eocene Planktonic Foraminifera*, volume 41, pages 327–342. Cushman Foundation Special Publication, 2006.

P. N. Pearson and W. P. Chaisson. Paleocene to Midde Miocene Planktonic Foraminifer Biostratigraphy of the Ceara Rise. In N. J. Shackleton, W. B. Curry, F. M. Richter, and T. J. Bralower, editors, *Proceedings of the Ocean Drilling Program, Scientific Results*, volume 154, pages 33–68. Ocean Drilling Program, College Station, Texas, 1997.

P. N. Pearson, P. W. Ditchfield, J. Singano, K. G. Harcourt-Brown, C. J. Nicholas, R. K. Olsson, N. J. Shackleton, and M. A. Hall. Warm tropical sea surface temperatures in the Late Cretaceous and Eocene epochs. *Nature*, 413:481–487, 2001.

P. N. Pearson, R. K Olsson, B. T. Huber, C. Hemleben, and W. A. Berggren. *Atlas of Eocene Planktonic Foraminifera*, volume 41 of *Cushman Foundation Special Publication*. Cushman Foundation for Foraminiferal Research, 2006.

P. N. Pearson and M. R. Palmer. Middle Eocene Seawater pH and Atmospheric Carbon Dioxide Concentrations. *Science*, 284:1824–1826, 1999.

P. N. Pearson and M. R. Palmer. Atmospheric carbon dioxide concentrations over the past 60 million years. *Nature*, 406:695–699, 2000.

P. N. Pearson, N. J. Shackleton, and M. A. Hall. Stable isotope palaeoecology of Middle Eocene planktonic foraminifera and multi-species isotope stratigraphy, DSDP Site 523, South Atlantic. *Journal of Foraminiferal Research*, 23:123–140, 1993.

T. F. Pederson and N. B. Price. The geochemistry of manganese carbonate in Panama Basin sediments. *Geochemica et Cosmochimica Acta*, 46:59–68, 1982.

S. F. Pekar, N. Christie-Blick, M. A. Kominz, and K. G. Miller. Calibration between eustatic estimates from backstripping and oxygen isotopic records for the Oligocene. *Geology*, 30:903–906, 2002.

S. F. Pekar, R. M. DeConto, and D. M. Harwood. Resolving a late Oligocene conundrum: Deep-sea warming and Antarctic glaciation. *Palaeogeography, Palaeoclimatology, Palaeoecology*, 231:29–40, 2006.

S. F. Pekar, A. Hucks, M. Fuller, and S. Li. Glacioeustatic changes in the Early and Middle Eocene (51-42 Ma): Shallow-water stratigraphy from ODP Leg 189 Site 1171 (South Tasman Rise) and deep-sea δ^{18}O records. *GSA Bulletin*, 117(7/8):1081–1093, 2005.

L. D. Pena, E. Calvo, I. Cacho, S. Eggins, and C. Pelejero. Identification and removal of Mn-Mg rich contaminant phases on foraminiferal tests: Implications for Mg/Ca past temperature reconstructions. *Geochemistry, Geophysics, Geosystems*, 6: doi:10.1029/2005GC000930, 2005.

Perkin Elmer. OPTIMA 4000 DV SERIES; optical system and Segmented-array Charge-coupled Device (SCD) detector. *Available at http://www.perkinelmer.com*, 2002.

J. R. Petit, J. Jouzel, D. Raynaud, N. I. Barkov, J. M. Barnola, I. Basile, M. Benders, J. Chappellaz, M. Davis, G. Delaygue, M. Delmotte, V. M. Kotlyakov, M. Legrand, V. Y. Lipenkov, C. Lorius, L. Pépin, C. Rotz, E. Saltzman, and M. Stievard. Climate and atmospheric history of the past 420,000 yr from the Vostok ice core, Antarctica. *Nature*, 399:429–436, 1999.

M. R. Petrizzo. The onset of the Paleocene -Eocene Thermal Maximum (PETM) at Sites 1209 and 1210 (Shatsky Rise, Pacific Ocean) as recorded by planktonic foraminifera. *Marine Micropaleontology*, 63:187–200, 2007.

P. R. Pinet, P. Popenoe, and D. F. Nelligan. Gulf Stream: Reconstruction of Cenozoic flow patterns over the Blake Plateau. *Geology*, 9:266–270, 1981.

R. Z. Poore and R. K. Matthews. Oxygen isotope ranking of Late Eocene and Oligocene planktonic foraminifers - implications for Oligocene sea-surface temperatures and global ice-volume. *Marine Micropaleontology*, 9:111–134, 1984.

C. J. Poulsen, D. Pollard, and T. S. White. General circulation model simulation of the δ^{18}O content of continental precipitation in the middle Cretaceous: A model-proxy comparison. *Geology*, 35:199–202, 2007.

I. Premoli-Silva and A. Boersma. Atlantic Eocene planktic foraminiferal biogeography and paleohydrographic indicators. *Palaeogeography, Palaeoclimatology, Palaeoecology*, 67:315–356, 1988.

I. Premoli-Silva and A. Boersma. Atlantic Paleogene Planktonic Foraminiferal Bioprovincial Indices. *Marine Micropaleontology*, 14:357–371, 1989.

I. Premoli-Silva, B. S. Wade, and P. N. Pearson. Taxonomy, biostratigraphy and phylogeny of *Globigerinatheka* and *Orbulinoides*. In P. N. Pearson, R. K. Olsson, B. T. Huber, C. Hemleben, and W. A. Berggren, editors, *Atlas of Eocene Planktonic Foraminifera*, volume 41, pages 169–215. Cushman Foundation Special Publication, 2006.

F. Proto Decima and H. M. Bolli. Evolution and Variability of *Orbulinoides beckmanni* (Saito). *Eclogae Geologicae Helvetiae*, 63:883–905, 1970.

F. Quillévéré, R. D. Norris, D. Kroon, and P. A Wilson. Transient ocean warming and shifts in carbon resevoirs during the early Danian. *Earth and Planetary Science Letters*, 265:600–615, 2008.

I. Raffi. Precision and accuracy of nannofossil biostratigraphic correlation. In *Astronomical (Milankovitch) Calibration of the Geological Time-Scale*, volume 357 of *Philosophical Transactions of the Royal Society of London, Series A: Mathematical, Physical and Engineering Sciences*, pages 1975–1993. Royal Society Publishing, London, 1999.

I. Raffi, J. Backman, E. Fornaciari, H. Pälike, D. Rio, L. J. Lourens, and F. Hilgen. A review of calcareus nannofossil astrobiochronology encompassing the past 25 million years. *Quaternary Science Reviews*, 25:3113–3137, 2006.

I. Raffi, J. Backman, D. Rio, and N. J. Shackleton. Plio-pleistocene nannofossil biostratigraphy and calibration to oxygen isotope stratigraphies from Deep Sea Drilling Project Site 607 and Ocean Drilling Program Site 677. *Paleoceanography*, 8:387–403, 1993.

D. M. Raup. Biological extinction in earth history. *Science*, 231:1528–1533, 1986.

A. C. Ravelo and R. G. Fairbanks. Oxygen isotopic composition of multiple species of planktonic foraminifera: recorders of the modern photic zone temperature gradient. *Paleoceanography*, 7:815–831, 1992.

G. E. Ravizza, R. D. Norris, J. Blusztajn, and M. P. Aubry. An Osmium isotope excursion associated with the late Paleocene Thermal Maximum: Evidence of intensified chemical weathering. *Paleoceanography*, 16:155–163, 2001.

M. E. Raymo and M. E. Ruddiman. Teconic forcing of late Cenozoic climate. *Nature*, 359:117–122, 1992.

A. P. Roberts. High-resolution magnetic analysis of sediment cores: Strengths, limitations and strategies for maximizing the value of long-core magnetic data. *Physics of the Earth and Planetary Interiors*, 156:162–178, 2006.

A. P. Roberts and J. C. Lewin-Harris. Marine magnetic anomalies; evidence that 'tiny wiggles' represent short-period geomagnetic polarity intervals. *Earth and Planetary Science Letters*, 183:375–388, 2000.

A. P. Roberts, J. S. Stoner, and C. Richter. Coring-induced magnetic overprints and limitiations of the long-core paleomagnetic measurement technique: some observations from Leg 160, Eastern Mediterranean Sea. In K. C. Emesi, A. H. F. Robertson, and C. Richter, editors, *Proceedings of the Ocean Drilling Program, Initial Reports*, volume 160, pages 497–505. College Station, Texas, 1996.

A. Robock. Volcanic Eruptions and Climate. *Review of Geophsics*, 38:191–219, 2000.

U. Röhl, T. Westerhold, T. J. Bralower, and J. C. Zachos. On the duration of the Paleocene-Eocene thermal maximum (PETM). *Geochemistry, Geophysics, Geosystems*, 8:doi:10.1029/2007GC001784, 2007.

U. Röhl, J. C. Zachos, E. Thomas, D. C. Kelly, B. Donner, and T. Westerhold. Multiple Early Eocene Thermal Maximums. *EOS, Transactions of the American Geophysical Union*, 85, Fall Meeting Abstract PP14A-02, 2004.

Y. Rosenthal, E. A. Boyle, and N. Slowey. Temperature control on the incorporation of magnesium, strontium, fluorine and cadmium into benthic foraminiferal shells from Little Bahama Bank: Prospects for thermocline paleoceanography. *Geochemica et Cosmochimica Acta*, 61:3633–3643, 1997.

Y. Rosenthal, G. P. Lohmann, K. C. Lohmann, and R. M. Sherrell. Incorporation and preservation of Mg in *Globigerinioides sacculifer*: Implications for reconstructing the temperature and O-18/O-16 of seawater. *Paleoceanography*, 15:135–145, 2000.

D. L. Royer, R A. Berner, I. P. Montañez, N. J. Tabor, and D. J. Beerling. CO_2 as a primary driver of Phanerozoic climate. *Geological Society Today*, 14:4–10, 2004.

D. L. Royer, S. L. Wing, D. J. Beerling, D. W. Jolley, P. L. Koch, L. J. Hickey, and R A. Berner. Paleobotanical Evidence for Near Present-Day Levels of Atmospheric CO_2 During Part of the Tertiary. *Science*, 292:2310–2313, 2001.

T. Saito. Eocene Planktonic Foraminifera from Hahajima (Hillsborough Island). *Transactions of the Palaeontological Society of Japan, N. S.*, 45:209–225, 1962.

J. Salaj. *Microbiostratigraphie du Crétacé et du Paléogène de la Tunisie septentrionale et orientale (Hypostratotypes Tunisiens)*. Geologicky Ustav Dionyza Stura, Bratislava.

B. K. Samanta. Middle Eocene planktonic foraminifera from Lakhpat, Cutch, western India. *Micropaleontology*, 16:185–215, 1970.

S. M. Savin, R. G. Douglas, and F. G. Stehli. Tertiary marine paleotemperatures. *Geological Society of America Bulletin*, 86:1499–1510, 1975.

B. Schmitz, B. Peucker-Ehrenbrink, C. Heilmann-Clausen, G. berg, F. Asaro, and C-T. A. Lee. Basaltic explosive volcanism, but no comet impact, at the paleocene-eocene boundary: high resolution chemical and isotopic records from egypt, spain and denmark. *Earth and Planetary Science Letters*, 225:1–17, 2004.

D. P. Schrag, J. F. Adkins, K. McIntyre, J. L. Alexander, D. A. Hodell, C. D. Charles, and J. F. McManus. The oxygen isotopic composition of seawater during the Last Glacial Maximum. *Quaternary Science Reviews*, 21:331–342, 2002.

G. Scopelliti, A. Bellanca, R. Coccioni, V. Luciani, R. Neri, F. Baudin, M. Chiari, and M. Marcucci. High-resolution geochemical and biotic records of the Tethyan 'Bonarelli Level' (OAE2, latest Cenomanian) from the Calabianca-Guidaloca composite section, northwestern Sicily, Italy. *Palaeogeography, Palaeoclimatology, Palaeoecology*, 208: 293–317, 2004.

P. F. Sexton, P. A. Wilson, and R. D. Norris. Testing the Cenozoic multisite composite δ^{18}O and δ^{13}C curves: New monospecific Eocene records from a single locality, Demerara Rise (Ocean Drilling Program Leg 207). *Paleoceanography*, 21: doi:10.1029/2005PA0011253, 2006a. PA2019.

P. F. Sexton, P. A. Wilson, and P. N Pearson. Palaeoecology of late middle Eocene planktic foraminifera and evolutionary implications. *Marine Micropaleontology*, 60: 1–16, 2006b.

N. J. Shackleton. Attainment of isotopic equilibrium between ocean water and the benthonic foraminifera genus *Uvigerina*: Isotopic changes in the ocean during the last glacial. *Centre National de la Recherche Scientifique*, 219:203–209, 1974.

N. J. Shackleton, A. Berger, and W. R. Peltier. An alternative astronomical calibration of the lower Pleistocene timescale based on ODP Site 677. *Transactions of the Royal Society of Edinburgh, Earth Sciences*, 81:251–261, 1990.

N. J. Shackleton and J. P. Kennett. Paleotemperature History of the Cenozoic and the Initiation of Antarctic Glaciation: Oxygen and Carbon Stable Isotope Analyses in DSDP Sites 277, 279 and 281. In J. P. Kennett, R. E. Houtz, et al., editors, *Initial*

Reports of the Deep Sea Drilling Project, volume 29, pages 743–755. U.S. Government Printing Office, Washington D. C., 1975.

N. J. Shackleton and N. D. Opdyke. Oxygen isotope and paleomagnetic stratigraphy of equatorial Pacific core V28-239: Oxygen isotope temperatures and ice volumes on a 10^5 year and 10^6 year scale. *Quaternary Research*, 3:39–55, 1973.

Shipboard Scientific Party. Site 647. In S. P. Srivastara, M. A. Arthur, B. Clement, et al., editors, *Proceedings of the Ocean Drilling Program, Initial Reports (Part A)*, volume 105, pages 419–674. College Station, Texas (Ocean Drilling Program), 1987.

Shipboard Scientific Party. Site 1051. In R. D. Norris, D. Kroon, and A. Klaus, editors, *Proceedings of the Ocean Drilling Program, Initial Reports*, volume 171B, pages 171–239. College Station, Texas (Ocean Drilling Program), 1998.

Shipboard Scientific Party. Leg 198 Summary. In T. J. Bralower, I. Premoli Silva, M. J. Malone, et al., editors, *Proceedings of the Ocean Drilling Program, Initial Reports*, volume 198, page doi:10.2973/odp.proc.ir.198.101.2002. College Station, Texas (Ocean Drilling Program), 2002a.

Shipboard Scientific Party. Leg 199 summary. In M. Lyle, P. A. Wilson, T.R. Janecek, et al., editors, *Proceedings of the Ocean Drilling Program, Initial Reports*, volume 199, page doi:10.2973/odp.proc.ir.199.101.2002. College Station, Texas (Ocean Drilling Program), 2002b.

Shipboard Scientific Party. Site 1260. In J. Erbacher, D. C. Mosher, M. J. Malone, et al., editors, *Proceedings of the Ocean Drilling Program, Initial Reports*, volume 207, page doi:10.2973/odp.proc.ir.207.108.2004. College Station, Texas (Ocean Drilling Program), 2004.

H. Sigurdsson, S. Kelley, R. M. Leckie, S. Carey, T. J. Bralower, and J. King. History of circum-Caribbean explosive volcanism: $^{40}Ar/^{39}Ar$ dating of tephra layers. In M. R. Leckie, H. Sigurdsson, G. Acton, and G. Draper, editors, *Proceedings of the Ocean Drilling Program. Scientific Results.*, volume 165, pages 299–314. Ocean Drilling Program, College Station, Texas, 2000.

C. W. Sinton and R. A. Duncan. Potential links between ocean plateau volcanism and global ocean anoxia at the Cenomaian-Turonian boundary. *Economic Geology*, 92: 836–842, 1997.

A. Sluijs, S. Schouten, M. Pagani, M. Woltering, H. Brinkhuis, J. S. Sinninghe Damste, G. R. Dickens, M. Huber, G. J. Reichart, R. Stein, J. Mattheissen, L. J. Lourens, N. Pedentchouk, J. Backman, K. Moran, and Expedition Scientists. Subtropical Arctic Ocean temperatures during the Palaeocene/Eocene thermal maximum. *Nature*, 441: 610–613, 2006.

R. P. Speijer, B. Schmitz, M. P. Aubry, and S. D. Charisi. The latest Paleocene benthic extinction event: punctuated turnover in outer neritic foraminiferal faunas from Gebel Aweina, Egypt. In M.-P. Aubry and C. Benjamini, editors, *Paleocene/Eocene boundary events in space and time*, volume 44 of *Israel Journal of Earth Sciences*, pages 207–222. 1996.

C. Spencer-Cervato, H. R. Thiersten, D. B. Lazarus, and J-P. Beckmann. How synchronous are Neogene marine plankton events? *Paleoceanography*, 9:739–763, 1994.

H. J. Spero. Do planktic foraminifera accurately record shifts in the carbon isotopic composition of sea water CO_2? *Marine Micropaleontology*, 19:275–285, 1992.

H. J. Spero and M. J. DeNiro. The influence of symbiont photosynthesis on the δ^{18}O and δ^{13}C values of planktonic foraminiferal shell calcite. *Symbiosis*, 4:213–228, 1987.

H. J. Spero and D. F. Williams. Extracting environmental information from planktonic foraminiferal δ^{13}C data. *Nature*, 335:717–719, 1988.

D. J. A. Spofforth, C. Agnini, H. Pälike, E. Fornaciari, L. Giusberti, L. Lanci, V. Luciani, G. Muttoni, D. Rio, and S. M. Bohaty. Evidence for the Middle Eocene Climatic Optimum ("MECO") in the Venetian Alps. In *European Geophysical Union General Assembly*, volume EGU2008-A-07758, Vienna, 2008.

H. M. Stoll and D. P Schrag. Effects of Quaternary sea level changes on strontium isotopes in seawater. *Geochimica et Cosmochimica Acta*, 62:1107–1118, 1998.

H. M. Stoll, D. P. Schrag, and S. C. Clemens. Are seawater Sr/Ca variations preserved in Quaternary foraminifera? *Geochimica et Cosmochimica Acta*, 63:3535–3547, 1999.

M. Storey, R. A. Duncan, and C. Tegner. Timing and duration of volcanism in the North Atlantic Igneous Province: Implications for geodynamics and links to the Iceland hotspot. *Chemical Geology*, 241:264–281, 2007.

L. D. Stott and J. P. Kennett. Antarctic Paleogene Planktonic Foraminifer Biostratigraphy: ODP Leg 113, Sites 689 and 690. In *Proceedings of the Ocean Drilling Program, Scientific Results*, volume 113, pages 549–569. Ocean Drilling Program, College Station, Texas, 1990.

N. N. Subbotina. *Iskopaemye foraminifery SSSR (Globigerinidy, Khantokeninindy i Globorotaliidy): Trudy Vsesoyznogo Nauchno-Issle-dovatel'skogo Geologo-razvedochnogo Instituta (VNIGRI)*, volume 76. GOSTOPETEKHIZDAT, Leningrad, 1953.

Y. Suganuma and J. G. Ogg. Campanian through Eocene magnetostratigraphy of Sites 1257-1261, ODP Leg 207, Demerara Rise (western equatorial Atlantic). In D. C. Mosher, J. Erbacher, and M. J. Malone, editors, *Proceedings of the Ocean Drilling*

Program, Scientific Results, volume 207, page doi:10.2973/odp.proc.sr.207.102.2006. College Station, Texas (Ocean Drilling Program), 2006.

J. A. Tarduno, W. V. Sliter, L. Kroenke, M. R. Leckie, H. Mayer, J. J. Mahoney, R. Musgrave, M. Storey, and E. L. Winterer. Rapid formation of the Ontong Java Plateau by Aptian mantle plume volcanism. *Science*, 18:399–403, 1991.

L. Tauxe and P. Hartl. 11 million years of Oligocene geomagnetic field behaviour. *Geophysical Journal International*, 128:217–229, 1997.

E. Thomas and N. J. Shackleton. The Paleocene-Eocene benthic foraminiferal extinction and stable isotope anomalies. In R. W. O'B Knox, R. M. Corfield, and R. E. Dunay, editors, *Correlation of the early Paleogene in northwest Europe: Geological Society of London Special Publication*, volume 101, pages 401–441. 1996.

R. C. Tjalsma and G. P. Lohmann. *Paleocene-Eocene Bathyal and Abyssal Benthic Foraminifera from the Atlantic Ocean*, volume 4 of *Micropaleontology Special Publication*. Micropaleontology Press, 1983.

M. Toumarkine and H. Luterbacher. Paleocene and Eocene planktic foraminifera. In H. M. Bolli, J. B. Saunders, and K. Perch-Nielson, editors, *Plankton Stratigraphy*, pages 87–154. Cambridge University Press, Cambridge, 1985.

A. Tripati, J. Backman, H. Elderfield, and P. Ferretti. Eocene bipolar glaciation associated with global carbon cycle changes. *Nature*, 436:341–346, 2005.

S. C. Turgeon and R. A. Creaser. Cretaceous oceanic anoxic event 2 triggered by a massive magmatic episode. *Nature*, 454:323–326, 2008.

F. J. Vine and D. H. Matthews. Magnetic anomalies over oceanic ridges. *Nature*, 199: 947–949, 1963.

B. S. Wade. Planktonic foraminiferal biostratigraphy and mechanisms in the extinction of *Morozovella* in the late middle Eocene. *Marine Micropaleontology*, 51:23–38, 2004.

B. S. Wade, N. Al-Sabouni, C. Hemleben, and D. Kroon. Symbiont bleaching in fossil planktonic foraminifera. *Evolutionary Ecology*, 22:doi:10.1007/10682–007–9176–6, 2007.

B. S. Wade and D. Kroon. Middle Eocene regional climate instability: Evidence from the western North Atlantic. *Geology*, 30:1011–1014, 2002.

B. S. Wade, D. Kroon, and R. D. Norris. Orbitally forced climate change in late mid-Eocene time at Blake Nose (Leg 171B): evidence from stable isotopes in foraminifera. In D. Kroon, R. D. Norris, and A. Klaus, editors, *Western North Atlantic Paleogene and Cretaceous Palaeoceanography*, volume 183, pages 273–291. The Geological Society of London, Special Publications, London, 2001.

T. Wang. Inductively Coupled Plasma Optical Emission Spectrometry. In J. Cazes, editor, *Ewing's Analytical Instrumentation Handbook*, pages 57–74. CRC Press, third edition, 2004.

M. W. Wara, L. D. Anderson, S. A. Schellenberg, R. Franks, C. A. Ravelo, and M. L. Delaney. Application of a radially viewed inductively coupled plasma-optical emission spectrophotometer to simultaneous measurement of Mg/Ca, Sr/Ca and Mn/Ca ratios in marine biogenic carbonates. *Geochemistry, Geophysics, Geosystems*, 4: doi:10.1029/2003GC000525, 2003.

M. Y. Warraich and H. Nishi. Eocene Planktic Foraminiferal Biostratigraphy of the Sulaiman Range, Indus Basin, Pakistan. *Journal of Foraminiferal Research*, 33:219–236, 2003.

R. Weeks, C. Laj, L. Endignoux, M. Fuller, A. P. Roberts, R. Manganne, E. Blanchard, and W. Goree. Improvements in long-core measurement techniques: applications in palaeomagnetism and palaeoceaography. *Geophysical Journal International*, 114:651–662, 1993.

J. A. Wolfe. Distribution of major vegetational types during the Tertiary. In E. T. Sundquist and W. S. Broecker, editors, *The Carbon Cycle and Atmospheric CO_2; Natural Variations Archaean to Present*, volume 32 of *Geophysical Monographs*, pages 357–375. American Geophysical Union, Washington, DC, 1985.

G. Wu and W. H. Berger. Planktonic foraminifer: differential dissolution and the Quaternary stable isotope record in the west equatorial Pacific. *Paleoceanography*, 4: 181–198, 1989.

J. C. Zachos, J. R. Breza, and S. W. Wise. Early Oligocene ice-sheet expansion on Antarctica: Stable isotope and sedimentological evidence from Kerguelen Plateau, southern Indian Ocean. *Geology*, 20:569–573, 1992.

J. C. Zachos, M. Pagani, L. Sloan, E. Thomas, and K. Billups. Trends, Rhythms, and Aberrations in Global Climate 65 Ma to Present. *Science*, 292:686–693, 2001.

J. C. Zachos, U. Röhl, S. A. Schellenberg, A. Sluijs, D. A. Hodell, D. C. Kelly, E. Thomas, M. Nicolo, I. Raffi, L. J. Lourens, and D. Kroon. Rapid Acidification of the Ocean During the Paleocene-Eocene Thermal Maximum. *Science*, 308:1611–1615, 2005.

J. C. Zachos, L. D. Stott, and G. P. Lohmann. Evolution of early Cenozoic marine temperatures. *Paleoceanography*, 9:353–387, 1994.

J. C. Zachos, M. W. Wara, S. M. Boharty, M. L. Delaney, M. R. Petrizzo, A. Brill, T. J. Bralower, and I. Premoli-Silva. A Transient Rise in Tropical Sea Surface Temperature During the Paleocene-Eocene Thermal Maximum. *Science*, 302:1551–1554, 2003.

J. D. A. Zijderveld. Ac demagnetization of rocks: analysis of results. In D. W. Collinson, K. M. Creer, and S. K. Runcorn, editors, *Methods in Palaeomagnetism*, pages 254–286. Elseiver, New York, 1967.